The University of
Nottingham

UNITED KINGDOM · CHINA · MALAYSIA

ELECTROCHEMISTRY OF MOLECULES IN NANOTUBES

Robert Luke M^{c}Sweeney, MSci

Thesis submitted to the University of Nottingham
for the degree of Doctor of Philosophy

February 2016

Abstract

The work presented in this thesis describes the use of carbon nanotubes as both electrodes and containers for electrochemical reactions. The cyclic voltammetry (CV) and coulometry of metallocenes, half-sandwich complexes, fullerene containing molecules and organic molecules are presented.

The nanoscale confinement in carbon nanotubes affects both the spatial confinement and the electronic properties of the guest-molecule. Encapsulation of molecules can also lead to a change in the electronic properties of the host-nanotube. The specific nature of the interactions between the guest-molecule and nanotube was investigated by the encapsulation of molecules inside carbon nanotubes followed by measurements of the electrochemical redox processes of the guest-molecules using CV and coulometry.

The internal diameter of the single-walled carbon nanotubes (SWNT) used throughout this thesis is commensurate with the size of single molecules, which leads to the mechanism of reactions being influenced by the limited space around the guest-molecule. This can also lead to the products of some electrochemical reactions being templated by the nanotube's shape and size. Furthermore, the unique electronic band structure of carbon nanotubes affects interactions of certain guest-molecules with the internal wall of the nanotube, the magnitude and type of interaction associated with different guest-molecules depends on the energy of the highest occupied molecular orbital (HOMO) of the guest-molecule as well as the electronic states and the Fermi level of the host-nanotube. The effect of this

interaction on both the guest-molecule and host-nanotube is determined using CV, coulometry and linear sweep voltammetry (LSV).

An example of this is the encapsulation of cobaltocene and ferrocene in SWNT, a strong interaction between cobaltocene ($Co(Cp)_2$) and the nanotube is observed, but only a weak interaction is observed between ferrocene ($Fe(Cp)_2$) and the nanotube through changes in the cyclic voltammetry (CV) of the encapsulated molecules. Additionally, these interactions affect the electronic bands of the nanotube due to the injection of electrons into the nanotube conduction band. Using coulometry and LSV, the magnitude of this charge injection into the nanotube and whether the nanotube will be metallic or semiconducting is determined. The redox processes of the electrochemically induced ligand exchange of $Cp^{Me}Mn(CO)_3$ inside single-walled carbon nanotubes is probed, investigating how a reaction that relies on both an external nucleophile and the elimination of a ligand is changed when confined in the nanoscale channel of the nanotube. Finally, the use of nanotubes as a reaction vessel for an internal electrochemical reaction is investigated, whereby the nanotubes pre-arrange the reactant molecule in position for particular reactions. The confinement enables an electrochemical reaction that wouldn’t occur in bulk solution and the carbon nanotube templates a new product inaccessible by other means.

The electronic and steric interactions of nanotubes with guest-molecules change the properties of the host and the guest, thus leading to exciting new materials and new products that cannot be synthesised otherwise. The results presented in this thesis demonstrate the significance of the electrochemistry of molecules in nanotubes for fundamental chemistry and provide a new methodology of making novel products by utilising carbon nanotubes as reaction vessels and nanoscale electrodes.

Publications

1. R. L. McSweeney, T. W. Chamberlain, E. S. Davies and A. N. Khlobystov, Single-walled carbon nanotubes as nano-electrode and nano-reactor to control the pathways of a redox reaction, *Chem. Commun.* , 2014, **50**, 14338.

2. R. L. McSweeney, T. W. Chamberlain, M. Baldoni, M. A. Lebedeva, E. S. Davies, E. Besley and A. N. Khlobystov, Direct Measurement of Electron Transfer in Nanoscale Host-Guest Systems: Metallocenes in Carbon Nanotubes, *Accepted. Chemistry- A European Journal, 2016*

Acknowledgements

There are a number of people I would like to express my gratitude to for support and guidance during my time working towards my PhD. Firstly and most importantly to my supervisor, Prof. Andrei Khlobystov, who has continually been enthusiastic and supporting of my project. He has always provided riveting scientific discussions, excellent suggestions that have progressed my doctoral studies and he has always pointed me in the right direction. Andrei has gone to extra lengths to provide me with the tools required for my project, always supporting me in my suggestions of equipment that will further my work. I would also like to thank him for the many hours he has spent imaging my samples, providing me with invaluable data that would be inaccessible without him.

Secondly, I would like to thank Dr. Thomas Chamberlain for his daily support. Tom has helped to steer my project planting many seeds for scientific ideas. He is always happy to help, often going out of his way to discuss an idea or problem. I am extremely grateful for his assistance and patience. He has helped me to develop my presentation and writing skills, taking extra time to teach me and allowing me to evolve my own style. He has also aided me experimentally by supplying some of the nanotube-guest samples that I used for this research, such as the C_{60}dimer@SWNT. Despite Tom moving to a different university he has continued to support me through my thesis which is above and beyond the call of duty. Without his support, this thesis would not have been possible and I am indebted to him. Tom has become a friend over the time of my PhD, we have had many heated but good humoured non-scientific discussions, played many games of cricket, golf (mini and mega) and I hope that we remain in contact.

Dr. Stephen Davies has been invaluable for all his electrochemical discussions. He has ensured that I have considered all eventualities and that the fundamental electrochemistry is correct with all my outlandish ideas. Some of my suggestions have taken him out of his comfort zone but he has endeavoured to bring conversation back to first principles and therefore improving the science. I have greatly enjoyed our discussions and am grateful for all his help.

I would like to thank the rest of the Nottingham Nanocarbon Group, in particular Dr. Graham Rance for always making time for my questions and also for making suggestions for this thesis. I would also like to thank Masha Lebedeva for teaching me how to use electrochemistry and the joys that come with it, she also synthesised the C_{60}dimer that I used for my electrochemical experiments. I would like to thank Craig Stoppiello and Bradley Thomas for critiquing many of my presentations and along with Scott Miners for all the scientific discussions. I am also grateful to Craig for imaging some of my samples. I have been lucky to supervise an excellent undergraduate student, Lewis Pickard, whose work helped to further this thesis. All the members Nottingham Nanocarbon group have provided a happy working environment and made my time here particularly enjoyable through a friendly atmosphere and the numerous social events.

My thanks go to Dr. Matteo Baldoni and Prof. Elena Besley, who I was fortunate to collaborate with. Matteo has performed calculations for many of the nanotube-guest species included in this thesis, providing hard numbers to back up our theories, often tailoring his calculations for our specific needs. He is always willing to explain his calculations to me and I would like to thank him for all his help.

I would like to express my deepest gratitude to my family. My Mum and Dad supported me in my decision to pursue chemistry and then to progress onto a PhD. They have provided me with love and kindness, always being on the other end of the phone for advice. Finally, I would like to thank my wife, Samantha M^{c}Sweeney. She has been with me from the beginning of my chemistry career and stuck with me through the hardships of my PhD. We married in my third year of PhD so she had only limited help for wedding organisation. I love her more today than I did yesterday but less than I will tomorrow. I could not have achieved this without her.

“Success is 1% inspiration, 98% perspiration and 2% attention to detail” – P. H. Dunphy 2012

Acronyms

A.U.	Arbitary units
BDD	Boron doped diamond
CAR	β-carotene
CNT	Carbon nanotube
$Co(Cp)_2$	Cobaltocene
CV	Cyclic voltammetry
CVD	Chemical vapour deposition
DA	Dopamine
DCM	Dichloromethane
DFT	Density functional theory
DMF	Dimethyl formamide
DNA	Deoxyribonucleic acid
DOQ	Dopamine ortho-quinone
DOS	Density of states
DPV	Differential pulse voltammetry
DWNT	Double-walled carbon nanotube
EDX	Energy dispersive X-ray spectroscopy
E_F	Fermi level
Fc	Ferrocene
$Fe(Cp)_2$	Ferrocene
$Fe(Cp^{4Me})_2$	Octamethyl ferrocene
$Fe(Cp^{5Me})_2$	Decmethyl ferrocene
$Fe(Cp^{Me})_2$	Dimethyl ferrocene
GC	Glassy carbon
GCE	Glassy carbon electrode
GNF	Graphetised nanofibre
HOMO	Highest occupied molecular orbital
HOPG	Highly ordered pyrolytic graphite

HR	High resolution
IR	Infra-red
LASER	Light amplification by stimulated emission of radiation
L-M	Ligand to metal
LSV	Linear sweep voltammetry
LUMO	Lowest unocupied molecular orbital
M-L	Metal to ligand
MOF	Metal organic framework
MWNT	Multi-walled carbon nanotubes
N.B.	Nota bene
oDCB	ortho-dichlorobenzene
PES	Photoemmission spectroscopy
PTFE	Polytetrafluoroethylene
S-GNR	Sulfur terminated graphetised nanoribbon
SOMO	Singly occupied molecular orbital
SWNT	Single-walled carbon nanotubes
TBA	Tetra butyl ammonium
TEM	Transmission electron miscroscopy
TGA	Thermogravimetric analysis
TR	Time resolved
TTF	Tetrathiofulvalene
UV-vis	Ultraviolent-visible
XAS	X-ray absorbtion spectroscopy
XPS	X-ray photoelectron spectroscopy

Symbols

θ_p	Pyrimidalisation angle
[O]	Concentration of oxidised molecules
[R]	Concentration of reduced molecules
A	Electrode area
C_0	Concentration
D_0	Diffusion coefficient of solvent
d_{NT}	Nanotube diameter
E	Energy
E	Redox potential of the guest-molecule of interest in solution electrochemistry
$E_{1/2}$	Half wave potential
E_F	Fermi level
E^{Θ}	Potential of the Fermi level of metallic SWNT or the potential of the bottom of the conduction band in semiconducting nanotubes
F	Faraday constant
i_p	Peak current
iR	Current x resistance
m	Weight of material
M	Molar mass
n	Number of electrons transferred
Q	Charge
r	Radius
R	Gas constant
T	Temperature
v	Scan rate
z	Number of electrons
ΔEp	Anodic and cathodic peak splitting in CV
$\Delta G^{\#}$	Gibbs energy of activation

$\Delta H^{\#}$	Activation enthalpy
$\Delta S^{\#}$	Activation entropy
ν	Wavenumber
υ_1	C=C stretching mode

Contents

1 Carbon in electrochemistry

1.1 Carbon for electrodes **1**

1.1.1 Glassy carbon (GC) as an electrode 2

1.1.2 Highly ordered pyrolytic graphite (HOPG) as an electrode 5

1.1.3 Diamond as an electrode 7

1.2 Nanocarbons for electrochemistry **9**

1.2.1 Graphene for electrochemistry 9

1.2.2 Carbon nanotubes for electrochemistry 12

1.3 Electrochemistry of molecules encapsulated in single-walled carbon nanotubes **17**

1.4 Summary **29**

1.5 References **30**

2 Methodology development

2.1 Introduction **35**

2.2 Aim and objectives **35**

2.3 Experimental set-up **36**

2.3.1 Calculating the surface area of the SWNT electrode 38

2.3.2 Calculating the number of molecules in the diffusion layer of GCE for comparison with the number of encapsulated guest-molecules in SWNT 40

2.4 Electrochemical properties of nanotubes **40**

2.4.1 Linking electrochemistry with theoretical calculations 41

2.5 Electron transfer regime 45

2.5.1 Non-zero ΔEp for guest@SWNT 46

2.5.2 Effects of immobilisation of $Fe(Cp)_2$ observed in CV 49

2.5.3 The effect of different solvents in the electrochemical cell 46

2.6 Fill percentage values for guest@SWNT 52

2.6.1 Geometrical considerations 52

2.6.2 Application of chronocoulometry to determine fill percentage 54

2.6.3 Gravimetric analysis 56

2.6.4 Thermogravimetric analysis (TGA) 57

2.6.5 Quantitative EDX 58

2.6.6 TEM imaging approximation 59

2.6.7 Summary of different methods for nanotube fill percentage determination 61

2.7 TEM imaging for metallocene@SWNT 62

2.8 Conclusions 65

2.9 References 66

3 The effect of nanotube encapsulation on guest-molecules

3.1 Introduction 68

3.1.1 Use of spectroscopic methods to investigate nanotube-guest interactions 68

3.2 Aim and objectives 71

3.3 Results and discussion 72

3.3.1 Filling of SWNT with different metallocenes 72

3.3.2 Cyclic voltammetry of ferrocene@SWNT 73

3.3.3 Cyclic voltammetry of cobaltocene@SWNT 75

3.3.4 Cyclic voltammetry of different methylated ferrocenes inside SWNT 79

3.3.5 Comparison of cyclic voltammetry of ferrocene in carbon nanotubes of different internal diameter (SWNT and DWNT) 87

3.4 Conclusions 88

3.5 Experimental 89

3.5.1 Preparation of nanotube samples 89

3.5.2 HRTEM and EDX 91

3.5.3 Electrochemistry 98

3.5.4 Theoretical calculations 99

3.6 References 99

4 The effect of guest-molecules on the host-nanotube

4.1 Introduction 101

4.2 Aim and objectives 102

4.3 Results and discussion 102

4.3.1 Chronocoulometry methodology 102

4.3.2 Electrochemical characterisation of the DOS of empty SWNT 107

4.3.3 Determining the doping of host-nanotubes by the encapsulation of guest-molecules 110

4.3.4 Chronocoulometry of $Fe(Cp^{XMe})_2$ 114

4.3.5 Quantitative determination of the electron transfer between guest-molecule and host-nanotube 118

4.4 Conclusions 121

4.5 Experimental 122

4.5.1 Preparation of metallocene filled nanotubes 122

4.5.2 Fill percentage calculated by TEM extrapolation 122

4.5.3 Electrochemistry 122

4.5.4 Theoretical calculations 125

4.5.5 HRTEM and EDX 125

4.6 References 126

5 Utilising nanotubes to control the pathway of the redox induced reactions of $Cp^{Me}Mn(CO)_3$ 127

5.1 Introduction 127

5.2 Aim and objectives 127

5.2.1 Manganese piano stool complexes 128

5.3 Results and discussion 129

5.3.1 Filling of SWNT with $Cp^{Me}Mn(CO)_3$ 129

5.3.2 Electrochemistry of $Cp^{Me}Mn(CO)_3$/SWNT 132

5.3.3 Electrochemistry of $Cp^{Me}Mn(CO)_3$@SWNT 137

5.3.4 Change in the pathway of the electrochemical reaction 140

5.4 Conclusions 142

5.5 Experimental 143

5.5.1 General 143

5.5.2 Preparation of $Cp^{Me}Mn(CO)_3$@SWNT 144

5.5.3 Electrochemistry 144

5.5.4 Infrared spectroscopy 144

5.5.5 HRTEM 145

5.5.6 EDX 145

5.6 References 145

6 Nanotubes as templates for electrochemical synthesis

6.1 Introduction 147

6.1.1 The effect of potential on reactions in solution compared to anchored molecules 147

6.1.2 The role of carbon nanotubes as templates 150

6.2 Aim and objectives 152

6.3 Results and discussion 153

6.3.1 Cyclic voltammetry of C_{60}@SWNT 153

6.3.2 Cyclic voltammetry of C_{60}dimer@SWNT 154

6.3.3 Electrochemical transformation of fulleropyrrolidino ferrocene ($C_{60}Fe(Cp)_2$) 164

6.3.4 Electrochemical conversion of TTF to S-GNR 176

6.4 Conclusions 185

6.5 Experimental 186

6.5.1 Synthesis of $C_{60}Fe(Cp)_2$ 186

6.5.2 Synthesis of C_{60}dimer 188

6.5.3 Preparation of SWNT samples 188

6.5.4 Electrochemistry 190

6.5.5 HRTEM 190

6.5.6 EDX 191

6.6 References 191

Concluding remarks 194

1 Carbon in electrochemistry

1.1 Carbon for electrodes

There are numerous materials that can be used as electrodes such as carbon, metals and metal oxides. Metals such as platinum, gold and silver are highly conductive with a high density of states (DOS) resulting in low capacitive currents. Furthermore, metal electrodes have the advantage that they are easy to assemble and manipulate. Metal oxides are less widely used, however, they are semiconducting resulting in interesting electrochemical reactions occurring at their surface such as the production of a photocurrent upon irradiation of an electrode with light or due to a photolytic reaction occurring in the solution near the electrode surface. Moreover, metal oxides such as tin and indium oxides, can be fabricated so that they are optically semi-transparent, providing a platform for performing spectroelectrochemical and photoelectrochemical studies. Whilst metals and metal oxides are useful electrodes, they are often non-innocent in catalysis and can interact with analyte molecules, an alternative material is carbon. There is a veritable plethora of different types of carbon electrodes such as glassy carbon, graphite, diamond, carbon fibres and carbon black. Electrochemical reactions are often slower at carbon electrodes than metallic electrodes due to the lower DOS and electron transfer kinetics that depend on structure and surface preparation.[1] Some forms of carbon have a high surface activity forming many functional groups of carboxyl and hydroxyl groups allowing for the introduction of high levels of dopants[2] but also an increased susceptibility to electrode poisoning. So why use carbon as an electrode? Carbon is a fascinating material whereby different structures of the same element result in hugely different properties such as electrical transport, optical and thermal properties.[2] Carbon has been used since the early days of electrochemistry research[3] due to its versatility and interesting properties. There are many different allotropes of carbon such as glassy carbon (GC), highly ordered pyrolytic carbon (HOPG), diamond, graphene and carbon nanotubes. Each of these allotropes exhibit different properties which will be described throughout this chapter. These different forms of carbon are of great interest in electrochemical studies and for possible applications in energy storage,[2, 4-6] electrochemical sensing[7-11] and fuel cells,[12-15] amongst many other uses.

1.1.1 Glassy carbon (GC) as an electrode

One of the most commonly used electrode materials is glassy carbon (GC), it is isotropic and mostly composed of sp^2 carbons. GC has very high thermal stability, is reported to have a closed porosity and is chemically resistant. It is a favourable electrode for studying catalytic reactions as GC does not participate in the catalysis unlike some metal electrodes. However, due to its hardness and relative fragility the size and shape of prepared electrodes is limited, though reproducible.[16] It is suggested that the structure consists of a tangled network of graphitic ribbons, where individual ribbons are bound by either weak π-π bonds (weak confluence) or strong covalent bonds (strong confluence) (Figure 1).[17] This would suggest a high level of edge carbon which are often functionalised with reactive groups such as hydroxyl or carboxyl groups.

However, the proposed open structure and presence of many edge carbons, hence reactive dangling bonds, does not account for the reported closed porosity or the low reactivity. A number of different suggestions have been put forward for the structure of GC such as graphite-like fibrils with carbyne-like chains[18] and more interestingly fullerene-like structures (Figure 2a).[19, 20] It is reported that the structure of GC observed in transmission electron microscopy (TEM) consists of tightly curled single carbon layers (Figure 2) and was attributed to an imperfect multi-layered giant fullerene, with some small clusters of fullerene also present.[21] However, it is usual to find fullerene molecules in most carbon samples, especially those that have been heat treated to 2500 °C so it is unlikely that these fullerenes form a major part of the GC structure. The presence of five membered rings is also reported[21] but with no direct proof. While the evidence for this structure is questionable, a disordered graphite structure is convincing and would explain the apparent chemical inertness and closed porosity, with far fewer edge carbons and a much lower porosity.

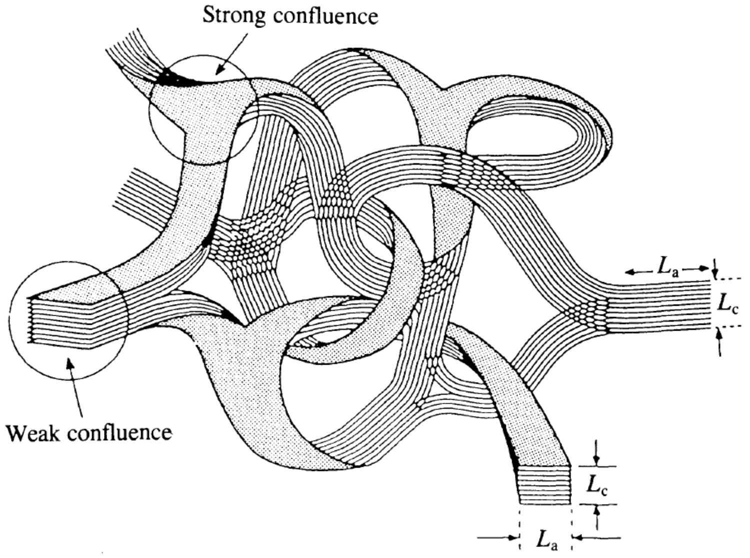

Figure 1. Representation of the structure of glassy carbon. The confluence is the junction of carbon ribbons. There are two types of confluence in GC, one whereby the junction is bound by weak π-π bonds between graphitic layers (weak confluence) and another that involves covalent bonding of carbon between strands (strong confluence).[16, 17]

It is incredible that there is such uncertainty over the structure of such a commonly used material such as GC. What is certain is that GC is constructed of mostly sp^2 carbons and can be made into a consistent shape for electrodes. Glassy carbon does not include any metals in the preparation ensuring the electrode does not participate in any catalytic processes, it also provides a good platform for the addition of other carbon materials such as nanocarbons.[22-26]

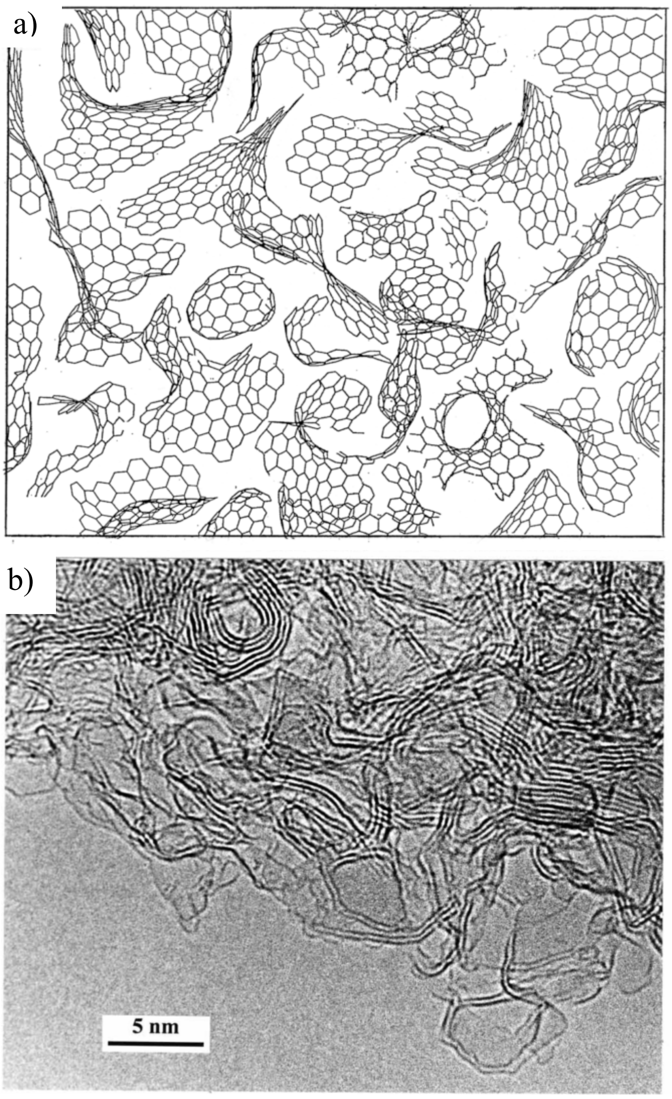

Figure 2. a) Proposed structure of glassy carbon. Small graphitic sections that contain five membered rings allowing for curvatures similar to fullerene. b) A TEM image of glassy carbon.[19]

1.1.2 Highly ordered pyrolytic graphite (HOPG) as an electrode

HOPG is a commonly used alternative to GC, it is a high purity graphite and has an angular spread in the stacking of its graphite sheets of less than 1^{o}.[27] Due to the anisotropy, many of its physical properties such as thermal, electrical and optical properties are different in different orientations,[28] the edge plane sites (Figure 3) are reported to be where the electron transfer occurs.[1, 29] Further to this, it was reported that the basal plane of sp^2 carbon is inert to electron transfer even to outer-sphere redox couples[30, 31] and this was extended to the sidewalls of single walled nanotubes.[32, 33] However, recent studies using scanning probe microscopy and scanning electrochemical cell microscopy to probe electrochemical processes of outer sphere redox couples at HOPG, state that the electroactivity at the basal plane of HOPG is far greater than previously reported.[34, 35] Similar studies also report fast electron transfer at nanotube sidewalls[36-38] which will be discussed later in the chapter. These publications have implications for the use of many graphitic electrodes and how they are fabricated. They are of particular interest to the fields of nanotubes and graphene where the "basal" planes dominate the structures.

In the density of states (DOS) of single layer graphene, the valence and conduction bands intersect, creating a zero band gap semiconductor. Upon addition of further layers of graphene there is a small overlap in the conduction and valence bands. When subsequent layers are added to form graphite, an overlap of about 41 meV is observed, resulting in semi-metallic behaviour[39] which increases electron transfer kinetics at the Fermi level.

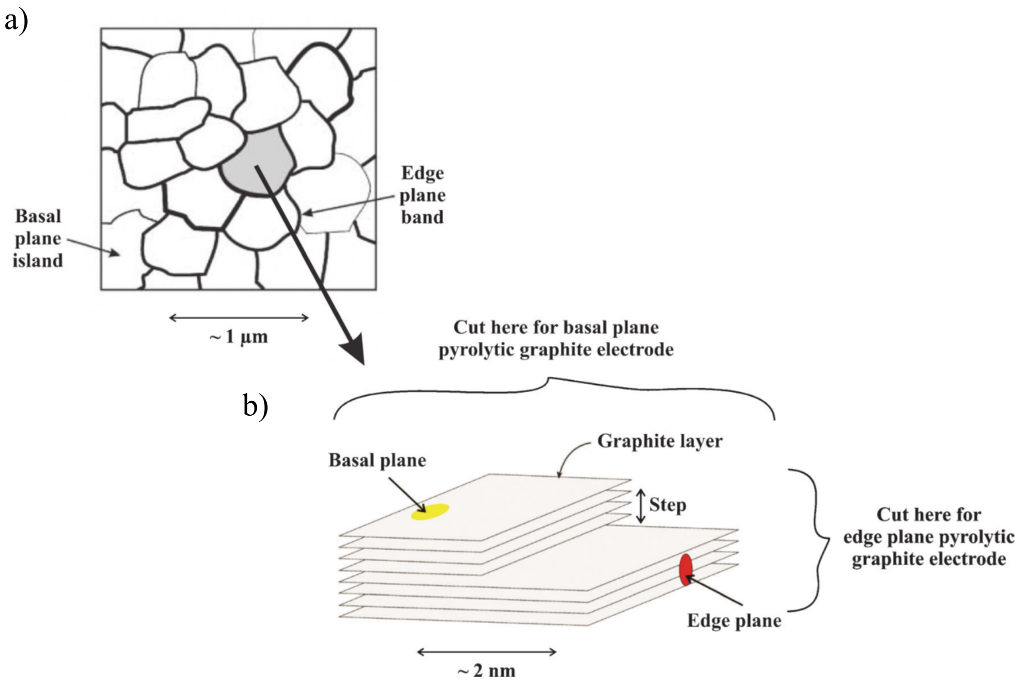

Figure 3. a) Schematic of a HOPG surface showing basal plane and edge plane islands. b) Schematic of HOPG surface showing its basal plane and edge plane sites. The electron transfer kinetics dominate at the edge plane compared to the basal plane.[40]

The graphene layers of HOPG are weakly bonded together via π-π interactions so layers can be peeled off, providing an atomically smooth, surface with step-edges that can be used to reasonably mimic graphene.[41] This highly ordered plane has many possible uses, for instance nucleation or assembly of ordered structures such as metals[42-44] and metal oxide nanoribbons.[41, 45] This methodology of ordering metals and metal oxides on electrodes may relate to organising single-walled nanotubes (SWNT) on HOPG electrodes or the nucleation on the step-edges of graphetised nanofibres (GNF).[46-50] The same electrodeposition methods used on HOPG[42, 43, 45] could be used for the organisation of species on the step-edges of GNF attached to electrodes. The dangling bonds at the step-edge on HOPG can bend and form a highly strained, curved structure in some areas of HOPG samples (Figure 4),[51] this is similar to the step-edges observed in GNF again leading to a similar mechanism of nucleation of metals on HOPG and GNF step-edges.

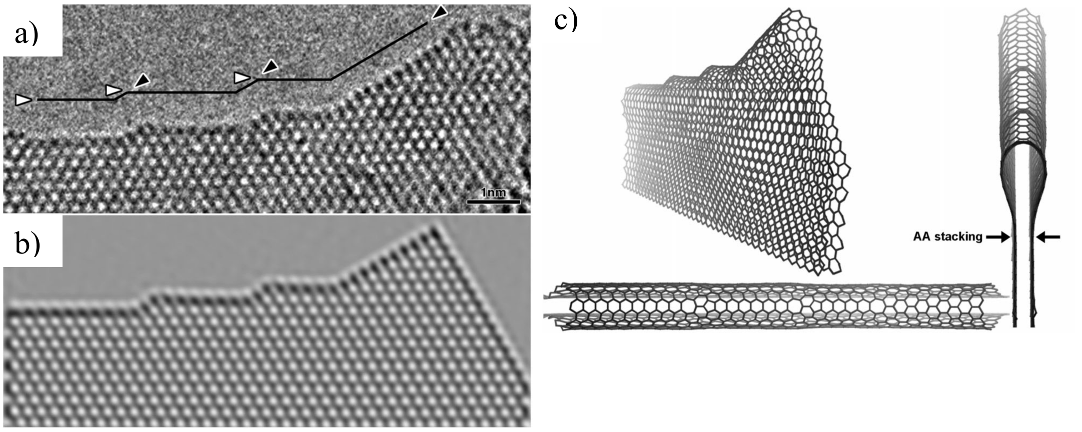

Figure 4. a) High resolution transmission electron microscopy (HRTEM) image of bilayer graphene. The zigzag and armchair directions are marked with white and black arrowheads. b) A simulated image of c) the folded monolayer graphene. Each intersecting point between the armchair and the zigzag areas has a pentagon-heptagon pair.[51]

1.1.3 Diamond as an electrode

Diamond is used as an electrode due to its extreme mechanical hardness, capacity to be doped,[52-54] chemical inertness[55-57] and, once doped, it possesses a wide potential window.[58] Diamond electrodes are receiving considerable interest in the literature, particularly boron doped diamond (BDD)[59-63] due to the relative inertness to surface oxidation and fouling, as well as maintaining a wide potential window.[64] Boron can be used to p-dope diamond by atom substitution into the lattice and, depending on the level of doping, the diamond becomes either semiconducting or metal like.[65]

BDD electrodes have a small capacitive current leading to an enhanced signal to noise ratio, which, combined with a low fouling rate, means BDD electrodes are a good candidate for sensing applications. Target analytes include trace hazardous metals such as lead, mercury, cadmium, arsenic, *etc* whose toxicity is of growing concern in the food industry. The use of BDD allows for detection limits to be as low as parts per trillion.[66] For use in bio-sensing, the immobilisation of a biomolecule is often required. This is one of the downfalls of BDD as the chemical inertness prevents such immobilisation, providing a challenge for its use in biosensors. However, recent studies have shown that it is possible to introduce sp^2 carbon onto BDD electrodes which can then be activated to produce quinone groups on the carbon.[67] Not only are the qunione groups useful for pH sensing but also act as a background for further functionalisation of receptor molecules. Another example using carbon on BDD is the sputtering of nanotubes with immobilised nickel oxide onto BDD for the sensing of L-serine.[68] The immobilisation of nickel hydroxide nanoparticles directly on BDD has also been achieved.[69, 70] These studies show that it is possible to use the beneficial inert structure and low capacitance of BDD along with the immobilisation of other more reactive groups to achieve new hybrids for the applications of sensing and catalysis.

Diamond is the only example presented here of non-sp^2 carbon being used as an electrode and shows the further versatility of carbon in both terms of structural and electrical properties. The inclusion of dopants generates electrical conductivity while retaining the strong interatomic bonding of sp^3 carbon.

1.2 Nanocarbons for electrochemistry

In general, nanocarbons possess high surface area, high conductivity and nanostructured features of commensurate size to molecules, allowing for controllable interactions at the molecular scale, bridging the gap between the nano- and macro-world. Therefore, nanocarbon is increasingly being used in electrochemistry, especially graphene and nanotubes as electrodes.

1.2.1 Graphene for electrochemistry

Graphene is a two-dimensional sheet of sp^2 bonded carbon atoms in a hexagonal array.[71] While previously known to be a component of many different carbon structures such as glassy carbon and HOPG, as well as a parent of many nanocarbons (Figure 5), it was only in 2004 that a new route was discovered for the preparation of single layer, atomically thin graphene sheets, whereby mechanical exfoliation using scotch tape was used to isolate single layer graphene.[72]

As stated earlier (section 1.1.2), graphene is a zero band gap semiconductor.[73] Graphene can be doped by electrochemical doping[74, 75] or introduction of heteroatoms into the lattice[76] which allows the electron transport and optical properties of the material to be tuned.[77, 78]

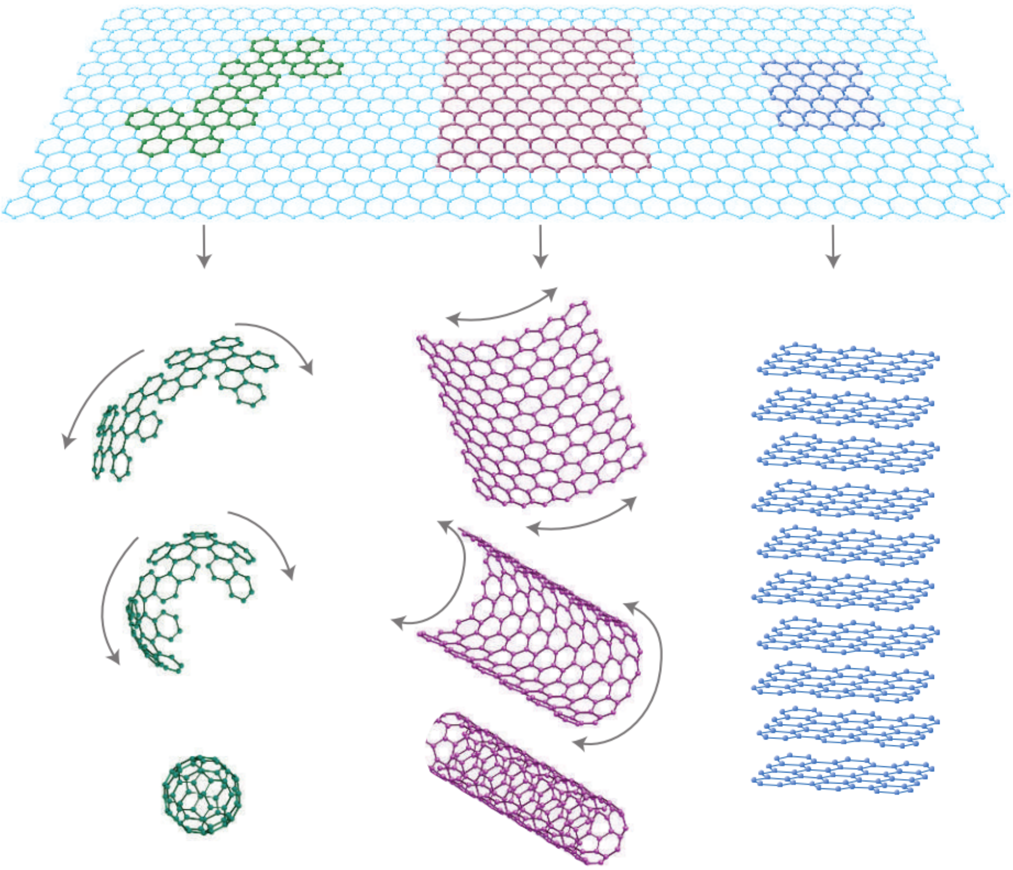

Figure 5. Graphene is structurally related to many carbon structures such as zero dimension fullerenes,[79] and is the primary component of one dimensional nanotubes or stacked to form three dimensional graphite.[73]

When used as an electrode, graphene acts in many ways like graphite, the exfoliation of graphite into smaller fragments of graphene increases the amount of basal planes per volume but the amount of available edge plane (Figure 3) remains similar. Therefore, it is suggested that using graphene rather than graphite does not provide many advantages for compounds that are electrochemically active at the edge plane but inactive at the basal plane.[80] Interestingly, a high coverage of single layer graphene slows the electron transfer rates due to blockage of the electroactive edges.[81] In order to improve the electrochemical activity, adaptations are made to graphene such as the introduction of defects or the increased concentration of graphene islands which are reported to dominate the electrochemical response of chemical vapour deposition (CVD) grown graphene[82] due to the increased availability of electron density at the edges and in defects. Similarly adding further layers of graphene increases the edge plane density, and therefore, the speed of heterogeneous electron transfer due to increased DOS.[83] Even so, it is still reported that, in the case of solely electrode kinetics, graphite is a superior electrode.[81] However, as discussed with HOPG, recent research shows the comparable electroactivity of the basal planes with the edge planes.[34, 35] Similar scanning electrochemical cell microscopy on graphene shows that the basal planes are electrochemically active as well as the edge planes for outer sphere redox couples[84] and has profound implications for the development for graphene technologies.

Graphene is transparent in the ultraviolet-visible (UV-Vis) spectrum, absorbing at fewer wavelengths than indium tin oxide,[85] allowing for fundamental spectroelectrochemical investigations of electron transfer mechanisms and applications in photovoltaics. Graphene also has advantages over conventional metal oxide electrodes including: chemical inertness, high electrical conductivity and the ease of surface modification. This transparency and mechanical strength make graphene a candidate for the production of flexible screens for electronics. One of the other big drives is the use of graphene as ultracapacitors. Graphene sheets are ideal for this due to their high surface area for increased storage and their high conductivity for fast power absorption, power release and a good performance over a wide range of potentials.[86]

The UV-Vis transparency, high surface area and the ability to dope graphene make it a versatile material for use in electrochemistry. Many possible applications are emerging such as use for flexible screens and ultracapacitors. Furthermore, the electronic structure and ability to functionalise graphene has led to some exciting new research in areas including optoelectronics,[87] coatings[88] and nanoelectromechanical systems.[89]

1.2.2 Carbon nanotubes for electrochemistry

Carbon nanotubes possess an astonishing array of physical and chemical properties and have been the focus of intensive of research since their discovery. The ballistic conductivity of carbon nanotubes[90] has prompted particular interest in the area of electrochemistry. Nanotubes are nanoscopic tubular structures comprised of sp^2 carbon atoms organised in a hexaganol array. The idealised wall of a nanotube cylinder is made of one or more concentric sheets of graphene. Whilst carbon nanotubes inherit many properties from the parent structure of graphene, such as the high electrical conductivity[91] and high surface area,[24] the unique structure of nanotubes improves upon many of these properties. Firstly, the nanoscale diameter and macroscopic length result in a much increased surface area due to the protrusion of nanotubes from the surface of an electrode, unlike graphene that lays flat. Furthermore, the lack of an electronic bandgap in graphene has hindered application in electronic devices, carbon nanotubes on the other hand, possess a tuneable band gap. Cutting graphene into strips, called nanoribbons, causes the opening of a gap between the conduction and valence bands of graphene, with the nanoribbon width inversely proportional to the introduced bandgap.[92-94] However, this is difficult to do on a preparative scale. Nanotubes can be viewed as rolled up nanoribbons,[40] therefore, inducing interesting electronic properties and the ability to be metallic or semiconducting, controlled purely by the diameter and chirality.[95] The rolling up of graphene imposes periodic phase boundaries that are not observed in graphene and therefore a quantisation of the electronic wavevector. This results in only certain allowed energies of electrons in the nanotube. If there are no allowed states at the nonbonding orbitals (Fermi level) of the SWNT then the SWNT is a semiconductor and therefore there will be slow electron transfer at these energies. On the other hand, if there are allowed states for an electron at the Fermi level, the nanotube is metallic, resulting in faster electron transfer in this energy region. Van Hove singularities are observed in the electronic density of states of SWNT which are due to low energy maxima or minima along the sub-bands present due to the quantisation of the electronic wavevector. A huge amount of states reside at these low energy minima, often tending to infinity (Figure 6).[96] These sharp spikes in the density of states change the electron transfer kinetics at different energies[97] and alter how nanotubes interact with molecules with HOMO at specific energies because at these energies there is a much higher concentration of electrons on the electrode. The ability to exhibit metallic or semiconducting properties, along with the van Hove singularities make SWNT an exciting prospect for use as electrodes.

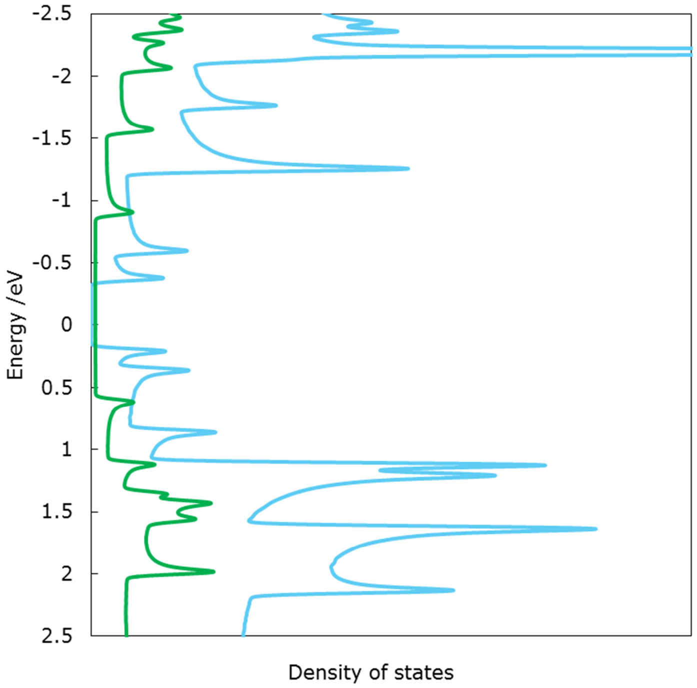

Figure 6. The density of states (DOS) between 2.5 eV and -2.5 eV for (17,0)SWNT (semiconducting) (blue) and (10,10)SWNT (metallic) (green). The DOS are plotted using *ab initio* density functional theory (DFT) performed by Dr. M. Baldoni.

The nature of the heterogeneous electron transfer at SWNT has attracted some debate. The electrochemical response of nanotubes has been compared to HOPG where the pristine walls of the nanotubes behave like the basal plane of graphite with slow heterogeneous electron transfer and the ends of nanotubes act like edge plane graphite with fast heterogeneous electorn transfer.[27, 98] This study was performed using multi-walled carbon nanotubes (MWNT) with a diameter of 10 – 20 nm which, have a much less curved outer surface than SWNT so the electron transfer properties are likely to differ compared to SWNT. A number of other studies also suggest that heterogeneous electron transfer occurs more readily at the open ends of a nanotube rather than the side wall.[26, 32, 99] This is of particular importance when considering the electrochemistry of molecules inside nanotubes due to the majority of molecules being in contact with only the SWNT sidewalls. Recent studies claim redox processes are observed for encapsulated guest-molecules inside nanotubes[10, 22] suggesting sufficient electron transfer does indeed occur through the interior walls of carbon nanotubes. A study performed by Miller *et al.* further supports this claim whereby a nanoscale electrochemical cell technique is used to examine the electrochemistry that occurs at either the closed ends or the sidewalls of SWNT in a nanotube 'forest' explicitly (Figure 7.).[38]

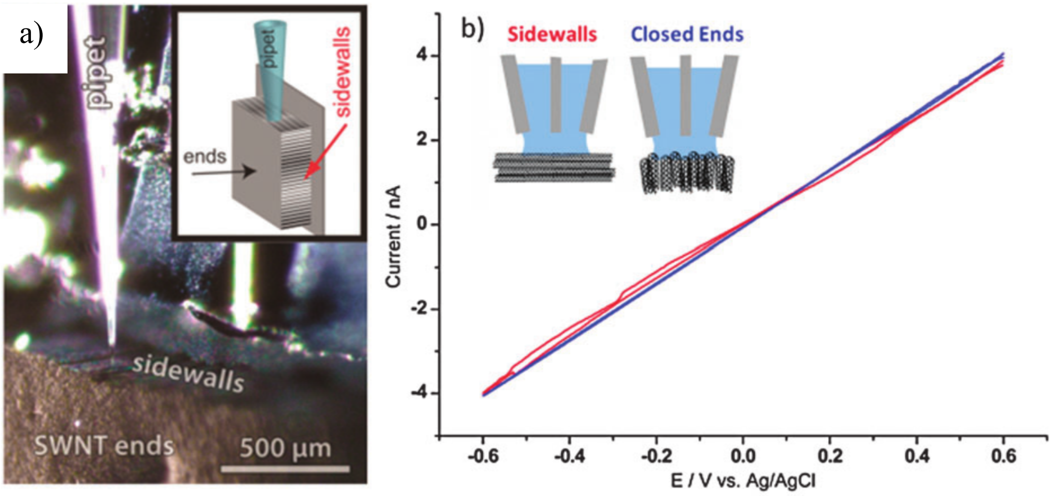

Figure 7. a) Photograph and schematic of the nanoscale electrochemical cell technique.[100] b) Current–voltage curves (forward and reverse) recorded on the closed ends (blue) and sidewalls (red), using a pipette of internal diameter 400 nm, containing 50 mM KCl, at 100 mV s^{-1}.[38]

This method enables the assessment of the contact area of the meniscus with the area of interest on the SWNT 'forest'. The results show the local electrochemical response to be almost identical at both the nanotube tips and the nanotube sidewalls and thus, both the closed ends and sidewalls SWNT should be considered highly electrochemically active, and capable of fast electron transfer.[38] Whilst this study is only assessing the external surface of the SWNT, combined with the successful electrochemistry of encapsulated molecules, it can be assumed that fast heterogeneous electron transfer also occurs at the interior sidewall of SWNT. Further related work has been performed on individual SWNT with the same conclusion.[36, 101]

The high surface area of a nanotube and the ability to encapsulate electron mediators[10] has prompted a large number of publications and research on the use of carbon nanotubes as sensors. Hybrid carbon nanotube structures have been shown to detect small molecules,[9, 102] neurotransmitters,[10, 23, 102, 103] glucose,[104] proteins,[105] nucleic acids[106] and cells.[107] Functionalisation of carbon nanotubes, while the success at a high ratio of functionalisation is debated,[108] provides a powerful tool to attach enzymes and other sensitisers through the nanotube to an electrode. Cai *et al.* covalently attached a probe DNA strand to SWNT via carboxylic acid groups. In the prescence of the analyte DNA strand an increased current is observed unlike when using a blank glassy carbon electrode (GCE) or unfunctionalised nanotubes (Figure 8).[106] The high surface area and ability to encapsulate electron mediators into carbon nanotubes or functionalise carbon nanotubes with DNA or enzymes, greatly improves the sensitivity of the nanotube sensors.

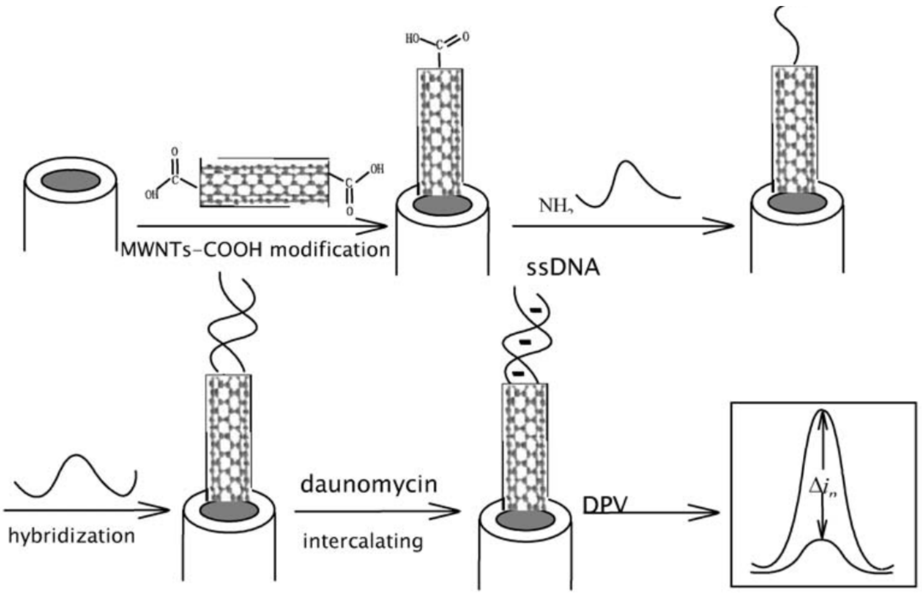

Figure 8. Schematic showing the covalently attached probe DNA strand to SWNT via carboxylic acid groups. In the prescence of daunomycin an increased current is observed in the differential pulse voltammetry (DPV) unlike when using a blank glassy carbon electrode (GCE) or unfunctionalised nanotubes.[106]

The combination of the unique physical structure and the high conductivity of carbon nanotubes result in an electrode with many possible applications in both fundamental science and as sensors. The evidence for fast heterogeneous electron transfer at both the nanotube sidewall and the tips, along with the use of nanotubes in sensors provides a spring board into electrocatalysis and investigation of reactions or interactions on the interior of nanotubes.

1.3 Electrochemistry of molecules encapsulated in single-walled carbon nanotubes

The unique electronic structure of SWNT [109] and the ability to exhibit either metallic or semiconducting properties while interacting effectively with electron donors[110-112] and acceptors[113] make nanotubes highly tuneable nanoscale containers with respect to electronic interactions with the guest-molecules encapsulated inside carbon nanotubes. The hollow structure of carbon nanotubes is perhaps one of the most exciting aspects, allowing for non-covalent doping by immobilisation of guest-molecules in the external cavity of the nanotube.[10, 112, 114, 115] This provides a means with which to further tune the bandgap for applications in solar cell technology[116, 117] and electronics.[118] The immobilisation of molecules and nanoparticles has been extensively used for catalysis[48, 49, 119, 120] and could find applications in electrocatalysis, whereby the catalyst is in electrical contact with the electrode with perfect control of oxidation state and therefore, of the catalytic reaction.

The curvature of the nanotube must be considered when investigating nanotube-guest interactions. The curved wall alters the position of the electron density, moving the π electron density from the concave inner surface to the convex outer surface as well as p-orbital misalignment (Figure 9).[114, 121, 122] As a result, molecules confined on the inside of nanotubes will interact with the e^- density of the nanotubes to a different amount compared to a guest on the outside of the nanotube so will display different properties. Pan *et al*. observed that while turnover frequencies for ammonia decomposition catalysed by ruthenium nanoparticles were lower inside nanotubes compared to outside,[121] the heat for CO adsorption onto the ruthenium nanoparticle was 12 kJ mol^{-1} lower inside the SWNT.[123] DFT was performed to evaluate to the location dependent shifts in electronic state of the catalyst. Figure 10 shows the differential electron density isosurfaces of a Ru_6 cluster inside and outside a SWNT. It was observed that the Ru_6 cluster donates electrons to the SWNT regardless to whether it is on the inside or outside.

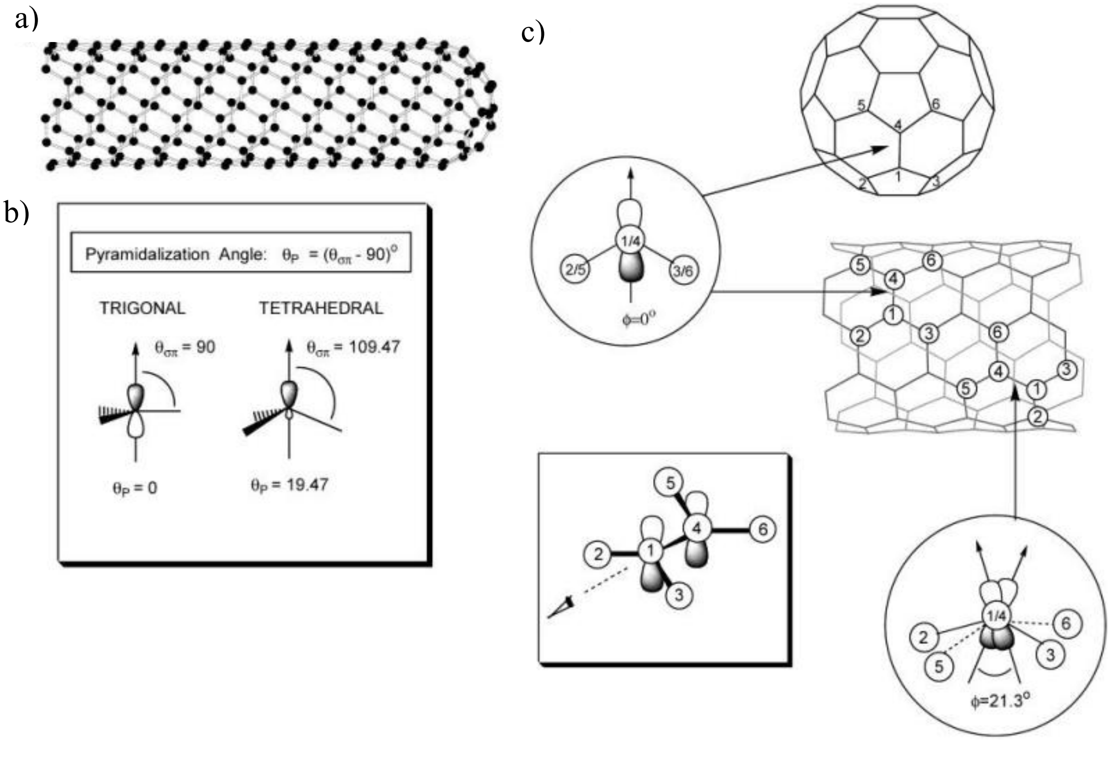

Figure 9. Diagrams of a) SWNT, b) pyrimidalisation angle in trigonal and tetrahedral molecules and c) the pyrimidalisation angles observed in the sidewall of the nanotube and the misalignment of the p-orbitals in certain positions in the nanotube sidewall due to the curvature. An increased π electron density is observed on the convex outer sidewall of the nanotube.[122]

However, theory predicts that more electron density was donated to the SWNT when the Ru_6 cluster was on the inside of the SWNT.[123] This agrees well with the previous work by Niyogi *et al.* that reports lower electron density on the inside of the nanotube,[122] promoting an increased electron donation from encapsulated molecules or nanoparticles.[123] The increased contact area of the Ru_6 cluster with the inside of the nantoube compared to the oustide of the nanotube is also likely to play a part in the increased electron transfer from the cluster when encapsulated, however, it is not mentioned in this theoretical study. The increased electron transfer observed from the cluster inside the nanotube demonstrates a benefit of confinement in carbon nanotubes, changing both the interactions between the metal cluster and the SWNT and also the efficiency of the catalysis. These studies prompt further interest in the interactions between and guest-molecules that can be investigated using electrochemistry.

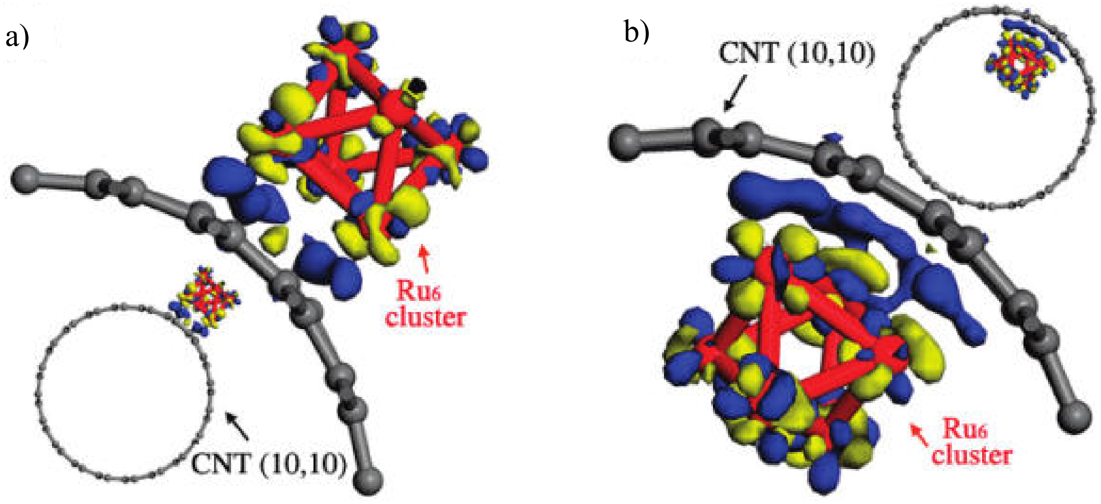

Figure 10. DFT calculated interactions of Ru_6 clusters with the a) exterior and b) the interior surfaces of a (10,10)SWNT, illustrating increased electron donation to the SWNT when the Ru_6 cluster is encapsulated inside the nanotube. The insets show the full cross-sectional view.[123]

As discussed (section 1.2.2, Figure 7), electron transfer at nanotube sidewalls is of comparable efficiency to that at the nanotube ends.[38] This is important for the electrochemistry of guest-molecules encapsulated in nanotubes. There is a limited number of examples of the CV of encapsulated molecules present in the literature, including the CV of ferrocene $Fe(Cp)_2$@SWNT/double walled carbon nanotubes (DWNT)[9, 10, 124] and C_{60}/C_{70}@SWNT/DWNT.[125, 126] There are also reports in the literature of the use of nanotubes to alter the electrochemical redox potential of an encapsulated guest-molecule for analysis with different spectroscopies such as Raman spectroscopy.[127-131] The restricted number of electrochemical studies of encapsulated molecules is surprising as this is the stepping stone towards the immobilisation of homogeneous catalysts in nanotubes. Encapsulation in nanotubes presents an exciting method with which to convert highly specific homogeneous catalysts into heterogeneous catalysts with increased recoverability and decreased fouling. Combined with the high affinity of reactant molecules for the nanotube cavity creating a higher local concentration of reactants inside the nanotube in close proximity with the catalyst[120, 132] and the possibility of changing the catalysts properties such as the redox potential of the reaction or the reactivity of molecules,[22] makes this an exciting new prospect.

An excellent example of how nanotubes can be used as hollow electrodes was demonstrated by Yanagi *et al*[131] who reported the potential dependent Raman spectroscopy of β-carotene@SWNT. Although there is no attempt to observe an electrochemical signal, this work further investigates the effect that changing the potential of the nanotube has on the guest, which in this example is β-carotene. One of the benefits of β-carotene is that the C=C stretching mode (υ_1) has a strong signal comparable to the G band of the host-SWNT so the Raman spectra of the encapsulated guest-molecule can be recorded upon application of potential, and from this, the doping of both the nanotube and the β-carotene can be approximately quantitative. Upon application of a negative potential, the intensity of the G band of the SWNT decreases with no observed change in the υ_1 mode, indicating electron injection into the nanotube but not β-carotene. However, upon application of a positive potential, the intensities of both the G band of the SWNT and the υ_1 mode change (Figure 11), the υ_1 mode requiring an increased overpotential.

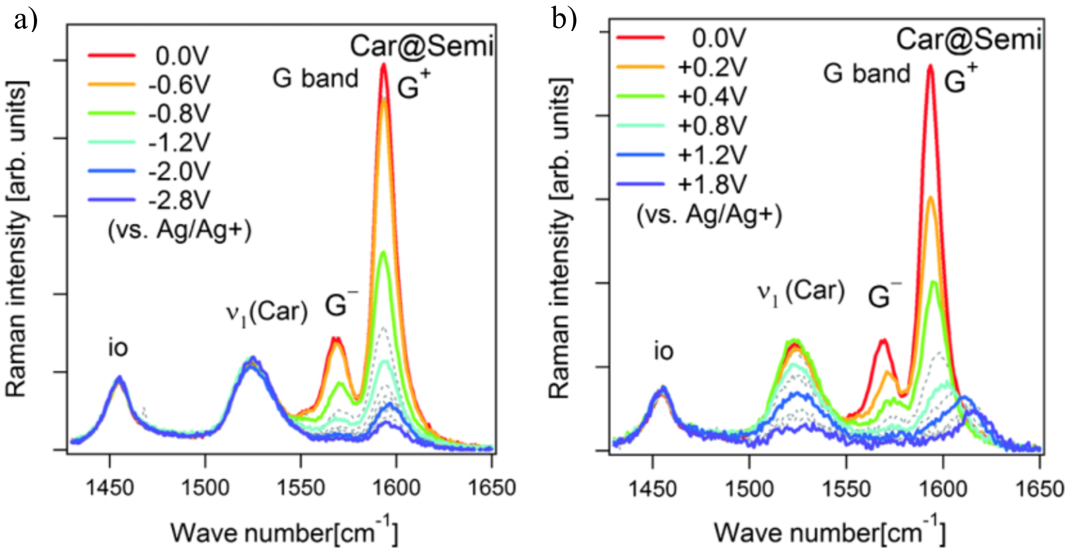

Figure 11. Raman spectra of β-carotene@SWNT (Car@Semi) at different applied potential of the nanotube a) negative potentials, b) positive potentials. The spectra were obtained at a 488 nm excitation wavelength. The dotted lines are Raman spectra at potentials between those described with the coloured solid lines.[131]

The removal of electron density from the nanotube before β-carotene is unexpected due to the higher energy of the β-carotene HOMO compared to the top of the nanotube valence band (Figure 12). It was postulated that this is due to a downshift in the HOMO of β-carotene as the external field was applied to the nanotube so that the HOMO dropped below the valence band of the nanotube (Figure 12). There are two alternate explanations. Firstly, if the semiconducting nanotubes used in this study are considered perfect, at the energy of the β-carotene HOMO there are no states of the nanotube for an oxidation to occur, therefore, electrons must be removed from the nanotube first with a small over-potential required to oxidise β-carotene. Secondly, if there are also metallic or narrow bandgap semiconducting nanotubes present in the sample then electrons may be removed from these before the β-carotene HOMO. This is a powerful technique for determining the nature of electron transfer between guest-molecules and the nanotube, however, it does rely on

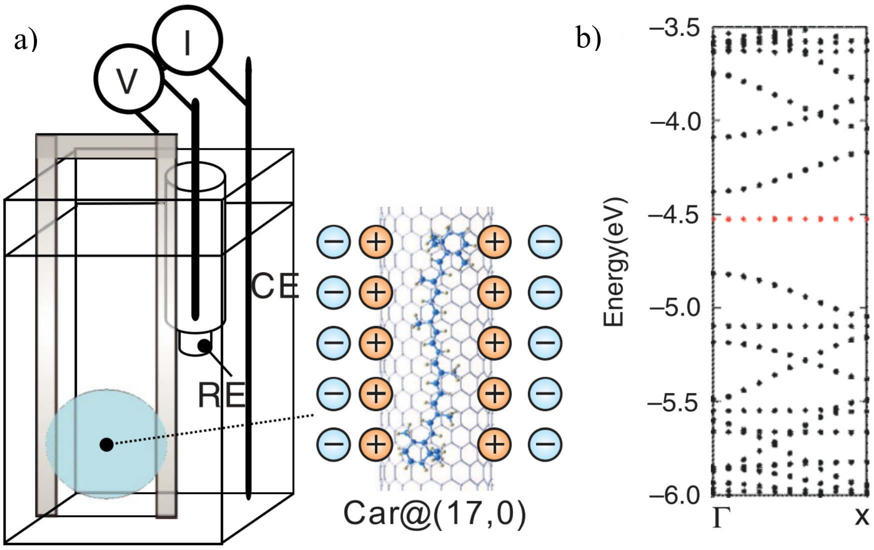

Figure 12. a) A schematic of the experimental, set up used for the potential dependent Raman spectroscopy of β-carotene@SWNT (Car@(17,0). RE and CE are reference and counter electrodes, respectively. b) The band structure of β-carotene@SWNT calculated using DFT. The red dotted line represents the HOMO band associated with β-carotene, and the black dots correspond to the bands of the SWNT.[131]

the guest-molecule having a strong Raman signal. On the other hand, it is still a useful technique in the absence of a Raman signal because strong dopants will greatly change the energies of electron removal from the nanotube, which will be observed through the intensity of the G-band.

The CV of C_{60}@SWNT and C_{70}@SWNT was performed by Kavan *et al* and was reported to be similar to that of empty SWNT.[133] They conclude that the faradic processes originating from the reduction of C_{60}/C_{70} is hampered due to inability of counter ions to reach the C_{60} ions. However, the use of potential dependent Raman spectroscopy is performed at 1.2 V and 1.5 V, using electrochemistry to p-dope C_{60}@SWNT and record the *in situ* Raman spectra.[130] An increased shift of the tangential displacement mode is observed for empty SWNT compared to

C_{60}@SWNT which indicates a delocalisation of positive charge to the encapsulated C_{60}.[127] Although no signal was observed, the shift in the tangential displacement mode suggests that some reduction of C_{60} is occurring and the elevated potential of the SWNT is having an influence on the encapsulated C_{60}.

Sun *et al.* and a subsequent study by, Wu *et al.* also reported the CV of C_{60}@SWNT, C_{70}@SWNT and C_{60}@DWNT (Figure 13). Unlike the study by Kavan *et al.*[129, 134] electrochemically reversible redox processes corresponding to C_{60}/C_{60}^{1-}, C_{60}^{1-}/C_{60}^{2-} and C_{60}^{2-}/C_{60}^{3-} are observed at -0.97 V, -1.42 V and -1.83 V respectively, confirming the ability for electron transfer to occur though the nanotube sidewalls.[125, 126]

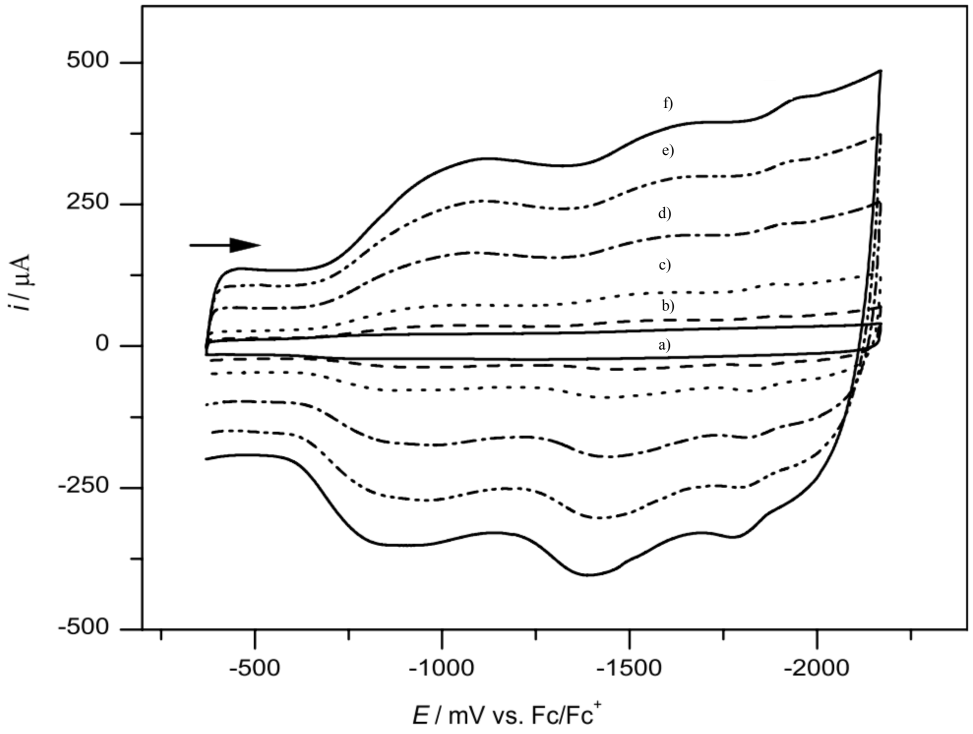

Figure 13. CV of C_{60}@SWNT at different scan rates; b) 0.05, c) 0.1, d) 0.25, e) 0.4, f) 0.5 (Vs^{-1}). Curve a) is a CV of empty SWNT at a scan rate of 0.05 Vs^{-1}. CV performed in acetonitrile containing 0.1 M Bu_4NClO_4 at a scan rate of 0.1 Vs^{-1}.[126] Note – more negative potentials are to the right.

The redox potentials of C_{60}@SWNT are very similar to those observed for C_{60} in a solution of acetonitrile and toluene, moreover, the CV of C_{70}@SWNT was reported to present similar results to C_{60}@SWNT.[126] A linear increase in peak current with respect to scan rate confirms the immobilisation of C_{60}. It was also reported that the choice of the electrolyte used is important due to the extra electrons on C_{60} requiring compensation by cations, which is not a problem in conventional solution electrochemistry. If the cation cannot penetrate the nanotube then a redox process is not observed for C_{60}@SWNT. When using $LiClO_4$ as an electrolyte in a mixture of toluene and acetonitrile no signal for C_{60} is observed,[135] however, when using Bu_4NPF_6 in the same solvent, three redox processes are observed. This was attributed to the ability of tetra butyl ammonium cations (TBA^+) to penetrate through the open ends and the nanotube defects in the sidewalls and form stable ion pairs where Li^+ cannot.[126] TBA^+ are relatively bulky in comparison to SWNT or the DWNT used (internal diameter of SWNT and DWNT in these studies appears to be 1-2.5 nm determined from TEM images), combined with the SWNT being filled with C_{60}, means it is unlikely that TBA^+ penetrates the SWNT. However, it is possible that TBA^+ penetrates the bundles of nanotubes, but remains on the outside of the nanotube, forming an ion pair through the highly polarisable nanotube sidewall.[136] The effect of solvent through nanotube side walls will be further investigated in chapter 2. The redox processes observed for fullerene inside nanotubes demonstrates the ability to perform the CV of molecules inside SWNT but also that there are other factors such as solvent and electrolyte that must be considered.

Cheng *et al.* report that the redox process of $Fe(Cp)_2$ (Fe^{III}/Fe^{II}) is observed during the CV of ferrocene@DWNT, again indicating electrical communication was achieved between the electrode and the guest-ferrocene.[10] The redox process occurs at 0.38 V (vs. saturated calomel electrode) and is shifted slightly in the positive direction, attributed to a charge transfer from ferrocene to the nanotube. A linear increase in peak current with respect to scan rate is observed confirming the immobilisation of $Fe(Cp)_2$. The peak current remains the same after 50 scans unlike the same experiment where ferrocene is on the outside of the DWNT, confirming that the current does indeed originate from encapsulated molecules. Studies on the electrochemistry on $Fe(Cp)_2$@SWNT have been reported by Guan *et al.*[124] and Sun *et al.*[9] Both report similar electrochemical responses for $Fe(Cp)_2$@SWNT to those reported by Cheng *et al.* for $Fe(Cp)_2$@DWNT.

The main objective of the study performed by Cheng *et al.* was to investigate and improve the sensing of dopamine (DA) using $Fe(Cp)_2$@DWNT whereby the encapsulated $Fe(Cp)_2$ acts as an electron mediator for the electrocatalysis of dopamine. Upon addition of dopamine, the current due to reduction of $Fe(Cp)_2$ decreased (0.45 V, P_c) and the current due to oxidation of $Fe(Cp)_2$ increased (0.25 V, P_a) (Figure 14) characteristic of the electrocatalytic reaction of $Fe(Cp)_2$ with dopamine.

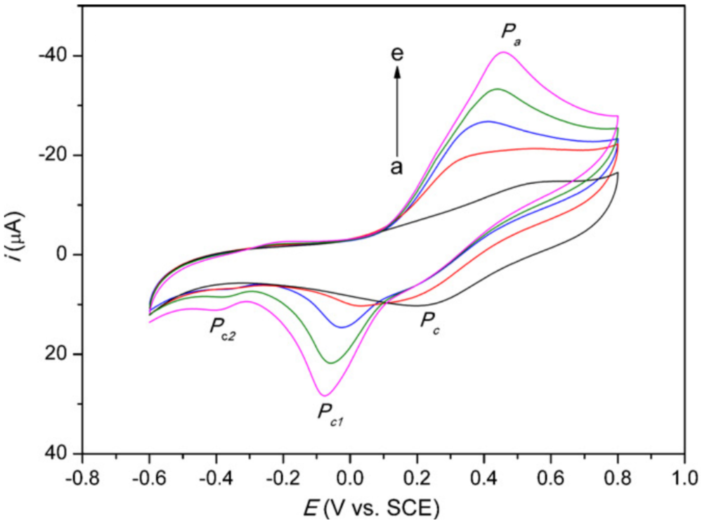

Figure 14. CV at different concentrations of dopamine using a $Fe(Cp)_2$@DWNT electrode in 0.1 M phosphate buffered saline containing 0.1 M $LiClO_4$ at a scan rate of 100 mV s^{-1}. The concentration of dopamine (µM): a) 0, b) 50, c) 100, d) 150, e) 200.[10]

A mechanism for this electrocatalytic reaction was proposed, where $Fe(Cp)_2^+$ is reduced by dopamine to form dopamine ortho-quinone (DOQ) (Figure 15). The regenerated $Fe(Cp)_2$ is then re-oxidised, hence, the enhanced oxidative current and diminished reductive current observed in the CV (Figure 14), confirming the ability to sense dopamine using ferrocene@DWNT.

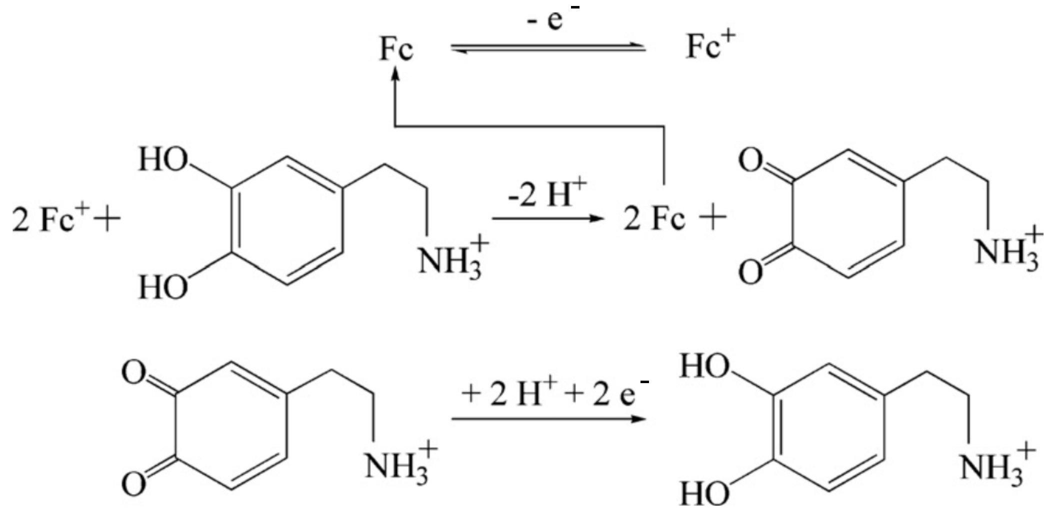

Figure 15. Mechanism of the reaction of dopamine on the Fe(Cp)$_2$@DWNT. (Fc is ferrocene for the purpose of this figure).[10]

Sun *et al.* report that Fe(Cp)$_2$@SWNT can be used for sensing hydrogen peroxide. An increased current for both oxidation and reduction peaks is observed upon increasing the concentration of hydrogen peroxide, attributed to the electron mediation abilities of encapsulated Fe(Cp)$_2$.[9] The reaction involves the oxidation of H_2O_2 to O_2 and the reduction of H_2O_2 to H_2O, mediated by encapsulated ferrocene molecules. The current is measured at a fixed potential, when applying an oxidising potential, the current decreases upon addition of H_2O_2 and when applying a reducing potential the current increases upon addition of H_2O_2.

These studies demonstrate how the immobilisation of catalysts inside nanotubes can be used to improve the sensitivity and stability of catalysts in electrocatalytic reactions. It is likely that the majority of the electrocatalytic reaction occurs close to the ends of the nanotubes due to the narrow internal cavity of DWNT/SWNT filled with $Fe(Cp)_2$ preventing movement of significant quantities of DA from traversing the nanotube interior. However, the use of a wider DWNT may allow some of the dopamine to penetrate into the nanotube and access more of the $Fe(Cp)_2$ centres. The use of even wider nanotubes of nanofibers may further increase the sensitivity by allowing movement of analyte molecules along the nanotube and also have application in preparative electrocatalysis where mass transport is even more crucial.

1.4 Summary

While there are some reports of the electrochemistry of molecules inside nanotubes, the concept is new, still without detailed understanding of the host-guest interactions and the effects of electrochemical potential on encapsulated guest-molecules. There is great promise using electrochemistry of molecules inside carbon nanotubes as a tool for the application of sensing such as that observed with ferrocene@SWNT/DWNT. This could be extended towards molecules or nanoparticles encapsulated in GNF. Further to this, the electron mediation of small molecules prompts investigation into more complicated electrochemical reactions inside carbon nanotubes, there is also scope for using CV to discover fundamental aspects of interactions involved with encapsulated guest-molecules inside carbon nanotubes. Whilst not reported in the literature, preparative electrocatalysis using molecules or metals inside carbon nanotubes is an exciting challenge that all of the studies presented here lead towards and is the next big step for this area of science.

Results in this thesis will hopefully develop this field, making preparative electrocatalysis possible in the near future.

1.5 References

1. R. L. McCreery, *Electroanalytical chemistry*, New York, 1991.
2. S. Huang, J. E. Weis, S. Costa, M. Kalbac and M. S. Dresselhaus, in *Electrochemistry of Carbon Electrodes*, eds. R. Alkire, C, P. Bartlett, N and J. Lipowski, Wiley, 2015, vol. 16, ch. 1, pp. 1.
3. J. O. Besenhard and H. P. Fritz, *Angew. Chem. Int. Ed.*, 1983, **22**, 950.
4. A. L. Reddy, M. M. Shaijumon, S. R. Gowda and P. M. Ajayan, *Nano Lett.*, 2009, **9**, 1002.
5. S. W. Lee, N. Yabuuchi, B. M. Gallant, S. Chen, B. S. Kim, P. T. Hammond and Y. Shao-Horn, *Nat. Nanotechnol.*, 2010, **5**, 531.
6. K. T. Lee, J. C. Lytle, N. S. Ergang, S. M. Oh and A. Stein, *Adv. Funct. Mater.*, 2005, **15**, 547.
7. B. Sljukic, C. E. Banks and R. G. Compton, *Nano Lett.*, 2006, **6**, 1556.
8. M. A. Gilmartin and J. P. Hart, *Analyst*, 1995, **120**, 1029.
9. N. Sun, L. Guan, Z. Shi, N. Li, Z. Gu, Z. Zhu, M. Li and Y. Shao, *Anal. Chem.*, 2006, **78**, 6050.
10. H. Cheng, H. Qiu, Z. Zhu, M. Li and Z. Shi, *Electrochim. Acta*, 2012, **63**, 83.
11. S. Yabuki, F. Mizutani and Y. Hirata, *Sensor Actuat. B-Chem.*, 2000, **65**, 49.
12. C. Wang, M. Waje, X. Wang, J. M. Tang, R. C. Haddon and Y. S. Yan, *Nano Lett.*, 2004, **4**, 345.
13. T. Matsumoto, T. Komatsu, K. Arai, T. Yamazaki, M. Kijima, H. Shimizu, Y. Takasawa and J. Nakamura, *Chem. Commun.*, 2004, **17**, 840.
14. T. Hyeon, S. Han, Y. E. Sung, K. W. Park and Y. W. Kim, *Angew. Chem. Int. Ed.*, 2003, **42**, 4352.
15. G. Girishkumar, K. Vinodgopal and P. V. Kamat, *J. Phys. Chem. B*, 2004, **108**, 19960.
16. C. M. A. Brett and A. M. O. Brett, *Electrochemistry principles, Methods and Applications*, Bookcraft (Bath) Ltd., 1993.
17. G. M. Jenkins and K. Kawamura, *Nature*, 1971, **231**, 175.
18. L. A. Pesin and E. M. Baitinger, *Carbon*, 2002, **40**, 295.
19. P. J. F. Harris, *Philos. Mag.*, 2004, **84**, 3159.
20. P. J. F. Harris, *J. Mater. Sci.*, 2013, **48**, 565.
21. P. J. F. Harris and S. C. Tsang, *Philos. Mag. A.*, 1997, **76**, 667.
22. R. L. McSweeney, T. W. Chamberlain, E. S. Davies and A. N. Khlobystov, *Chem. Commun.*, 2014, **50**, 14338.
23. P. J. Britto, K. S. V. Santhanam and P. M. Ajayan, *Bioelectrochem. Bioenerg.*, 1996, **41**, 121.
24. H. X. Luo, Z. J. Shi, N. Q. Li, Z. N. Gu and Q. K. Zhuang, *Anal. Chem.*, 2001, **73**, 915.
25. K. E. Moore, B. S. Flavel, A. V. Ellis and J. G. Shapter, *Carbon*, 2011, **49**, 2639.

26. J. Li, A. Cassell, L. Delzeit, J. Han and M. Meyyappan, *J. Phys. Chem. B*, 2002, **106**, 9299.
27. R. R. Moore, C. E. Banks and R. G. Compton, *Anal. Chem.*, 2004, **76**, 2677.
28. J. Cervenka, M. I. Katsnelson and C. F. J. Flipse, *Nat. Phys.*, 2009, **5**, 840.
29. R. L. McCreery, *Chem. Rev.*, 2008, **108**, 2646.
30. T. J. Davies, C. E. Banks and R. G. Compton, *J. Solid State Electrochem.*, 2005, **9**, 797.
31. T. J. Davies, R. R. Moore, C. E. Banks and R. G. Compton, *J. Electroanal. Chem.*, 2004, **574**, 123.
32. A. Chou, T. Bocking, N. K. Singh and J. J. Gooding, *Chem. Commun.*, 2005, 842.
33. J. J. Gooding, *Electrochim. Acta*, 2005, **50**, 3049.
34. C. G. Williams, M. A. Edwards, A. L. Colley, J. V. Macpherson and P. R. Unwin, *Anal. Chem.*, 2009, **81**, 2486.
35. S. C. S. Lai, A. N. Patel, K. McKelvey and P. R. Unwin, *Angew. Chem. Int. Ed.*, 2012, **51**, 5405.
36. A. G. Guell, K. E. Meadows, P. V. Dudin, N. Ebejer, J. V. Macpherson and P. R. Unwin, *Nano Lett.*, 2014, **14**, 220.
37. A. G. Guell, N. Ebejer, M. E. Snowden, K. McKelvey, J. V. Macpherson and P. R. Unwin, *Proc Natl Acad Sci U S A*, 2012, **109**, 11487.
38. T. S. Miller, N. Ebejer, A. G. Guell, J. V. Macpherson and P. R. Unwin, *Chem. Commun.*, 2012, **48**, 7435.
39. B. Partoens and F. M. Peeters, *Phys. Rev. B*, 2006, **74**.
40. C. E. Banks and R. G. Compton, *Analyst*, 2006, **131**, 15.
41. Y. Xuan, Y. Q. Wu, T. Shen, M. Qi, M. A. Capano, J. A. Cooper and P. D. Ye, *Appl. Phys. Lett.*, 2008, **92**.
42. F. Gloaguen, J. M. Leger, C. Lamy, A. Marmann, U. Stimming and R. Vogel, *Electrochim. Acta*, 1999, **44**, 1805.
43. J. L. Zubimendi, L. Vazquez, P. Ocon, J. M. Vara, W. E. Triaca, R. C. Salvarezza and A. J. Arvia, *J. Phys. Chem.*, 1993, **97**, 5095.
44. M. F. Juarez, S. Fuentes, G. J. Soldano, L. Avalle and E. Santos, *Faraday Discuss.*, 2014, **172**, 327.
45. M. P. Zach, K. Inazu, K. H. Ng, J. C. Hemminger and R. M. Penner, *Chem. Mater.*, 2002, **14**, 3206.
46. W. A. Solomonsz, G. A. Rance, M. Suyetin, A. La Torre, E. Bichoutskaia and A. N. Khlobystov, *Chem. Eur. J.*, 2012, **18**, 13180.
47. W. A. Solomonsz, G. A. Rance and A. N. Khlobystov, *Small*, 2014, **10**, 1866.
48. W. A. Solomonsz, G. A. Rance, B. J. Harris and A. N. Khlobystov, *Nanoscale*, 2013, **5**, 12200.
49. M. A. Lebedeva, T. W. Chamberlain, M. Schröder and A. N. Khlobystov, *Chem. Mater.*, 2014, **26**, 6461.
50. A. La Torre, C. Gimenez-Lopez Mdel, M. W. Fay, C. H. Lucas, P. D. Brown and A. N. Khlobystov, *Small*, 2015, **11**, 2756.
51. Z. Liu, K. Suenaga, P. J. Harris and S. Iijima, *Phys. Rev. Lett.*, 2009, **102**, 015501.
52. K. B. Holt, A. J. Bard, Y. Show and G. M. Swain, *J. Phys. Chem. B*, 2004, **108**, 15117.
53. J. Pernot, P. N. Volpe, F. Omnes, P. Muret, V. Mortet, K. Haenen and T. Teraji, *Phys. Rev. B*, 2010, **81**.
54. M. Panizza and G. Cerisola, *Electrochim. Acta*, 2005, **51**, 191.

55. G. M. Swain, *J. Electrochem. Soc.*, 1994, **141**, 3382.
56. R. Ramesham and M. F. Rose, *Diamond Relat. Mater.*, 1997, **6**, 17.
57. G. M. Swain, *Adv. Mater.*, 1994, **6**, 388.
58. Y. V. Pleskov, A. Y. Sakharova, M. D. Krotova, L. L. Bouilov and B. V. Spitsyn, *J. Electroanal. Chem.*, 1987, **228**, 19.
59. T. Yano, D. A. Tryk, K. Hashimoto and A. Fujishima, *J. Electrochem. Soc.*, 1998, **145**, 1870.
60. J. Iniesta, P. A. Michaud, M. Panizza, G. Cerisola, A. Aldaz and C. Comninellis, *Electrochim. Acta*, 2001, **46**, 3573.
61. M. C. Granger, M. Witek, J. Xu, J. Wang, M. Hupert, A. Hanks, M. D. Koppang, J. E. Butler, G. Lucazeau, M. Mermoux, J. W. Strojek and G. M. Swain, *Anal. Chem.*, 2000, **72**, 3793.
62. C. Hebert, E. Scorsone, A. Bendali, R. Kiran, M. Cottance, H. A. Girard, J. Degardin, E. Dubus, G. Lissorgues, L. Rousseau, P. Mailley, S. Picaud and P. Bergonzo, *Faraday Discuss.*, 2014, **172**, 47.
63. L. Meng, J. G. Iacobini, M. B. Joseph, J. V. Macpherson and M. E. Newton, *Faraday Discuss.*, 2014, **172**, 421.
64. J. H. Luong, K. B. Male and J. D. Glennon, *Analyst*, 2009, **134**, 1965.
65. J. V. Macpherson, in *Electrochemistry of Carbon Electrodes*, eds. R. Alkire, C, P. Bartlett, N and J. Lipowski, Wiley, 2015, vol. 16, pp. 163.
66. E. Fortin, E. Vieil, P. Mailley, S. Szunerits and T. Livache, *Anal. Chem.*, 2007, **79**, 3741.
67. Z. J. Ayres, A. J. Borrill, J. C. Newland, M. E. Newton and J. V. Macpherson, *Anal. Chem.*, 2016, **88**, 974.
68. W. Dai, H. Li, M. Li, C. Li, X. Wu and B. Yang, *Acs Applied Materials & Interfaces*, 2015, **7**, 22858.
69. L. A. Hutton, M. Vidotti, A. N. Patel, M. E. Newton, P. R. Unwin and J. V. Macpherson, *The Journal of Physical Chemistry C*, 2011, **115**, 1649.
70. M. E. Teixeira, G. C. Sedenho and N. R. Stradiotto, *Anal. Sci.*, 2015, **31**, 773.
71. M. Pumera, *Chem. Soc. Rev.*, 2010, **39**, 4146.
72. K. S. Novoselov, A. K. Geim, S. V. Morozov, D. Jiang, Y. Zhang, S. V. Dubonos, I. V. Grigorieva and A. A. Firsov, *Science*, 2004, **306**, 666.
73. A. K. Geim and K. S. Novoselov, *Nat. Mater.*, 2007, **6**, 183.
74. M. Kalbac, H. Farhat, J. Kong, P. Janda, L. Kavan and M. S. Dresselhaus, *Nano Lett.*, 2011, **11**, 1957.
75. M. Kalbac, J. Kong and M. S. Dresselhaus, *J. Phys. Chem. C*, 2012, **116**, 19046.
76. J. C. Meyer, S. Kurasch, H. J. Park, V. Skakalova, D. Kunzel, A. Gross, A. Chuvilin, G. Algara-Siller, S. Roth, T. Iwasaki, U. Starke, J. H. Smet and U. Kaiser, *Nat. Mater.*, 2011, **10**, 209.
77. N. Jung, N. Kim, S. Jockusch, N. J. Turro, P. Kim and L. Brus, *Nano Lett.*, 2009, **9**, 4133.
78. W. Zhang, C. T. Lin, K. K. Liu, T. Tite, C. Y. Su, C. H. Chang, Y. H. Lee, C. W. Chu, K. H. Wei, J. L. Kuo and L. J. Li, *ACS Nano*, 2011, **5**, 7517.
79. A. Chuvilin, U. Kaiser, E. Bichoutskaia, N. A. Besley and A. N. Khlobystov, *Nat. Chem.*, 2010, **2**, 450.
80. A. Ambrosi, C. K. Chua, A. Bonanni and M. Pumera, *Chem. Rev.*, 2014, **114**, 7150.
81. D. A. C. Brownson, L. J. Munro, D. K. Kampouris and C. E. Banks, *RSC Advances*, 2011, **1**, 978.

82. D. A. Brownson and C. E. Banks, *Phys. Chem. Chem. Phys.*, 2011, **13**, 15825.
83. A. G. Gueell, N. Ebejer, M. E. Snowden, J. V. Macpherson and P. R. Unwin, *J. Am. Chem. Soc.*, 2012, **134**, 7258.
84. M. Velicky, D. F. Bradley, A. J. Cooper, E. W. Hill, I. A. Kinloch, A. Mishchenko, K. S. Novoselov, H. V. Patten, P. S. Toth, A. T. Valota, S. D. Worrall and R. A. W. Dryfe, *Acs Nano*, 2014, **8**, 10089.
85. C. M. Weber, D. M. Eisele, J. P. Rabe, Y. Liang, X. Feng, L. Zhi, K. Mullen, J. L. Lyon, R. Williams, D. A. Vanden Bout and K. J. Stevenson, *Small*, 2010, **6**, 184.
86. M. D. Stoller, S. Park, Y. Zhu, J. An and R. S. Ruoff, *Nano Lett.*, 2008, **8**, 3498.
87. K. S. Kim, Y. Zhao, H. Jang, S. Y. Lee, J. M. Kim, K. S. Kim, J.-H. Ahn, P. Kim, J.-Y. Choi and B. H. Hong, *Nature*, 2009, **457**, 706.
88. A. Reina, X. Jia, J. Ho, D. Nezich, H. Son, V. Bulovic, M. S. Dresselhaus and J. Kong, *Nano Lett.*, 2009, **9**, 30.
89. J. T. Robinson, M. Zalalutdinov, J. W. Baldwin, E. S. Snow, Z. Wei, P. Sheehan and B. H. Houston, *Nano Lett.*, 2008, **8**, 3441.
90. C. T. White and T. N. Todorov, *Nature*, 1998, **393**, 240.
91. T. W. Ebbesen, H. J. Lezec, H. Hiura, J. W. Bennett, H. F. Ghaemi and T. Thio, *Nature*, 1996, **382**, 54.
92. L. Yang, C.-H. Park, Y.-W. Son, M. L. Cohen and S. G. Louie, *Phys. Rev. Lett.*, 2007, **99**, 186801.
93. K. Wakabayashi, *Phys. Rev. B*, 2001, **64**, 125428.
94. D. V. Kosynkin, A. L. Higginbotham, A. Sinitskii, J. R. Lomeda, A. Dimiev, B. K. Price and J. M. Tour, *Nature*, 2009, **458**, 872.
95. T. W. Odom, J. L. Huang, P. Kim and C. M. Lieber, *J. Phys. Chem. B*, 2000, **104**, 2794.
96. E. Joselevich, *Chemphyschem.*, 2004, **5**, 619.
97. I. Heller, J. Kong, K. A. Williams, C. Dekker and S. G. Lemay, *J. Am. Chem. Soc.*, 2006, **128**, 7353.
98. C. E. Banks, R. R. Moore, T. J. Davies and R. G. Compton, *Chem. Commun.*, 2004, 1804.
99. A. F. Holloway, K. Toghill, G. G. Wildgoose, R. G. Compton, M. A. H. Ward, G. Tobias, S. A. Llewellyn, B. Ballesteros, M. L. H. Green and A. Crossley, *J. Phys. Chem. C*, 2008, **112**, 10389.
100. T. S. Miller, J. V. Macpherson and P. R. Unwin, *Phys. Chem. Chem. Phys.*, 2014, **16**, 9966.
101. J. Kim, H. Xiong, M. Hofmann, J. Kong and S. Amemiya, *Anal. Chem.*, 2010, **82**, 1605.
102. S. Sansuk, E. Bitziou, M. B. Joseph, J. A. Covington, M. G. Boutelle, P. R. Unwin and J. V. Macpherson, *Anal. Chem.*, 2013, **85**, 163.
103. P. Y. Chen, R. Vittal, P. C. Nien and K. C. Ho, *Biosens. Bioelectron.*, 2009, **24**, 3504.
104. L. Zhu, R. Yang, J. Zhai and C. Tian, *Biosens. Bioelectron.*, 2007, **23**, 528.
105. J. Wang, T. Tangkuaram, S. Loyprasert, T. Vazquez-Alvarez, W. Veerasai, P. Kanatharana and P. Thavarungkul, *Anal. Chim. Acta*, 2007, **581**, 1.
106. H. Cai, X. Cao, Y. Jiang, P. He and Y. Fang, *Anal. Bioanal. Chem.*, 2003, **375**, 287.

107. Q. Shen, S. K. You, S. G. Park, H. Jiang, D. D. Guo, B. A. Chen and X. M. Wang, *Electroanal.*, 2008, **20**, 2526.
108. S. Fogden, R. Verdejo, B. Cottam and M. Shaffer, *Chem. Phys. Lett.*, 2008, **460**, 162.
109. P. Kim, T. W. Odom, J. L. Huang and C. M. Lieber, *Phys. Rev. Lett.*, 1999, **82**, 1225.
110. T. Fukumaru, T. Fujigaya and N. Nakashima, *Sci. Rep.*, 2015, **5**, 7951.
111. L. J. Li, A. N. Khlobystov, J. G. Wiltshire, G. A. Briggs and R. J. Nicholas, *Nat. Mater.*, 2005, **4**, 481.
112. E. L. Sceats and J. C. Green, *J. Chem. Phys.*, 2006, **125**, 12.
113. D. M. Guldi, G. M. A. Rahman, F. Zerbetto and M. Prato, *Acc. Chem. Res.*, 2005, **38**, 871.
114. D. A. Britz and A. N. Khlobystov, *Chem. Soc. Rev.*, 2006, **35**, 637.
115. M. V. Kharlamova, M. Sauer, T. Saito, Y. Sato, K. Suenaga, T. Pichler and H. Shiozawa, *Nanoscale*, 2015, **7**, 1383.
116. X. Li, L. M. Guard, J. Jiang, K. Sakimoto, J.-S. Huang, J. Wu, J. Li, L. Yu, R. Pokhrel, G. W. Brudvig, S. Ismail-Beigi, N. Hazari and A. D. Taylor, *Nano Lett.*, 2014, **14**, 3388.
117. R. H. Baughman, A. A. Zakhidov and W. A. de Heer, *Science*, 2002, **297**, 787.
118. V. Meunier and B. G. Sumpter, *J. Chem. Phys.*, 2005, **123**, 24705.
119. X. Pan and X. Bao, *Chem. Commun.*, 2008, 6271.
120. A. N. Khlobystov, *Acs Nano*, 2011, **5**, 9306.
121. X. Pan and X. Bao, *Acc. Chem. Res.*, 2011, **44**, 553.
122. S. Niyogi, M. A. Hamon, H. Hu, B. Zhao, P. Bhowmik, R. Sen, M. E. Itkis and R. C. Haddon, *Acc. Chem. Res.*, 2002, **35**, 1105.
123. S. Guo, X. Pan, H. Gao, Z. Yang, J. Zhao and X. Bao, *Chem. Eur. J.*, 2010, **16**, 5379.
124. L. H. Guan, Z. J. Shi, M. X. Li and Z. N. Gu, *Carbon*, 2005, **43**, 2780.
125. K. Y. Wu, H. X. Qiu, J. B. Hu, N. J. Sun, Z. W. Zhu, M. X. Li and Z. J. Shi, *Carbon*, 2012, **50**, 4401.
126. N. J. Sun, L. H. Guan, Z. J. Shi, Z. W. Zhu, N. Q. Li, M. X. Li and Z. N. Gu, *Electrochem. Commun.*, 2005, **7**, 1148.
127. L. Kavan, M. Kalbac, M. Zukalova, M. Krause and L. Dunsch, *Chemphyschem.*, 2004, **5**, 274.
128. L. Kavan, M. Kalbac, M. Zukalova, M. Krause, L. Dunsch and H. Kataura, *Fuller. Nanotub. Car. N*, 2005, **13**, 115.
129. L. Kavan, M. Kalbac, M. Zukalova and L. Dunsch, *Carbon*, 2006, **44**, 99.
130. L. Kavan and L. Dunsch, *Chemphyschem.*, 2011, **12**, 47.
131. K. Yanagi, R. Moriya, N. T. Cuong, M. Otani and S. Okada, *Phys. Rev. Lett.*, 2013, **110**, 086801.
132. M. J. Ledoux, R. Vieira, C. Pham-Huu and N. Keller, *J. Catal.*, 2003, **216**, 333.
133. L. Kavan, L. Dunsch and H. Kataura, *Carbon*, 2004, **42**, 1011.
134. L. Kavan, L. Dunsch, H. Kataura, A. Oshiyama, M. Otani and S. Okada, *J. Phys. Chem. B*, 2003, **107**, 7666.
135. L. Kavan, L. Dunsch and H. Kataura, *Elec. Soc. S*, 2003, **2003**, 323.
136. S. A. Miners, G. A. Rance and A. N. Khlobystov, *Chem. Commun.*, 2013, **49**, 5586.

2 Methodology development

2.1 Introduction

A number of the experimental methods used throughout this thesis, while reported, are novel with respect to how they are applied to concepts explored herein. Both the research areas of solid state electrochemistry and solution electrochemistry are extremely well developed but the methods applied here bridge the gap between these two areas and therefore deserve detailed explanation.

For example, individual carbon nanotubes are known for their extreme conductivity but how do they perform as a bulk material? Understanding this is the gateway to further applications. Herein, the differences between the electrochemistry of molecules and our hybrid nanomaterials where molecules are entrapped inside nanotubes are discussed as well as other characterisation methods.

2.2 Aim and objectives

The aim of this chapter is to describe and explain the concepts behind the experimental aspects associated with the electrochemistry of carbon nanotube hybrids applied during this thesis.

The fundamental electrochemistry of nanotubes will be probed, such as how electrons travel to and from encapsulated guest-molecule and how changing the solvent affects the observed electrochemistry. These electrochemical observations will be correlated with TEM and computational modelling.

2.3 Experimental set-up

A three electrode cell was used as with conventional solution electrochemistry. A platinum counter electrode, a GCE and a Ag/AgCl reference electrode were used. Carbon nanotubes were attached to a GCE using a drop casting method[1, 2] where SWNT were dispersed in a non-polar organic solvent such as dimethyl formamide (DMF)[3] and dropped onto the electrode surface (Figure 1). Owing to their surface area and large aspect ratio, SWNT are subject to significant van der Waals forces and have a high tendency to bundle together and adhere strongly to the GCE.[4] CV was performed using an electrode with empty SWNTs attached to it (Figure 1, a), this results in an increase in current compared to the CV using a naked GCE (section 2.3.1), due simply to the increased surface area of the electrode upon nanotube adhesion. The electrochemical properties of empty SWNT have been extensively studied and will be discussed in the next section.[5-9]

The focus of this thesis is the electrochemistry of guest-molecules encapsulated in SWNT with no analyte (molecules under investigation) in solution (Figure 1, b). Therefore, all analyte molecules are electronically connected to the electrode through the nanotube sidewalls so the oxidation state of the guest molecule can be changed by applying electrochemical potential to the electrode. This also results in an observed increase in current, compared to solution electrochemistry, as there are significantly more molecules inside the SWNT, compared to the number reduced in the solution electrochemistry experiment at 0.1 Vs^{-1} (section 2.3.2). In contrast to solution electrochemistry, the redox processes in the nanotube do not rely on diffusion and thus enables investigation into the electronic and steric interactions between guest-molecules and nanotubes using electrochemical measurements. However, there are intricacies involved with this novel type of electrochemistry which are addressed in this chapter.

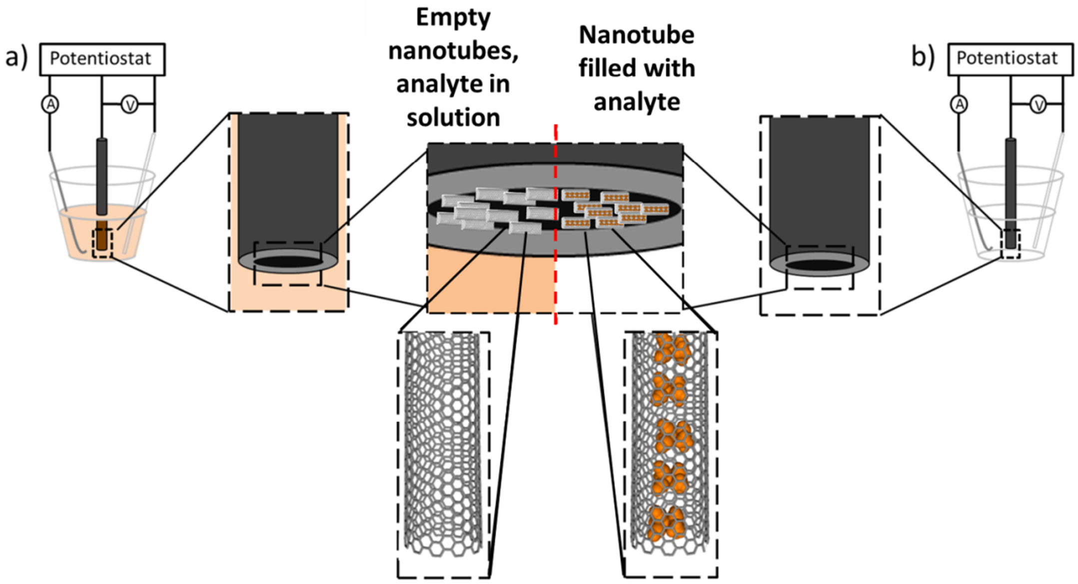

Figure 1. Schematic representation of the experimental set up. A three electrode cell is used as with conventional solution electrochemistry. A platinum counter electrode, a GCE and a Ag/AgCl reference electrode are used. a) Empty carbon nanotubes are attached to the GCE, increasing the surface area but having no effect on the potential of the redox process. b) Carbon nanotubes containing guest-molecules can also be attached with no analyte in solution allowing investigation of redox processes in the nanotube using electrochemical measurements.

2.3.1 Calculating the surface area of the SWNT electrode

As discussed in the previous section, the current observed in CV experiments where the molecules are in solution increases when empty nanotubes are attached to a GCE, this is due to an increase in the surface area of the electrode due to the highly conducting SWNT. The electrochemical surface area of a flat electrode can be calculated using the Randles-Sevcik equation (Equation 1). To apply this equation to SWNT electrodes an assumption is made that the electrode is flat. This is not the case with SWNT/GCE so this calculation only provides an estimate in the difference in surface area. The CV of $Fe(Cp)_2$ in acetonitrile of known concentration was recorded at a series of different scan rates (0.3, 0.2, 0.1, 0.05, 0.02 Vs^{-1}) (Figure 2). The peak current was plotted against the square root of the scan rate. From the gradient of this graph the area was calculated (equation 2). The diffusion coefficient of acetonitrile was calculated using an electrode of know area, ferrocene of known concentration at selected scan rates.

$$i_p = 2.69\ x\ 10^5 n^{3/2} A D_0{}^{1/2} v^{1/2} C_0$$ Equation 1. Randles-Sevcik equation.

$$Gradient = 2.69\ x\ 10^5 n^{3/2} A D_0{}^{1/2} C_0$$ Equation 2.

i_p = peak current, n = number of electrons transferred, A = electrode area, D_0 = diffusion coefficient of solvent, v = scan rate, C_0 = concentration.

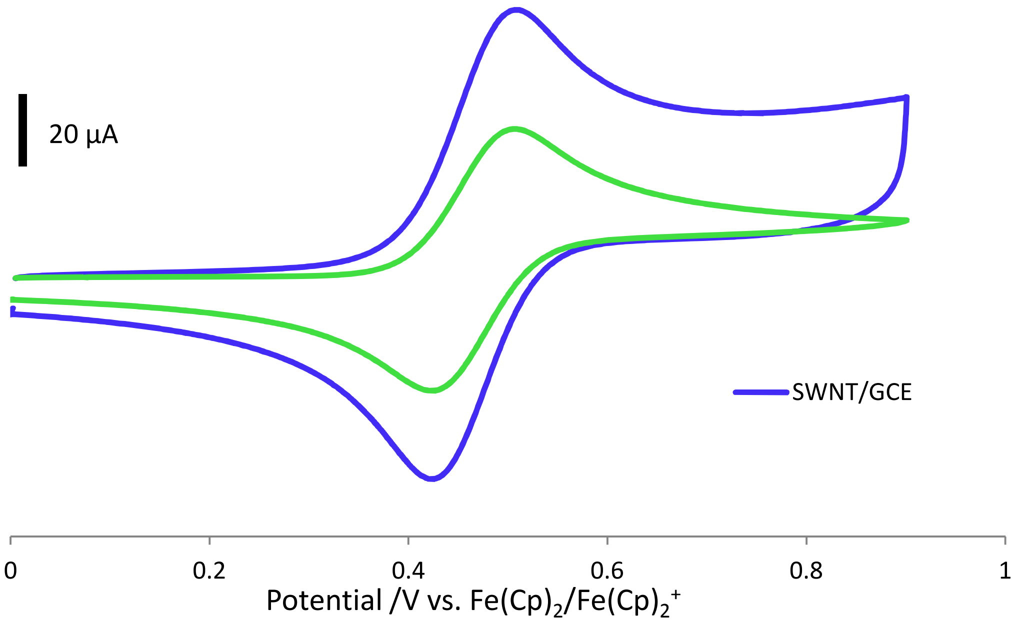

Figure 2. Cyclic voltammograms of $Fe(Cp)_2$ using a GCE (green) and a SWNT/GCE (blue). Both voltammograms were recorded in the same solution. The cyclic voltammetry experiments were performed in MeCN containing $[N^nBu_4][BF_4]$ (0.1 M) as the supporting electrolyte at 293 K and a scan rate of 100 mVs^{-1}.

The physical area of the GCE was calculated using geometric calculations (πr^2, r = 1.5 mm, A = 0.071 cm^2) and the electrochemical area was calculated using the Radles-Sevcik equation (0.0721 cm^2). Using a similar approach, the electrochemical surface area of the SWNT/GCE where 0.01 mg of SWNT was deposited on the GCE was calculated to be 0.27 cm^2, which corresponds to an estimated increase in surface area of 375% as a result of carbon nanotube deposition.

2.3.2 Calculating the number of molecules in the diffusion layer of GCE for comparison with the number of encapsulated guest-molecules in SWNT

An approximation of the number of molecules in the diffusion layer in comparison with the number of molecules encapsulated in SWNT was performed. In this example, $Cp^{\mathbf{Me}}Mn(CO)_3$ was used. Integration of the total current measured when scanning past the peak potential by 118 mV for the first oxidation of $Cp^{\mathbf{Me}}Mn(CO)_3$ during the CV of $Cp^{\mathbf{Me}}Mn(CO)_3$ (3 mmol, 0.1 V s^{-1}) reveals the total amount of charge generated for 99% of the molecules in the diffusion layer. Using Faraday's law, the weight of molecules in the diffusion layer at this time in the experiment was calculated to be 5.78 x 10^{-5} mg, this is 38 times less than the approximate weight of encapsulated $Cp^{\mathbf{Me}}Mn(CO)_3$ in a typical $Cp^{\mathbf{Me}}Mn(CO)_3$@SWNT electrode (0.0022 mg, using geometric models combined with fill percentages) (Section 2.6). This explains the high currents observed when performing the CV of guest-molecules inside SWNT.

2.4 Electrochemical properties of nanotubes

The use of SWNT as hollow electrodes is significantly different to using metals or glassy carbon as electrodes. There are interactions between the hollow nanotube electrodes and guest-molecules upon encapsulation inside the nanotubes which alters the observed electrochemistry. The interactions of fullerene (C_{60}) with nanotubes have been extensively investigated as it was the first guest-molecule inserted into carbon nanotubes.[10-12] The perfect geometrical match of truncated icosahedral fullerene cages and the cylindrical interior of nanotubes provide extremely effective van der Waals interactions that can be as high as 3 eV per molecule.[10] In contrast, although metal complexes have been encapsulated in nanotubes for a wide variety of applications, including catalysis,[13-15] spintronics,[16] and sensors,[17] very little has been reported about the nature of their interactions with the nanotube cavity. The electric charge, asymmetrical distribution of the electron density, and the irregular shape of metal complexes make this a difficult challenge.

SWNT can be semiconducting or metallic depending on diameter and chirality.[18, 19] Within a sample of the SWNT we use, on average there is 31% metallic SWNT and 69% semiconducting SWNT[20] so semiconducting nanotubes must be considered,[21] as they will interact differently with guest-molecules that have different energy highest occupied molecular orbitals (HOMO) because of the presence of a bandgap making SWNT an interesting prospect. (section 2.4.1). A new methodology based on electrochemical measurement is employed in this thesis to probe the interactions between metallocenes and SWNT and to harness the well-defined redox properties of these guest-species to control the electronic properties of the host SWNT.

2.4.1 Linking electrochemistry with theoretical calculations

In LSV measurements of SWNT, electric potential is applied to carbon nanotubes attached to a glassy carbon electrode, and the current between the nanotube and electrode is measured. The magnitude of the current varies significantly and reveals distinguishable charging/discharging processes for the SWNT (average diameter of

1.4 nm) (Figure 3a, red curve). We assume SWNT to be a quantum capacitance dominated electrode such that application of potential in this system causes the shift of the Fermi level.[22, 23] Mapping the experimental measurements onto the calculated DOS of metallic (10,10) and semiconducting (17,0) SWNT representative for this sample (Figure 3a, blue and green curves respectively) helps to understand the observed voltammogram.[20] Hodge *et al* report a similar observation and measure the band gap of nanotubes by CV.[24] In general, the increase in current is associated with the increase in density of full or empty states of the SWNT which are depleted or populated with electrons as the applied potential becomes more positive or negative respectively. For instance, increased current is observed at -0.3 V, 0.50 V and 1.1 V which corresponds to the three major maxima in DOS of nanotubes (van Hove singularities). Similarly, in the region between 0.1 V and -0.28 V very low current is observed in the LSV which correlates with the low DOS of SWNT present in this energy window. Thus the two axis representing the applied potential (red vertical axis, Figure 3a) and the energy levels of SWNT (black vertical axis, Figure 3a) plotted inverse to one another, can link the LSV measurements with theoretically calculated DOS for nanotube samples.

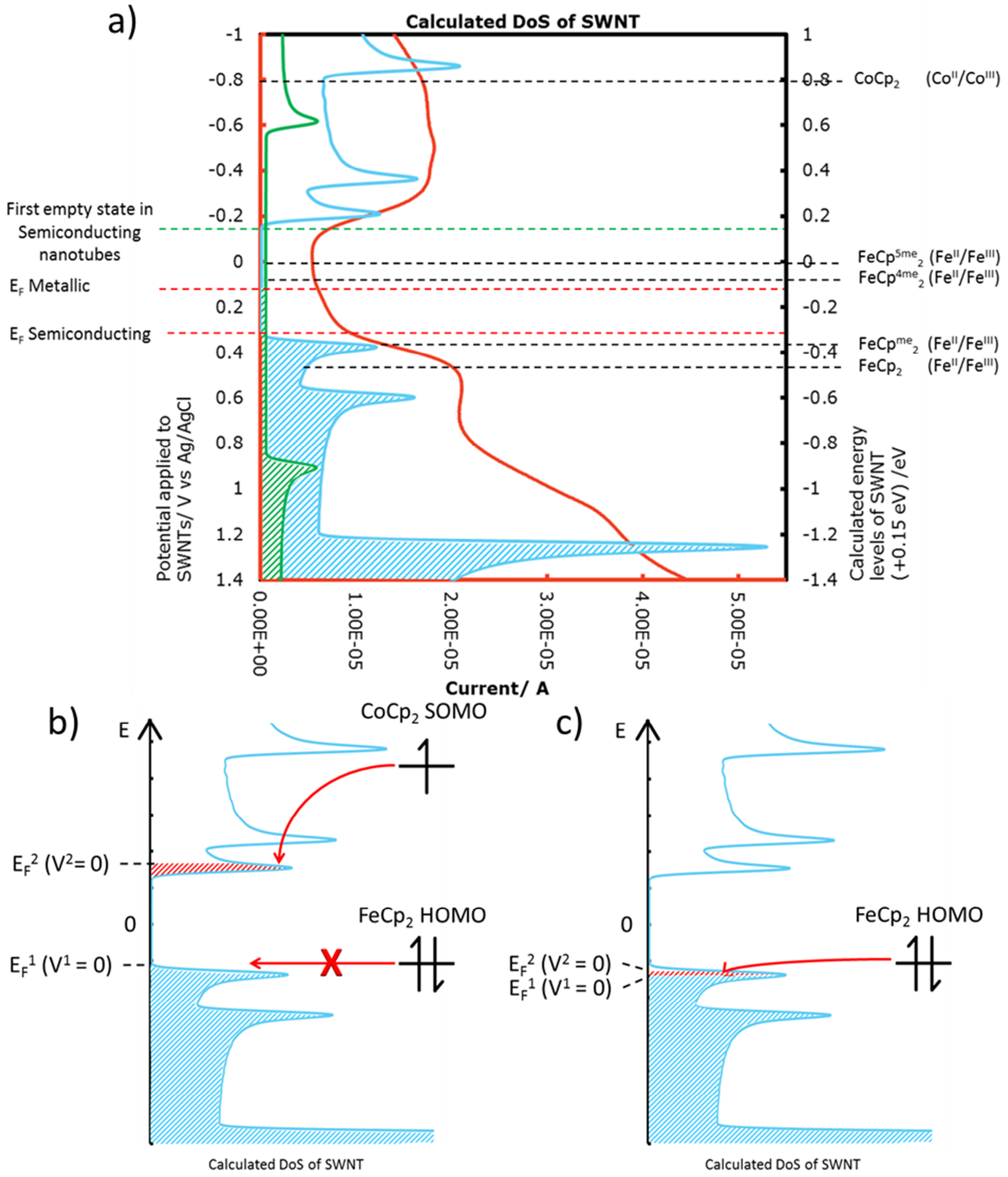

Figure 3. a) Linear sweep voltammogram (LSV) of empty SWNT attached to a GCE (red, red axis) in MeCN containing $[N^nBu_4][BF_4]$ (0.1 M) as the supporting electrolyte at 293 K and at a scan rate of 100 mVs^{-1}. The DOS of semiconducting (17,0) SWNT (blue, black axis) and metallic (10,10) SWNT (green, black axis) calculated by *ab initio* DFT (performed by Dr. Matteo Baldoni). The DOS have been shifted by +0.15, as the energy of the DOS is arbitrary with respect to the electrochemical measurement which is referenced to Ag/AgCl, not absolute potentials eV so that bandgap observed in the LSV matches with that of the calculations. The intensity of the DOS is corrected to represent the ratio of metallic to semiconducting nanotubes in the sample (31:69, metallic : semiconducting)[25] and the higher number of atoms in the calculation of the wider (17,0) SWNT (204:240 atoms) by multiplying by these ratios. The Fermi levels (E_F) are marked by a red dashed line and the lowest energy empty state of the (17,0) SWNT is marked by a green dashed line. The HOMO/singly occupied molecular orbital (SOMO), obtained

from the solution CV experiment of selected guest-molecules are labelled and marked by black dashed lines. Between 0.1 V and -0.28 V a region of low current is observed at the same position as the band gap shown in the DOS of the (17,0) SWNT. Increased current is observed at -0.3 V, 0.50 V and 1.1 V correlating to an increased DOS. b) Shows that electron transfer is possible from the guest-molecule to pristine nanotube in $Co(Cp)_2$@SWNT but not in $Fe(Cp)_2$@SWNT due to the energy level of the HOMO/SOMO of the metallocene with respect to the Fermi level and empty nanotube states. As a result of electron transfer from $Co(Cp)_2$, the Fermi level of SWNT (and therefore zero potential) changes to E_F^2. c) In reality most SWNT are slightly p-doped so that a small amount of electron transfer from $Fe(Cp)_2$ to the SWNT may take place (E_F^2 marks the new Fermi level).

Electrochemical measurements of free molecules, i.e. not encapsulated but in solution, allow the measurement of the first redox potential required to remove an electron from the HOMO/SOMO of the molecule. However, as electronic interactions between the host and the guest in molecule@SWNT systems will result in at least partial electron transfer, the oxidation state of the confined guest-molecule has been altered by encapsulation even before an externally applied potential. As a result of this electron transfer, the energy of the Fermi level of the nanotube also shifts (Figure 3b), so that when electric potential is applied, electrons are removed from a higher (in the case of an electron donating guest-molecule) or lower (in the case of an electron accepting guest-molecule) energy level of the hybrid molecule@SWNT system. Overall, the encapsulation of redox active species into nanotubes can result in hybrid nanostructures with complex electrochemical properties, dramatically different to the properties of the individual components, which may complicate experimental measurements. However, if the synergistic effects of host-guest interactions are understood they can shed light onto the fundamental aspects of electron transfer. This will be discussed in chapters 2 and 3.

2.5 Electron transfer regime

Upon application of potential in conventional solution electrochemistry, analyte molecules are reduced or oxidised at the surface of the electrode, creating a concentration gradient by which subsequent analyte molecules diffuse to the electrode. This means that bulk techniques that require a certain oxidation state of an analyte material require the use of large surface area electrodes, stirring and a long time to oxidise or reduce all of the molecules within the solution. Guest@SWNT materials allow for almost instant oxidation or reduction of all of the molecules in the systems as they are all located inside the nanotubes which are in intimate contact with the electrode. It is important to note that there is still a resistance associated with electron tunnelling between individual nanotubes within the bundles of nanotubes attached to the electrode (see next section 2.5.1). This instant oxidation/reduction of all molecules has possible applications in catalysis as the ability to instantly control the oxidation state of organometallic complexes allows for the initiation and termination of catalysis processes. In conventional solution electrochemistry the products of an electrochemical reaction diffuse away and cannot further react. When performed in the nanotube the kinetic factor of a redox reaction is overridden by the confinements of the analyte in contact with the extended nanotube electrode. These phenomena have an effect on the CV and other electrochemical measurements.

2.5.1 Non-zero ΔE_p for guest@SWNT

Molecules adsorbed on an electrode surface should show a symmetric redox signal (Figure 4) rather than a Nernstian shape because the process is not controlled/limited by diffusion of the analyte to the electrode surface, i.e. molecules do not have to diffuse to the electrode, instead the oxidation or reduction occurs instantly.

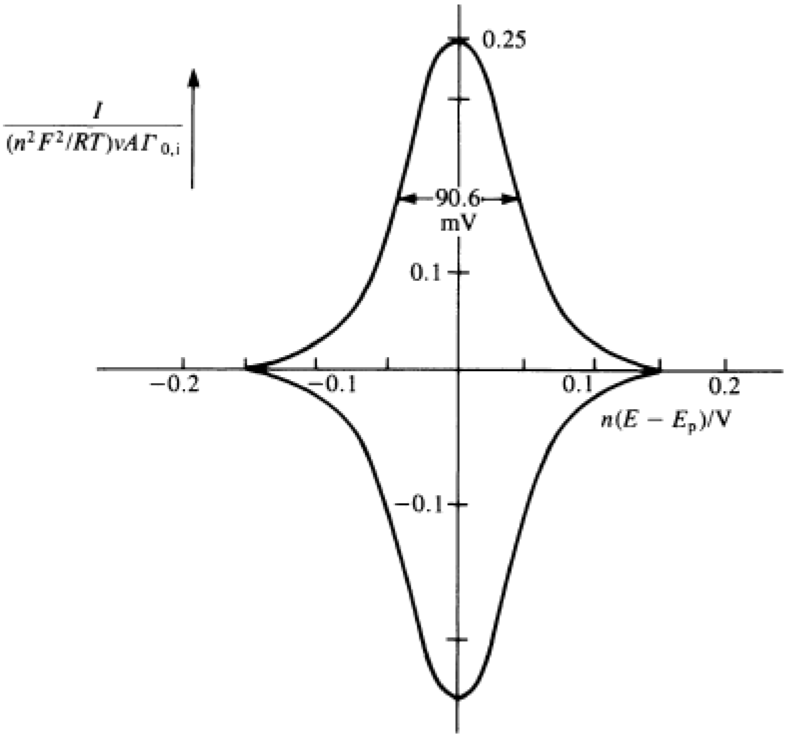

Figure 4. A CV of a species adsorbed on an electrode.[26] A symmetrical wave is observed rather than a Nernstian style wave where ΔE_p = 57 mV. The vertical axis is current.[27]

Voltammograms of molecules encapsulated in a nanotube and attached to an electrode show a peak splitting (ΔE_p) greater than zero. There is a range of values from wide ΔE_p to a ΔE_p too small to be diffusion controlled (ΔE_p < 57 mV). This has been reported as an iR (current x resistance) drop due to intermolecular interactions, π-π stacking and van der Waals forces between $Fe(Cp)_2$ and the SWNT.[17, 28-30] While carbon nanotubes are highly conductive along the length of the nanotube, electron transfer between two carbon nanotubes requires the electron to tunnel and a resistance associated with tunnelling is therefore observed. The observation of a wide ΔE_p was attributed to a resistance to electron transfer between individual nanotubes within the layers and bundles present on the GCE causing an iR drop between the nanotube closest to the electrode and the nanotube furthest from the electrode. Moreover, the guest molecules inside nanotubes in direct contact with the electrode will be oxidised or reduced instantly but an overpotential proportional to the resistance would be required to oxidise or reduce guest-molecules in subsequent nanotubes (Figure 5). A less ordered or thicker stack of nanotubes on the GCE would result in an increased ΔE_p.

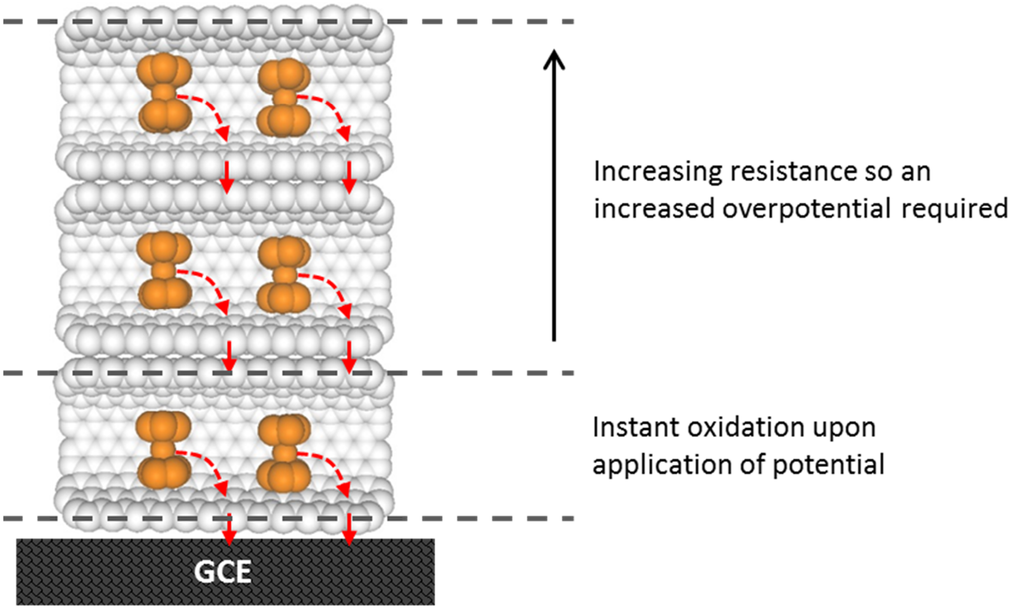

Figure 5. Schematic showing the possible mechanism to explain the presence of a ΔE_p in $Fe(Cp)_2$@SWNT as an example. The $Fe(Cp)_2$ molecules encapsulated in nanotubes attached directly to the electrode are instantly oxidised upon application of an oxidising potential whilst, as a result of increased resistance due to electron tunnelling between nanotubes the $Fe(Cp)_2$ molecules encapsulated in the nanotube furthest from the electrode require an overpotential for oxidation. The electron transfer between $Fe(Cp)_2$ and the nanotube is shown by a dashed red arrow and the electron tunnelling between nanotubes is show as a small solid red arrow (H-atoms omitted)

2.5.2 Effects of immobilisation of $Fe(Cp)_2$ observed in CV

The CV of $Fe(Cp)_2$@SWNT was performed at a selection of scan rates (0.3, 0.2, 0.1, 0.05, 0.02 Vs^{-1}) (Figure 6). The current of the redox process is linear with respect to the scan rate rather than the square route of scan rate (Figure 7). This implies that the oxidation process is not diffusion controlled and non-faradic. Any $Fe(Cp)_2$ adsorbed on the surface is washed off quickly in the electrolytic solvent as reported by Cheng *et al*,[17] confirming that the signal originates from $Fe(Cp)_2$ inside the nanotube.

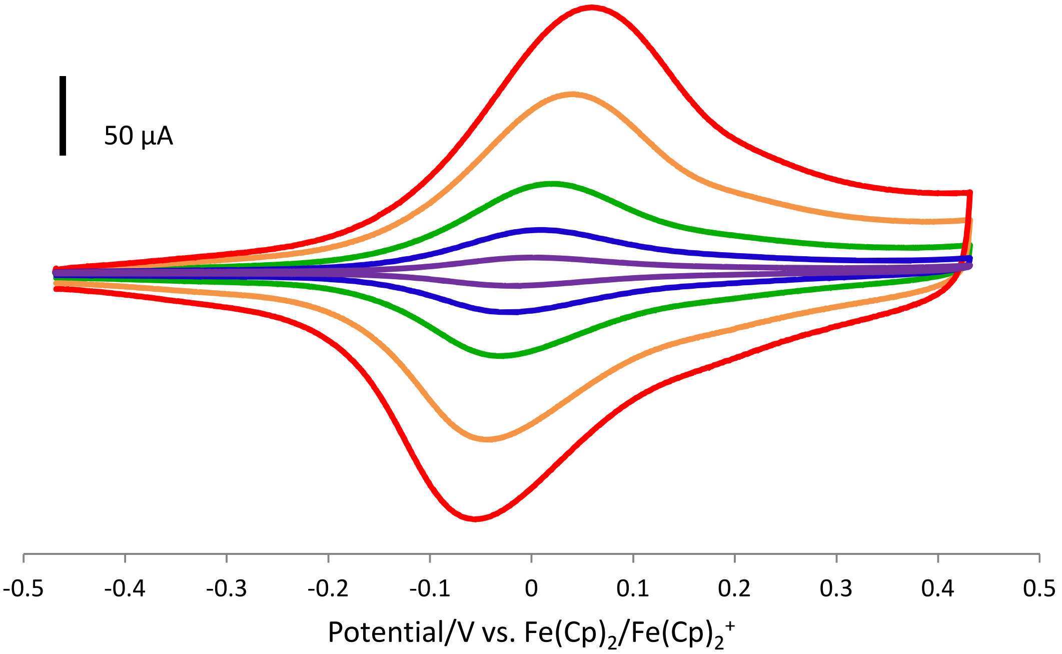

Figure 6. CV of $Fe(Cp)_2$@SWNT at different scan rates (0.3, 0.2, 0.1, 0.05, 0.02 Vs^{-1}, red to violet) in MeCN containing $[N^nBu_4][BF_4]$ (0.1 M) as the supporting electrolyte at 293 K and at a scan rate of 100 mVs^{-1}.

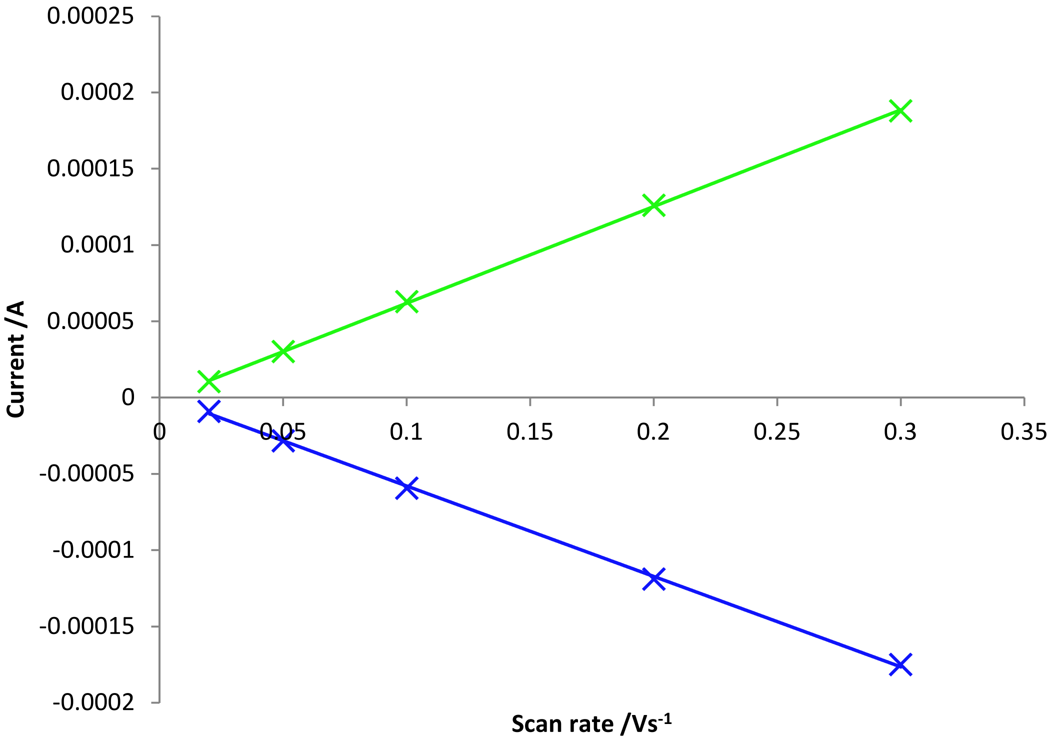

Figure 7. Plot of scan rate vs peak current for $Fe(Cp)_2$@SWNT for the reduction (blue) and oxidation (green). The trend is linear with respect to the scan rate rather than the square route of scan rate so the oxidation process is not diffusion controlled, confirming the $Fe(Cp)_2$ is inside the nanotube.

2.5.3 The effect of different solvents in the electrochemical cell

The protective role played by the nanotube within electrochemistry experiments of guest@SWNT has been reported previously in which the nanotube is demonstrated to prevent a reaction between the electrochemically activated guest and reactive solvent molecules.[31] The choice of solvent for a CV experiment where the species of interest resides in the bulk solution is important, not only for electrical conductance and the range of potentials that can be applied, but also the local environment of the analyte species. Properties such as dielectric constant and the polarity of the solvent perturb the electron density on the analyte species which directly influences its' redox behaviour. For example, when the CV of $Fe(Cp)_2$ in solution is performed with a GCE in five different solvents the redox potential ($E_{1/2}$) of the Fe^{III}/Fe^{II} couple occurs over a wide range of potentials between 0.650 V (ortho-dichlorobenzene) and 0.428 V (acetonitrile) (Figure 8). This is a direct consequence of the different solvent-Fe(Cp)$_2$ interactions altering the electron density on the iron centre to varying extents.

When Fe(Cp)$_2$ is located inside the nanotube, *i.e.* in the absence of any solvent molecules within the immediate environment of Fe(Cp)$_2$, it may be assumed that the potential of the Fe^{III}/Fe^{II} couple of Fe(Cp)$_2$@SWNT would occur at the same potential regardless of the electrolytic solvent. However, although the redox potential of Fe(Cp)$_2$ inside SWNT is significantly less affected by the solvent, a spread of potentials of 0.13 V is observed as compared to 0.22 V for free Fe(Cp)$_2$ in the same set of solvents (Figure 8).

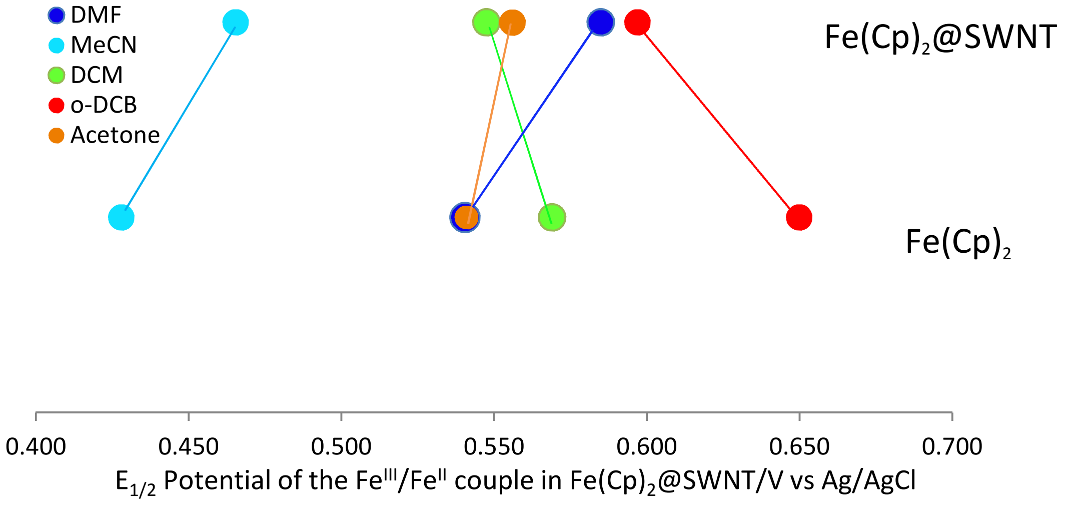

Figure 8. Plot showing the E$_{1/2}$ of Fe^{III}/Fe^{II} of Fe(Cp)$_2$@SWNT (top) and the Fe^{III}/Fe^{II} couple of Fe(Cp)$_2$/GCE (bottom) in five different solvents. When in a nanotube: the E$_{1/2}$ of Fe^{III}/Fe^{II} shifts in the positive direction in MeCN and DMF, acetone also shifts the E$_{1/2}$ in the positive direction but to a much lesser extent; o-DCB and DCM both shift Fe(Cp)$_2$ E$_{1/2}$ in the negative direction, as compared to Fe(Cp)$_2$ in solution. Overall, the effect of solvent on the E$_{1/2}$ of Fe^{III}/Fe^{II} in nanotube is diminished.

Thus the solvent of the electrochemical cell clearly affects the redox process inside the nanotube, i.e. even though the nanotube acts as a protective shell, preventing the solvent from surrounding the $Fe(Cp)_2$ molecules, the influence of the solvent still influences the $Fe(Cp)_2$ through the nanotube. This has been attributed to the highly polarisable nanotube sidewalls[32] mirroring the dipole of the solvent molecules and partially transferring it to the encapsulated $Fe(Cp)_2$ (Figure 9). This demonstrates that even though the nanotube protects the guest species from unwanted reactions with solvent molecules,[31] it does not completely shield the guest from all interactions with the solvent.

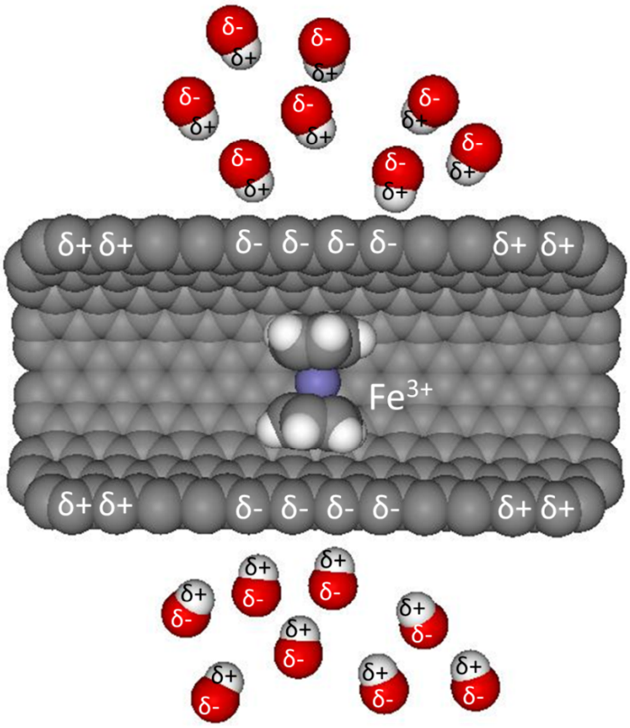

Figure 9. Schematic illustration of how the nanotube mimics the charge on the oxidised $Fe(Cp)_2^+$. The highly polarisable nanotube sidewalls[32] mirror the dipole of the solvent molecules and partially transfer it to the encapsulated $Fe(Cp)_2$. An arbitrary solvent with a dipole forms a solvent cage around the localised charge on the nanotube resulting from the oxidised $Fe(Cp)_2^+$ species to stabilise this accumulation of charge.

2.6 Fill percentage values for guest@SWNT

The fill percentage is the number of encapsulated molecules in a sample compared to the theoretical maximum possible number of molecules that could be encapsulated in a nanotube. To determine this percentage an approach was developed using a comparison of experimental techniques such as coulometry, quantitative energy dispersive X-ray (EDX), TEM imaging, gravimetric analysis and thermogravimetric analysis with geometrical considerations. All of these methods were applied to only $Cp^{Me}Mn(CO)_3$@SWNT but a selection of the most effective methods were used for the majority of samples, most notably TEM imaging. The methods are described below using $Cp^{Me}Mn(CO)_3$ as an example.

2.6.1 Geometrical considerations

The maximum fill ratio of $Cp^{Me}Mn(CO)_3$@SWNT was approximated theoretically by inserting as many $Cp^{Me}Mn(CO)_3$ molecules as possible inside a [10,10]SWNT of known length in a molecular simulation package (ViewerPro), *i.e.* the maximum number of $Cp^{Me}Mn(CO)_3$ without unreasonable distortion of the molecules and nanotube considering the relative van der Waals radii (Figure 10). This gave a maximum number of molecules of $Cp^{Me}Mn(CO)_3$ per number of C atoms in the unit length of nanotube used. Using this ratio of $Cp^{Me}Mn(CO)_3$:C atoms and simply converting the mass of nanotubes within a sample into the number of C atoms present (assuming the entire mass of a sample consists of C atoms within) nanotubes of [10,10]SWNT the total number of $Cp^{Me}Mn(CO)_3$ which can be encapsulated in a SWNT can be approximated. Details of the calculations used are given below. This provided a theoretical 100% fill percentage to compare against experimental samples. Thus all experimental fill values are quoted as a percentage compared to this theoretical maximum packing.

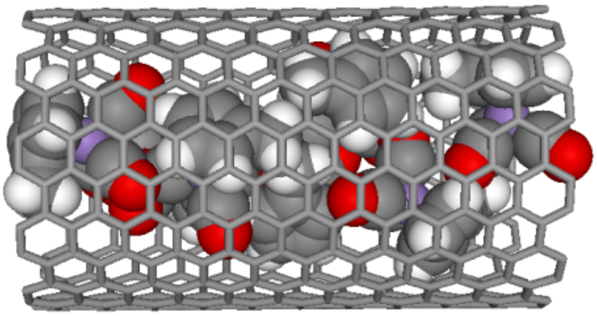

Figure 10. Molecular diagram showing the absolute maximum packing of $Cp^{Me}Mn(CO)_3$ into a [10,10]SWNT made up of 462 C atoms without reasonable distortion considering the relative van der Waals radii.

Calculation of maximum weight % of metal complex in $Cp^{Me}Mn(CO)_3$@SWNT

Number of Mn atoms in seven $Cp^{Me}Mn(CO)_3$ molecules = 7

Weight of $Cp^{Me}Mn(CO)_3$ = 218.09 g mol^{-1}

Number of carbon atoms in a [10,10]SWNT required to encapsulate seven $Cp^{Me}Mn(CO)_3$ molecules = 462

Maximum weight of carbon required to encapsulate seven $Cp^{Me}Mn(CO)_3$ molecules = 462 x 12 = 5544 g mol^{-1}

Weight percentage of guest-molecule in $Cp^{Me}Mn(CO)_3$@[10,10]SWNT sample = [(218.09 x 7) / ((218.09 x 7) + 5544] x 100 = **21.6 %**

Calculation of maximum atomic ratio of Mn:C in $Cp^{me}Mn(CO)_3$@SWNT

Number of Mn atoms in seven $Cp^{Me}Mn(CO)_3$ molecules = 7

Number of carbon atoms in a [10,10]SWNT required to encapsulate seven $Cp^{Me}Mn(CO)_3$ molecules = 462

Number of carbon atoms in seven $Cp^{Me}Mn(CO)_3$ molecules = 63

Atomic percent of Mn:C = [7 / (462 + 63)] x 100 = **1.3 %**

2.6.2 Application of chronocoulometry to determine fill percentage

Using Faraday's law, the charge due to the oxidation of encapsulated molecules was recorded and related to the number of molecules involved in the one electron oxidation. This was compared to geometrical considerations described above. Guest@SWNT lend themselves to this type of characterisation as the guest-molecules are permanently attached to the electrode so do not rely upon diffusion through solution, and therefore, a finite charge is observed in coulometry measurements for guest@SWNT.

A potential 118 mV more positive than the first oxidation of the guest was applied (1.45 V) to $Cp^{Me}Mn(CO)_3$@SWNT attached to an electrode (Figure 11). The charge generated over time (600 s) was recorded and linked to the number of molecules participating in the oxidation by the following equation.

$$m = \frac{QM}{zF}$$ Equation 3. Faraday's Law

m = Weight of material, Q = Charge, M = Molar mass, z = Number of electrons, F = Faraday constant

N.B. This method is only possible if there is not significant electron transfer to or from the SWNT. A more developed method is required in this case that involve oxidation or reduction of the guest-molecules completely to one oxidation state prior to the experiment.

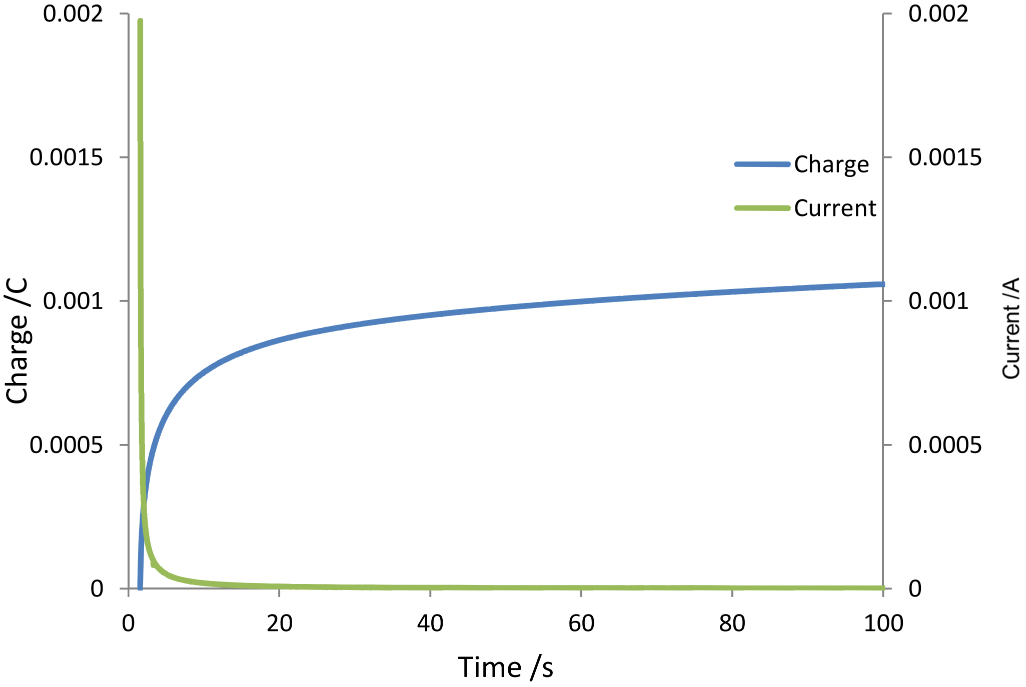

Figure 11. A plot of charge generated by oxidation of $Cp^{Me}Mn(CO)_3$@SWNT over time upon application of 1.45 V. Experiment was performed in MeCN containing $[N^nBu_4][BF_4]$ (0.1 M) as the supporting electrolyte at 293 K.

A significant amount of charge is generated almost instantly due to the fast oxidation of the majority of encapsulated guest-molecules in nanotubes attached to the electrode, this is followed by a steady increase in charge attributed to the resistance over the nanotube layers or slow decomposition of solvent. The current due to solvent decomposition is approximated to be 0.00001 A obtained from a background measurement. When the current dropped to 0.00001 A, the total charge due to $Cp^{Me}Mn(CO)_3$@SWNT oxidation was measured. To prevent any other contributions to the measured charge other than electrons produced from the oxidation of the guest-molecule, the charge generated by empty nanotubes in a separate experiment is subtracted from the charge generated by $Cp^{Me}Mn(CO)_3$@SWNT at the same potential. Faraday's Law is applied to calculate the weight of $Cp^{Me}Mn(CO)_3$ in the $Cp^{Me}Mn(CO)_3$@SWNT sample (0.01 mg) cast onto the GCE and to determine the fill percentage of the nanotubes as summarised by Table 1.

Table 1. Coulometry results to determine the nanotube fill percentage. The calculations for the two experiments are shown (Exp 1 and Exp 2).

	Exp 1	**Exp 2**
Current drops to almost zero (0.00001 A) at t =	15.50 s	14.91s
Total charge at t seconds generated by $Cp^{Me}Mn(CO)_3$@SWNT material	8.26×10^{-4} C	7.30×10^{-4} C
Total charge from Empty SWNT at t	5.70×10^{-5} C	5.70×10^{-5} C
Total charge of $Cp^{Me}Mn(CO)_3$@SWNT minus charge of empty nanotubes	8.07×10^{-4} C	6.73×10^{-4} C
Amount of molecules contributing to the charge (from Equation 3)	1.82×10^{-6} g	1.52×10^{-6} g
Fill percentage	**84 %**	**70 %**

2.6.3 Gravimetric analysis

The empty SWNTs were weighed prior to performing the $Cp^{Me}Mn(CO)_3$ filling experiment using a microbalance. After the filling experiment the nanotubes were weighed again and the difference equated to the weight of encapsulated complex in the $Cp^{Me}Mn(CO)_3$@SWNT sample (Table 2).

Table 2. Results and percentages from gravimetric analysis. Each experiment was performed under the same conditions.

Experiment	Weight SWNT (mg)	Weight $Cp^{Me}Mn(CO)_3$@SWNT (mg)	Encapsulated $Cp^{Me}Mn(CO)_3$	Weight percent $Cp^{Me}Mn(CO)_3$ /%	Fill percentage /%
1	5.57	6.45	0.88	14	63
2	5.27	6.08	0.81	13	62
3	11.46	13.58	2.12	16	72

2.6.4 Thermogravimetric analysis (TGA)

TGA was performed to determine the percentage weight of the encapsulated complex in $Cp^{Me}Mn(CO)_3$@SWNT. A small amount of water is present in the samples (Figure 12) and was accounted for (Table 3).

Table 3. Results and percentages from the TGA experiment. Experiment 1 and 3 were heated to 1000 °C at a rate of 10 °C min^{-1}. Experiment 2 was heated to 1000 °C at a rate of 1 °C min^{-1} All TGA experiments were performed under an atmosphere of air. The percentage of water of the total sample weight was 6.76 %, 5.38 % and 5.69 % for experiments 1, 2 and 3 respectively.

Experiment	Weight percent of complex in $Cp^{Me}Mn(CO)_3$@SWNT /%	Weight percent of sample after water removal /%	Fill percentage /%
1	12	93	58
2	10	95	48
3	9	94	45

The residual weight at the end of the experiment is slightly higher than that observed in the TGA plot of empty SWNTs. This was attributed to manganese oxide formation that is not further oxidised until temperatures surpassing 1000 °C. TGA was performed on a TGA Q 500.

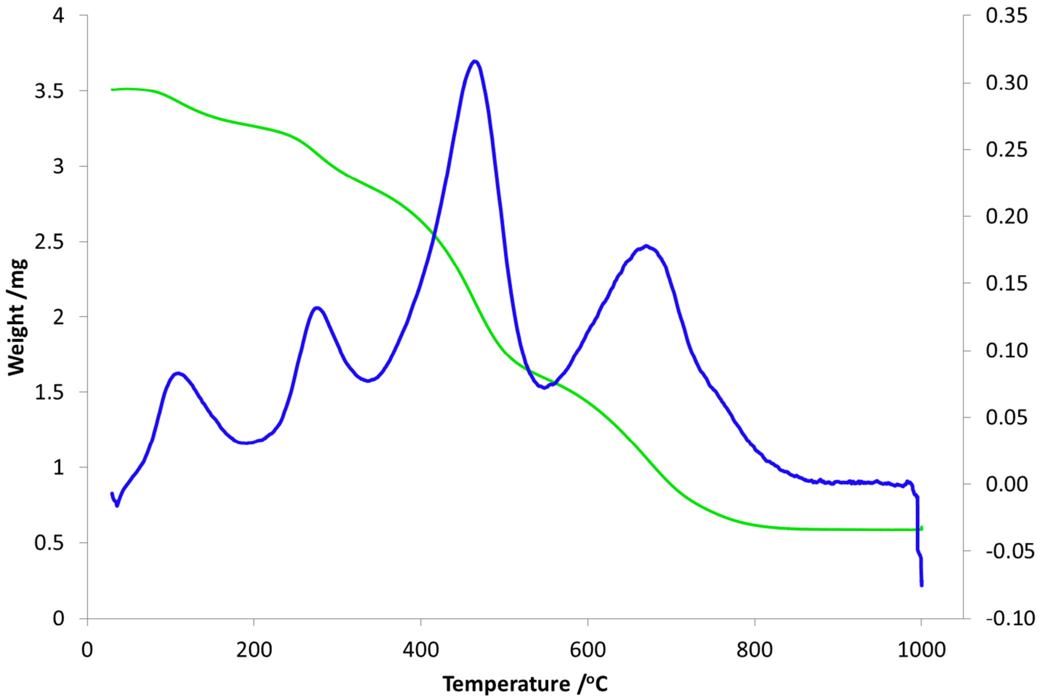

Figure 12. TGA graph showing the weight loss vs. temperature (green) and the derivative weight vs. temperature (blue) for a sample of $Cp^{Me}Mn(CO)_3@SWNT$. The first weight loss (70-180 °C) was attributed to water loss, the second two to $Cp^{Me}Mn(CO)_3$ decomposition and the fourth to SWNT oxidation. TGA experiment performed in an atmosphere of air.

2.6.5 Quantitative EDX

EDX analysis was performed on suspended bundles of nanotubes of about 50 – 100 supported on an amorphous carbon film using a 100 keV electron beam. The beam was focused on a 3 nm spot using condenser aperture number 3. The atomic percent of carbon to manganese was obtained and compared to the maximum fill ratio obtained using geometric considerations (Section 2.6.1) (Table 4).

Table 4. Showing the atomic percent of carbon and manganese $Cp^{Me}Mn(CO)_3@SWNT$ determined by EDX.

C (%)	Mn (%)	Mn:C ratio
88.67	0.15	0.00169
86.05	0.15	0.00174
91.57	0.17	0.00186
91.37	0.11	0.00120

The average atomic ratio of Mn:C from EDX is 0.00162 ± 0.0004, which compared to the maximum atomic ratio calculated from geometric considerations (0.0133) indicates the fill percentage is [0.00162 / 0.0133] x 100 = 12.5 %. This is lower than expected compared to other methods, which is possibly a result of the fact that EDX is likely to overestimate the amount of carbon in the sample, as the sample is suspended on an amorphous carbon film which can increase the EDX signal of carbon.

2.6.6 TEM imaging approximation

High resolution transmission electron microscopy (HRTEM) of $Cp^{Me}Mn(CO)_3@SWNT$ confirms the successful encapsulation of the Mn guest complex with metallic nanoparticles observed in the interior of the SWNT as a result of decomposition of the guest under the electron beam (Figure 14). The nanoparticles are estimated to be 25 Mn atoms as most of the nanoparticles are small, < 0.5 nm. This was estimated by measuring the diameter and therefore the volume of the nanoparticles, then using the density of bulk metal determining the number of atoms per nanoparticle. Nanoparticles are less dense than bulk metal producing the number of atoms per nanoparticle to be between 23 and 33. A value of

25 Mn atoms was utilised for the calculations as it produced sensible fill rates (not over 100 % and consistent with other methods described in this section).

Counting the nanoparticles per length of nanotube, considering the number of metal atoms in a nanoparticle and comparing with the maximum packing of $Cp^{Me}Mn(CO)_3$ per length of nanotube in the model allows an estimation of the fill percentage (Table 5).

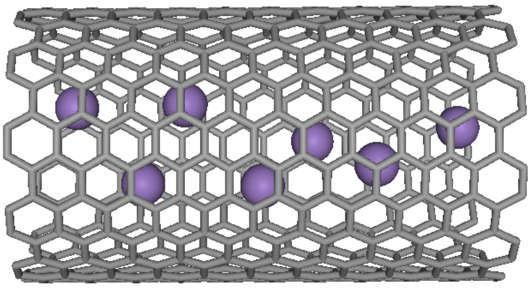

Figure 13. Molecular diagram showing the maximum packing of $Cp^{Me}Mn(CO)_3$ with the ligands removed in a nanotube of length 2.53 nm. This figure is the same model as in Figure 10 but with the atoms of the ligands removed to aid clarity.

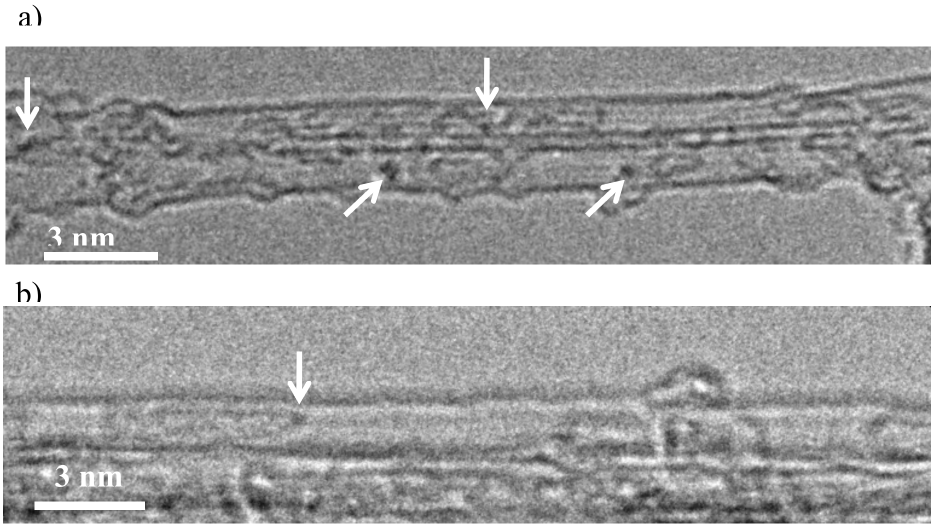

Figure 14. HRTEM images of $Cp^{Me}Mn(CO)_3$@SWNT showing Mn metal as dark contrast (white arrows) located solely inside the SWNT a) shows nanotube 1 (top) and 2 (bottom). b) shows nanotube 3. The number of metal atoms is approximated to be 25 per nanoparticle.

Table 5. Calculation performed to determine the fill percentage of $Cp^{Me}Mn(CO)_3@SWNT$ using TEM imaging.

Nanotube	**1**	**2**	**3**
Length (nm)	32.9	32.9	27.7
Number of nanoparticles	2	2	2
Mn atoms per nanoparticle	25	25	25
Mn atoms per length nanotube in model (Mn nm^{-1})	2.77	2.77	2.77
Mn atoms per length nanotube in TEM image (Mn nm^{-1})	1.52	1.52	1.81
Fill percentage	**55 %**	**55 %**	**65 %**

2.6.7 Summary of different methods for nanotube fill percentage determination

The fill percentages determined by different methods for the same experimentally prepared $Cp^{Me}Mn(CO)_3@SWNT$ material ranged from 13 % to 84 % of maximum fill rate of complex in $Cp^{Me}Mn(CO)_3@SWNT$ and have been determined by different methods for the same material. As discussed, quantitative EDX yields a far lower than expected fill percentage, however, it is a useful technique to compare relative fill rates. Apart from EDX all other methods show a high fill rate between 44% and 84% (Table 6).

Table 6. A summary of all methods and the respective fill percentage.

Method	**Experiment number**	**Fill percentage (%)**
Chronocoulometry	1	84
	2	70
Gravimetric analysis	1	63
	2	62
	3	72
TGA	1	53
	2	47
	3	44
Quantitative EDX	1	13
TEM imaging	1	55
	2	55
	3	65

TEM was chosen as the method to use to characterise all nanotubes filled with guest-molecule throughout all studies in this thesis. Not only does this method quantify percentage of guest-molecules in nanotubes for each sample, as discussed above, but it is also the only technique which unambiguously determines that the complex is located inside the nanotubes.

2.7 TEM imaging for metallocene@SWNT

The quantification of fill percentage from TEM imaging was particularly useful for metallocenes@SWNT. The nanoparticles are estimated to be 25 Fe atoms as discussed above for $Cp^{Me}Mn(CO)_3$@SWNT (Section 2.6.6). Comparative determination of fill rates for ferrocenes and methylated ferrocenes was performed by TEM and calculated as discussed below (following the same logic as for $Cp^{Me}Mn(CO)_3$@SWNT as described in Section 2.6.6). The maximum amount of guest-molecules were put inside a [10,10]SWNT of known length in a molecular simulation package (ViewerPro), *i.e.* the maximum number of guest without unreasonable distortion of the molecules and nanotube considering the relative van der Waals radii, then the ligands were removed (Figure 15). The HRTEM of the samples that were used for these calculations are in the experimental of chapter 3 (Table 7).

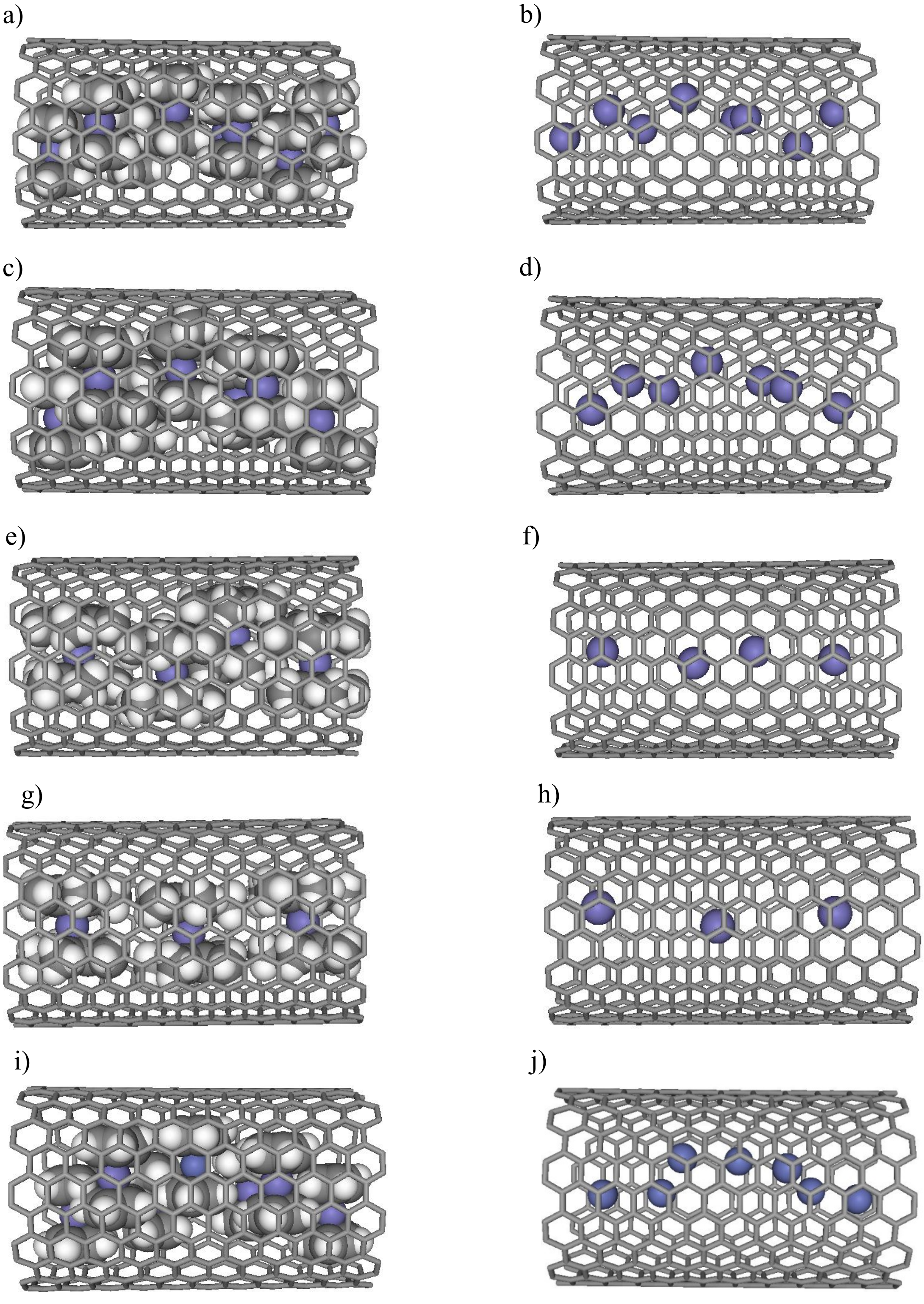

Figure 15. Molecular diagrams showing the maximum packing of (a, b) $Fe(Cp)_2$, (c, d) $Fe(Cp^{Me})_2$, (e, f) $Fe(Cp^{4Me})_2$, (g, h) $Fe(Cp^{5Me})_2$ and (i, j) $Co(Cp)_2$ with ligands (a, c, d, e, g and i) and without ligands (b, d, f, h and j) in a nanotube of length 2.53 nm.

Table 7. Calculation performed to determine the fill percentage of X@SWNT using TEM imaging.

X@SWNT	**Length (nm) of SWNT in TEM experiment**	**Number of NPs in SWNT observed in TEM**	**Number of metal atoms per NP**	**Number of metal atoms per length nanotube in model (metal atom nm^{-1})**	**Number of metal atoms per length nanotube in TEM experiment (metal atom nm^{-1})**	**Fill percentage / %**
$Fe(Cp)_2$@SWNT	30.3	3	25	3.17	2.48	78
	24.8	3	25	3.17	3.02	95
	Average:					**87**
$Fe(Cp^{Me})_2$@SWNT	31.4	3	25	2.77	2.39	86
	30.0	3	25	2.77	2.50	90
	Average:					**88**
$Fe(Cp^{4Me})_2$@SWNT	35.8	2	25	1.58	1.39	88
	32.3	2	25	1.58	1.55	98
$Co(Cp)_2$@SWNT	38.1	4	25	2.77	2.62	95
	38.1	4	25	2.77	2.63	95
	Average:					**95**
$Fe(Cp^{5Me})_2$@SWNT	35.8	1	25	1.19	0.7	59
	35.8	1	25	1.19	0.7	59
	27.0	1	25	1.19	0.7	78
	27.2	1	25	1.19	0.7	78
	Average:					**69**

All nanotubes samples had a high fill percentage, the lowest being $Fe(Cp^{5Me})_2$. It is worth noting that the guest-molecules with a higher van der Waals volume ($Fe(Cp^{5Me})_2$ and $Fe(Cp^{4Me})_2$) had a similar fill percentage to those with a lowered van der Waals volume ($Fe(Cp)_2$, $Fe(Cp^{Me})_2$ and $Co(Cp)_2$) but due to their size, fewer molecules of $Fe(Cp^{5Me})_2$ and $Fe(Cp^{4Me})_2$ are encapsulated at these fill percentages. As a consequence, when analysing currents observed from encapsulated molecules, this must be considered.

2.8 Conclusions

This chapter introduces novel concepts that are important to this thesis, including the development of electrochemical approaches for the determination of the fill percentage of SWNT with electrochemically active guest molecules. Considerations of the SWNT electronic structure with respect to guest-molecules, including the semiconducting SWNT and the van Hove singularities in the SWNT DOS, allow the development of experiments to probe the electronic effect of nanotube encapsulation in detail in chapters 3 and 4. It was determined that the iR drop due to resistance originates from electron tunnelling between nanotubes and it was also confirmed that the oxidation processes observed in CV of guest@SWNT were from the confined guest-molecules. The confirmation that these processes occur inside the nanotube and that these measurements can be used to determine the nature of the redox processes observed are essential in the work discussed in this thesis. The iR drop across nanotube layers explains the variation in ΔE_p, observed for molecules in nanotubes throughout this thesis, but especially in chapter 6 where irreversible reactions of guest-molecules occur in nanotubes, confirmed by changes in the CV curves, including the ΔE_p. The effect of solvent is particularly important with respect to chapter 5 where the solvent acts as a reactant, and chapter 6 where changes in the CV curve of guest@SWNT can be explained by decreased solvent stabilisation. It is also further evidence of the highly mobile electrons in the nanotube moving to compensate for changes induced by internal and external stimuli.[32] Finally, the ability to measure the fill percentage of guest-molecules in SWNT confirms the presence of guest-molecules, but more importantly it allows for quantitative analysis of oxidation state and electron transfer as demonstrated in chapter 4.

This chapter is intended to introduce key aspect of nanotubes as electrodes and molecular containers specific to our host-guest systems. It explores some of the phenomena imperative for understanding later chapters, bridging the gap between solution electrochemistry and solid state electrochemistry.

2.9 References

1. L. H. Guan, Z. J. Shi, M. X. Li and Z. N. Gu, *Carbon*, 2005, **43**, 2780.
2. C. Y. Liu, A. J. Bard, F. Wudl, I. Weitz and J. R. Heath, *Electrochem. Solid St.*, 1999, **2**, 577.
3. G. P. Keeley and M. E. G. Lyons, *Int J Electrochem Sc*, 2009, **4**, 794.
4. Y. Y. Chan, A. Y. S. Eng, M. Pumera and R. D. Webster, *Chemelectrochem*, 2015, **2**, 1003.
5. A. Merkoci, M. Pumera, X. Llopis, B. Perez, M. del Valle and S. Alegret, *Trac-Trend. Anal. Chem.*, 2005, **24**, 826.
6. M. Pumera, T. Sasaki and H. Iwai, *Chem. Asian. J.*, 2008, **3**, 2046.
7. M. Pumera, *Chem. Eur. J.*, 2009, **15**, 4970.
8. I. Dumitrescu, P. R. Unwin and J. V. Macpherson, *Chem. Commun.*, 2009, **45**, 6886.
9. X. B. Ji, R. O. Kadara, J. Krussma, Q. Y. Chen and C. E. Banks, *Electroanal.*, 2010, **22**, 7.
10. H. Ulbricht, G. Moos and T. Hertel, *Phys. Rev. Lett.*, 2003, **90**, 095501.
11. A. N. Khlobystov, D. A. Britz, J. W. Wang, S. A. O'Neil, M. Poliakoff and G. A. D. Briggs, *J. Mater. Chem.*, 2004, **14**, 2852.
12. L. A. Girifalco, M. Hodak and R. S. Lee, *Phys. Rev. B.*, 2000, **62**, 13104.
13. M. A. Lebedeva, T. W. Chamberlain, M. Schröder and A. N. Khlobystov, *Chem. Mater.*, 2014, **26**, 6461.
14. W. A. Solomonsz, G. A. Rance and A. N. Khlobystov, *Small*, 2014, **10**, 1866.
15. X. Pan and X. Bao, *Chem. Commun.*, 2008, 6271.
16. C. Gimenez-Lopez Mdel, F. Moro, A. La Torre, C. J. Gomez-Garcia, P. D. Brown, J. van Slageren and A. N. Khlobystov, *Nat. Commun.*, 2011, **2**, 407.
17. H. M. Cheng, H. X. Qiu, Z. W. Zhu, M. X. Li and Z. J. Shi, *Electrochim. Acta*, 2012, **63**, 83.
18. P. Kim, T. W. Odom, J. L. Huang and C. M. Lieber, *Phys. Rev. Lett.*, 1999, **82**, 1225.
19. T. W. Odom, J. L. Huang, P. Kim and C. M. Lieber, *J. Phys. Chem. B*, 2000, **104**, 2794.
20. A. Pekker and K. Kamaras, *Phys. Rev. B.*, 2011, **84**, 075475.
21. A. M. Schimpf, K. E. Knowles, G. M. Carroll and D. R. Gamelin, *Acc. Chem. Res.*, 2015, **48**, 1929.

22. I. Heller, J. Kong, H. A. Heering, K. A. Williams, S. G. Lemay and C. Dekker, *Nano Lett.*, 2005, **5**, 137.
23. I. Heller, J. Kong, K. A. Williams, C. Dekker and S. G. Lemay, *J. Am. Chem. Soc.*, 2006, **128**, 7353.
24. S. A. Hodge, M. K. Bayazit, H. H. Tay and M. S. Shaffer, *Nat. Commun.*, 2013, **4**, 1989.
25. S. Cambre, W. Wenseleers, E. Goovaerts and D. E. Resasco, *Acs Nano*, 2010, **4**, 6717.
26. C. M. A. Brett and A. M. O. Brett, *Electrochemistry principles, Methods and Applications*, Bookcraft (Bath) Ltd., 1993.
27. A. J. Bard and L. R. Faulkner, *Electrochemical Methods: Fundamentals and Applications*, John Wiley and Sons, Inc., 2001.
28. N. J. Sun, L. H. Guan, Z. J. Shi, Z. W. Zhu, N. Q. Li, M. X. Li and Z. N. Gu, *Electrochem. Commun.*, 2005, **7**, 1148.
29. L. Kavan, M. Kalbac, M. Zukalova, M. Krause, L. Dunsch and H. Kataura, *Fuller. Nanotub. Car. N*, 2005, **13**, 115.
30. N. Sun, L. Guan, Z. Shi, N. Li, Z. Gu, Z. Zhu, M. Li and Y. Shao, *Anal. Chem.*, 2006, **78**, 6050.
31. R. L. McSweeney, T. W. Chamberlain, E. S. Davies and A. N. Khlobystov, *Chem. Commun.*, 2014, **50**, 14338.
32. S. A. Miners, G. A. Rance and A. N. Khlobystov, *Chem. Commun.*, 2013, **49**, 5586.

3 The effect of nanotube encapsulation on guest-molecules

3.1 Introduction

The confinement of individual molecules inside nanoscale containers is a powerful method which allows the exploration of chemistry at the single-molecule level.[1, 2] As the dimensions of the host container approaches the size of the encapsulated molecule, the effects of extreme spatial constraint result in changes in van der Waals interactions and electron transfer leading to new dynamic behaviour and the emergence of physicochemical properties of the confined molecules unattainable in the bulk.[3-6]

SWNT are an increasingly popular choice as molecular containers because not only do they possess nanoscale cavities in the range of 0.7 - 2.0 nm, commensurate with small and medium sized molecules, but they also boast exciting electronic properties. The unique electronic structure[7] of SWNT and the ability to exhibit either metallic or semiconducting behaviour depending only on chirality,[8] while interacting effectively with electron donors and acceptors, make nanotubes highly tuneable nanoscale containers with respect to electronic interactions with guest-molecules.

3.1.1 Use of spectroscopic methods to investigate nanotube-guest interactions

Previous work studying the nature of interactions between nanotubes and guest-molecules include the application of UV-vis[5] and infra-red (IR)[1] spectroscopies to probe the confined molecules. For example, the UV-vis spectrum of $Co(Cp)_2$ shows two strong absorption bands for the metal to ligand (M-L) and ligand to metal (L-M) charge-transfer transitions. Upon $Co(Cp)_2$ encapsulation in SWNT, a smearing of the M-L absorption and a shift in the L-M absorption to lower energy was attributed to the formation of cobaltocenium ions in the SWNT.[5, 9] On the other hand, nanotubes absorb most UV-vis radiation, resulting in weak and hard to interpret signals so it is difficult to draw outright conclusions or quantitative information from this result. Shifts in the υ(CO) bands in the IR spectrum of hexacarbonyls such as $Re_2(CO)_{10}$, $Os_3(CO)_{12}$ and $W(CO)_6$ suggest an electron transfer between the guest metal carbonyl molecule and the nanotube.[1] However, it is difficult to determine the exact nature and magnitude of this interaction due to the suppression of the υ(CO) band by the host-nanotube.[10] Therefore, use of UV-vis and IR spectroscopies can be challenging due to absorption of radiation by the host-nanotube which may obscure many important subtle features of the nanotube-molecule interactions. Other techniques have been employed to analyse the nanotube and guest-molecule oxidation state in $Fe(Cp)_2$@SWNT using separate probes such as X-ray photoelectron spectroscopy (XPS), photo emission spectroscopy (PES) and X-ray absorption (XAS) which determined an n-type electron transfer to SWNT from $Fe(Cp)_2$. These measurements were performed on metallicity sorted nanotubes and the charge transfer was observed to be 30 % less in semiconducting nanotubes in comparison to metallic, demonstrating the importance of considering the contribution of both semiconducting and metallic nanotubes to host-guest interactions. The type of interaction between the SWNT and $Fe(Cp)_2$ was determined using PES, it was assigned as an ionic interaction due to the weak hybridisation between the Fe 3d orbital and carbon states.[11] The combination of these methods provides a powerful tool for determining the doping of SWNT, however, there are notorious difficulties associated with data interpretation as well as only being surface techniques. Another interesting method has been reported that utilises an electrode to elevate the potential of the nanotube, which in turn perturbs the electronic state of an encapsulated guest-molecule. This work was performed using β-carotene@SWNT, β-carotene has strong C=C stretching modes that can be measured using Raman spectroscopy and are changed depending on the potential applied to the nanotube, however, this method is limited to guest-molecules that have Raman active vibrations (Chapter 1).[12] Overall, as SWNT interact strongly and absorb a wide range of electromagnetic radiation (UV-vis, IR, near-IR), the use of spectroscopy to probe guest-molecules inside nanotubes can be challenging and in many cases ambiguous as the spectroscopic signal of molecules adsorbed on the nanotube surface overpowers the weak signals of encapsulated molecules due the shielding by SWNT.

An alternative approach is to exploit the highly electrically conductive nature of SWNT, which enables efficient charge transfer between guest-molecules and the nanotube to probe the confined molecules.[13] In particular, electrochemical measurements offer an ideal method for precise characterisation of host-guest interactions between molecules and nanotube.[14] Cyclic voltammetry has been utilised successfully to study confined molecules and to tune their functional properties, as demonstrated in metal-organic frameworks (MOF),[15, 16] zeolites[17] and molecular cages.[18-20] However, poor electrical conductivity of most of these host-structures prohibits reliable pathways for charge transfer between the electrode and confined guest-molecules. In contrast, charge transport through the nanotube onto confined guest-molecules is uninhibited and very efficient making SWNT the ideal host systems for studying redox phenomena at the nanoscale.

Herein, an electrochemical study of redox active guest-molecules confined within carbon nanotubes is reported and it is demonstrated that the oxidation state of guest-molecules is altered due to electron transfer to the nanotubes. The amount of electron transfer is determined by the energy of the guest HOMO/singularly occupied molecular orbital (SOMO) and the diameter of the SWNT.

3.2 Aim and objectives

The aim is to determine the influence of the confinement imposed by SWNT encapsulation on the guest-molecules using electrochemistry.

The objectives to complete this aim are to encapsulate a series of guest-molecules in firstly SWNT and then a select molecule in varying diameter SWNT and DWNT. Electrochemical methodologies will then be developed and explored to determine the effects of encapsulation. Using CV, the series of molecules encapsulated inside SWNT will be probed and any changes in redox potential or current may be linked to a change in oxidation state of the guest-molecule which, by considering direct comparisons with *ab initio* DFT (as performed my Dr. Matteo Baldoni), will provide information on the nature and magnitude of the host-guest interaction.

3.3 Results and discussion

3.3.1 Filling of SWNT with different metallocenes

The most successful method for inserting metallocenes ($Fe(Cp)_2$, $Fe(Cp^{Me})_2$, $Fe(Cp^{4Me})_2$, $Fe(Cp^{5Me})_2$ and $Co(Cp)_2$) into nanotubes was through a vapour phase filling where opened SWNT are sealed with the metallocene in an ampule at a low pressure (10^{-6} mbar) then heated past the sublimation temperature for the metallocene. The highest filling rates were observed when temperatures well above the sublimation point were used. This was attributed to an activation energy associated with the molecules entering the SWNT. Air sensitive molecules such as $Co(Cp)_2$ were prepared under the inert conditions of the glove box then transferred to the vacuum in the absence of air. These methods elegantly work as purification where only those molecules that have sublimed at the chosen temperature are filled into the SWNT, leaving any contaminants or unwanted molecules as a solid in the bottom of the ampule. HRTEM and EDX were performed on all nanotube samples (see Chapter 2). Upon encapsulation in carbon nanotubes ferrocene can adopt two orientations, parallel or perpendicular to the nanotube length (Figure 1) geometry optimisation calculations performed by Dr Matteo Baldoni determine the parallel orientation to be most stable in the absence of external potential.

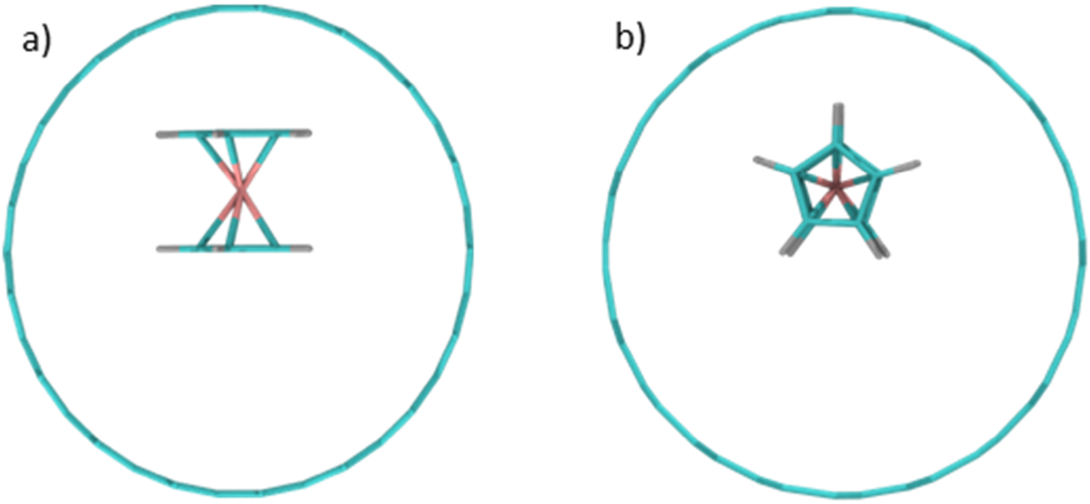

Figure 1. *Ab initio* geometry optimised model of $Fe(Cp)_2$@(10,10)SWNT in both the perpendicular a) and parallel b) orientations. The calculations reveal that both orientations are stable inside the nanotube but that the parallel orientation is more stable than the perpendicular orientation. Where ΔE (ΔE= E(Metallocene@CNT)-E(Metallocene)-E(SWNT)) is -7.65 kcal mol^{-1} and -3.67 kcal mol^{-1} respectively. Calculations and figure produced by Dr. Matteo Baldoni.

3.3.2 Cyclic voltammetry of ferrocene@SWNT

The electrochemistry of ferrocene ($Fe(Cp)_2$) is the most studied among organometallic complexes, so this molecule represents the best starting point for investigation of host-guest interactions with SWNT. The CV was performed with empty SWNT (arc-discharge, 1.4 nm internal diameter) on a GCE and $Fe(Cp)_2$ in solution (Chapter 2, Figure 1). An increased current is observed compared to a bare GCE due to the increase in surface area of the electrode (Chapter 2). The potential of the ferrocene redox process is unchanged when using empty SWNT on a GCE, therefore, the redox process is unchanged from that in solution. The redox potential ($E_{1/2}$) of the Fe^{III}/Fe^{II} couple of $Fe(Cp)_2$@SWNT (Figure 2) is observed to shift by +0.04 V compared to the same measurement performed for $Fe(Cp)_2$ in solution, outside nanotubes (Figure 2). Such a small but measurable shift of the Fe^{III}/Fe^{II} couple was previously observed in other nanocontainers with a positive charge,[18-21] and can be attributed to a decrease in electron density on the iron centre of $Fe(Cp)_2$ compared to the CV of $Fe(Cp)_2$ in solution which is supported by theoretical studies showing the increased electron transfer for molecules encapsulated inside SWNT.[22] The HOMO of $Fe(Cp)_2$ is below the Fermi level of the pristine nanotubes which means that theoretically no spontaneous electron transfer can occur (Chapter 2, Figure 3). However, in practice carbon nanotubes have defects decorated with oxygen-containing groups resulting in a lower Fermi level (*i.e.* some degree of p-doping)[23, 24] to below the $Fe(Cp)_2$ HOMO which allows for some electron transfer to occur from ferrocene to the top of the valence band of the SWNT (Chapter 2 Figure 3, c). Furthermore, the host-nanotube partially screens the guest-molecule from the solvent, so that the effects of the different solvents on the redox potential of $Fe(Cp)_2$ inside nanotube are dampened (see Chapter 2). While confinement in nanotubes has a definite and measurable impact on ferrocene, the fundamental redox properties of $Fe(Cp)_2$ inside the nanotube remain largely similar to the properties of the free molecule in solution thus indicating that electron transfer plays only a minor role in host-guest interactions in this system.

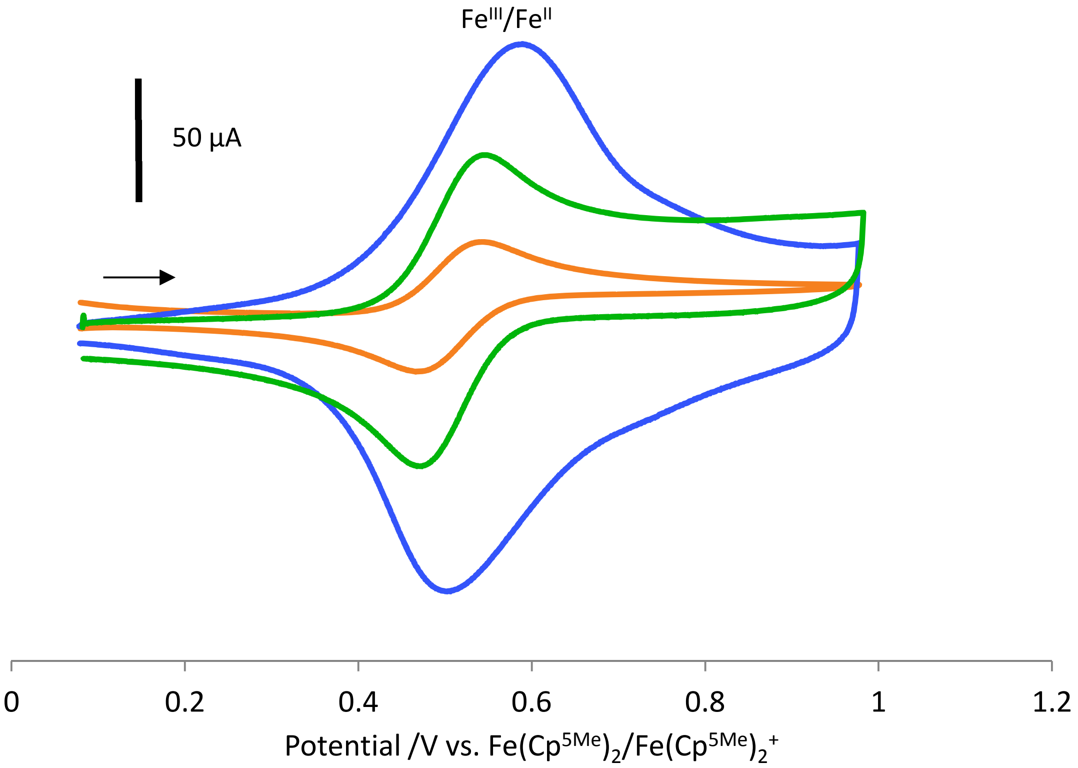

Figure 2. Cyclic voltammograms of Fe(Cp)$_2$ in solution using a GCE (Fe(Cp)$_2$/GCE) (orange), Fe(Cp)$_2$ in solution using a GCE with SWNT attached (Fe(Cp)$_2$/SWNT/GCE) (green) and Fe(Cp)$_2$ encapsulated in SWNT attached to a GCE (Fe(Cp)$_2$@SWNT/GCE) (blue). All CV experiments were performed in acetonitrile (MeCN) containing [N^{n}Bu$_4$][BF$_4$] (0.1 M) as the supporting electrolyte at 293 K and a scan rate of 100 mVs^{-1}. Arrow indicates potential sweep direction. The potential is held at the start potential for a period of 5 seconds before the potential sweep. Redox process of Fe(Cp)$_2$/GCE and Fe(Cp)$_2$/SWNT/GCE occurs at 0.51 V and the redox process of Fe(Cp)$_2$@SWNT occur at 0.55 V.

3.3.3 Cyclic voltammetry of cobaltocene@SWNT

Co(Cp)$_2$, was successfully inserted into carbon nanotubes in the gas phase by an adaptation of a previously reported method,[5] (see experimental). Co(Cp)$_2$ is a strong reducing agent and undergoes oxidation on exposure to air, for this reason the majority of the encapsulation procedure was performed in a glove box. Upon encapsulation in SWNT, the two Co(Cp)$_2$ redox couples, Co^{II}/Co^{I} and Co^{III}/Co^{II}, are observed, however, both couples occur at significantly shifted potentials when compared to the values obtained for free $Co(Cp)_2$ in solution (Figure 3). It must be noted that the relative currents are not equal, as one would expect for two, one-electron reductions, due to underlying contributions from the SWNT energy levels (van Hove singularities) as described in the LSV measurements, which manifest as an uneven non-faradic background in CV measurements.

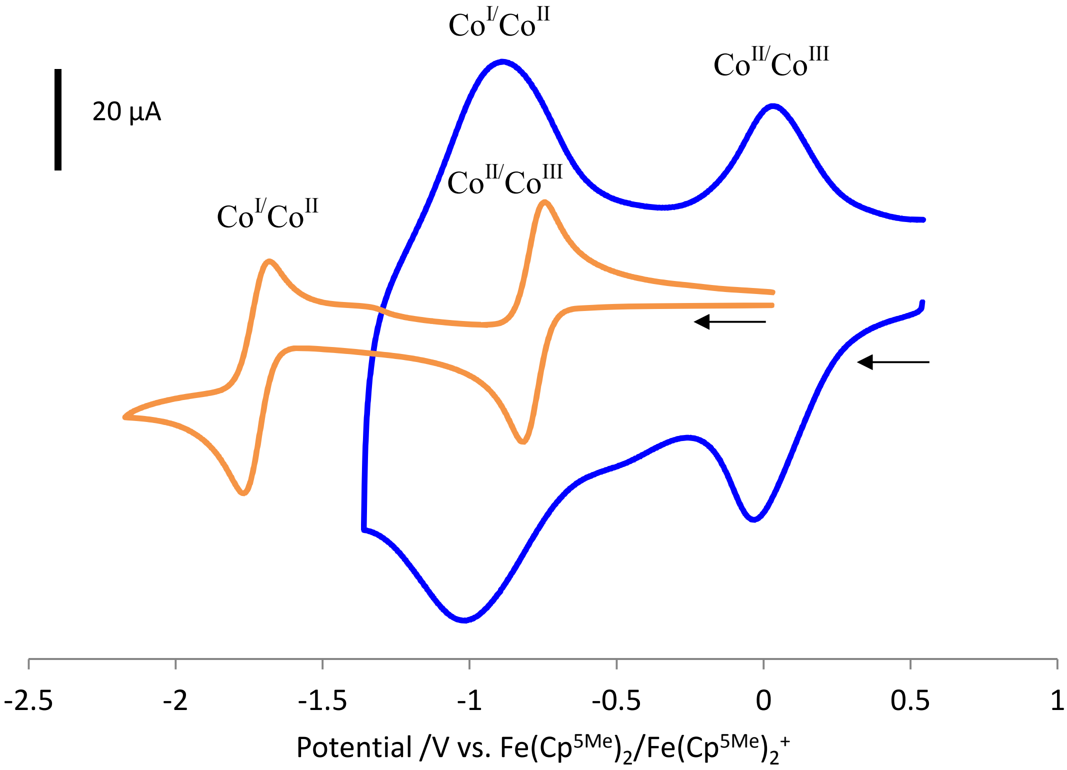

Figure 3. CV of $Co(Cp)_2$/GCE (orange) and $Co(Cp)_2$@SWNT/GCE (blue). All CV experiments were performed in MeCN containing $[N^nBu_4][BF_4]$ (0.1 M) as the supporting electrolyte at 293 K and a scan rate of 100 mVs^{-1}. Arrow indicates potential sweep direction. The potential is held at the start potential for a period of 5 seconds before the potential sweep. The redox processes occur at -1.73 and -0.78 V for $Co(Cp)_2$/GCE and -0.96 V and 0 V for $Co(Cp)_2$@SWNT.

The observed redox potentials of $Co(Cp)_2$@SWNT of -0.96 V (Co^{II}/Co^{I}) and 0 V (Co^{III}/Co^{II}) (vs. $Fe(Cp^{5Me})_2/Fe(Cp^{5Me})_2^+$) are significantly less negative than those observed for $Co(Cp)_2$ in solution, a shift of 0.77 V and 0.78 V respectively, and can be explained by significant electron transfer from the high lying $Co(Cp)_2$ SOMO to the nanotube conduction band (Figure 4b) so that complete oxidation of cobaltocene to cobaltocenium occurs upon encapsulation, resulting in a strong stabilisation of the Co^{II} state.[25] This is not possible with $Fe(Cp)_2$ as the energy of the $Fe(Cp)_2$ HOMO is lower in energy than any empty nanotube states as shown in Chapter 2, Figure 3a. These electrochemical measurements are in agreement with previously reported spectroscopy measurements for $Co(Cp)_2$@SWNT[5] and our theoretical calculations that predict a shift in energy of the $Co(Cp)_2$ SOMO to a more negative energy by -1.02 eV (more positive potential) which corroborates the shift observed in the CV (Figure 3). Our theoretical calculations also predict the effective injection of an electron from $Co(Cp)_2$ into the nanotube conduction band which is in agreement with those reported previously by Green *et al.*[26, 27]

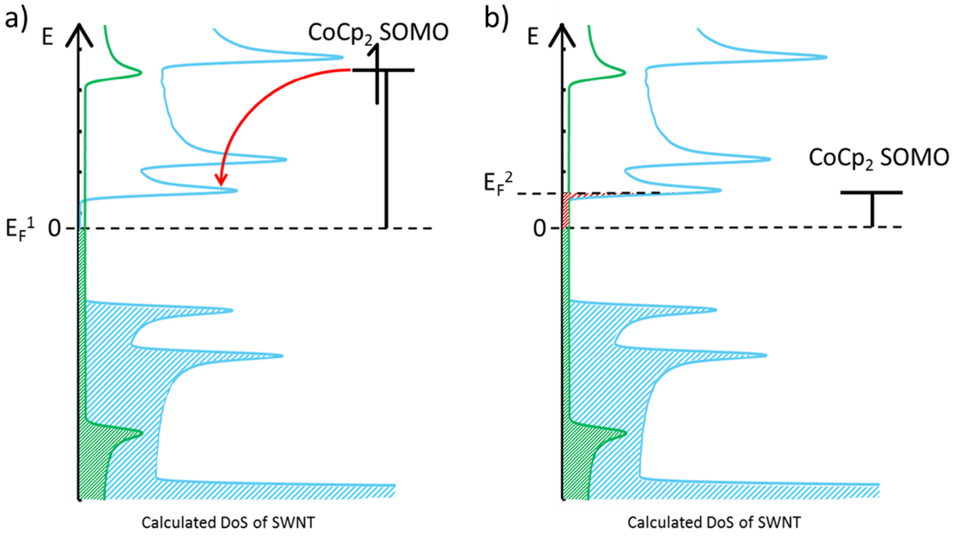

Figure 4. Encapsulation of cobaltocene in SWNT leads to a shift in the energy of the $Co(Cp)_2$ SOMO and an effective injection of electrons into the nanotube DOS, increasing the energy of the Fermi level from E_F^1 to E_F^2. The nanotube stabilises the Co^{II} state due to an electron transfer and electrostatic interaction with the $Co(Cp)_2$ SOMO. As a result the potential required to perform a redox reaction of $Co(Cp)_2$ inside nanotube has decreased by 0.77 V. Red shading shows the newly filled states and the red arrow signifies an electron transfer.

Theoretical studies state that an ionic composite is formed between $Co(Cp)_2$ and the nanotube and that the LUMO of encapsulated $Co(Cp)_2$ is slightly dispersive (Figure 5, states A and B). Electrostatic forces resulting from the charge transfer are observed[26] as well as a small (π-type) overlap of the orbitals on the cyclopentadienyl ligands with orbitals on the SWNT.[27] The decreased energy required to reduce then re-oxidise $Co(Cp)_2$ when encapsulated in a nanotube, causing the Co^{III}/Co^{II} redox potential to become more positive, was attributed to the electron transfer from $Co(Cp)_2$ to the SWNT and the resulting electrostatic forces.

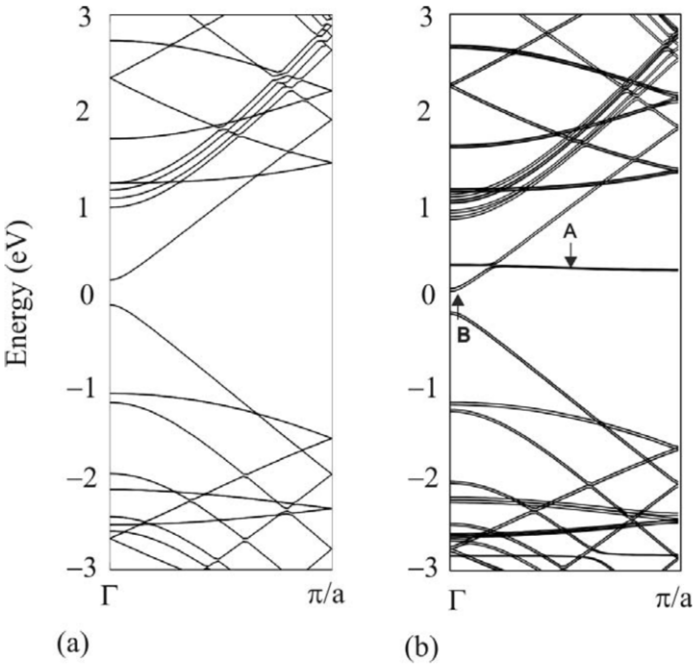

Figure 5. Electronic band structures for (a) pristine [12,0]SWNT and (b) $Co(Cp)_2$@[12,0]SWNT. In both plots, the Fermi level is shifted to 0 eV. A indicates the SOMO of $Co(Cp)_2$ and B indicates the conductance band of the SWNT. Both A and B are singly occupied.[27]

3.3.4 Cyclic voltammetry of different methylated ferrocenes inside SWNT

Ferrocene and cobaltocene represent two extreme cases where the magnitude of electron transfer to the nanotube is very small or very high respectively. To explore whether electron transfer between the host and the guest can be finely tuned through size, shape and functionality of the guest-molecule, a series of methylated $Fe(Cp)_2$ (purchased from Sigma Aldrich and Alfa Aesar then purified during encapsulation) derivatives with a varying number of methyl groups on the cyclopentadienyl (Cp) ring, were encapsulated in SWNT and the CV performed (Figure 7, Figure 8 and Figure 9).

The introduction of an increasing number of methyl groups onto the $Fe(Cp)_2$ (zero to ten) increases the energy of the HOMO as observed in the change in redox potential of the respective ferrocene molecule and therefore increases the observed shift in redox potential (from 0.04 V for $Fe(Cp)_2$ to 0.20 V for $Fe(Cp^{5Me})_2$) for the guest-molecule inside the nanotube of each $Fe(Cp^{xMe})_2$@SWNT (X = Me, 4Me, 5Me) system. The increase in energy of the ferrocene HOMO with the number of methyl groups is a well-known inductive effect, a greater number of methyl groups on the molecule lead to more electron density transferred to the nanotube and therefore a shift of the redox potential in the negative direction (Figure 6a). While the HOMO of ferrocene and $Fe(Cp^{Me})_2$ are high enough to enable a small amount of electron transfer to the p-doped nanotubes (Chapter 2 Figure 3, c), the addition of 8 and 10 methyl groups increases the HOMO energy of $Fe(Cp^{4Me})_2$ and $Fe(Cp^{5Me})_2$ to above the Fermi level of the metallic (10,10) nanotubes, and therefore no longer relies on the p-doped nanotubes for electron transfer, hence resulting in a sharp increase in electron transfer, measured as an increased shift in redox potential of the guest-molecule when encapsulated in the nanotube compared with the solution CV (Figure 6, Figure 7, Figure 8 and Figure 9). In general, the shift of redox potential can be interpreted as a measure of charge transfer from the guest-molecule to the nanotube, and therefore is related to the strength of host-guest interactions. The clear correlation between potential shift and electron donating ability of the metallocenes further indicates that the nature of the interactions with SWNT is primarily electrostatic, unlike in the case of fullerene where van der Waals interactions dominate.

Ab initio DFT calculations were performed by Dr. Matteo Baldoni to corroborate the link between the strength of host-guest interactions and electron transfer. The calculated energies of encapsulation (ΔE), defined as ΔE = E(Metallocene@SWNT) - E(Metallocene) - E(SWNT), for different ferrocene molecules in SWNT correlate well with the experimentally measured shifts in redox potential for the different metallocenes upon nanotube confinement (Table 1). This is a strong indication that the electron transfer from metallocenes to the nanotube results in a stronger interaction with the internal cavity of the SWNT, which provides a mechanism to gauge not only the nature of the interaction between the nanotube and the guest-molecule but also the strength of the interaction using electrochemistry methods.

Table 1. Comparison of the calculated ΔE encapsulation of different ferrocene molecules in a (17,0)SWNT to the shift in redox potential of the guest-molecules observed in CV experiments.

Guest-molecule	**ΔE Encapsulation /eV (vs. $Fe(Cp)_2$@(17,0)SWNT)**	**Shift in redox potential (encapsulated vs. free molecule)/V**
$Fe(Cp)_2$	0.00	0.04
$Fe(Cp^{Me})_2$	-0.02	0.05
$Fe(Cp^{4Me})_2$	-0.16	0.18
$Fe(Cp^{5Me})_2$	-0.26	0.20

Table 2. Comparison of the $E_{1/2}$ values for different ferrocene molecules in solution using a GCE and the $E_{1/2}$ of the same molecules encapsulated in a SWNT. The ΔE_p is also shown.

Guest-molecule	**$E_{1/2}$ for the redox process in solution using a GCE/V**	**ΔE_p for redox process in solution/V**	**$E_{1/2}$ for the redox process for guest@SWNT/V**	**ΔE_p for redox process in SWNT/V**
$Fe(Cp)_2$	0.00	0.060	0.04	0.077
$Fe(Cp^{Me})_2$	-0.11	0.113	-0.06	0.086
$Fe(Cp^{4Me})_2$	-0.42	0.068	-0.24	0.075
$Fe(Cp^{5Me})_2$	-0.49	0.074	-0.29	0.039

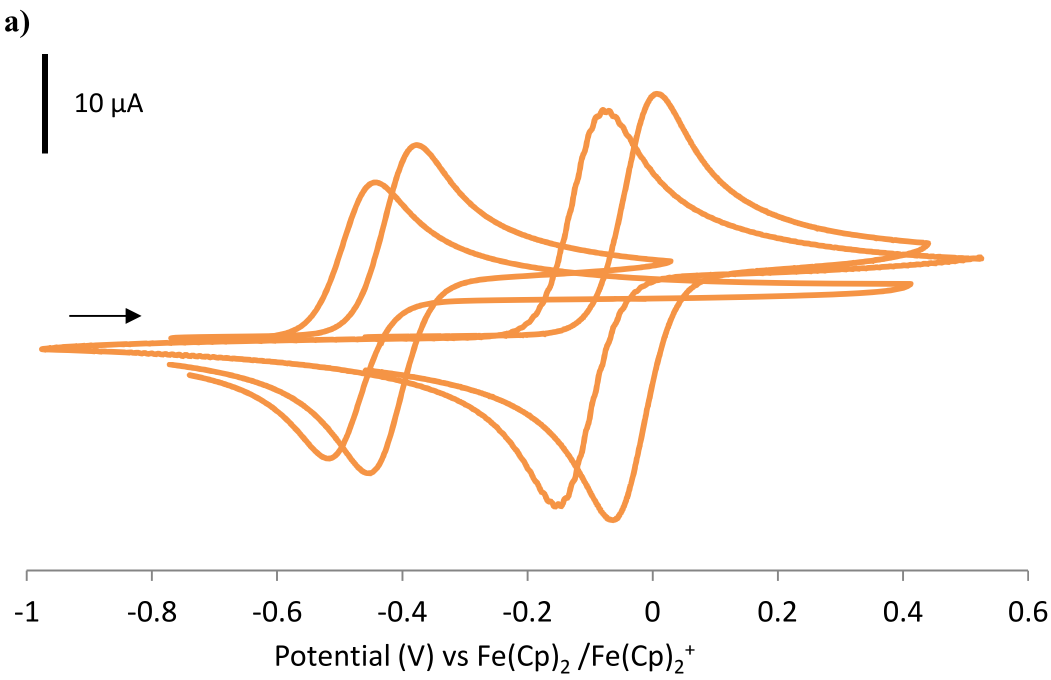

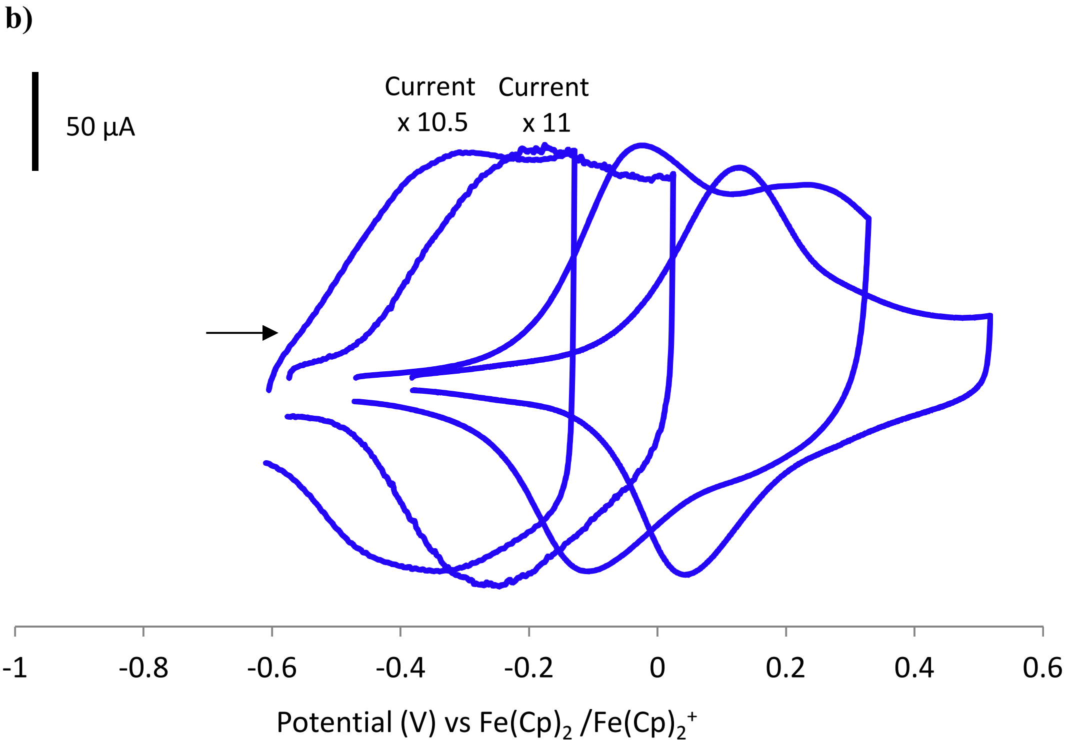

Figure 6. a) CV of $Fe(Cp)_2$, $Fe(Cp^{Me})_2$, $Fe(Cp^{4Me})_2$ $Fe(Cp^{5Me})_2$ right to left in solution using a GCE. b) CV of $Fe(Cp)_2$@SWNT, $Fe(Cp^{Me})_2$@SWNT, $Fe(Cp^{4Me})_2$@SWNT and $Fe(Cp^{5Me})_2$@SWNT right to left. All CV experiments were performed in MeCN containing $[N^nBu_4][BF_4]$ (0.1 M) as the supporting electrolyte at 293 K and a scan rate of 100 mVs^{-1}. Arrow indicates potential sweep direction. The potential is held at the start potential for a period of 5 seconds before the potential sweep.

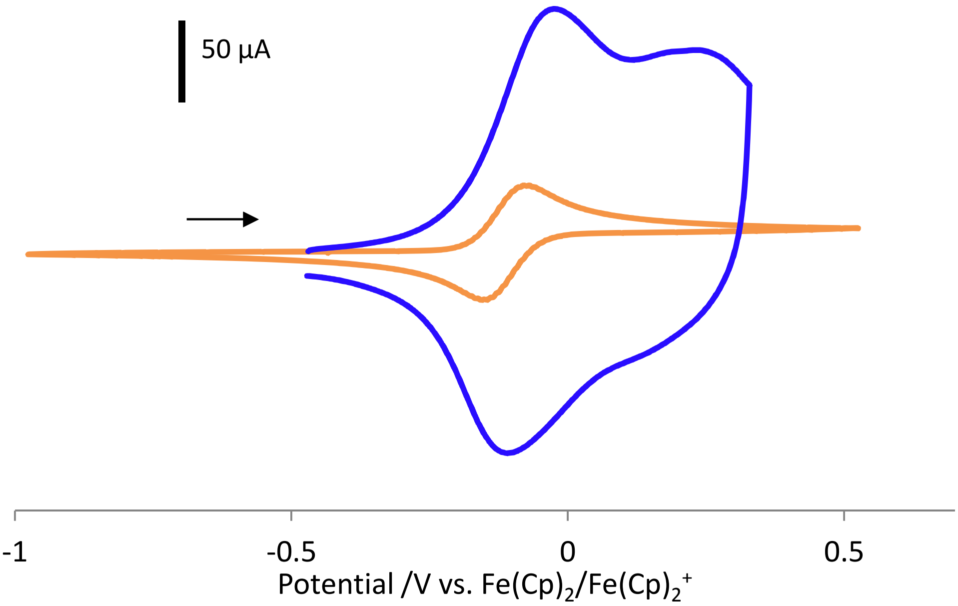

Figure 7. CV of Fe(Cp^{Me})$_2$ /GCE (orange) and Fe(Cp^{Me})$_2$@SWNT (blue). All CV experiments were performed in MeCN containing [N^{n}Bu$_4$][BF$_4$] (0.1 M) as the supporting electrolyte at 293 K and a scan rate of 100 mVs^{-1}. Arrow indicates potential sweep direction. The potential is held at the start potential for a period of 5 seconds before the potential sweep. The redox processes occur at of -0.12 V for Fe(Cp^{Me})$_2$/GCE and -0.06 V for Fe(Cp^{Me})$_2$@SWNT. A shift of +0.05 V is observed when encapsulated in a SWNT.

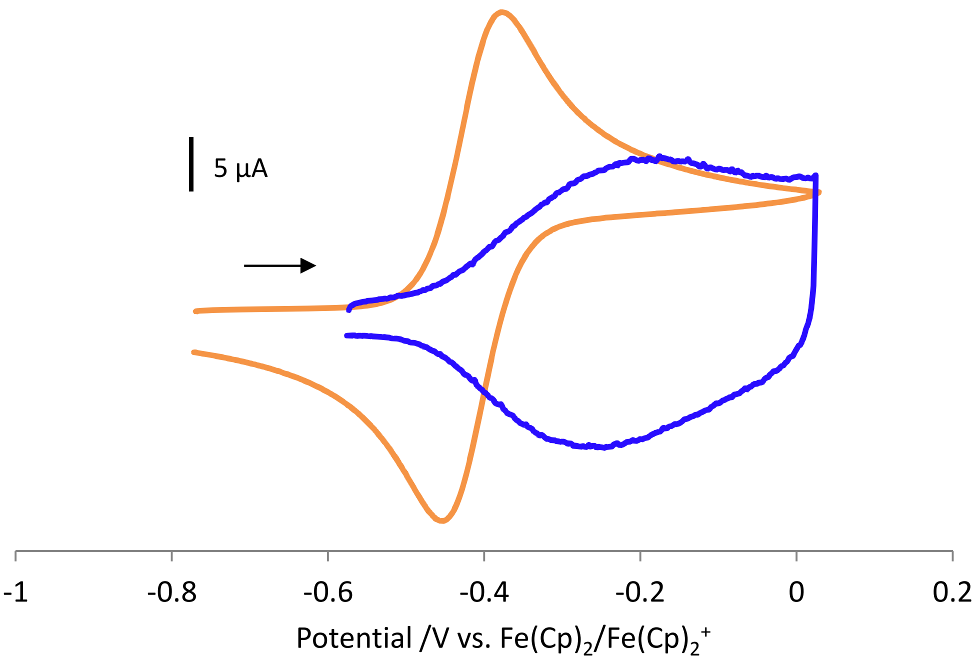

Figure 8. CV of Fe(Cp^{4Me})$_2$ /GCE (orange) and Fe(Cp^{4Me})$_2$@SWNT (blue). All CV experiments were performed in MeCN containing [N^{n}Bu$_4$][BF$_4$] (0.1 M) as the supporting electrolyte at 293 K and a scan rate of 100 mVs^{-1}. Arrow indicates potential sweep direction. The potential is held at the start potential for a period of 5 seconds before the potential sweep. Redox processes occurs at -0.41 V for Fe(Cp^{4Me})$_2$/GCE and -0.24 and -0.25 V for Fe(Cp^{4Me})$_2$@SWNT. A shift of +0.18 V is observed when encapsulated in a SWNT.

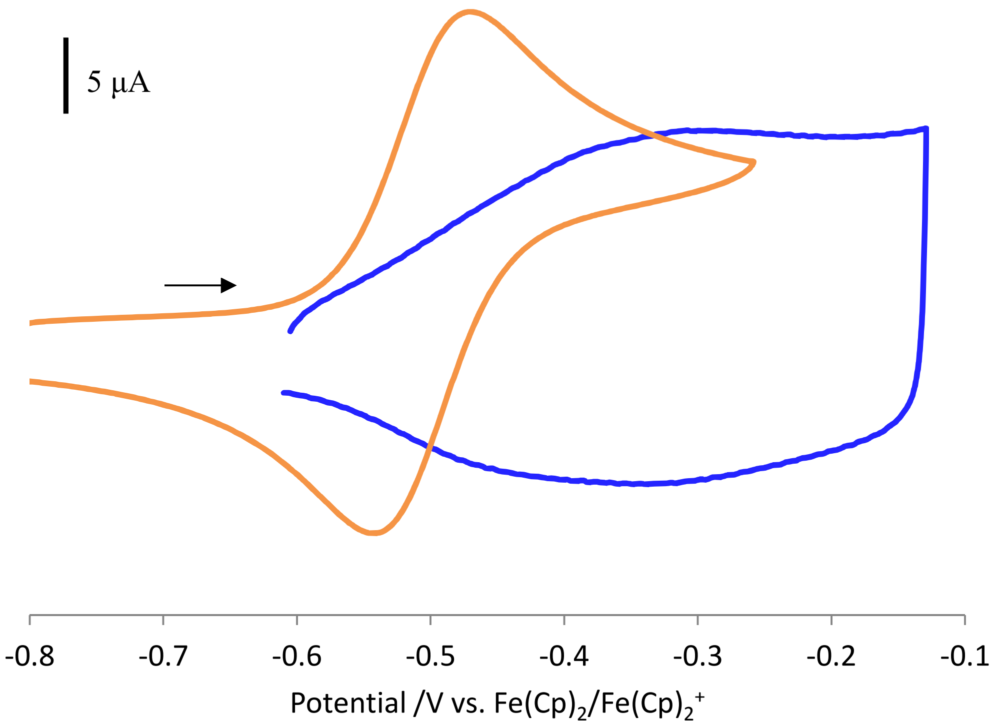

Figure 9. CV of $Fe(Cp^{5Me})_2$ /GCE (orange) and $Fe(Cp^{5Me})_2$@SWNT (blue). All CV experiments were performed in MeCN containing $[N^nBu_4][BF_4]$ (0.1 M) as the supporting electrolyte at 293 K and a scan rate of 100 mVs^{-1}. Arrow indicates potential sweep direction. The potential is held at the start potential for a period of 5 seconds before the potential sweep. Redox processes occur at -0.51 V for $Fe(Cp^{5Me})_2$ /GCE and -0.31 V for $Fe(Cp^{5Me})_2$@SWNT. A shift of +0.20 V is observed when encapsulated in a SWNT.

The observed signals for $Fe(Cp^{5Me})_2$ and $Fe(Cp^{4Me})_2$ are very broad making it difficult to assign an $E_{1/2}$ and therefore there is a bigger error in the measured shift. The highest current in the region of the peak was taken from both the oxidation and reduction process for calculating the $E_{1/2}$. The reason for the broadness is that both molecules have methyl groups functionalising the cyclopentadienyl ring. The extra bulk increases the resistance for electrical contact between the guest-molecule and the nanotube sidewall. This means that rotations and rearrangements are required for the redox process to occur. For example, there is one orientation of octamethylferrocene that a methyl group is not present allowing for a more efficient redox process (Figure 10). These rotations increase the time of the electron transfer, adding a kinetic aspect to the redox process, resulting in broad, weak signals (Figure 10). The methyl groups also decrease the number of guest-molecules in the SWNT due to their bulk. In the examples here, eight $Fe(Cp)_2$ compared to only three $Fe(Cp^{5Me})_2$ fit into the small section of nanotube (Chapter 2) this means an expected 3/8 the current observed for $Fe(Cp)_2$ and $Fe(Cp^{Me})_2$ is observed for for $Fe(Cp^{5Me})_2$ and $Fe(Cp^{4Me})_2$. A decrease in current with an increase in methyl groups is observed in the solution experiments due to the increase in size, slowing diffusion, increasing the diffusion coeficient and decreasing the number of molecules on the electrode and in the diffusion layer.

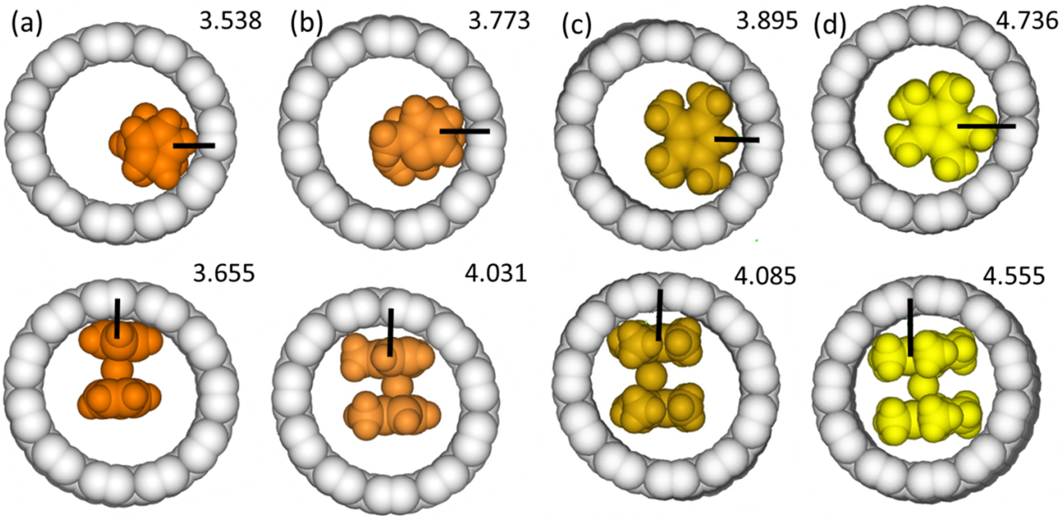

Figure 10. Models to determine the distances for electron transfer between guest-molecules and the nanotube. Where a) is ferrocene, b) dimethylferrocene, c) octamethylferrocene and d) decamethylferrocene. The distance increases for an increasing number of methyl groups and rotations are required for an intimate interaction with the nanotube sidewall in the case of octamethylferrocene. This adds a kinetic factor and an increased resistance for the redox process resulting in broad signals with weak currents in CV experiments.

3.3.5 Comparison of cyclic voltammetry of ferrocene in carbon nanotubes of different internal diameter (SWNT and DWNT)

CV measurements reveal that the internal diameter of the host-nanotube also has an effect on the magnitude of the shift of the $E_{1/2}$ of the $Fe(Cp)_2$ (Table 2) (Figure 11), with the observed shift ranging from 0.05 V for the narrowest nanotubes (d_{NT} = 1.0 nm) to 0.01 V for the widest nanotubes studied (d_{NT} = 2.5 nm) and appears to be inversely proportional to the nanotube diameter (Table 3). Nanotubes with a narrow diameter have a wider band gap resulting in the top of the valence band residing at a lower energy. Assuming that as-received SWNT are slightly p-doped, the Fermi level and the small amount of empty states in the valence band of a narrower nanotube will be at a lower energy facilitating electron transfer from $Fe(Cp)_2$ to the nanotube, which further proves that the electrostatic forces which determine the effectiveness of host-guest interactions rely on electron transfer from the guest-molecule to the host-nanotube.

Table 3. Measured $E_{1/2}$ and the shift in redox potential of ferrocene encapsulated in nanotubes of different internal diameters compared to ferrocene in solution.

Sample	**Average nanotube internal diameter (nm)**	**$E_{1/2}$ redox potential for $Fe(Cp)_2$@ nanotube (V)**	**Shift vs. $Fe(Cp)_2$ in solution (V)**
$Fe(Cp)_2$@(13,0)SWNT	1.0	0.55	0.05
$Fe(Cp)_2$@(17,0)SWNT	1.4	0.52	0.04
$Fe(Cp)_2$@(30,0)DWNT	2.5	0.50	0.01
$Fe(Cp)_2$ in solution/GCE	-	0.49	0.00

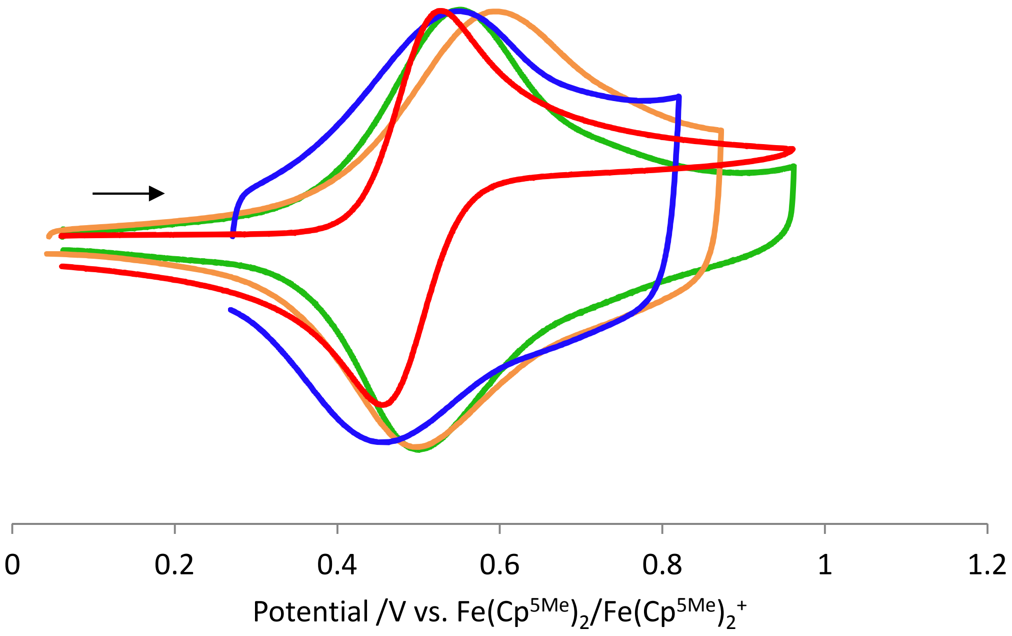

Figure 11. Overlay of CVs for $Fe(Cp)_2$@SWNT in nanotubes of varying internal diameter. SWNT: 1 nm (orange), SWNT: 1.4 nm (green), DWNT: 2.5 nm (blue) in MeCN containing $[N^nBu_4][BF_4]$ (0.1 M) as the supporting electrolyte at 293 K and a scan rate of 100 mVs^{-1}. The currents have been scaled for direct comparison. Arrow indicates potential sweep direction. The potential is held at the start potential for a period of 5 seconds before the potential sweep. $E_{1/2} = (E_p^c+E_p^a)/2$. The most positive potentials are observed for the nanotube with the smallest internal diameter and the most negative potential for the nanotube with the biggest internal diameter. For redox potentials, see Table 3.

3.4 Conclusions

A methodology has been developed based on an electrochemical analysis that allows probing of the mechanisms of interactions between redox active guest-molecules and carbon nanotubes. Using CV the effect nanotube encapsulation has on the guest-molecules was demonstrated, measured by shifts in the redox potential compared with CV measurements in solution. This shift is characteristic of a stabilisation effect by the nanotube for Co^{II} and Fe^{II} states in $Co(Cp)_2$ and $Fe(Cp)_2$, whereby the nanotube exerts a positive field upon the orbitals of the guest-molecule. The magnitude of the shift is indicative of the amount of charge transfer between the nanotube and guest-molecule. A range of guest-molecules with differing HOMO energies were encapsulated into nanotubes of different internal diameters and it was shown that a decreasing internal diameter of nanotube resulted in an increased shift of the redox potential of $Fe(Cp)_2$@SWNT due to the wider band gap and therefore, a lower energy Fermi level. This study demonstrates a complex interplay between the HOMO/SOMO of guest-molecules with the electronic bands of host-nanotubes. Encapsulation of redox active guest-molecules triggers electron transfer to the nanotube, the extent of which depends on several parameters: the energy of HOMO/SOMO of the guest-molecule, the internal diameter of nanotube and whether the nanotube is metallic or semiconducting. This new knowledge significantly improves the understanding of host-guest interactions and opens up new avenues for controlling the oxidation state of guest-molecules as well as for tuning the electronic properties of host-nanotubes.

3.5 Experimental

3.5.1 Preparation of nanotube samples

Batches of nanotubes are purchased from Carbon Solutions Inc., Chengdu Organic Chemicals Co. Ltd and NanoIntegris Inc.. Each new batch is analysed using TEM whereby the diameter of nanotubes is measured over a wide range of tubes and the average diameter (quoted diameter in this thesis) and standard deviation are determined. The method of TEM preparation involves the sonication of a substantial amount of nanotubes which is further diluted meaning the nanotubes that appear in TEM are representative of the whole batch. There is a range of different chiral indices present in the nanotube sample which have been analysed by Pekker *et al.*[28] These are not from the same batch that were used but are from the same company and preparation method. They determine that the ratio of metallic nanotubes to semiconducting nanotubes is 31:69 respectively. When using DOS plots for specific chiral indices, chiral indices reported to be present in the material and also representative for the diameter of nanotubes are used.[28] Further details of nanotube synthesis and oxidation method are provided in the experimental.

3.5.1.1 Preparation of $Fe(Cp^{XMe})_2$@SWNT (1.4 nm internal diameter)

SWNT (25 mg) (arc-discharge, P2-SWNT, Carbon Solutions Inc.) were annealed (600 ^{o}C, 25 min) in air to open their termini and remove any residual amorphous carbon from the internal cavities; a 50% weight loss was observed. $Fe(Cp^{xMe})_2$ (0.18 mmol) (used as supplied, Sigma Aldrich, Alfa Aesar) was added to the SWNT (10 mg) and sealed in a glass ampule under reduced pressure (10^{-6} mbar). The mixture was heated (300 ^{o}C) for three days then cooled quickly. The resulting black powder was washed with diethyl ether (3 x 20 mL) and filtered through a PTFE membrane to remove any $Fe(Cp^{xMe})_2$ from the exterior of the SWNT. The product was analysed using TEM, EDX and electrochemistry.

3.5.1.2 Preparation of $Fe(Cp)_2$@SWNT (1 nm internal diameter) and $Fe(Cp)_2$@DWNT (2.5 nm internal diameter)

The preparation was the same as for $Fe(Cp^{xMe})_2$ apart from the annealing conditions of the nanotubes. DWNT (25 mg) (CVD, Timesnano-DWNT, Chengdu Organic

Chemicals Co. Ltd.) were annealed (570 °C, 15 min) in air. SWNT (25 mg, HiPco, NanoIntegris Inc.) were annealed (380 °C, 30 min) in air then stirred in conc. HCl (15 mL, 30 min). The resulting nanotube suspension was filtered through a PTFE membrane and washed with copious water. The black powder was dried in air at (250 °C, 60 min).

3.5.1.3 Preparation of $Co(Cp)_2$@SWNT (1.4 nm internal diameter)

SWNT (25 mg) (arc-discharge, P2-SWNT, Carbon Solutions Inc.) were annealed (600 °C, 25 min) in air to open their termini and remove any residual amorphous carbon from the internal cavities, a 50% weight loss was observed. Cobaltocene (34.0 mg, 0.18 mmol) (used as supplied, Acros) was added to the SWNT (10 mg) in a glove box then transferred anaerobically to the vacuum filling rig and sealed in a glass ampule under reduced pressure (10^{-6} mbar). The mixture was heated (300 °C) for three days then cooled quickly. The resulting black powder was washed with diethyl ether (3 x 20 mL) and filtered through a PTFE membrane to remove any cobaltocene from the exterior of the SWNT. The product was analysed using TEM, EDX and CV.

3.5.2 HRTEM and EDX

HRTEM analysis was performed on a JEOL JEM-2100F FEG microscope with an information limit of 0.12 nm at 100 kV. The imaging conditions were carefully tuned by lowering the accelerating voltage of the microscope to 100 kV and lowering the beam current density to a minimum. Suspensions of guest@nantoube in HPLC grade isopropanol were dropped onto lacey carbon grids for TEM analysis.

Local EDX spectra were acquired for samples mounted on TEM grids using an Oxford Instruments INCA X-ray microanalysis system. The electron beam was condensed onto areas of specimens (bulk specimen or nanotube bundles) suspended over holes of the amorphous carbon film.

HRTEM of $Fe(Cp)_2$ @SWNT (1.4 nm)

Six iron nanoparticles are observed inside the SWNT as shown by white arrows.

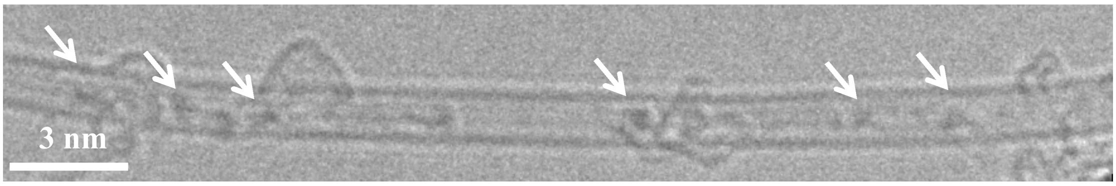

Figure 12. HRTEM image of $Fe(Cp)_2$@SWNT showing Fe metal as dark contrast (white arrows) located solely inside the SWNT.

EDX Spectrum for $Fe(Cp)_2$@SWNT. Electron band transitions are attributed to iron

L → K, M → K and M → L.

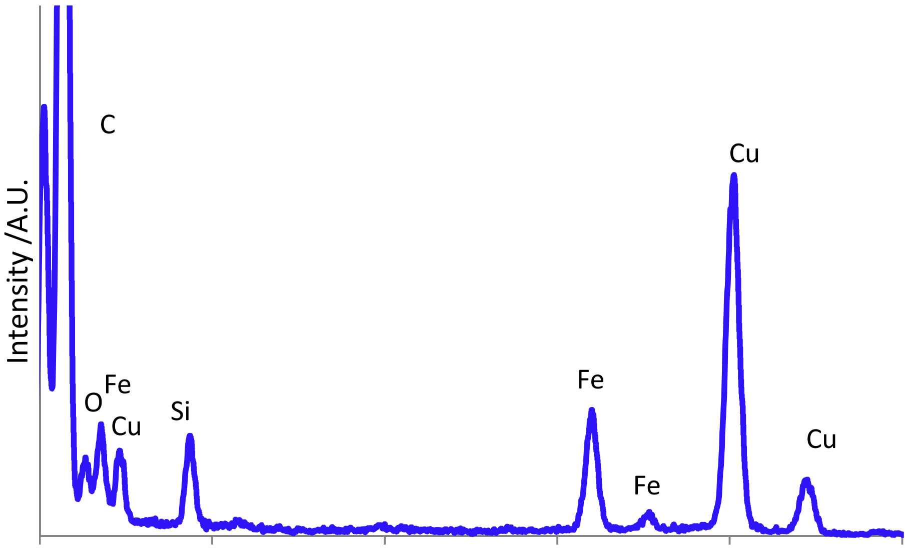

Figure 13. EDX of $Fe(Cp)_2$@SWNT. Copper peaks originate from the sample holder.

HRTEM of $Fe(Cp^{Me})_2$@SWNT (1.4 nm)

Seven iron nanoparticles are observed inside the small bundle of SWNT as shown by white arrows.

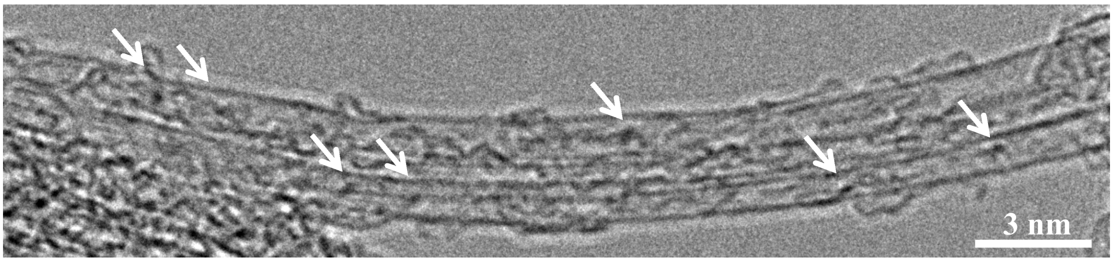

Figure 14. HRTEM image of $Fe(Cp^{Me})_2$@SWNT showing Fe metal as dark contrast (white arrows) located solely inside the SWNT.

EDX Spectrum for $Fe(Cp^{Me})_2$@SWNT. Electron band transitions are attributed to iron L → K, M → K and M → L.

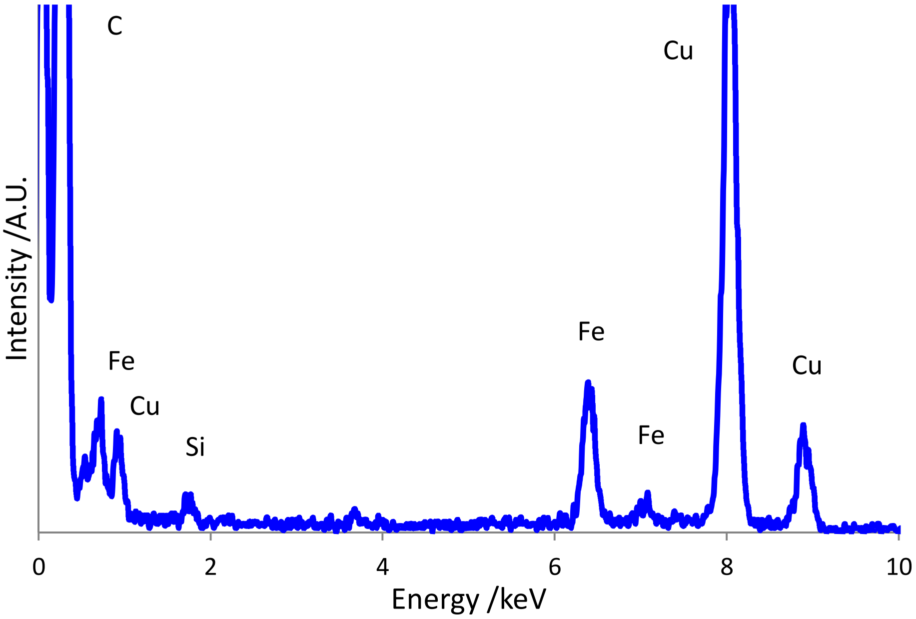

Figure 15. EDX of $Fe(Cp^{Me})_2$@SWNT. Copper peaks originate from the sample holder.

HRTEM of Fe(Cp^{4Me})$_2$@SWNT (1.4 nm)

Five iron nanoparticles are observed inside the SWNT as shown by white arrows.

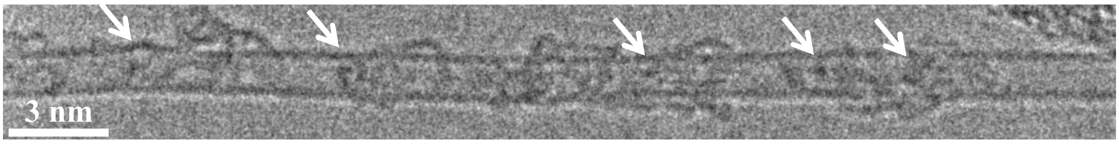

Figure 16. HRTEM image of Fe(Cp^{4Me})$_2$@SWNT showing Fe metal as dark contrast (white arrows) located solely inside the SWNT.

EDX Spectrum for Fe(Cp^{4Me})$_2$@SWNT. Electron band transitions are attributed to iron L → K, M → K and M → L.

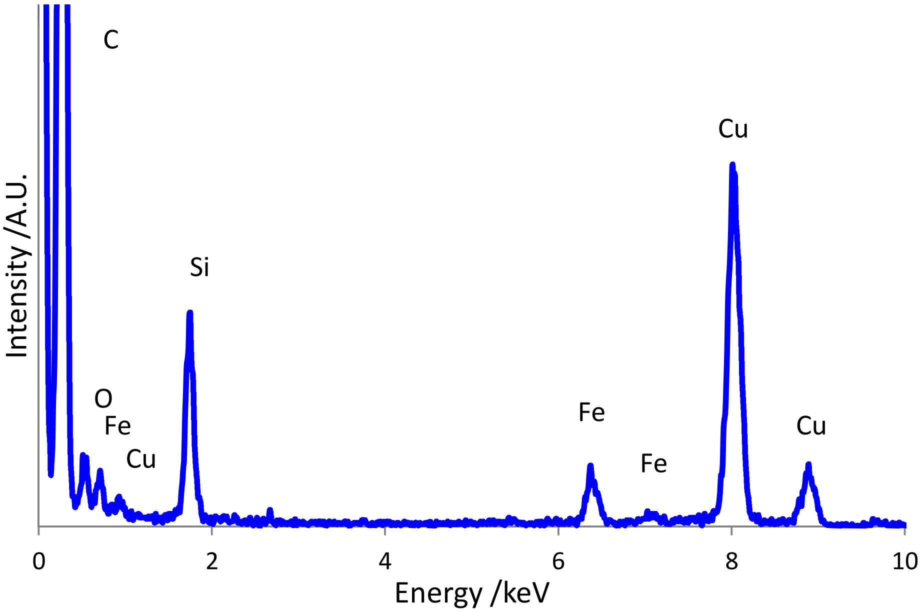

Figure 17. EDX of Fe(Cp^{4Me})$_2$@SWNT. Copper peaks originate from the sample holder.

HRTEM of Fe(Cp^{5Me})$_2$@SWNT (1.4 nm)

Three iron nanoparticles are observed inside the small bundle of SWNT as shown by white arrows.

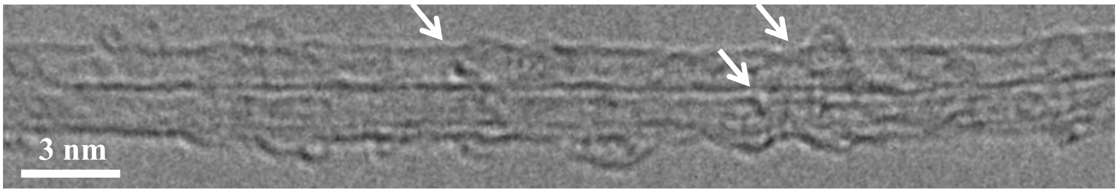

Figure 18. HRTEM image of Fe(Cp^{5Me})$_2$@SWNT showing Fe metal as dark contrast (white arrows) located solely inside the SWNT

EDX Spectrum for Fe(Cp^{5Me})$_2$@SWNT. Electron band transitions are attributed to iron L → K, M → K and M → L.

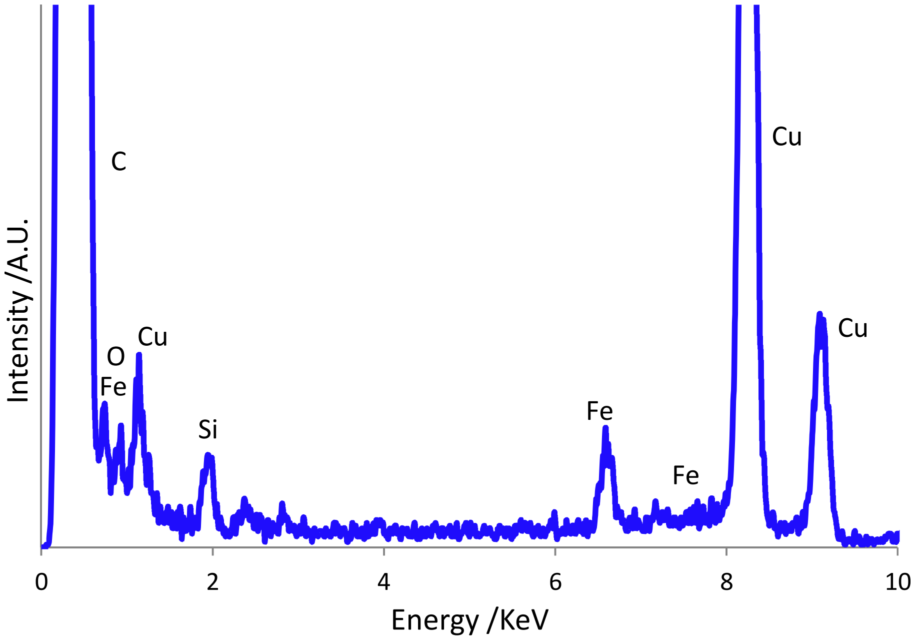

Figure 19. EDX of Fe(Cp^{5Me})$_2$@SWNT. Copper peaks originate from the sample holder.

HRTEM of Co(Cp)$_2$@SWNT (1.4 nm)

Eight cobalt nanoparticles are observed inside the small bundle of SWNT as shown by white arrows.

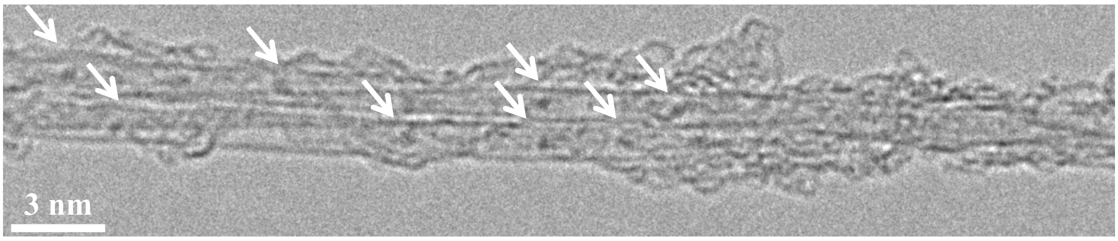

Figure 20. HRTEM image of Co(Cp)$_2$@SWNT showing Co metal as dark contrast (white arrows) located solely inside the SWNT

EDX Spectrum for Co(Cp)$_2$@SWNT. Electron band transitions are attributed to cobalt L → K, M → K and M → L.

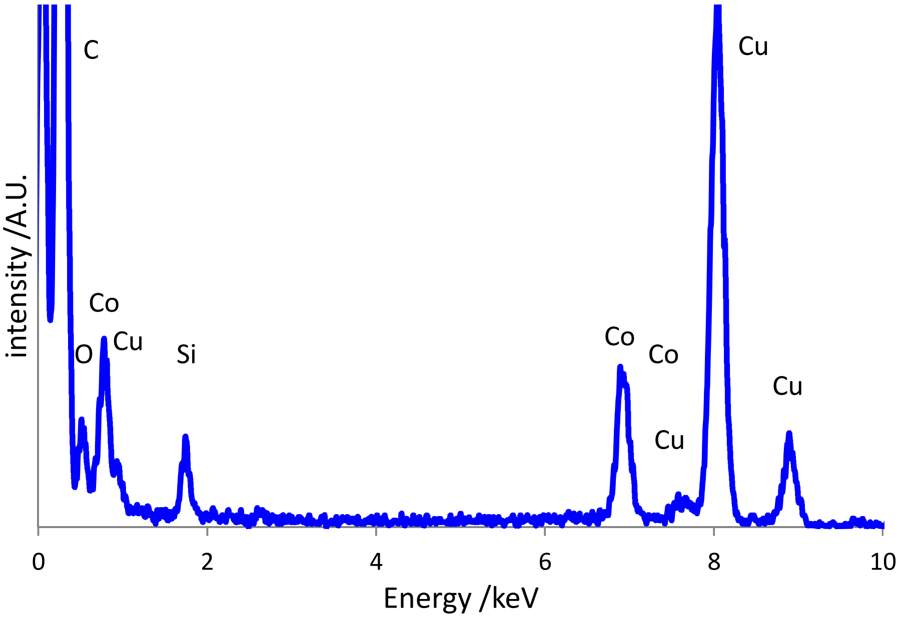

Figure 21. EDX of Co(Cp)$_2$@SWNT. Copper peaks originate from the sample holder.

3.5.2.1 Fill percentage calculated from TEM imaging

The percentages of nanotube cavities filled in metallocenes@SWNT were estimated using TEM imaging and are detailed in Chapter 2 (Table 4).

Table 4. Showing the percentages of nanotube cavities filled as calculated using TEM imagine (see Chapter 2).

Guest-molecule	**Percentages of nanotube cavities filled / %**
$Fe(Cp)_2$	87
$Fe(Cp^{Me})_2$	88
$Fe(Cp^{4Me})_2$	93
$Fe(Cp^{5Me})_2$	69
$Co(Cp)_2$	95

3.5.3 Electrochemistry

Electrochemistry experiments were performed on an Autolab PGSTAT302N. Electrodes were purchased from IJCambria and Metrohm. The electrochemistry was performed using a three electrode set up with a Ag/AgCl reference electrode, a platinum counter electrode and a glassy carbon working electrode on which the molecule@SWNT is deposited. The nanotube filled with molecules (0.5 mg) was sonicated (15 min) in dry DMF (0.5 mL) to form an ink. The ink (10 µL) was cast onto the GCE using a micro-pipette and allowed to dry in air for 1 h. The electrode was then rinsed in dry acetonitrile and allowed to dry in air. All CV experiments start with the application of the starting potential for 5 seconds.

3.5.4 Theoretical calculations

Calculations of empty SWNT DOS, guest@SWNT DOS, energies of encapsulation and charge transfer were performed by Dr Matteo Baldoni on different guest-nanotube model systems at the gradient-corrected spin-polarised DFT level by applying the PBE[29] exchange-correlation functional as implemented in the SIESTA program package.[30] Electronic states were expanded by a double-ζ basis set with norm-conserving pseudopotentials for the description of core levels[31] and a plane-wave representation of the charge density with a cut-off of 240 Ry. Polarisation functions were added to the metallic centres. Periodic boundary conditions were applied to the cell and a supercell approach was used in the two directions perpendicular to the axis of the nanotube. Geometries of all systems were relaxed until a maximum gradient of 0.02 eV/Å on forces was reached and the stress tensor was less than 0.03 GPa. In band structure calculations, reciprocal space was sampled using a $1 \times 1 \times 5$ Monkhorst-Pack[4] k-point grid. SWNT density of states was renormalised to the number of C atoms in the simulation cell. Energies of encapsulation (ΔE) were calculated as ΔE = E(Metallocene@SWNT) - E(Metallocene) - E(SWNT). Obtained results are in line with previous theoretical works.[26, 27]

3.6 References

1. T. W. Chamberlain, T. Zoberbier, J. Biskupek, A. Botos, U. Kaiser and A. N. Khlobystov, *Chem. Sci.*, 2012, **3**, 1919.
2. W. A. Solomonsz, G. A. Rance, B. J. Harris and A. N. Khlobystov, *Nanoscale*, 2013, **5**, 12200.
3. D. A. Britz and A. N. Khlobystov, *Chem. Soc. Rev.*, 2006, **35**, 637.
4. X. Pan and X. Bao, *Acc. Chem. Res.*, 2011, **44**, 553.
5. L. J. Li, A. N. Khlobystov, J. G. Wiltshire, G. A. Briggs and R. J. Nicholas, *Nat. Mater.*, 2005, **4**, 481.

6. S. A. Miners, G. A. Rance and A. N. Khlobystov, *Chem. Commun.*, 2013, **49**, 5586.
7. P. Kim, T. W. Odom, J. L. Huang and C. M. Lieber, *Phys. Rev. Lett.*, 1999, **82**, 1225.
8. T. W. Odom, J. L. Huang, P. Kim and C. M. Lieber, *J. Phys. Chem. B*, 2000, **104**, 2794.
9. Y. S. Sohn, Hendrick.Dn and H. B. Gray, *J. Am. Chem. Soc.*, 1971, **93**, 3603.
10. D. V. Kazachkin, Y. Nishimura, H. A. Witek, S. Irle and E. Borguet, *J. Am. Chem. Soc.*, 2011, **133**, 8191.
11. M. Sauer, H. Shiozawa, P. Ayala, G. Ruiz-Soria, X. J. Liu, A. Chernov, S. Krause, K. Yanagi, H. Kataura and T. Pichler, *Carbon*, 2013, **59**, 237.
12. K. Yanagi, R. Moriya, N. T. Cuong, M. Otani and S. Okada, *Phys. Rev. Lett.*, 2013, **110**, 086801.
13. S. Hong and S. Myung, *Nat. Nanotechnol.*, 2007, **2**, 207.
14. R. L. McSweeney, T. W. Chamberlain, E. S. Davies and A. N. Khlobystov, *Chem. Commun.*, 2014, **50**, 14338.
15. Z. D. Chang, N. S. Gao, Y. J. Li and X. W. He, *Anal. Methods*, 2012, **4**, 4037.
16. J. E. Halls, A. Hernan-Gomez, A. D. Burrows and F. Marken, *Dalton Trans.*, 2012, **41**, 1475.
17. C. A. Bessel and D. R. Rolison, *J. Am. Chem. Soc.*, 1997, **119**, 12673.
18. G. H. Clever, S. Tashiro and M. Shionoya, *Angew. Chem. Int. Ed.*, 2009, **48**, 7010.
19. W. Y. Sun, T. Kusukawa and M. Fujita, *J. Am. Chem. Soc.*, 2002, **124**, 11570.
20. C. M. Cardona, S. Mendoza and A. E. Kaifer, *Chem. Soc. Rev.*, 2000, **29**, 37.
21. C. Browne, S. Brenet, J. K. Clegg and J. R. Nitschke, *Angew. Chem. Int. Ed.*, 2013, **52**, 1944.
22. S. Guo, X. Pan, H. Gao, Z. Yang, J. Zhao and X. Bao, *Chem. Eur. J.*, 2010, **16**, 5379.
23. J. Vavro, M. C. Llaguno, J. E. Fischer, S. Ramesh, R. K. Saini, L. M. Ericson, V. A. Davis, R. H. Hauge, M. Pasquali and R. E. Smalley, *Phys. Rev. Lett.*, 2003, **90**, 065503.
24. Y. Iizumi, H. Suzuki, M. Tange and T. Okazaki, *Nanoscale*, 2014, **6**, 13910.
25. A. M. Schimpf, K. E. Knowles, G. M. Carroll and D. R. Gamelin, *Acc. Chem. Res.*, 2015, **48**, 1929.
26. E. L. Sceats and J. C. Green, *J. Chem. Phys.*, 2006, **125**, 12.
27. E. L. Sceats and J. C. Green, *Phys. Rev. B.*, 2007, **75**, 10.
28. A. Pekker and K. Kamaras, *Phys. Rev. B.*, 2011, **84**, 075475.
29. J. P. Perdew, K. Burke and M. Ernzerhof, *Phys. Rev. Lett.*, 1996, **77**, 3865.
30. M. S. José, A. Emilio, D. G. Julian, G. Alberto, J. Javier, O. Pablo and S.-P. Daniel, *J. Phys.: Condens. Matter*, 2002, **14**, 2745.
31. J. Junquera, O. Paz, D. Sanchez-Portal and E. Artacho, *Phys. Rev. B*, 2001, **64**, 235111.

4 The effect of guest-molecules on the host-nanotube

4.1 Introduction

While it is clear that CV experiments detecting precise changes in $E_{1/2}$ oxidation potential can be a useful measure of the redox state of guest-molecules within nanotubes, these experiments provide very limited information about the electronic state of the host-nanotube in terms of the amount of electron density injected into the SWNT from guest-molecules or the actual position of the Fermi level in the metallocene@nanotube system. There are a number of methods to measure the doping of nanotubes such as field effect transistors,[1, 2] scanning electrochemical cell microscopy,[3, 4] scanning tunnelling microscopy[5] and optical absorption.[6] However, a new type of experimental procedure has been developed and applied to the metallocene filled carbon nanotubes, providing an elegant method to measure both the doping of the SWNT but also the quantity of electron transfer from guest-molecules to the nanotube.

Herein, it was demonstrated that the amount of electron transfer between nanotubes and molecules is precisely determined by the energy of the guest-molecule HOMO/SOMO and the diameter of the SWNT. The interactions between molecules and nanotubes result in profound changes in the effective bandgap of the SWNT,[7] which can be modulated by choosing guest-molecules with the appropriate HOMO/SOMO, and gauged accurately using a new coulometric approach developed in this study.

4.2 Aim and objectives

The aim is to determine the influence encapsulation of different guest-molecules has on the electronic properties of SWNT.

The specific objectives to achieve this aim are to develop experiments to map the DOS of empty single-walled carbon nanotubes using electrochemistry and to relate this to the electronic influence of guest-molecules on host-nanotubes. Using the same technique, the DOS of guest-molecules@SWNT will be mapped to link the theoretical influence of guest-molecules to experimental results. Using these concepts, the next objective is to develop a method to quantify the electron transfer to the nanotubes from guest-molecules using the Nernst equation.

4.3 Results and discussion

4.3.1 Chronocoulometry methodology

A series of potentials that encompass the Fermi level of $Fe(Cp)_2$@SWNT were applied for 40 seconds and the charge measured. This methodology allows the determination of the doping of the nanotube and therefore whether the nanotube hybrid exhibits metallic or semiconducting like properties. To demonstrate this experiment, examples of an arbitrary metallic material and a semiconducting material are presented (Figure 1 and Figure 2).

Performing chronocoulometry on a metallic material results in a straight line, crossing the y axis at a voltage that corresponds to the Fermi level (Figure 1). At the Fermi level there are no electrons to remove from the valence band or add to the conduction band so a zero charge is observed because no current flows. An applied potential in the conduction band (Figure 1) results in a negative charge as electrons are flowing into the material so a negative current is observed. An applied potential in the valence band results in a positive charge because electrons are flowing from the material resulting in a positive current. The line is straight because the metal has a constant number of states at all energies.

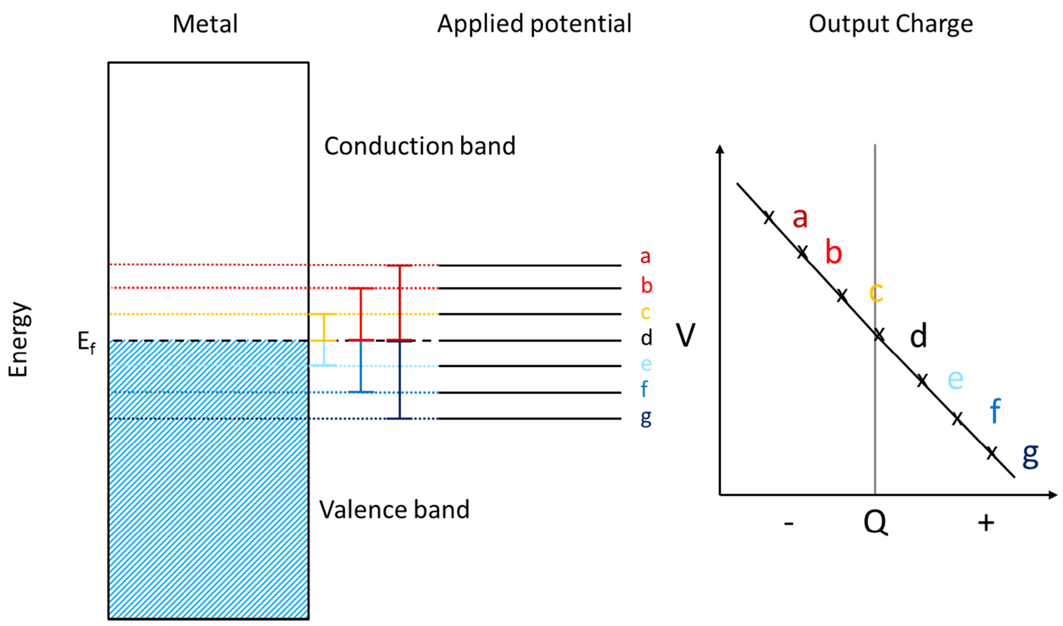

Figure 1. An example of the chronocoulometry experiment applied to a metallic material. A straight line is observed where the Fermi level is at 0 Q. V is the voltage and Q is the charge transferred between the electrode and material. a-g represent applied potentials. Blue shading represents filled states.

Performing chronocoulometry on a semiconducting material results in a curved line with a potential window of zero charge corresponding to a bandgap (Figure 2). In the band gap there are no electrons to remove as there are zero states present, so a zero charge is observed because no current flows. An applied potential in the conduction band results in a negative charge as electrons are flowing into the material so a negative current is observed. An applied potential in the valence band results in a positive charge because electrons are flowing from the material resulting in a positive current. The line is curved because the density of states increases at different energies. Therefore, the nature with which the voltage vs. charge plot crosses the y axis as well as the shape of the line provides information about the density of states (Figure 2).

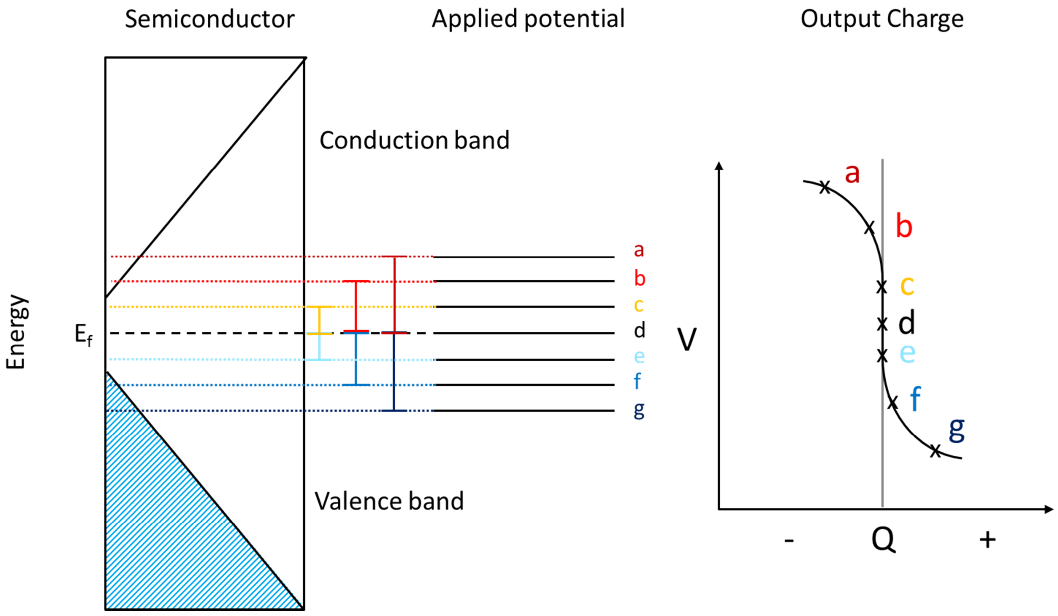

Figure 2. An example of the chronocoulometry experiment applied to a semiconducting material. A curved line is observed where the band gap is the region of zero charge. V is the voltage and Q is the charge transferred between the electrode and material. a-g represent applied potentials. Blue shading represents filled states.

Chronocoulometry was performed on $Fe(Cp)_2$@SWNT as a test experiment. However, the initial coulometry measurement, where a single potential is applied and the charge measured, affects the subsequent measurement due to the residual charge or capacitive effect of the oxidised or reduced guest-molecules inside the nanotube. If a sufficient wait time, where the potentiostat is not doing any work, is introduced between each measurement then the subsequent measurement is not affected by the previous application of potential. The relaxation of the guest-molecules is attributed to charge recombination within the cell between the working and counter electrode, whereby the charge carriers migrate in the opposite direction to the direction during the measurement. This phenomenon can occur in these nanotube systems as the reverse redox process does not rely on diffusion of the molecules back to the electrode. The charge recombination allows for both the re-filling of the nanotube DOS and the re-oxidation or re-reduction of guest-molecules. $Fe(Cp)_2$ is now in the same oxidation state and the nanotube Fermi level is at the same energy as the beginning of the experiment (original state).

To determine the amount of time required for relaxation an experiment was devised. Upon application of an oxidising potential (0.85 V) to $Fe(Cp)_2$@SWNT, a positive charge is measured associated with the oxidation of $Fe(Cp)_2$. The immediate application of a reducing potential (0.1 V) results in a negative charge of similar magnitude due to the oxidation, as the reverse reaction is occurring (see 0 s – 2000 s total time in Figure 3). If a wait time is introduced between applications of the oxidising (0.85 V) and reducing (0.1 V) potentials, the positive and negative charge are not at the same magnitude as would be expected due to a small amount of charge recombination in the cell which means some of the guest-molecules have been re-oxidised or re-reduced by charge carriers migrating from the counter electrode (2000 s – 13000 s in Figure 3).

The wait time between the applications of the oxidising and reducing potential of $Fe(Cp)_2$@SWNT was increased from 0 s to 4000 s which resulted in the negative charge corresponding to the reduction of $Fe(Cp)_2$@SWNT decreasing until almost zero at 4000 s (13000 s total experiment time) which is the charge expected if the $Fe(Cp)_2$@SWNT is in its original state before the application of potential (Figure 3). 4000 s was determined to be the amount of time required to allow $Fe(Cp)_2$ to relax to its original stated before the application of external potential. An increased wait time of 7200 s was used to ensure a sufficient amount of time to allow the sample to return to its original state before the application of external potential and to account for different samples so that subsequent applications of potential can be performed without the previous application of potential affecting the result.

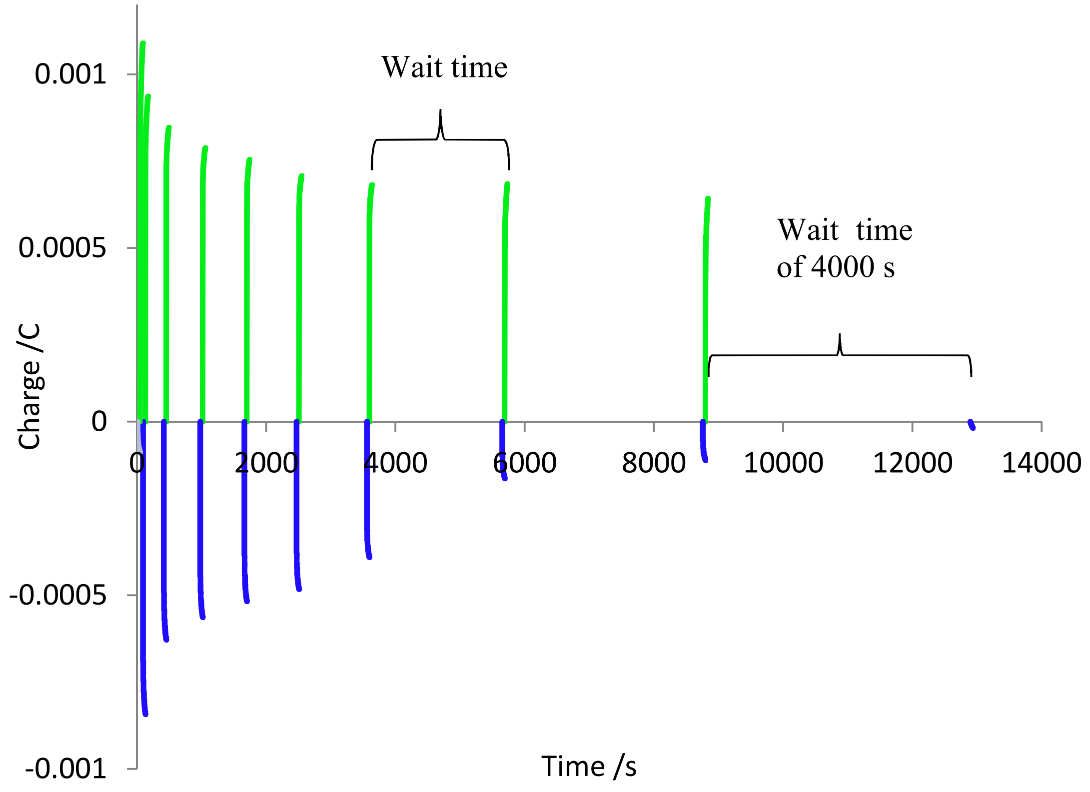

Figure 3. The chronocoulometry experiment method development for the coulometry experiments, the wait time between the oxidation (0.85 V, green plots) and reduction (0.1 V, blue plots) of $Fe(Cp)_2$@SWNT was increased from 0 s to 4000 s (13000 s total experiment time) and is the time between each green and blue plot. The increase in wait time resulted in the negative charge corresponding to reduction decreasing until almost zero when the wait time is 4000 s (8750 s to 13000 s total time) which is the charge expected if the $Fe(Cp)_2$@SWNT is in its original state before the application of external potential state and unperturbed.

4.3.2 Electrochemical characterisation of the DOS of empty SWNT

A series of potentials which encompass the Fermi level were applied (1.2 V to -0.7 V) to empty SWNT attached to a glassy carbon electrode in an electrochemical cell (Figure 4), and the resultant charge was measured. Consequently, the current generated at a given potential applied to the nanotubes is proportional to the density of SWNT electronic states at that particular energy, allowing accurate mapping of the states which are filled or emptied upon application of a specific potential. Similarly to semiconducting materials discussed above, negative or positive charge registered by the potentiostat corresponds to electrons moving to or from nanotubes respectively (Figure 4). (We assume SWNT to be a quantum capacitance dominated electrode such that application of potential in this system causes the shift of the Fermi level.[8, 9]). Importantly, zero charge signifies the absence of any electronic states in the SWNT at that particular applied potential (resulting in a so-called resting potential window) (Figure 1 and Figure 2). Therefore, while the coulometry relates well to the LSV measurements (Chapter 2, Figure 3a), this method reveals important information about the electronic state of the host-nanotube, particularly around the Fermi energy. Thus, if the range of applied potentials falls within the bandgap of SWNT little or no charge will be registered which enables quantification of the size of the nanotube bandgap with the accuracy limited solely by the size of the steps in applied potential. The potential at which the first positive charge is observed indicates the position of the top of the valence band and can therefore be correlated with the Fermi level of the SWNT, whereas the potential at which the first negative charge is observed corresponds to the first empty state of the SWNT (i.e. the bottom of the conduction band). In these experiments empty single-walled carbon nanotubes (arc-discharge, 1.4 nm average diameter) exhibit a low charge region between -0.13 V to 0.40 V in the coulometry scan (Figure 4), which is characteristic of the bandgap of semiconducting nanotubes predominant in this sample[10] and corresponds well to calculations (Chapter 2, Figure 3a).

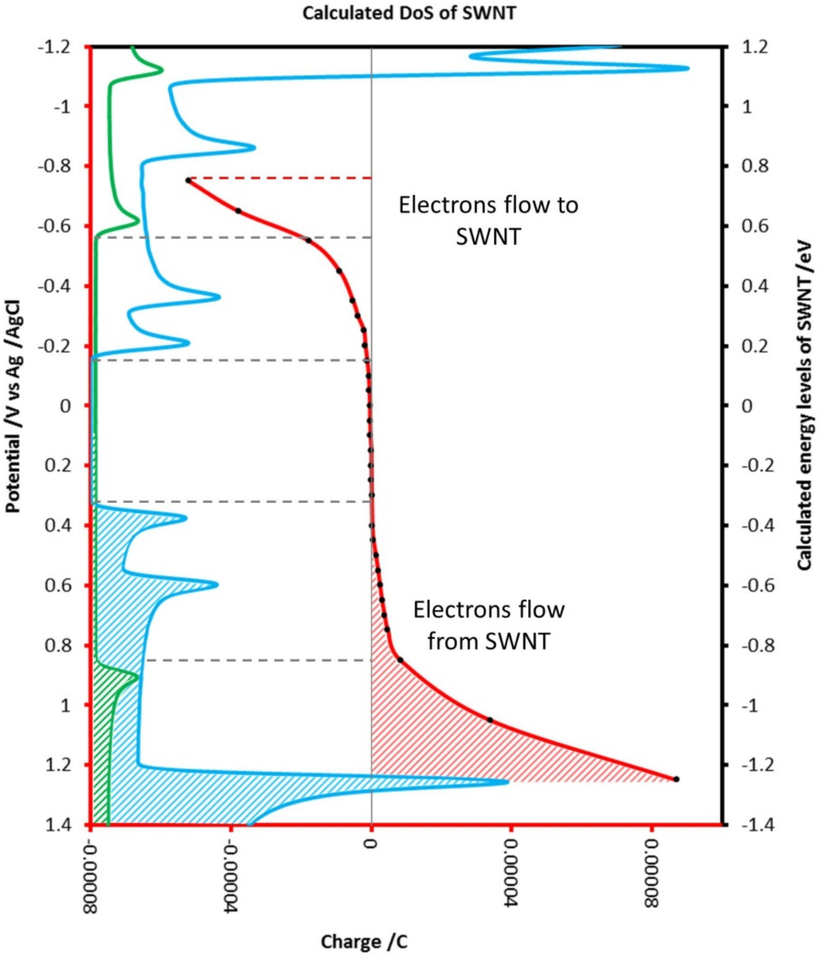

Figure 4. Coulometry measurements at a series of potentials around the Fermi level of empty SWNTs (red curve, red axes). The shaded area under the curve represents charge generated due to electrons being removed from the SWNTs (positive charge), and the unshaded area cordoned by the red dashed line represents electrons flowing into the SWNTs from the electrode (negative charge). The experiment was performed in MeCN containing $[N^nBu_4][BF_4]$ (0.1 M) as the supporting electrolyte at 293 K, and the amount of transferred charge was measured for 40 s at each applied potential. The DOS of semiconducting (17,0) SWNTs (blue curve, black axes) and metallic (10,10) SWNTs (green curve, black axes) calculated by *ab initio* DFT (performed by Dr. Matteo Baldoni). These are DOS representative of the sample but the nanotube sample will have a wide range of nanotubes with a range of chiral indices. The DOS of nanotubes is corrected to match the typical ratio of metallic to semiconducting nanotubes in the sample (31:69, metallic : semiconducting)[11] and the higher number of atoms in the calculation of the wider (17,0) SWNT (204:240 atoms) by multiplying by these ratios. A resting potential window (zero / low charge) observed in the coulometry curve matches the bandgap of semiconducting nanotubes (indicated by green dashed lines), and a sharp increase in current is observed when the applied potential is set in the region of high nanotube DOS (e.g. the van Hove singularities).[12]

4.3.3 Determining the doping of host-nanotubes by the encapsulation of guest-molecules

The coulometry methodology developed for empty nanotubes was then utilised to explore the electronic band structure of nanotubes filled with molecules such as $Fe(Cp)_2@SWNT$ (Figure 5) and $Co(Cp)_2@SWNT$ (Figure 6). The coulometric $Fe(Cp)_2@SWNT$ curve is similar to SWNT but with a resting potential window 0.23 V narrower than empty nanotubes (Figure 5), whilst $Co(Cp)_2@SWNT$ shows no resting potential window with the charge only reaching zero at a potential of 0 V, which is the position of the Fermi level, implying that the nanotubes in $Co(Cp)_2@SWNT$ effectively do not possess a bandgap. Furthermore, the coulometric behaviour of nanotubes filled with methylated ferrocenes, $Fe(Cp^{4Me})_2@SWNT$ and $Fe(Cp^{Me})_2@SWNT$, appear to be intermediate between $Fe(Cp)_2@SWNT$ and $Co(Cp)_2@SWNT$, with the resting potential window becoming narrower as the number of methyl groups increases.

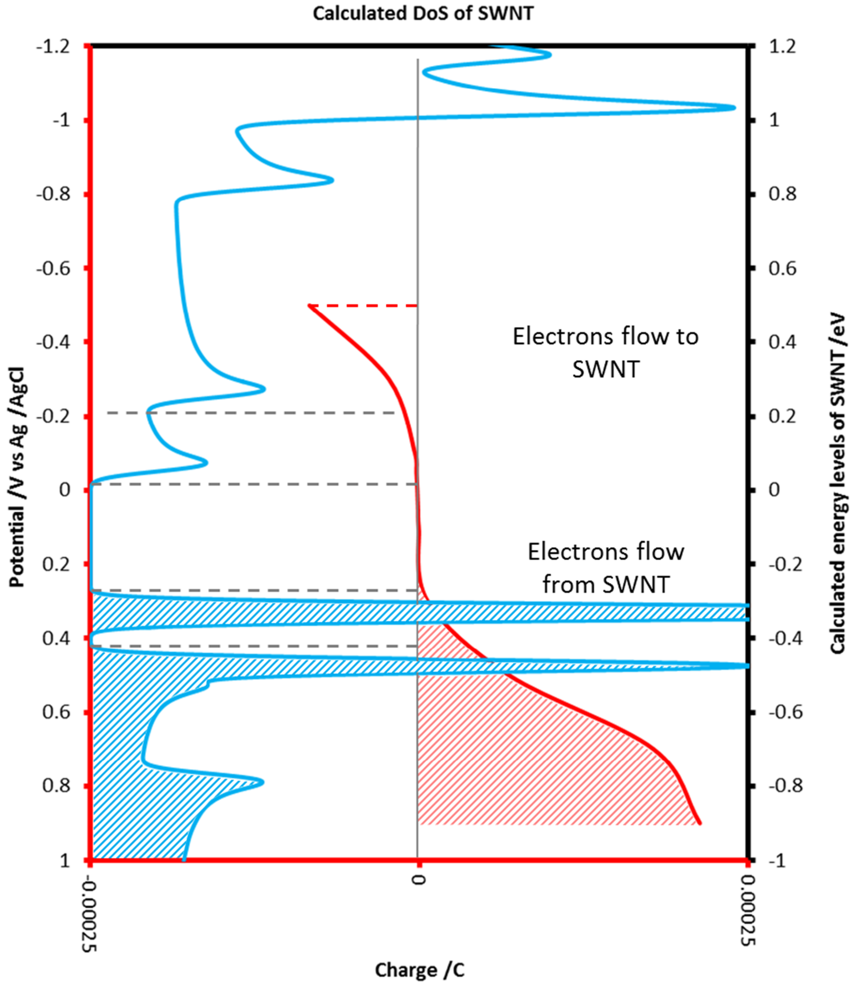

Figure 5. Coulometry measurements at a series of potentials for $Fe(Cp)_2$@SWNT (red curve, red axis). The shaded area under the curve represents charge generated due to electrons being removed from the SWNT (positive charge), and the unshaded area cordoned by the red dashed line represents electrons flowing into the SWNT from the electrode (negative charge). The experiment was performed in MeCN containing $[N^nBu_4][BF_4]$ (0.1 M) as the supporting electrolyte at 293 K, and the amount of transferred charge was measured for 40 sec at each applied potential. The DOS of $Fe(Cp)_2$@(17,0)SWNT where $Fe(Cp)_2$ is in a perpendicular orientation to the nanotube (blue curve, black axis) calculated by *ab initio* DFT. $Fe(Cp)_2$ will be encapsulated in different nanotubes with different chiral indices. (17,0) was chosen as an example semiconducting nanotube representative of the sample. The sharp increases in DOS at 0.35 V and 0.5 V originate from $Fe(Cp)_2$ orbitals hybridising with the electronic states of SWNT just below the Fermi level, which along with partial electron transfer from the guest-molecule, leads to the observed narrowing of the resting potential window.

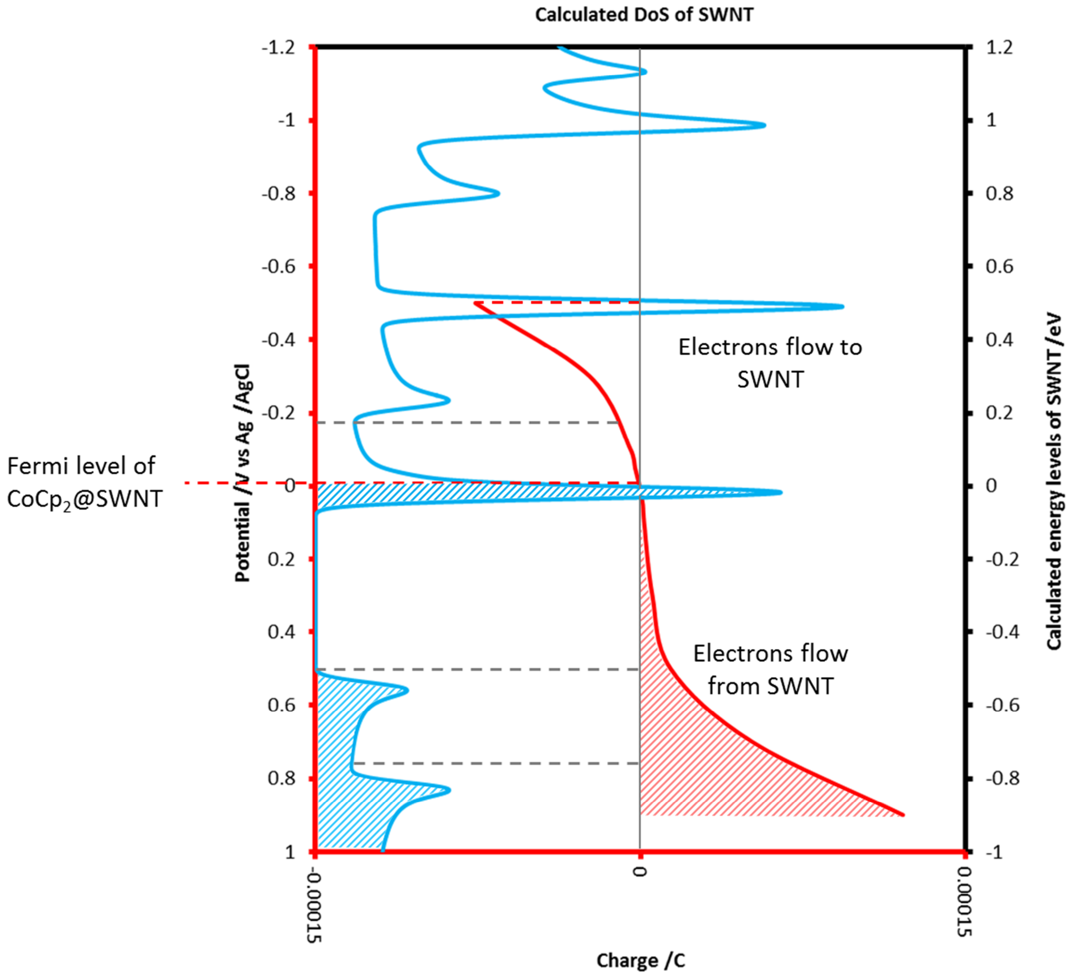

Figure 6. Coulometry measurements at a series of potentials for Co(Cp)$_2$@SWNT (red curve, red axis). The shaded area under the curve represents charge generated due to electrons being removed from the SWNT (positive charge), and the unshaded area cordoned by the red dashed line represents electrons flowing into the SWNT from the electrode (negative charge). The experiment was performed in MeCN containing [N^{n}Bu$_4$][BF$_4$] (0.1 M) as the supporting electrolyte at 293 K, and the amount of transferred charge was measured for 40 sec at each applied potential. The DOS of Co(Cp)$_2$@(17,0)SWNT where Co(Cp)$_2$ is in a perpendicular orientation to the nanotube (blue curve, black axis) calculated by *ab initio* DFT. Co(Cp)$_2$ will be encapsulated in different nanotubes with different chiral indices. (17,0) was chosen as an example semiconducting nanotube representative of the sample. The sharp increases in DOS at 0 V and -0.5 V originate from the Co(Cp)$_2$ orbitals. The significant electron transfer from Co(Cp)$_2$ to the SWNT results in mixing of the host and guest orbitals, thus raising the Fermi level above the intrinsic nanotube bandgap.

These observations can be rationalised by considering the nature and electronic configuration of the guest-molecules within the nanotubes. For example, the energy of the $Fe(Cp)_2$ HOMO is lower than the Fermi level of the host-nanotube so electrons can only be transferred into the holes in the valence band created by p-doping as described earlier (Chapter 2, Figure 3c). Therefore, even though the encapsulation of $Fe(Cp)_2$ does not significantly change the density of electrons on the nanotube, the apparent bandgap of $Fe(Cp)_2$@SWNT (measured as the resting potential window) becomes smaller due to $Fe(Cp)_2$ molecular orbital states (HOMO) at about 0.3 V (Figure 4).

In contrast, $Co(Cp)_2$ is a strong electron donor with a high energy SOMO and is oxidised in air. Upon encapsulation, a significant amount of electron density is transferred from $Co(Cp)_2$ to the SWNT, as demonstrated in the CV measurements, leading to an increase in the energy of the Fermi level into the conduction band of the nanotube (i.e. above the intrinsic bandgap of SWNT (Figure 6). This results in the electronic structure of $Co(Cp)_2$@SWNT containing a high density of states either side of the Fermi level which explains the absence of a resting potential window in the coulometry of $Co(Cp)_2$@SWNT. Interestingly, a lower rate of electron transfer from $Co(Cp)_2$@SWNT to the electrode in the potential range -0.5 to 0 V is observed due to the relatively low DOS of electron doped metallic nanotubes in this range, as compared to a higher rate of electron transfer from the electrode to $Co(Cp)_2$@SWNT between 0.5 V to 0.9 V due to a much higher density of empty states just above the E_F in this sample (Figure 6).

4.3.4 Chronocoulometry of $Fe(Cp^{XMe})_2$

Nanotubes filled with methylated ferrocenes, which have a HOMO of increasing energy as the number of methyl groups increases (Chapter 2, Figure 3a) follow the trend of a narrowing band gap (e.g. decreasing the resting potential window in coulometry) (Figure 7, Figure 8 and Figure 9). The impact of the guest-molecule on the host-nanotube is more pronounced for $Fe(Cp^{4Me})_2$ and $Fe(Cp^{5Me})_2$ because their HOMO energy is sufficiently high for their valence electrons to be transferred to the empty states of the metallic nanotubes as well as the p-doped semiconducting nanotubes in the sample, whereas $Fe(Cp^{Me})_2$ can only transfer electrons to p-doped semiconducting SWNT, however, the HOMO of $Fe(Cp^{4Me})_2$ and $Fe(Cp^{5Me})_2$ are still not high enough in energy to n-dope the semiconducting nanotubes as in the case of $Co(Cp)_2$.

The effective bandgap is measured in all these experiments by the potential window of low charge (Table 1). This must be normalised to the individual samples because each experiment involves a slightly different quantity of nanotube material on the electrode resulting in a different overall magnitude of charge measured for each sample. The charge was normalised to the charge transferred between the nanotube sample and the electrode at 0.9 V in 40 seconds. 0.9 V was chosen because it is the highest positive potential applied for the $Fe(Cp^{xMe})_2$ and the highest measured charge in 40 s for the majority of experiments. The zero charge and therefore the effective bandgap was determined to be any voltage where the charge is less than 2% of the charge at 0.9 V. This number is used for comparison between experiments and so the values for band-gap width are not absolute but allow for the comparison between different guest@SWNT materials.

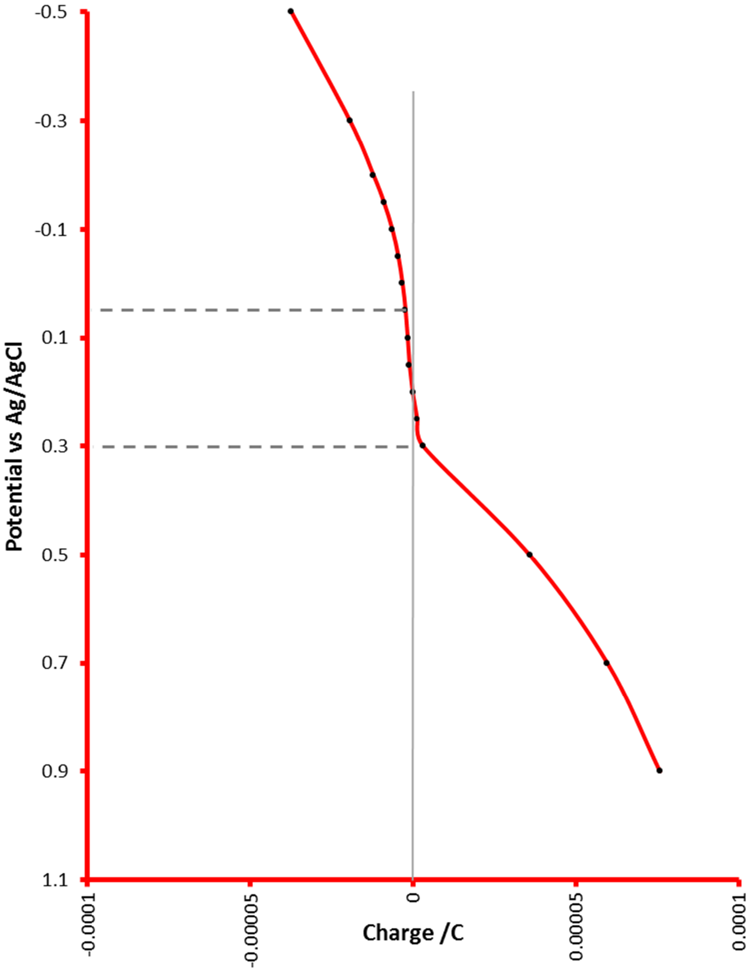

Figure 7. Chronocoulometry measurements for dimethylferrocene@SWNT performed in MeCN containing [N^nBu_4][BF_4] (0.1 M) as the supporting electrolyte at 293 K, the amount of transferred charge was measured for 40 sec at each applied potential. The band gap is determined to be 0.25 V, marked by the dashed grey lines.

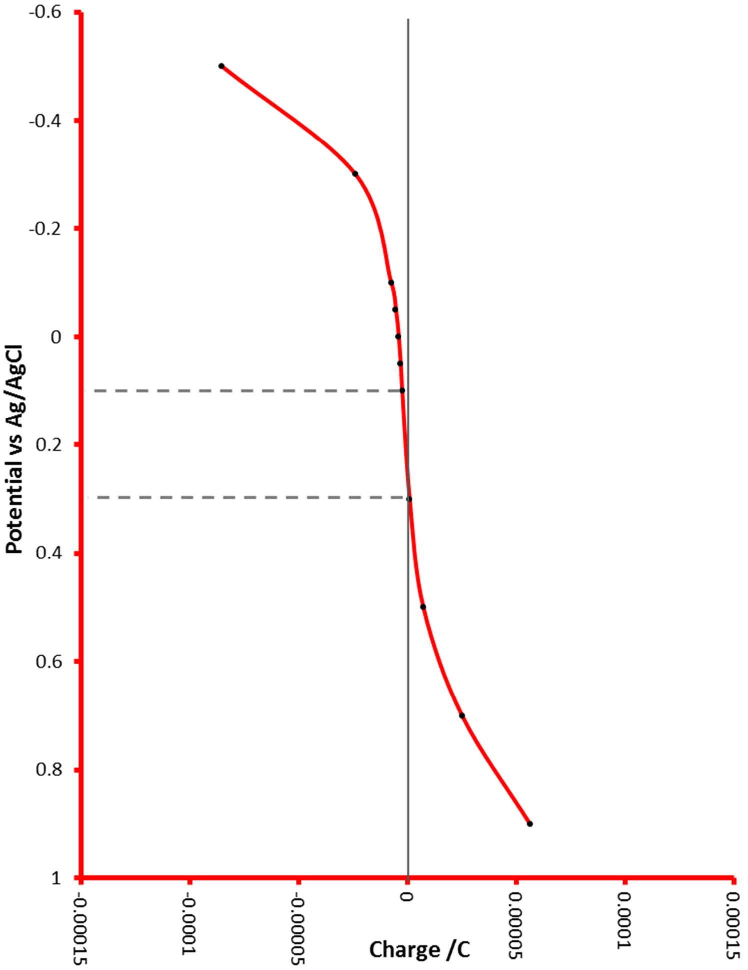

Figure 8. Chronocoulometry measurements for octamethylferrocene@SWNT performed in MeCN containing [N^{n}Bu$_4$][BF$_4$] (0.1 M) as the supporting electrolyte at 293 K, the amount of transferred charge was measured for 40 sec at each applied potential. The band gap is determined to be 0.2 V, marked by the dashed grey lines.

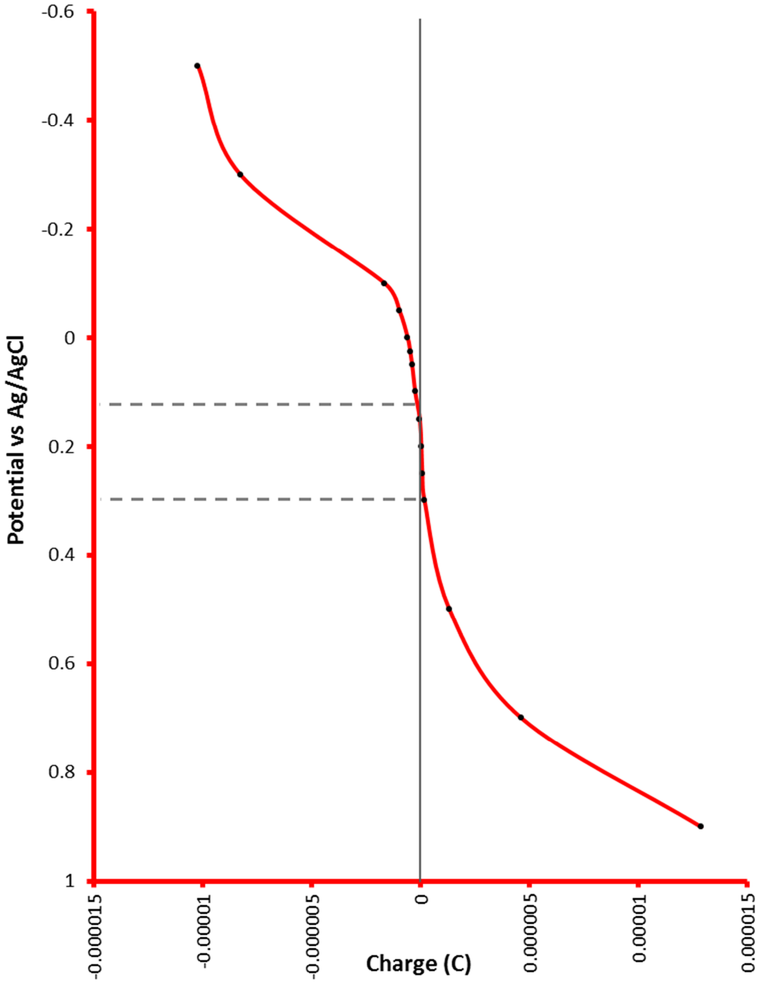

Figure 9. Chronocoulometry measurements for decamethylferrocene@SWNT performed in MeCN containing $[N^nBu_4][BF_4]$ (0.1 M) as the supporting electrolyte at 293 K, the amount of transferred charge was measured for 40 sec at each applied potential. The band gap is determined to be 0.175 V, marked by the dashed grey lines.

Table 1. Resting potential windows of $Fe(Cp^{xMe})_2@SWNT$ (X = 2, 8, or 10) and empty SWNT as determined by chronocoulometry experiments. The effective bandgap is measured in all these experiments by the potential window of low charge. The charge measured for each sample was normalised to the charge measured at 0.9 V when abstracting information from the graphs to account for slightly different amounts of nanotubes on the electrode in different experiments. The resting potential window which determines the effective band gap is defined as the range of potentials where the observed current is 2% or less of the charge measured at 0.9 V (a small charge associated with metallic nanotubes is always present regardless of the amount of doping).

Sample	**Resting potential window (V)**
Empty SWNT	0.63
$Fe(Cp)_2@SWNT$	0.40
$Fe(Cp^{Me})_2@SWNT$	0.25
$Fe(Cp^{4Me})_2@SWNT$	0.20
$Fe(Cp^{5Me})_2@SWNT$	0.18
$Co(Cp)_2@SWNT$	0.00

4.3.5 Quantitative determination of the electron transfer between guest-molecule and host-nanotube

Chronocoulometry allows accurate determination of the electronic band structure of the SWNT around the Fermi level of nanotubes filled with guest-molecules, providing important information about the nature of electron transfer between the molecule and nanotube, which cannot be readily obtained from Raman, photoluminescence or absorption spectroscopy of filled nanotubes. However, coulometry on its own does not provide quantitative information about the extent of any electron transfer processes. This can only be achieved by considering the exact value of the oxidation potential (HOMO/SOMO energy) of the specific guest-molecules in nanotubes measured by CV experiments. The coulometry measurements quantitatively establish the Fermi level of empty metallic and semiconducting nanotubes (Figure 4), and therefore the potential experienced by any guest-molecule encapsulated in a host-nanotube, is 0.13 V and -0.11 V (vs.

Ag/AgCl) respectively. The Fermi level of the metallic nanotube is determined to be the potential at which the charge is zero (0.13 V). The first potential with negative charge is the bottom of the conduction band (-0.11 V) (Figure 4). These potentials (0.13 V and -0.11 V) for metallic and semiconducting nanotube respectively are the oxidising potential applied in the absence of any external potential by the SWNT on encapsulated molecules. Correlation of the guest-molecule HOMO/SOMO energy with the Fermi level of the host-nanotube using the Nernst equation (Equation 1) provides an estimate of the percentage of molecules that transfer their valence electrons to the nanotube (Table 2). A similar considcoulometreration method has been applied previously using performed considering different a series of salts on a graphene crystal.[13]

$$E = \mathrm{E}^{\Theta} - \frac{RT}{nF}\sum ln\frac{[O]}{[R]} \qquad \textbf{Equation 1}$$

E = Redox potential of the guest-molecule of interest in solution electrochemistry; E^{Θ} = Potential of the Fermi level of metallic SWNT or the potential of the bottom of the conduction band in semiconducting nanotubes; R = Gas constant; T = Temperature; n = Number of electrons; F = Faraday constant; $[O]$ = Concentration of oxidised molecules; $[R]$ = Concentration of reduced molecules.

For example, the Nernst equation applied to $Fe(Cp)_2$@SWNT and $Fe(Cp^{Me})_2$@SWNT predicts no measurable electron transfer to the nanotube so the majority of $Fe(Cp)_2$ and $Fe(Cp^{Me})_2$ remain unchanged upon encapsulation, which is consistent with the CV measurements reported in Chapter 3. A similar calculation for $Co(Cp)_2$@SWNT results in a complete electron transfer from the guest $Co(Cp)_2$ to the nanotube, again consistent for the CV of $Co(Cp)_2$@SWNT. Interestingly, the predicted behaviour of $Fe(Cp^{4Me})_2$ and $Fe(Cp^{5Me})_2$ guest-molecules falls in between ferrocene and cobaltocene, as according to the Nernst equation, the methylated ferrocene molecules are able to transfer a valence electron to metallic SWNT but not semiconducting SWNT (Table 2).

Table 2. Percentage of guest-molecules that transfer an electron to the nanotube in a bulk sample, as estimated by Nernst equation. The Fermi level potential of metallic and semiconducting nanotubes is 0.13 V and -0.11 V (vs. Ag/AgCl) respectively. The redox potential of the free molecule (i.e. in solution) is listed vs. $Fe(Cp)_2/Fe(Cp)_2^+$ in brackets. The overall electron transfer in the sample is calculated assuming a ratio of 31:69, metallic:semiconducting nanotubes.[11]

Guest-molecule in SWNT	**Guest-molecules that transfer an electron to metallic nanotubes / %**	**Guest-molecule that transfer an electron to semiconducting nanotubes / %**	**Overall electron transfer in the sample / %**	**Average oxidation state of metal atom in sample**
$Fe(Cp)_2$ (0 V)	2×10^{-4}	0	7×10^{-5}	2.00+
$Fe(Cp)^{Me}{}_2$ (-0.10 V)	1×10^{-2}	0	4×10^{-3}	2.00+
$Fe(Cp)^{4Me}{}_2$ (-0.41 V)	96.1	0.2	30.0	2.30+
$Fe(Cp)^{5Me}{}_2$ (-0.46 V)	99.4	1.1	31.6	2.32+
$Co(Cp)_2$ (-1.27 V)	100.0	100.0	100.0	3.00+

These figures correlate well with the CV measurements of guest@SWNT probing the oxidation state of the metal centre in guest-molecules: the small percentage of electron transfer from $Fe(Cp)_2$ and $Fe(Cp)^{Me}{}_2$ to the nanotube predicted by the Nernst equation (Equation 1) is matched by the small shift observed in the redox potential of $Fe(Cp)_2$@SWNT and $Fe(Cp^{Me})_2$@SWNT (Fe^{III}/Fe^{II}) as compared to the molecule in solution (Table 1). The high percentage of electron transfer from $Co(Cp)_2$ to the nanotube matches a big shift in the redox potential of $Co(Cp)_2$@SWNT. The guest-molecules $Fe(Cp^{5Me})_2$ and $Fe(Cp^{4Me})_2$ represent a special case as they are able to transfer electrons to the metallic nanotubes present in the sample, but not the majority of semiconducting nanotubes (Table 2), which also correlates with the shifts of their redox potentials inside the SWNT as measured by CV (Table 1). As a result, within the samples of $Fe(Cp^{5Me})_2$@SWNT and $Fe(Cp^{4Me})_2$@SWNT there will be molecules that have transferred an electron to the host-nanotube and those which remained unchanged upon encapsulation depending on whether the host-nanotube is metallic or semiconducting respectively. Within this framework of considerations, linking cyclic voltammetry and coulometry data *via* the Nernst equation, enables the determination of the precise oxidation state guest-molecules in carbon nanotubes.

4.4 Conclusions

A novel electrochemical method that allows determination of nanotube doping and quantification of the electron transfer from guest-molecules to the host-nanotube was developed. Specifically, coulometry reveals the impact of guest-molecules on the electronic levels of the host-nanotube; and cyclic voltammetry combined with information about the actual Fermi level in molecule@SWNT system obtained from coulometry, determines the real oxidation state of the guest-molecule. A prior prediction and spectroscopy measurements of the oxidation state of guest-molecules in carbon nanotubes is difficult, but the developed electrochemical approach determines the oxidation state with great precision. Furthermore, the nature of the guest-molecules encapsulated inside nanotubes greatly changes the electronic structure of the nanotube which can be directly gauged using electrochemistry. This opens up new avenues for tuning nanotube host-guest hybrids for use in solar cells, as chemical nanoreactors and as electric capacitors.

4.5 Experimental

4.5.1 Preparation of metallocene filled nanotubes

Nanotube samples were prepared as detailed in Chapter 3

4.5.2 Fill percentage calculated by TEM extrapolation

Table 3. The percentage of nanotube cavities that are filled as calculated using TEM extrapolation (see Chapter 2).

Guest-molecule in SWNT	**Fill percentage /%**
$Fe(Cp)_2$	87
$Fe(Cp^{Me})_2$	88
$Fe(Cp^{4Me})_2$	93
$Fe(Cp^{5Me})_2$	69
$Co(Cp)_2$	95

4.5.3 Electrochemistry

Electrochemistry experiments were performed on an Autolab PGSTAT302N potentiostat. Electrodes were purchased from IJCambria and Metrohm. The electrochemistry was performed using a three electrode set up with a Ag/AgCl reference electrode, a platinum counter electrode and a glassy carbon working electrode on which the guest-molecule@SWNT is deposited. The nanotube sample (0.5 mg) was sonicated (15 mins) in dry DMF (0.5 mL) to form an ink. 10 μL of the ink was cast onto the GCE using a micro-pipette and allowed to dry in air for 1 h. The electrode was then rinsed in dry acetonitrile and allowed to dry in air.

4.5.3.1 Chronocoulometry

The electrode and cell are prepared as in the previous section with the following exceptions. When preparing the cell, extra solvent and electrolyte are used and only a slow flow of Argon over a well-sealed cell is used to prevent the cell drying out due to the longer time required for the experiment (3 days). The cell is regularly checked to ensure the solvent level remains constant.

A series of potentials were applied to empty SWNT or guest-molecule@SWNT (Table 4) that encompass the Fermi level. The charge at each of these potentials was recorded for 40 seconds. 2 hours wait time was left between the application of each potential to allow the nanotube sample to return to its original state (before the sample is perturbed by the electrode) (see Section 4.3.1).

Table 4. Potentials applied to each guest@SWNT during the chronocoulometry experiment. A different number of potentials were applied to some of the SWNT material due to time constraints (experiments can require 3 days to complete). In the case of empty SWNT, an increased number of potentials were applied to increase the resolution due to the importance of the Fermi level and conduction band position of empty SWNT for experiments in Chapters 3 and 4.

Empty SWNT (V)	$Fe(Cp)_2$@SWNT (V)	$Fe(Cp^{Me})_2$@SWNT (V)	$Fe(Cp^{4Me})_2$@SWNT (V)	$Fe(Cp^{5Me})_2$@SWNT (V)	$Co(Cp)_2$@SWNT(V)
-0.75	-0.5	-0.5	-0.5	-0.5	-0.5
-0.65	-0.3	-0.3	-0.3	-0.3	-0.3
-0.55	-0.1	-0.2	-0.1	-0.1	-0.1
-0.45	-0.05	-0.15	-0.05	-0.05	-0.05
-0.35	0	-0.1	0	0	0
-0.3	0.05	-0.05	0.05	0.025	0.05
-0.25	0.1	0	0.1	0.05	0.1
-0.2	0.3	0.05	0.3	0.1	0.3
-0.15	0.5	0.1	0.5	0.15	0.5
-0.1	0.7	0.15	0.7	0.2	0.7
-0.05	0.9	0.2	0.9	0.25	0.9
0		0.25		0.3	
0.05		0.3		0.5	
0.1		0.5		0.7	
0.15		0.7		0.9	
0.2		0.9			
0.25					
0.3					
0.4					
0.45					
0.5					
0.55					
0.6					
0.65					
0.7					
0.75					
0.85					
1.05					
1.25					

The experiment was programmed using NOVA 1.10. The code is programmed so that the potentiostat applies the potential prior to the cell being turned on. The cell is turned on for 40 seconds then turned off so that no external potential is applied to the electrode. A wait time of 7500 seconds is applied here and the process is repeated at the next potential (Table 4).

4.5.4 Theoretical calculations

Calculations of empty SWNT DOS, guest@SWNT DOS and charge transfer were performed on different guest-nanotube model systems at the gradient-corrected spin-polarised DFT level by applying the PBE[14] exchange-correlation functional as implemented in the SIESTA program package.[15] Electronic states were expanded by a double-ζ basis set with norm-conserving pseudopotentials for the description of core levels[16] and a plane-wave representation of the charge density with a cut-off of 240 Ry. Polarisation functions were added to the metallic centres. Periodic boundary conditions were applied to the cell and a supercell approach was used in the two directions perpendicular to the axis of the nanotube. Geometries of all systems were relaxed until a maximum gradient of 0.02 eV/Å on forces was reached and the stress tensor was less than 0.03 GPa. In band structure calculations, reciprocal space was sampled using a 1 × 1 × 5 Monkhorst-Pack[4] k-point grid. CNTs density of states was renormalised to the number of C atoms in the simulation cell. Obtained results are in line with previous theoretical works.[17, 18]

4.5.5 HRTEM and EDX

HRTEM and EDX data for all materials is detailed in Chapter 3.

4.6 References

1. A. Javey, R. Tu, D. B. Farmer, J. Guo, R. G. Gordon and H. J. Dai, *Nano Lett.*, 2005, **5**, 345.
2. S. J. Wind, J. Appenzeller, R. Martel, V. Derycke and P. Avouris, *Appl. Phys. Lett.*, 2002, **80**, 3817.
3. A. G. Guell, K. E. Meadows, P. V. Dudin, N. Ebejer, J. V. Macpherson and P. R. Unwin, *Nano Lett.*, 2014, **14**, 220.
4. M. Kruger, M. R. Buitelaar, T. Nussbaumer, C. Schonenberger and L. Forro, *Appl. Phys. Lett.*, 2001, **78**, 1291.
5. T. W. Odom, J. L. Huang, P. Kim and C. M. Lieber, *J. Phys. Chem. B*, 2000, **104**, 2794.
6. S. Kazaoui, N. Minami, N. Matsuda, H. Kataura and Y. Achiba, *Appl. Phys. Lett.*, 2001, **78**, 3433.
7. M. V. Kharlamova, M. Sauer, T. Saito, Y. Sato, K. Suenaga, T. Pichler and H. Shiozawa, *Nanoscale*, 2015, **7**, 1383.
8. I. Heller, J. Kong, H. A. Heering, K. A. Williams, S. G. Lemay and C. Dekker, *Nano Lett.*, 2005, **5**, 137.
9. I. Heller, J. Kong, K. A. Williams, C. Dekker and S. G. Lemay, *J. Am. Chem. Soc.*, 2006, **128**, 7353.
10. A. Pekker and K. Kamaras, *Phys. Rev. B.*, 2011, **84**, 075475.
11. S. Cambre, W. Wenseleers, E. Goovaerts and D. E. Resasco, *Acs Nano*, 2010, **4**, 6717.
12. S. A. Hodge, M. K. Bayazit, H. H. Tay and M. S. Shaffer, *Nat. Commun.*, 2013, **4**, 1989.
13. S. A. Hodge, H. H. Tay, D. B. Anthony, R. Menzel, D. J. Buckley, P. L. Cullen, N. T. Skipper, C. A. Howard and M. S. Shaffer, *Faraday Discuss.*, 2014, **172**, 311.
14. J. P. Perdew, K. Burke and M. Ernzerhof, *Phys. Rev. Lett.*, 1996, **77**, 3865.
15. M. S. José, A. Emilio, D. G. Julian, G. Alberto, J. Javier, O. Pablo and S.-P. Daniel, *J. Phys.: Condens. Matter*, 2002, **14**, 2745.
16. J. Junquera, O. Paz, D. Sanchez-Portal and E. Artacho, *Phys. Rev. B*, 2001, **64**, 235111.
17. E. L. Sceats and J. C. Green, *J. Chem. Phys.*, 2006, **125**, 12.
18. E. L. Sceats and J. C. Green, *Phys. Rev. B.*, 2007, **75**, 10.

5 Utilising nanotubes to control the pathway of the redox induced reactions of $Cp^{Me}Mn(CO)_3$

5.1 Introduction

The insertion of guest-molecules into host-carbon nanotubes has been shown to modify the intrinsic electronic properties of the host-nanotubes, improving the electrochemical sensing of H_2O_2[1] and dopamine[2] or facilitating tuning of optical properties of the nanotube to be controlled by adjusting the applied potential.[3,4] This chapter demonstrates that a carbon nanotube electrode is not only a useful surface for enhancing the detection of redox processes, but also enables confinement of guest-molecules at the nanoscale which can change the pathways of their electrochemical transformations. In this case the nanotube is acting simultaneously as a nano-electrode and a nano-reactor.

5.2 Aim and objectives

The aim of this chapter is to investigate the use of nanotubes as a container for the electrochemically driven reaction of $Cp^{Me}Mn(CO)_3$ (**1**) with a nucleophile and determine the effect that confinement has on the reaction pathway.

The objectives to achieve this aim are to encapsulate $Cp^{Me}Mn(CO)_3$ inside SWNT and subsequently confirm the encapsulation using TEM, EDX and IR spectroscopy. Then employ the nanotube as an electron mediator between the macro electrode and the one dimensional array of molecules encapsulated in the nanotube in CV experiments. The effect the nanotube has on the pathway of the electrochemical reaction will be determined by comparing the electrochemical reaction observed in solution with that observed when the molecules are inside the nanotube. Molecular models will be used to help elucidate the mechanism of the confined reaction.

5.2.1 Manganese piano stool complexes

Copious amounts of work has been performed on reactions of $CpMn(CO)_3$, including reactions where the elimination of CO is induced by flash photolysis, and the lifetime of the transient species $CpMn(CO)_2$ is measured using (time resolved infra-red) TRIR and UV-vis spectroscopy.[5] In this study there is a strong influence from the chosen solvent and the concentration of the dissolved CO, whereby the solvent acts as a stabilising ligand affecting the kinetics of the elimination and re-combination steps, and CO acts as a competing ligand to any incoming ligand. The electrochemistry of $Cp^{Me}Mn(CO)_3$ has been extensively studied, particularly with regard to exploring the kinetics of the exchange of one of the CO ligands. Many different electrochemical ligand substitutions were performed, including the substitution of CO with acetonitrile.[6-8] Therefore, $Cp^{Me}Mn(CO)_3$ was chosen for this study due to the extensive solution electrochemical reactions reported in the literature, providing a basis with which to investigate the electrochemical reaction inside nanotubes.

$Cp^{Me}Mn(CO)_3$ is a liquid at room temperature allowing for facile encapsulation into the nanotubes by simply using capillary forces to drive the liquid into the empty nanotubes. $Cp^{Me}Mn(CO)_3$ possesses both the characteristics of metallocenes, firstly it has a Cp^{Me} ligand which provides effective interactions with the nanotube π-system, as well as three carbonyl ligands that can serve dually as spectroscopic markers and good leaving groups in the electrochemical reaction. The complex is also known to act as a catalyst for important processes such as CO fixation,[7] disulphide formation[9] and H_2 production,[9, 10] which makes the hybrid structures in which the complex **1** is encapsulated inside single-walled carbon nanotubes (**1**@SWNT) suitable for a number of possible applications.

5.3 Results and discussion

5.3.1 Filling of SWNT with $Cp^{Me}Mn(CO)_3$

In order to control the reactivity of molecules through nano-scale confinement it is essential that they are securely entrapped in the nanotubes. SWNT with an average diameter of 1.4 nm were used to match the size of small organometallic molecules and to provide efficient encapsulation. For example, metal hexacarbonyls[11] or metallocenes[12-16] can be inserted in SWNT tubes from gas or liquid (molten) phases forming 1D molecular arrays within the nanotube cavity.

SWNT (arc-discharge, 1.4 nm diameter) were opened by controlled thermal oxidation in air and immediately immersed in $Cp^{Me}Mn(CO)_3$, a liquid at room temperature, allowing encapsulation of the guest-molecules by capillary forces. The excess of **1** was removed from the surface of the SWNT using vacuum filtration with a PTFE membrane, followed by evaporation under nitrogen flow for 24 h to remove any molecules form the outer surface of the nanotubes.

The identity of **1**@SWNT was confirmed by IR spectroscopy in which characteristic υ(CO) stretching bands were observed at 2023 and 1940 cm^{-1} (Figure 1). These stretching bands clearly indicate successful insertion of complex **1** from the liquid phase into the nanotube cavity (Figure 1). The carbonyl stretching vibrations appear to be slightly blue-shifted (by 2 and 6 cm^{-1} respectively) as compared to the free complex, indicating a small amount of charge transfer from the Mn(I) centre to the nanotube sidewall. This is to be expected as the host-SWNT often behaves as effective electron acceptors with respect to encapsulated guest-molecules.[11] N.B. The observed signals are weak due to the cloaking effect of the nanotube, allowing only very strong IR signals through, however, the signals are significant peaks compared to the baseline.[17]

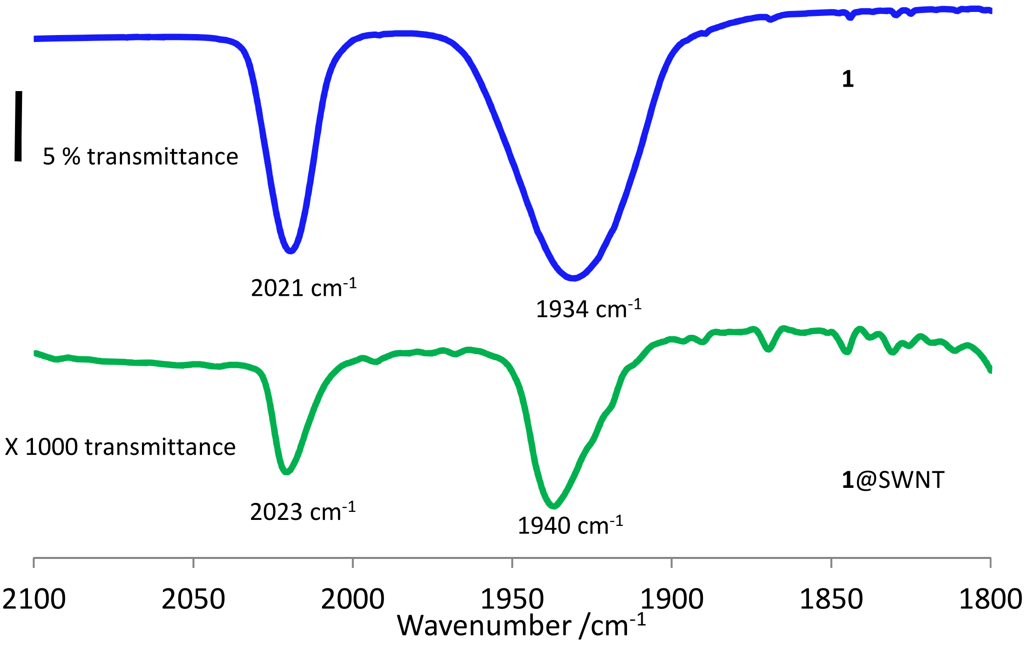

Figure 1. Infra-red spectra of free Cp^{Me}Mn(CO)$_3$ (blue) and Cp^{Me}Mn(CO)$_3$@SWNT (green) which shows a blue shift in υ(CO) upon nanotube confinement in SWNT. The intensity of the Cp^{Me}Mn(CO)$_3$@SWNT has been multiplied by 1000.

HRTEM of $Cp^{Me}Mn(CO)_3@SWNT$ enables local-probe analysis with near atomic resolution confirming that the nanotubes have no surface-adsorbed molecules of **1**, while their internal cavities contain dark-contrast features corresponding to Mn metal clusters made up of approximately 25 atoms (Figure 2). This was estimated by measuring the internal diameter and therefore the volume of the nanoparticles, then using the density of bulk metal to determine the number of atoms per nanoparticle. It is important to note that nanoparticles are typically less dense than bulk metal (Chapter 2). The molecules of complex **1** appear to be extremely unstable under the electron beam, rapidly losing ligands and decomposing into metallic Mn even at a low energy (100 keV) and dose rates of electrons ($\sim 10^6$ e nm^{-2} s^{-1}) on the specimen.[18] EDX analysis recorded for individual or small bundles of SWNT using a focused e-beam (diameter 3-5 nm) identifies the clusters inside the nanotubes as Mn atoms (Figure 3). The fact that Mn is always observed only on the inside of the nanotubes confirms the efficient encapsulation of the complex. The occupancy of the internal space within SWNT channels was determined to be *c.a.* 62 % by a number of independent methods including thermogravimetric analysis (TGA), chronocoulometry, TEM imaging, gravimetric analysis and semi-quantitative EDX (see Chapter 2). These methods indicate that the majority of host-nanotubes are filled with complex **1**, while some remain empty, perhaps due to internal blockages in the extremely narrow internal channels of the SWNT.

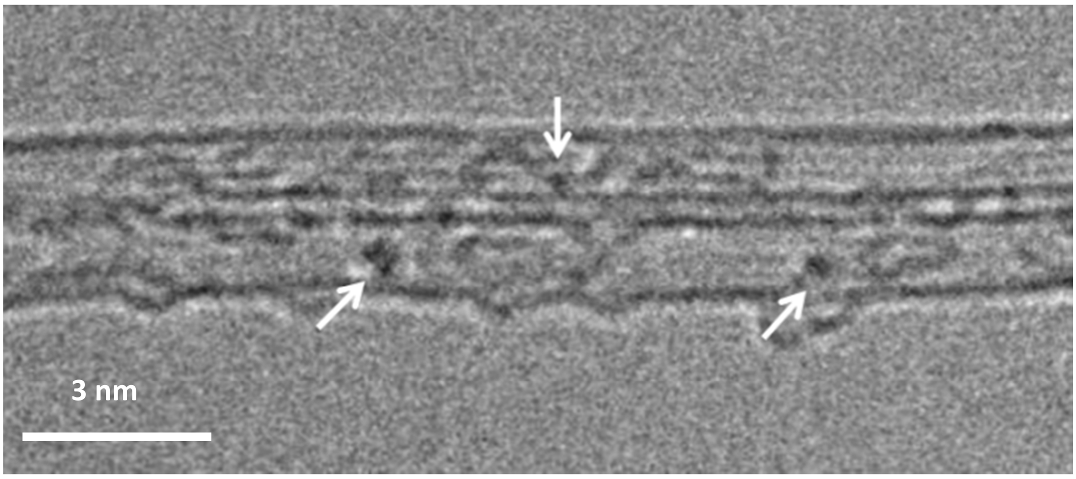

Figure 2. HRTEM image of two $Cp^{Me}Mn(CO)_3$@SWNT showing Mn metal as dark contrast (white arrows) located solely inside the SWNT.

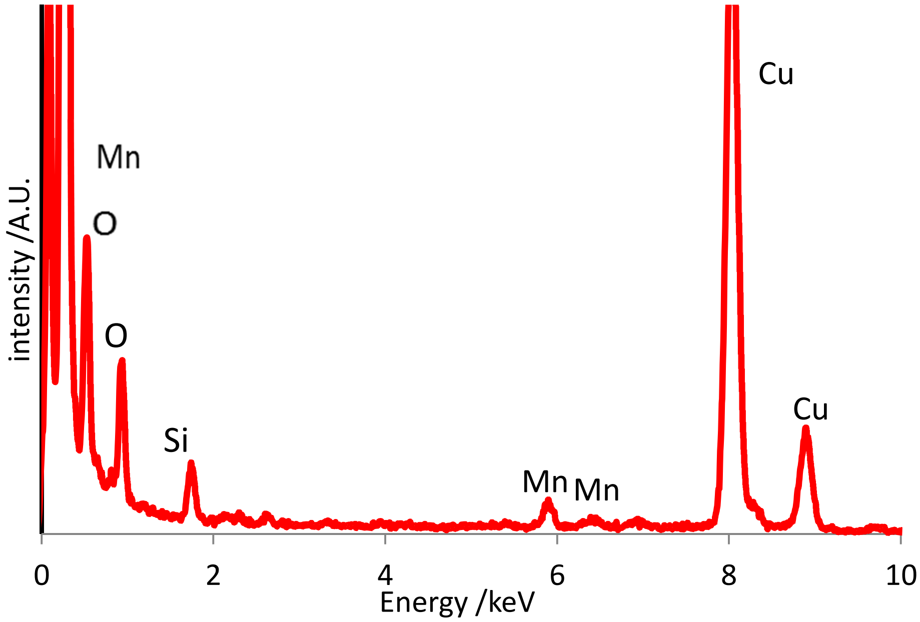

Figure 3. EDX spectrum confirming the presence of Mn in the $Cp^{Me}Mn(CO)_3$@SWNT sample (Cu peaks are due to the sample grid).

5.3.2 Electrochemistry of $Cp^{Me}Mn(CO)_3$/SWNT

In a solution based cyclic voltammetry experiment with acetonitrile as the solvent and using a GCE, an oxidation of complex **1** was observed at +0.80 V vs. $Fe(Cp)_2/Fe(Cp)_2^+$ corresponding to the Mn^{II}/Mn^{I} couple (Figure 4). The electrochemically generated **1**$^{1+}$ species is highly reactive and undergoes rapid nucleophilic substitution of one of the CO ligands by a molecule of the solvent (acetonitrile) (Figure 4) leading to the formation of a new $[Cp^{Me}Mn(CO)_2MeCN]^+$ (**2**$^{1+}$) complex. Complex **2**$^{1+}$ then reduces to its neutral form, $Cp^{Me}Mn(CO)_2MeCN$, at a significantly lower potential (-0.18 V vs. $Fe(Cp)_2^+/Fe(Cp)_2$; Figure 4) than would be expected for **1**$^{1+}$, so that the observed cyclic voltammogram can be rationalised as a result of an electrochemical reaction, **1** → **1**$^{1+}$ → **2**$^{1+}$ → **2** (Figure 5).[7, 9]

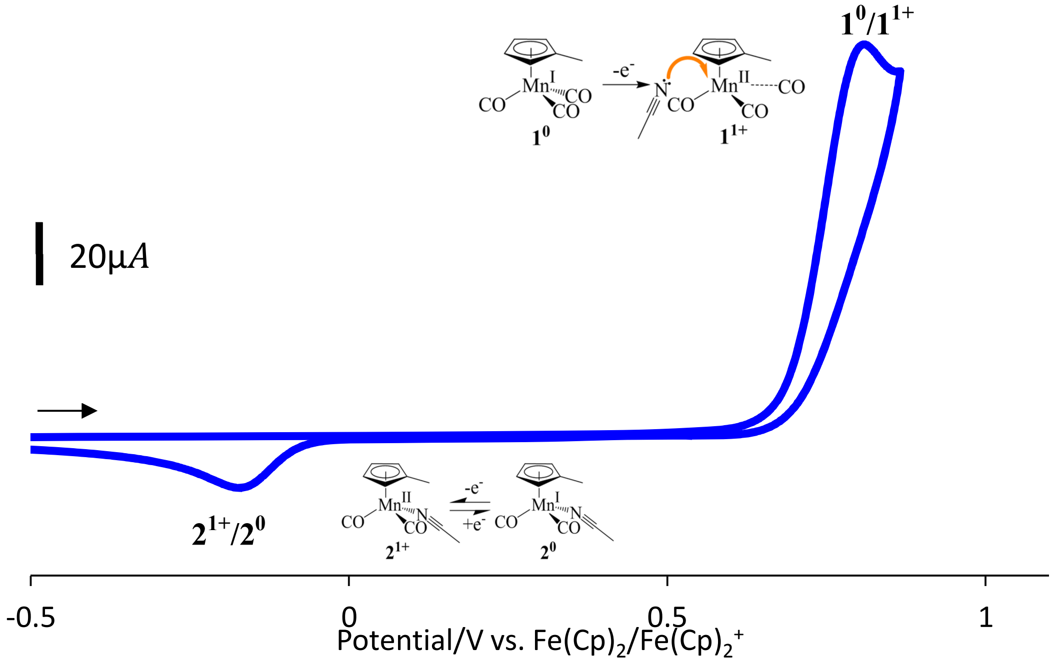

Figure 4. CV of $Cp^{Me}Mn(CO)_3$ using a GCE (blue) showing the oxidation of **1**^{0}/**1**$^{1+}$ and subsequent reaction of **1**$^{1+}$ with acetonitrile solvent to form **2**$^{1+}$ followed by reduction to form **2**^{0}. The cyclic voltammetry experiment was performed in acetonitrile containing $[N^nBu_4][BF_4]$ (0.1 M) as the supporting electrolyte at 293 K and a scan rate of 100 mVs^{-1}. The potential is held at the start potential for a period of 5 seconds before the potential sweep.

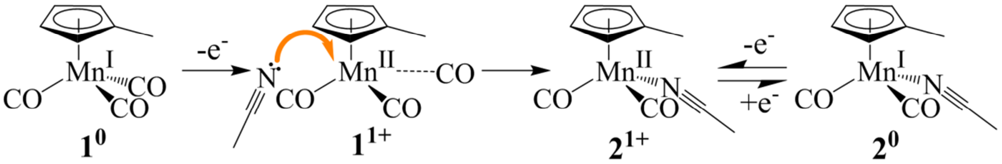

Figure 5. Schematic showing the oxidation of $\mathbf{1^0/1^{1+}}$ and subsequent reaction of $\mathbf{1^{1+}}$ with acetonitrile solvent to form $\mathbf{2^{1+}}$ followed by reduction to form $\mathbf{2^0}$.

The CV of **1** was also performed at -40 °C in an acetonitrile/dry ice bath to slow the reaction of $\mathbf{1^{1+}} \rightarrow \mathbf{2^{1+}}$ resulting in the appearance of a reduction process corresponding to the $\mathbf{1^{1+}/1^0}$ couple (Figure 6). The appearance of the reduction wave allows the determination of the $E_{1/2}$ of the redox process for comparison with the $E_{1/2}$ of **1**@SWNT. It also shows that the ligand substitution is still not prevented even at very low temperatures as a reduction of $\mathbf{2^{1+}/2^0}$ with a low current is still observed.

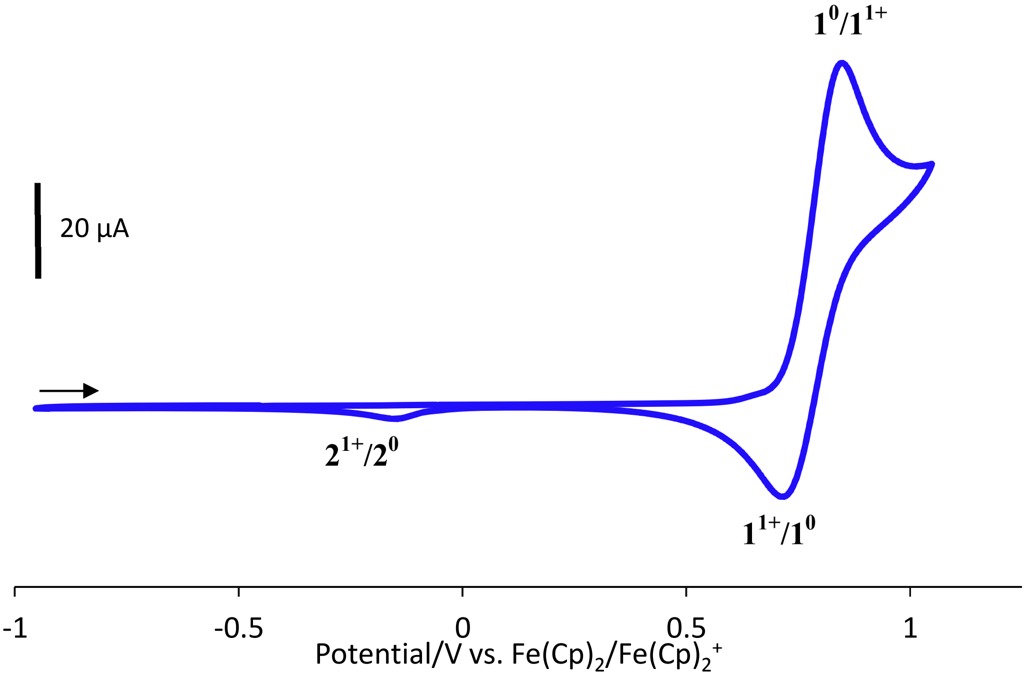

Figure 6. CV of Cp^{Me}Mn(CO)$_3$ using a GCE at -40 °C (using an acetonitrile dry ice bath) showing that at this temperature the electrochemical reaction of Cp^{Me}Mn(CO)$_3$ is quasi reversible. The $E_{1/2}$ for this oxidation is 0.78 V vs. Fe(Cp)$_2$/Fe(Cp)$_2^+$. The cyclic voltammetry experiment was performed in acetonitrile containing [N^{n}Bu$_4$][BF$_4$] (0.1 M) as the supporting electrolyte at 233 K and a scan rate of 100 mVs^{-1}. Arrow indicates the direction of potential sweep. The potential is held at the start potential for a period of 5 seconds before the potential sweep.

A solution CV was also performed using a non-coordinating solvent, dichloromethane (DCM), in an attempt to prevent ligand substitution. At fast scan rates (0.3 Vs^{-1}) the oxidation and corresponding reduction for the $\mathbf{1}^{1+}/\mathbf{1}^{0}$ couple is observed along with a second oxidation (Figure 7). The current of the reduction does not equal the current of the oxidation and at slow scan rates (0.05 Vs^{-1} and 0.02 Vs^{-1}) the reduction disappears due to the reaction of $Cp^{Me}Mn(CO)_3^+$ with DCM. The second peak in current could possibly be due to the elimination of a second CO ligand. This further demonstrates how reactive the $\mathbf{1}^{1+}$ species is, reacting even with a non-coordinating solvent.

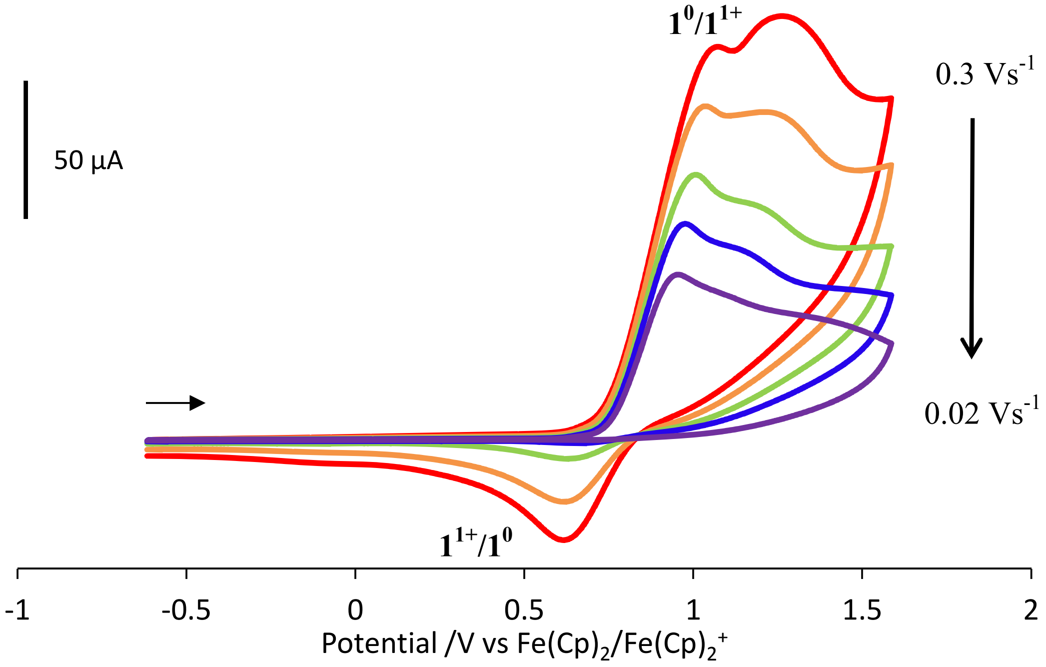

Figure 7. CV of $Cp^{Me}Mn(CO)_3$ in DCM using a GCE showing the redox processes of **1**. At fast scan rates (0.3 Vs^{-1}, red) the corresponding reduction to the initial oxidation is observed along with a second oxidation. The current of the reduction does not equal the current of the oxidation and at slow scan rates (0.05 Vs^{-1} and 0.02 Vs^{-1}, blue and purple) the reduction disappears due to reaction of $\mathbf{1}^{1+}$ with DCM. The cyclic voltammetry experiment was performed in DCM containing $[N^nBu_4][BF_4]$ (0.1 M) as the supporting electrolyte at 293 K and scan rates of 0.3 Vs^{-1} to 0.02 Vs^{-1}, red through to purple. Arrow indicates the direction of potential sweep.

Attaching empty SWNT (*c.a.* 0.14 mg cm^{-2} of electrode) to the GCE electrode surface increases the electrochemically active surface area by a factor of 3.75 (Chapter 2). This causes a significant increase in the observed current for the CV processes of the complex in solution (Figure 8 and Figure 9), however, the pathway of the reaction remains essentially the same, indicating that the redox process takes place in the solution around the nanotubes (*i.e.* within the diffusion layer), where the molecules are surrounded by acetonitrile which acts as a nucleophile.

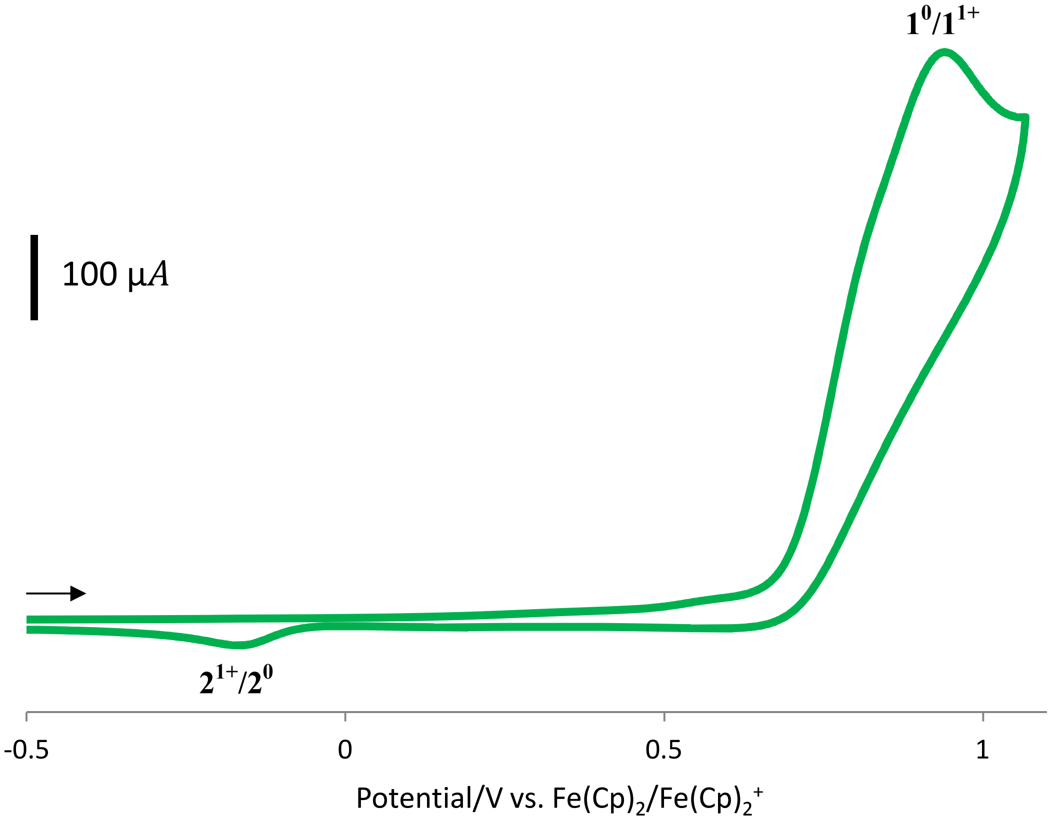

Figure 8. CV of Cp^{Me}Mn(CO)$_3$ using a GCE with empty SWNT attached showing a similar signal to that observed using just GCE. This demonstrates that there is no change in the reaction pathway when the electrochemical reaction occurs on the outside of the nanotube. The cyclic voltammetry experiment was performed in acetonitrile containing [N^{n}Bu$_4$][BF$_4$] (0.1 M) as the supporting electrolyte at 293 K and a scan rate of 100 mVs^{-1}. Arrow indicates the direction of potential sweep. The potential is held at the start potential for a period of 5 seconds before the potential sweep.

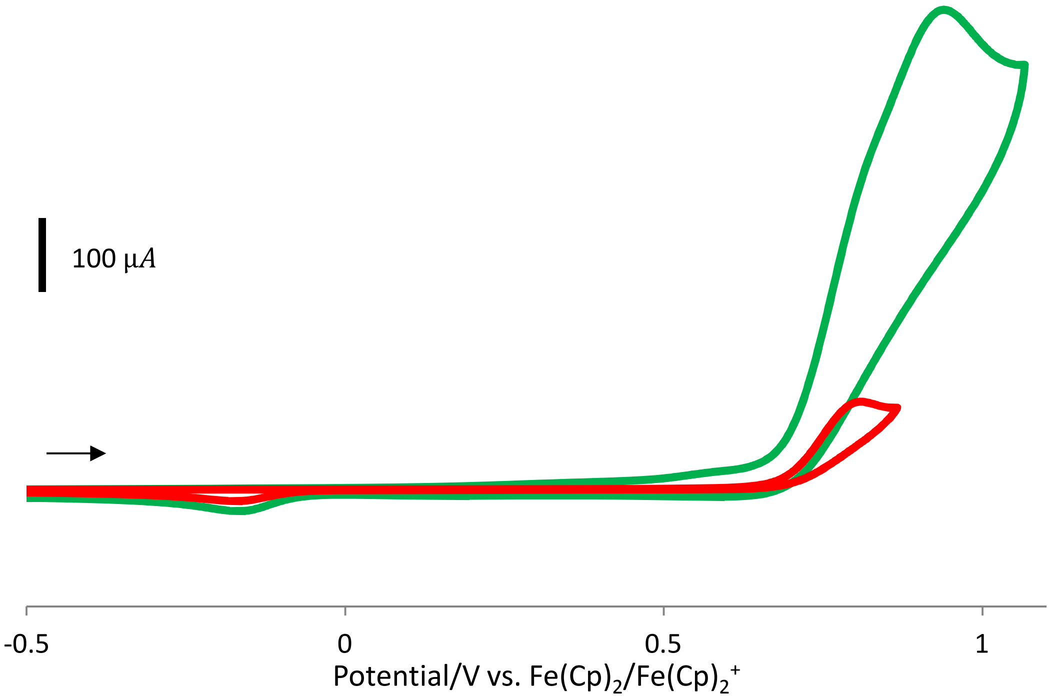

Figure 9. Overlay of the CV of $Cp^{Me}Mn(CO)_3$ using a GCE (red) and $Cp^{Me}Mn(CO)_3$ using a GCE with empty SWNT attached (green). The cyclic voltammetry experiment was performed in acetonitrile containing $[N^nBu_4][BF_4]$ (0.1 M) as the supporting electrolyte at 293 K and a scan rate of 100 mVs^{-1}. Arrow indicates the direction of potential sweep. The potential is held at the start potential for a period of 5 seconds before the potential sweep.

5.3.3 Electrochemistry of $Cp^{Me}Mn(CO)_3$@SWNT

In the solution electrochemistry of $Cp^{Me}Mn(CO)_3$ an electrochemical ligand exchange occurs upon oxidation of $\mathbf{1}^0$ to $\mathbf{1}^{1+}$. In contrast, when the complex, **1**, is encapsulated in nanotubes (*i.e.* no longer in solution), and the **1**@SWNT host-guest structures are securely attached to the GCE (Figure 10), the redox active molecules are in a different environment as compared to bulk solution experiments. In a typical CV experiment, the complex **1** remains inside the nanotubes. This indicates that all of the molecules are electrically connected to the GCE throughout the potential scan *via* the carbon nanotubes which act as a physical bridge between the individual encapsulated molecules and the macroscopic GCE electrode.

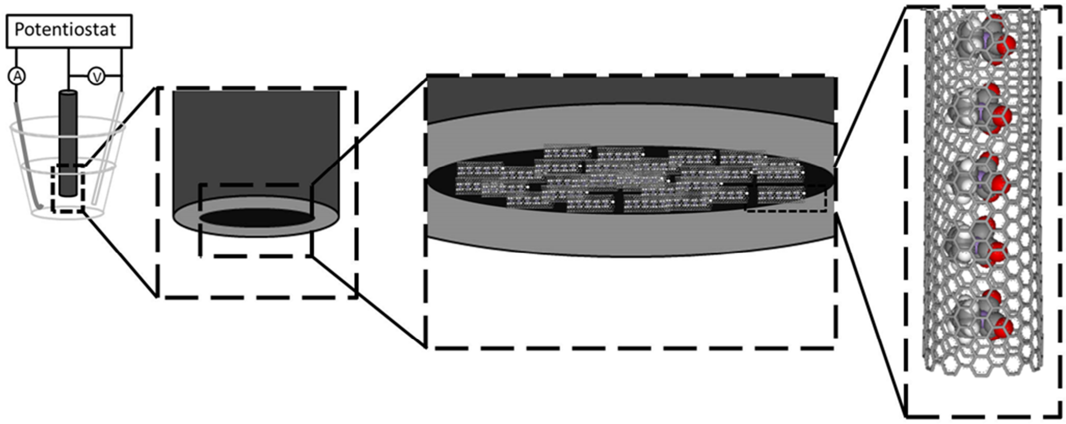

Figure 10. Schematic of the electrochemistry set up. A three electrode set up is used with a Ag/AgCl reference electrode, a platinum counter electrode and SWNT, deposited on a glassy carbon working electrode, in which the investigated species, $Cp^{Me}Mn(CO)_3$, is encapsulated.

Unlike the solution experiments, all of the molecules in **1**@SWNT undergo oxidation and reduction in each CV cycle, so that the current associated with these reactions is significantly greater than in the solution CV measurements (Figure 11). The size of the current observed is remarkable as the total amount of **1** in the CV experiment with **1**@SWNT is estimated to be ~1.3 µg (assuming a fill rate of 62 % of **1** in the amount of nanotube deposited on the electrode), which is 838 times less than experiments in which **1** is in solution. However this illustrates nicely the limitation of solution based CV as only the small fraction of molecules that are in the vicinity of the SWNT surface, i.e. the diffusion layer, are available to undergo the redox processes and thus detectable.

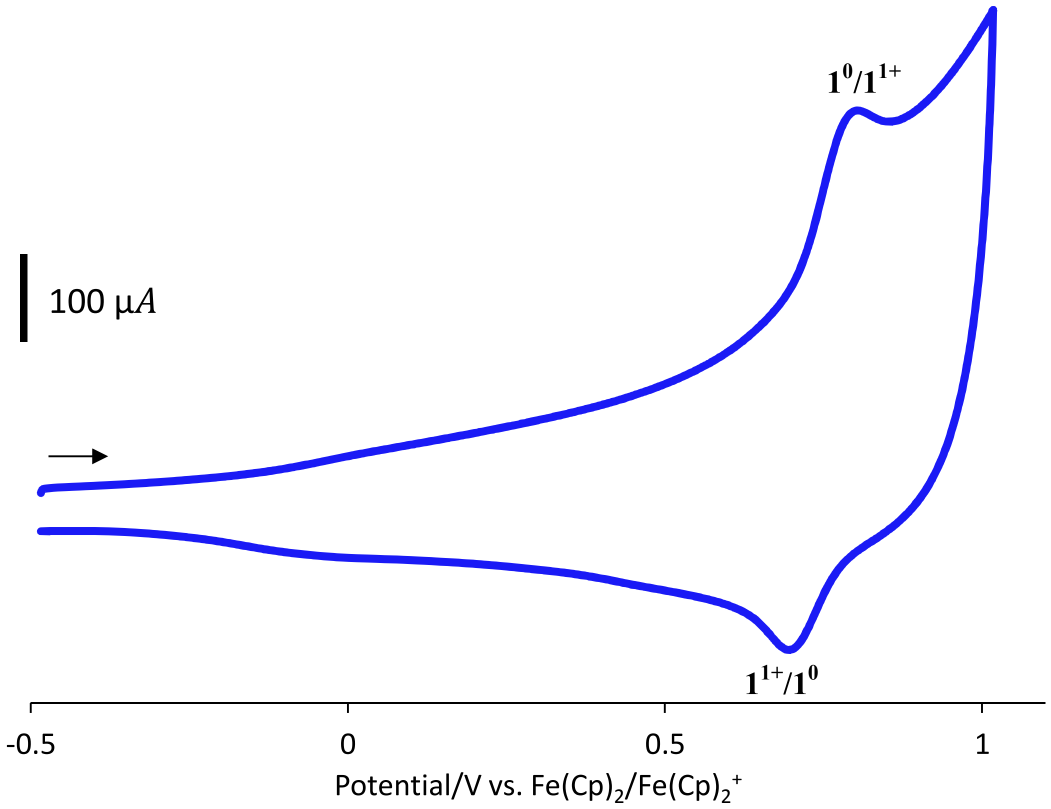

Figure 11. CV of $Cp^{Me}Mn(CO)_3$@SWNT with acetonitrile as the electrolytic solvent. Confinement of $Cp^{Me}Mn(CO)_3$ in SWNT prevents the reaction of $\mathbf{1}^{1+}$ with the acetonitrile solvent such that the reduction of $\mathbf{1}^{1+}$ is observed. Cyclic voltammetry experiments were performed in acetonitrile containing $[N^nBu_4][BF_4]$ (0.1 M) as the supporting electrolyte at 293 K and a scan rate of 100 mV s^{-1}. Arrow indicates the direction of potential sweep. The potential is held at the start potential for a period of 5 seconds before the potential sweep.

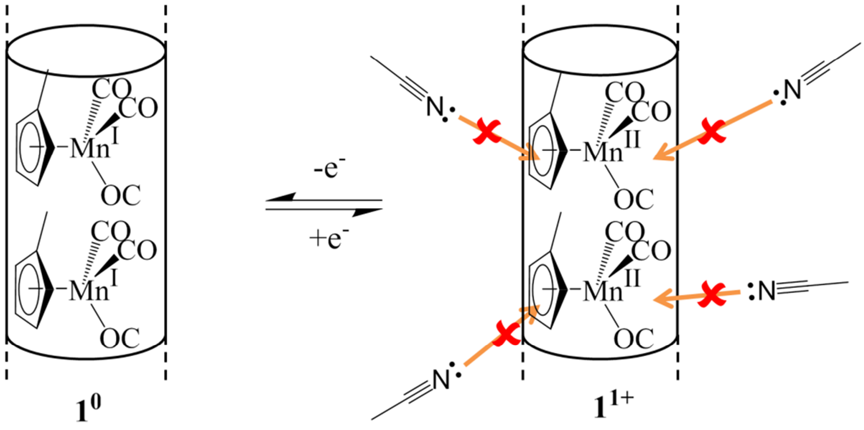

Figure 12. Schematic of the electrochemical reaction when $Cp^{Me}Mn(CO)_3$ is encapsulated in a nanotube. The complex, **1**, remains inside the nanotubes, which indicates that all of the molecules are electrically connected to the GCE throughout the potential scan *via* the carbon nanotubes. $\mathbf{1}^+$ is protected by the SWNT from nucleophilic attack by acetonitrile.

Another significant observation is that the oxidation potential (peak potential) of **1** inside nanotubes becomes more positive by +0.034 V with respect to free molecules of **1** in solution (Figure 6), when both are recorded at -40 ^{o}C.[7] The shift in oxidation potential at room temperature correlates well with the IR spectroscopy for **1**@SWNT with both indicating that the nanotube behaves as a weak electron acceptor. However, most importantly, the CV for **1**@SWNT indicates a clear redox process at $E_{1/2}$ = 0.75 V vs. $Fe(Cp)_2/Fe(Cp)_2^+$ associated with soley $\mathbf{1} \rightarrow \mathbf{1}^{1+} \rightarrow \mathbf{1}$ process which is absent for all experiments carried out with **1** in solution at room temperature.

5.3.4 Change in the pathway of the electrochemical reaction

It appears that the encapsulation of **1** in SWNT changes the pathways of the electrochemical transformations by making the previously irreversible oxidation of **1** chemically reversible (Figure 11). This is in contrast to the solution phase where immediately after oxidation, $\mathbf{1}^{1+}$ irreversibly transforms to $\mathbf{2}^{1+}$. In essence, the CV measurements for **1**@SWNT demonstrate that the nucleophilic substitution of CO for CH_3CN is hindered for the reactive intermediate $\mathbf{1}^{1+}$ due to the confinement imposed by the nanotube (Figure 12). Considerations of the basic geometry and size of the guest-molecules with respect to the nanotube channel suggest that the SWNT sidewall severely limits the mobility of the CO leaving group for most of the orientations of the complex (Figure 13).

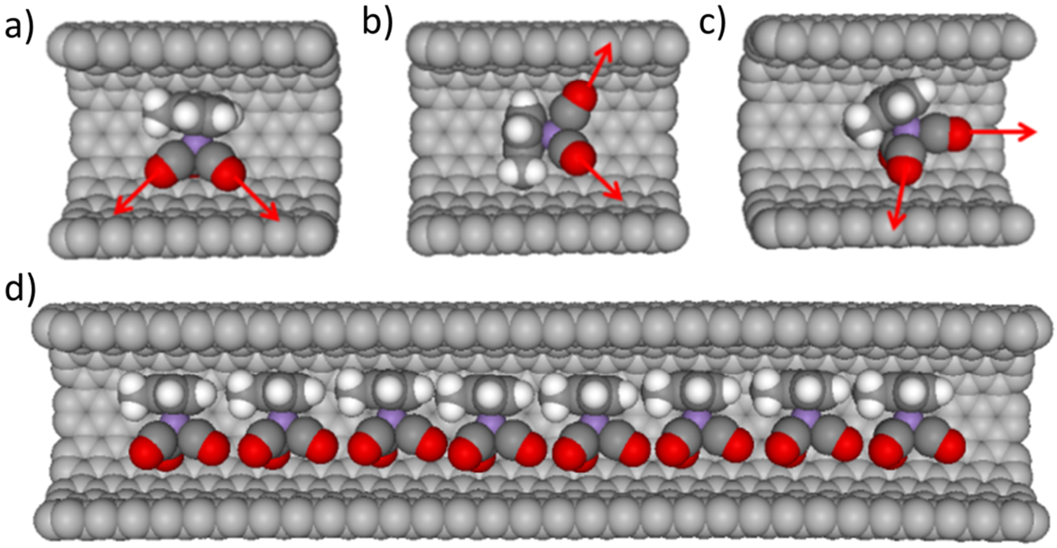

Figure 13. Molecular diagrams demonstrating that the elimination of CO cannot occur in a) and b) but only in certain orientations of the $Cp^{Me}Mn(CO)_3$ inside SWNT, such as c), due to the nanotube sidewall. If the correct orientation is achieved, there will be another adjacent $Cp^{Me}Mn(CO)_3$ molecule providing a further steric barrier to CO elimination d). i.e. Adjacent $Cp^{Me}Mn(CO)_3$ molecules and the nanotube prevent the possibility of nucleophilic substitution of CO by MeCN.

Even if dissociation of the Mn–CO bond is successful upon oxidation of **1** to $\mathbf{1}^{1+}$ and acetonitrile molecules are able to diffuse into the nanotube, the approach of a acetonitrile nucleophile to the Mn centre is hindered by the confinement imposed by the nanotube, prohibiting the transition state required for either S_N1 or S_N2 reaction mechanisms (Figure 14).[7] Overall, the severe geometrical restrictions in conjunction with a physical barrier to nucleophilic attack imposed by the nanotube preserves the reactive intermediate $\mathbf{1}^{1+}$ thus enabling a chemically reversible redox process ($\mathbf{1}^0/\mathbf{1}^+$).

Considering that carbon nanotubes themselves possess remarkable tuneable electrochemical properties,[19] which can be modified through sidewall functionalisation[20, 21] and effectively integrated with standard electrochemical devices,[22] the use of SWNT as electrochemical nanoreactors opens up new horizons for analytical and synthetic chemistry.

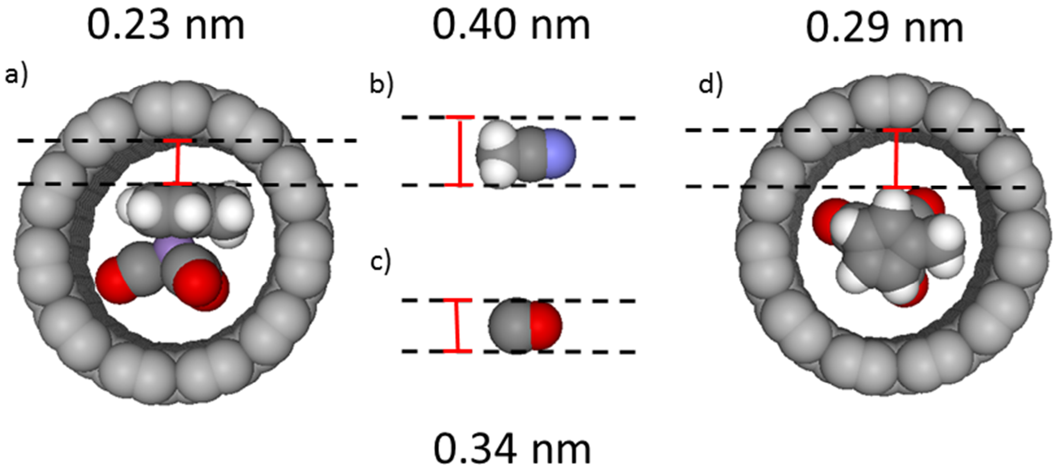

Figure 14. Molecular diagram showing the relative van der Waals radii of a) $Cp^{Me}Mn(CO)_3$@[10,10]SWNT, b) acetonitrile, c) CO and d) an alternate orientation of $Cp^{Me}Mn(CO)_3$@[10,10]SWNT. This demonstrates that the critical van der Waals size and shape of acetonitrile and CO are too large to fit between the nanotube sidewall and guest-molecules preventing diffusion of both solvent molecules (acetonitrile) into and along the nanotube and eliminated CO molecules along and out of the nanotube.

5.4 Conclusions

With their diameters at the nanoscale and nearly macroscopic lengths, carbon nanotubes are excellent structures for connecting the world of molecules with the macroscopic world. The high electric conductivity of SWNT was exploited to initiate and measure electrochemical transformations of redox active molecules. The nanotube external and internal surfaces significantly increase the active interface with redox molecules, thus improving the sensitivity of the macro-electrode. Most significantly, an electrochemical reaction pathway can be altered by restricting the reaction volume within the nanotube channel. Excitingly, this methodology can have applications in catalytic reactions whereby the oxidation state of catalysts can be instantly changed. Nanotubes offer a platform for converting specific homogeneous catalysts into heterogeneous catalysts, while using SWNT shielding to lower the probability of catalyst deactivation. This is a powerful new tool for controlling electrochemical reactivity at the nanoscale.

5.5 Experimental

5.5.1 General

Reagents and solvents were purchased from Aldrich and were used without further purification. SWNT (P2-SWNT, Carbon Solutions Inc., USA, lot# : 02-A006, carbonaceous purity: >90%) were annealed in air at 600 °C for 20 min to open the end caps and remove amorphous carbon from the internal channel prior to use. Batches of nanotubes are purchased from Carbon Solutions Inc. Each new batch is analysed using TEM whereby the diameter of nanotubes is measured over a wide range of tubes and the average diameter (quoted diameter in this thesis) and standard deviation are determined. The method of TEM preparation involves the sonication of a substantial amount of nanotubes which is further diluted meaning the nanotubes that appear in TEM are representative of the whole batch. There is a range of different chiral indices present in the nanotube sample which have been analysed by Pekker *et al.*[23] These are not from the same batch that were used but are from the same company and preparation method. They determine that the ratio of metallic nanotubes to semiconducting nanotubes is 31:69 respectively. Further details of nanotube synthesis and oxidation method are provided in the experimental.

5.5.2 Preparation of $Cp^{Me}Mn(CO)_3$@SWNT

Under an atmosphere of argon, freshly annealed SWNT were dropped onto stirring $Cp^{Me}Mn(CO)_3$. The mixture was extensively sonicated then left to stir for 3 h. The excess $Cp^{Me}Mn(CO)_3$ was removed by filtration on a PTFE membrane (pore size = 0.2 μm). Any remaining external $Cp^{Me}Mn(CO)_3$ was removed under a flow of nitrogen (24 hr). The product was analysed using TEM, EDX and electrochemistry.

5.5.3 Electrochemistry

Electrodes were purchased from IJCambria and Metrohm. Electrochemistry experiments were performed on an Autolab PGSTAT302N potentiostat. The nanotube sample (0.5 mg) was sonicated (15 mins) in dry DMF (0.5 mL) to form an ink. 10 μL of the ink was drop cast onto the GCE using a micro-pipette and allowed to dry in air for 1 h. The electrode was then rinsed in dry acetonitrile and allowed to dry in air. All CV experiments start with the application of the starting potential for 5 seconds. For the electrochemistry at -40 ^{o}C the cell was dipped in an acetonitrile/dry ice mixture.

5.5.4 Infrared spectroscopy

Infrared spectroscopy was performed on a Bruker Tensor 27 spectrometer with 64 scans over a range of 1800 – 2100 cm^{-1} with 1 cm^{-1} resolution using a sample pressed into a KBr pellet. KBr pellets were prepared using 0.1 mg of $Cp^{Me}Mn(CO)_3$@SWNT sample or $Cp^{Me}Mn(CO)_3$ and 300 mg of KBr. The press was evacuated on a vacuum line then pressed at 10 tonnes for 10 min.

5.5.5 HRTEM

HRTEM analysis was performed on a JEOL JEM-2100F FEG electron microscope with an information limit of 0.12 nm at 100 kV. The imaging conditions were carefully tuned by lowering the accelerating voltage of the microscope to 100 kV and reducing the beam current density to a minimum. Suspensions of $Cp^{Me}Mn(CO)_3$ in HPLC grade isopropanol were dropped onto lacey carbon grids for TEM analysis.

5.5.6 EDX

Local EDX spectra were acquired for samples mounted on TEM grids using an Oxford Instruments INCA X-ray microanalysis system. The electron beam was condensed onto areas of specimens (bulk specimen or nanotube bundles) suspended over holes of the amorphous carbon film.

5.6 References

1. N. Sun, L. Guan, Z. Shi, N. Li, Z. Gu, Z. Zhu, M. Li and Y. Shao, *Anal. Chem.*, 2006, **78**, 6050.
2. H. M. Cheng, H. X. Qiu, Z. W. Zhu, M. X. Li and Z. J. Shi, *Electrochim. Acta*, 2012, **63**, 83.
3. K. Yanagi, R. Moriya, N. T. Cuong, M. Otani and S. Okada, *Phys. Rev. Lett.*, 2013, **110**, 086801.
4. L. Kavan, L. Dunsch and H. Kataura, *Carbon*, 2004, **42**, 1011.
5. B. S. Creaven, A. J. Dixon, J. M. Kelly, C. Long and M. Poliakoff, *Organometallics*, 1987, **6**, 2600.
6. J. W. Hershberger, R. J. Klingler and J. K. Kochi, *J. Am. Chem. Soc.*, 1982, **104**, 3034.
7. J. W. Hershberger, R. J. Klingler and J. K. Kochi, *J. Am. Chem. Soc.*, 1983, **105**, 61.
8. J. W. Hershberger, C. Amatore and J. K. Kochi, *J. Organomet. Chem.*, 1983, **250**, 345.
9. J. W. Hershberger and J. K. Kochi, *J. Chem. Soc. Chem. Comm.*, 1982, 212.

10. J. W. Kee, Y. Y. Tan, B. H. G. Swennenhuis, A. A. Bengali and W. Y. Fan, *Organometallics*, 2011, **30**, 2154.
11. T. W. Chamberlain, T. Zoberbier, J. Biskupek, A. Botos, U. Kaiser and A. N. Khlobystov, *Chem. Sci.*, 2012, **3**, 1919.
12. L. J. Li, A. N. Khlobystov, J. G. Wiltshire, G. A. Briggs and R. J. Nicholas, *Nat. Mater.*, 2005, **4**, 481.
13. D. E. Luzzi, B. W. Smith, R. Russo, B. C. Satishkumar, F. Stercel and N. Nemes, *15th International Winter School on Electronic Properties on Novel Materials*, 2001, **591**, 622.
14. H. Shiozawa, C. E. Giusca, S. R. P. Silva, H. Kataura and T. Pichler, *Phys. Status Solidi B*, 2008, **245**, 1983.
15. M. Sauer, H. Shiozawa, P. Ayala, G. Ruiz-Soria, X. J. Liu, A. Chernov, S. Krause, K. Yanagi, H. Kataura and T. Pichler, *Carbon*, 2013, **59**, 237.
16. H. Shiozawa, T. Pichler, R. Pfeiffer, H. Kuzmany and H. Kataura, *Phys. Status Solidi B*, 2007, **244**, 4102.
17. D. V. Kazachkin, Y. Nishimura, H. A. Witek, S. Irle and E. Borguet, *J. Am. Chem. Soc.*, 2011, **133**, 8191.
18. T. W. Chamberlain, J. Biskupek, S. T. Skowron, P. A. Bayliss, E. Bichoutskaia, U. Kaiser and A. N. Khlobystov, *Small*, 2015, **11**, 622.
19. S. A. Hodge, S. Fogden, C. A. Howard, N. T. Skipper and M. S. P. Shaffer, *Acs Nano*, 2013, **7**, 1769.
20. D. Tasis, N. Tagmatarchis, A. Bianco and M. Prato, *Chem. Rev.*, 2006, **106**, 1105.
21. E. L. S. Wong and R. G. Compton, *J. Phys. Chem. C*, 2008, **112**, 8122.
22. R. T. Kachoosangi, M. M. Musameh, I. Abu-Yousef, J. M. Yousef, S. M. Kanan, L. Xiao, S. G. Davies, A. Russell and R. G. Compton, *Anal. Chem.*, 2009, **81**, 435.
23. A. Pekker and K. Kamaras, *Phys. Rev. B.*, 2011, **84**, 075475.

6 Nanotubes as templates for electrochemical synthesis

6.1 Introduction

6.1.1 The effect of potential on reactions in solution compared to anchored molecules

One of the key challenges of chemistry is to control the reactivity of molecules in order to achieve the desired products of a reaction. Discrimination of the production of one type of molecule over another by careful design of reaction conditions is at the forefront of modern synthetic chemistry because organic chemists invest a lot of effort to improve or modify the selectivity of different preparative reactions. A powerful alternative methodology exploits the concept of nanocontainers, systems which confine molecular guest-species at the single-molecule level, thus limiting their degrees of freedom, in which the reactants can be favourably pre-arranged for the formation of a specific product (activation entropy ($\Delta S^{\#}$) becomes less negative). The activation barrier of the desired reaction is lowered (activation enthalpy ($\Delta H^{\#}$) becomes less positive) by non-covalent interactions between the reactant molecules and nanocontainers (Figure 1).

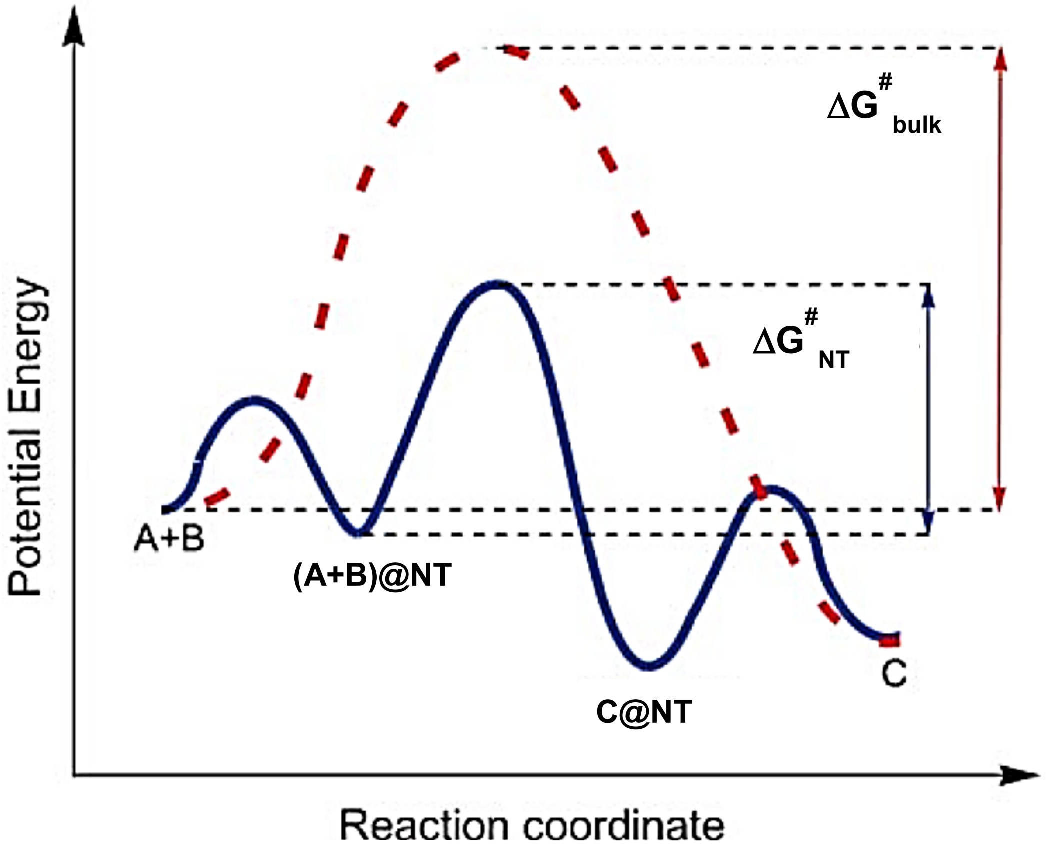

Figure 1. The red dashed line is the Gibbs energy of activation (ΔG$^{\#}$) for reactions in bulk solution and the blue line is the ΔG$^{\#}$ for reactions inside a nanotube. ΔG$^{\#}$ is smaller for a reaction inside a nanotube due to the pre-arrangement of the reactants for the formation the desired product.[1]

If the reaction is confined to the narrow channel of a nanotube, then it is possible to force the formation of a certain isomer.[2-4] For example, when the bromination of N-phenylacetamide is performed inside a SWNT, the para-product is forced over the ortho-product showing improved selectivity for reactions inside SWNT (Figure 2).[3]

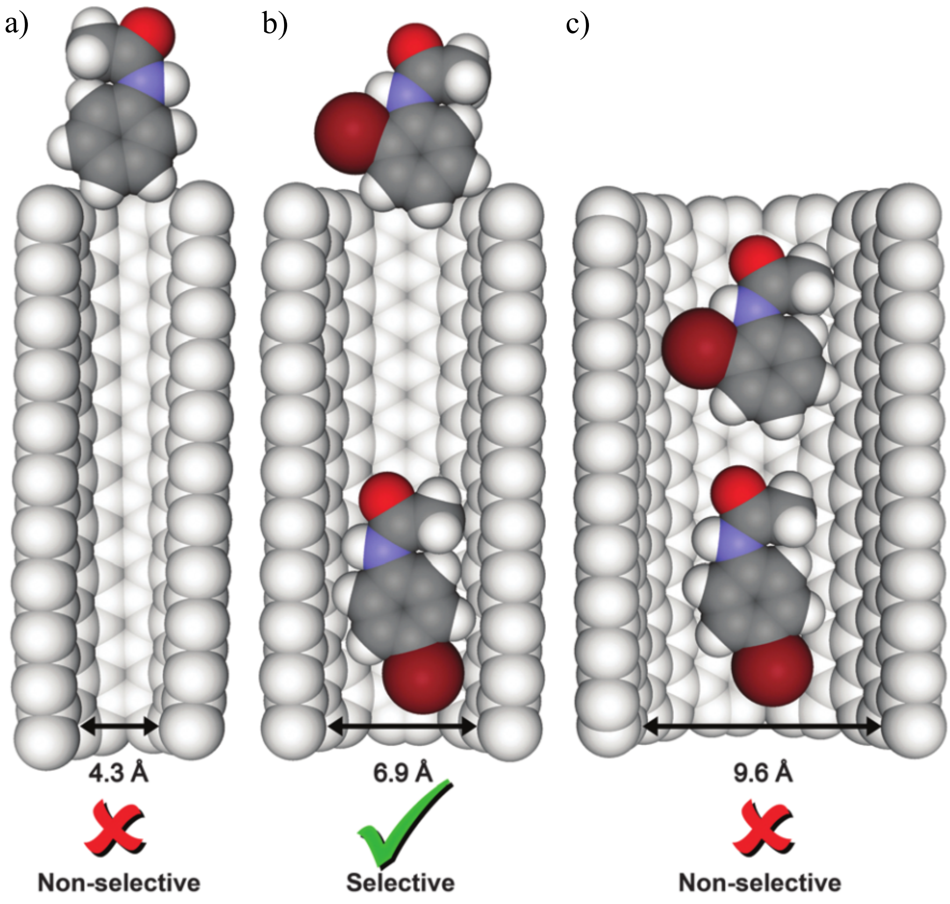

Figure 2. Comparison of the van der Waals diameter of the internal cavity (d_{NT}) of three types of nanotubes to the critical van der Waals diameter ($d_{critical}$) of reactant and product molecules. a) CoMoCAT SWNT (d_{NT} = 4.3 Å), too narrow to allow confinement of the reactant ($d_{critical}$ = 6.9 Å); b) HiPCO SWNT(d_{NT} = 6.9 Å), allowing the formation of para- but not ortho-product and c) wider arc discharge SWNT (d_{NT} = 9.6 Å) freely allowing the formation of both products.[3]

Carbon nanotubes specifically, have been shown to promote a linear C_{60} polymer product, a product that cannot be formed otherwise, inhibiting the branched polymer which is usually formed without confinement.[2] The powerful templating effect of the nanotube can be used to a further extent to direct the complete breakdown and rearrangement of guest-molecules as shown with the formation of a sulphur-terminated graphene nanoribbon (S-GNR) encapsulated in SWNT (S-GNR@SWNT).[5, 6]

6.1.2 The role of carbon nanotubes as templates

Nanotubes have been used as templates for a number of different reactions such as the formation of fullerene polymers[2, 7] or the growth of interior carbon nanotubes inside SWNT, creating DWNT.[8, 9] A recent example of nanotubes acting as a template and changing the products of a reaction, is the formation of sulfur terminated graphitised nanoribbons@SWNT.[5, 10] Graphene possesses unique physical and electrical properties. However, the lack of an electronic bandgap has hindered application in electronic devices. Carving graphene into strips, called nanoribbons, allows the opening of a gap between the conduction and valence bands of graphene, with the nanoribbon width inversely proportional to the introduced bandgap.[11-13] There are a number of methods for the formation of S-GNR,[14-18] however, these are complex, non-scalable and often produce S-GNR without a defined structure. Thermal energy (> 1000 ^{o}C) or kinetic energy of an electron beam causes sulfur-containing organic molecules to break into highly reactive fragments and atoms inside SWNT which then react to form a thermodynamically stable S-GNR within the nanotube cavity.[5, 10] For example, the nanotube restrains the reactant molecules of either sulfur containing functionalised fullerenes or tetrathiofulvalene (TTF) and reactive intermediates are formed, favouring growth of nanoribbons (Figure 3).

By changing the diameter of the host-nanotube it is possible to tune the width of the nanoribbon, formed from TTF in each case, and therefore alter the band gap of the nanoribbon making them attractive materials for electronics. Whilst this technique allows for the facile formation of S-GNR with tuneable band gaps, it requires very harsh conditions (heating > 1000 ^{o}C or e-beam irradiation) and is difficult to scale up to a preparative scale. The mechanism of S-GNR growth under these conditions is also not fully understood due to the high energies involved in breaking bonds indiscriminately in the reactant TTF. A new method is presented here using electrical potential, allowing for production of nanoribbons on a larger scale that is more sustainable as well as elucidating the possible mechanism for the formation of S-GNR. Development of the electrochemical formation of S-GNR@SWNT will build on a number of other examples of nanotubes used as containers for reactions presented in this chapter that use electrochemical potential to transform molecules inside nanotubes namely C_{60} containing molecules@SWNT due to the detailed understanding of the interactions of C_{60} with SWNT.

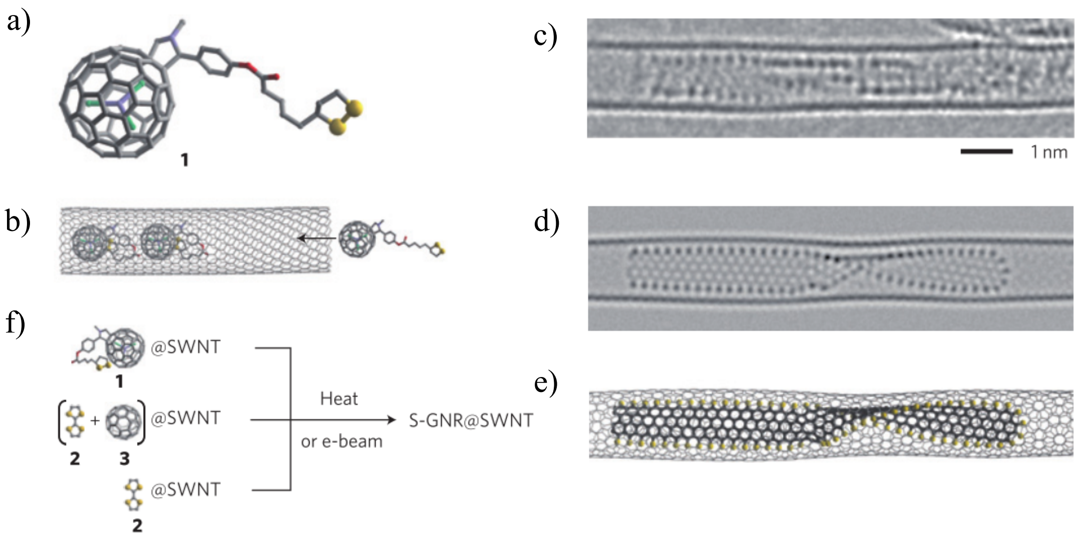

Figure 3. Functionalised fullerenes a) containing sulfur are filled into SWNT b) and, under prolonged exposure to the electron beam, the molecule decomposes and rearranges to form a sulfur terminated graphitised nanoribbon c). Other sulfur containing molecules can also form S-GNR f) at high temperatures or under the electron beam. e) shows a model of S-GNR@SWNT and d) an image simulated from the model.[5]

6.2 Aim and objectives

Among nanoreactors, carbon nanotubes are unique as they are chemically and thermally stable whilst also highly electrically conducting. The aim is to investigate the use of nanotubes as both templates and means to transfer electrons to encapsulated guest-molecules to perform electrochemically activated/driven reactions.

The objectives to achieve this aim involve initially recording the CV of starting materials inside SWNT to verify an efficient electrical contact between the encapsulated molecules and the macro-electrode mediated by the nanotube. The applied potential will then be used to trigger electrochemical reactions within the nanotube which will manifest as changes in the observed CV over time after repeated application of potential. Correlation between observed changes in CV and structural data obtained from HRTEM images of the encapsulated products will then be utilised to elucidate the reaction mechanism by which transformations of molecules in nanotubes occurs.

6.3 Results and discussion

6.3.1 Cyclic voltammetry of C_{60}@SWNT

Unlike metallocenes used in chapter 3 and 4, C_{60} is irreversibly trapped inside the single-walled nanotube channel due to the strong van der Waals interactions with the internal walls of the nanotube.[19] This makes C_{60} the ideal species to anchor desired groups, such as metal-containing complexes in SWNT.[20] Initially, unmodified C_{60} was encapsulated in SWNT, C_{60}@SWNT was attached to a glassy carbon electrode and the CV measurements were performed revealing two redox processes at -1.14 V (C_{60}^{1-}/C_{60}^{0}) and -1.33 V (C_{60}^{2-}/C_{60}^{1-}). A high negative current was observed at more negative potentials with no discernible redox processes. The $E_{1/2}$ of the C_{60}^{1-}/C_{60}^{0} and C_{60}^{2-}/C_{60}^{1-} redox processes shift by -0.14 V and -0.13 V compared to the solution CV for the first and second redox processes of C_{60} respectively (Figure 4). These changes in redox behaviour suggest C_{60} is harder to reduce in the nanotube and this is attributed to strong van de Waals interactions between C_{60} and the nanotube and slower kinetics. This destabilises the fulleride anions as well as the SWNT that is shielding the fulleride anion from the solvent which helps stabilise the negative charge of the C_{60} cage (see Chapter 2). The ability to observe signals for C_{60} redox processes allows the use of C_{60} as both an anchor and electrochemical marker for other guest-molecules tethered to the fullerene cage.

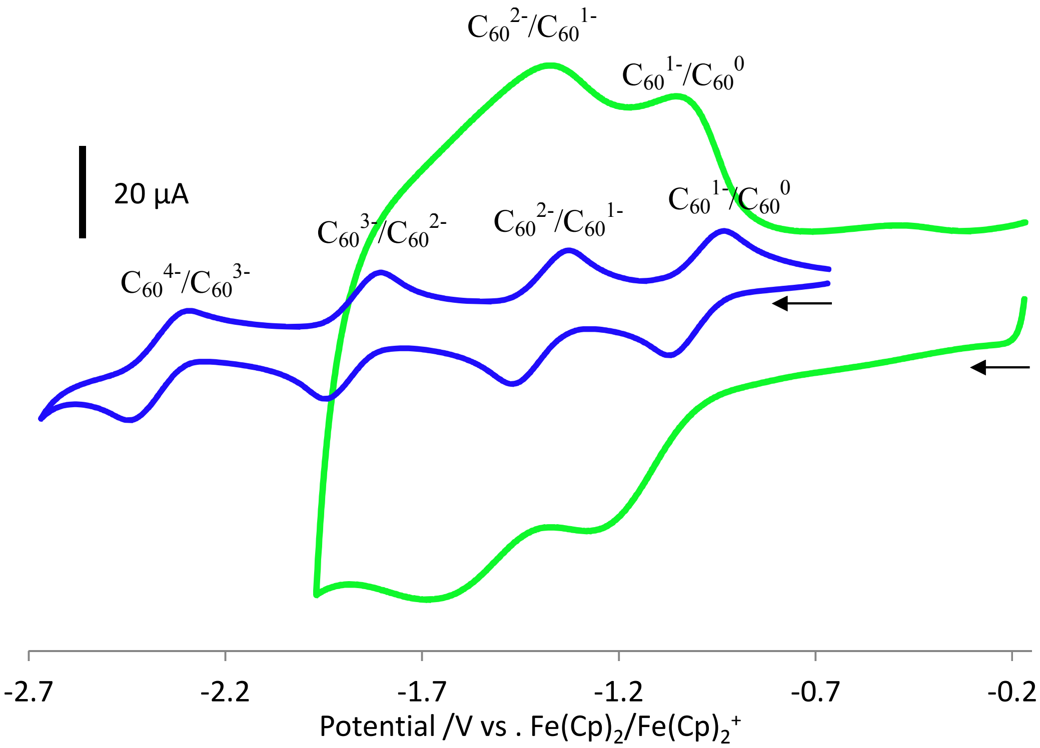

Figure 4. CV of C_{60}/GCE (blue) in the range of -0.7 V and -2.7 V and C_{60}@SWNT (green) in the range of 0.2 V and -2 V. Experiments were performed in oDCB containing $[N^nBu_4][BF_4]$ (0.5 M) as the supporting electrolyte at 293 K and at a scan rate of 0.1 Vs^{-1}. Arrow indicates direction of potential sweep. Reduction processes of C_{60}@SWNT occur at -1.142 V and -1.528 V. Reduction processes of C_{60} in solution occur at -1.00 V, -1.40 V and -1.88 V. There is a shift in the negative direction by -0.14 V and -0.13 V for C_{60}@SWNT compared to C_{60}/GCE. At increased negative potential a large negative current is observed with no further redox processes for C_{60}@SWNT.

6.3.2 Cyclic voltammetry of C_{60}dimer@SWNT

The CV of C_{60}dimers in solution have been previously reported by Lebedeva *et al* (Figure 5).[20] The CV is very similar to those of their monomeric precursors and does not appear to show interaction between the individual C_{60} cages within the dimer molecule during redox processes. This was attributed to a lack of an effective electronic communication pathway through the oxalate linker group.[21]

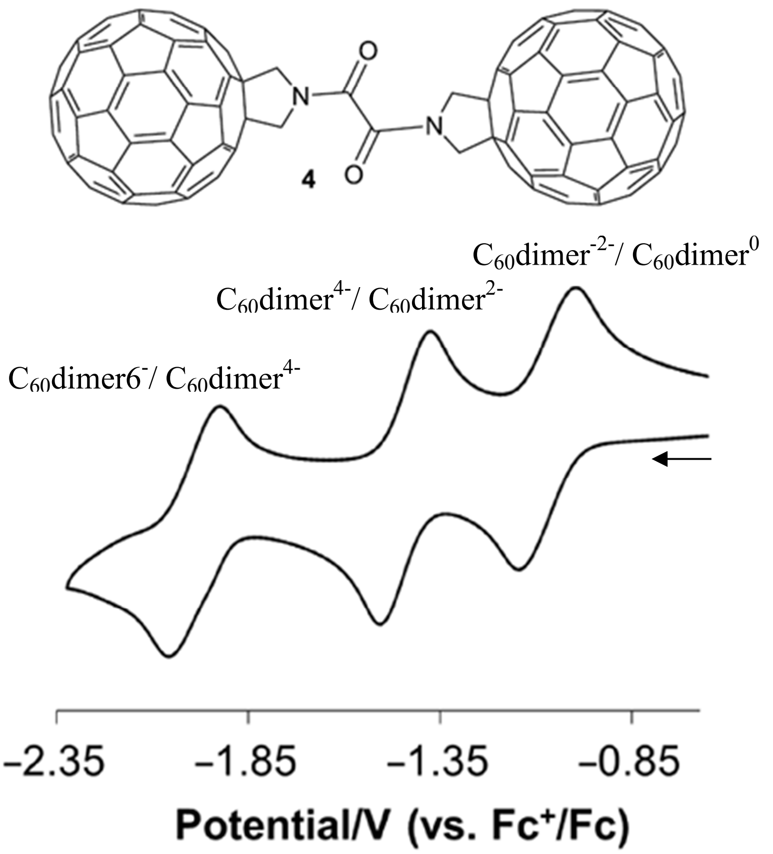

Figure 5. CV and structure of C$_{60}$dimer in solution in the range of -0.8 V and -2.35 V as reported by Lebedeva *et al.*[21] CV recorded in oDCB containing [N^{n}Bu$_4$][BF$_4$] (0.5 M) as the supporting electrolyte at 293 K and at a scan rate of 0.1 Vs^{-1}. The redox processes appear at -1.09 V, -1.47 V and -2.01 V.[21]

Upon encapsulation in SWNT the HRTEM images show pairs of C$_{60}$ molecules throughout the sample with a high fill rate (estimated to be 70-90%) (Figure 6). The first CV potential sweep of C$_{60}$dimer@SWNT (Figure 7) shows two obvious, though weak, redox processes at -1.03 V (C$_{60}$dimer^{2-}/C$_{60}$dimer^{0}) and -1.43 V (C$_{60}$dimer^{4-}/C$_{60}$dimer^{2-}), similar to the first two reductions observed for the dimer molecule in the solution CV (Figure 5). However, there are shoulders present on the reduction at -1.43 V, and the signal changes with further sweeps of potential (Figure 8). Following a potential sweep to -2.24 V at a scan rate of 0.1 Vs^{-1}, a third redox process is observed at -1.92 V (C_{60}dimer^{6-}/C_{60}dimer^{4-}), again at a similar potential to the third redox process of the dimer in solution (Figure 9). After multiple potential sweeps between -1.8 V and -0.6 V at a scan rate of 0.1 Vs^{-1} (~10 scans) the current of the dimer redox waves starts to diminish, and only weak redox waves akin to C_{60}@SWNT remain in the CV (Figure 4, Figure 10 and Figure 11).

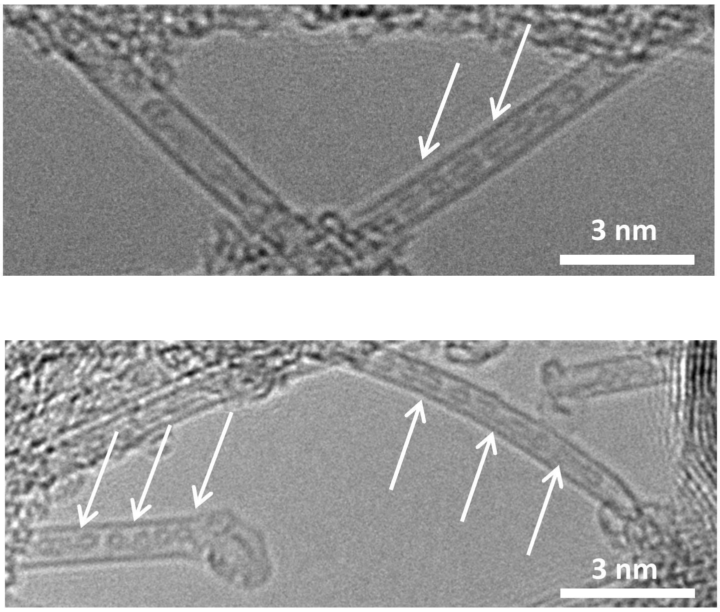

Figure 6. HRTEM micrographs of C_{60}dimer@SWNT showing pairs of C_{60} molecules (white arrows).

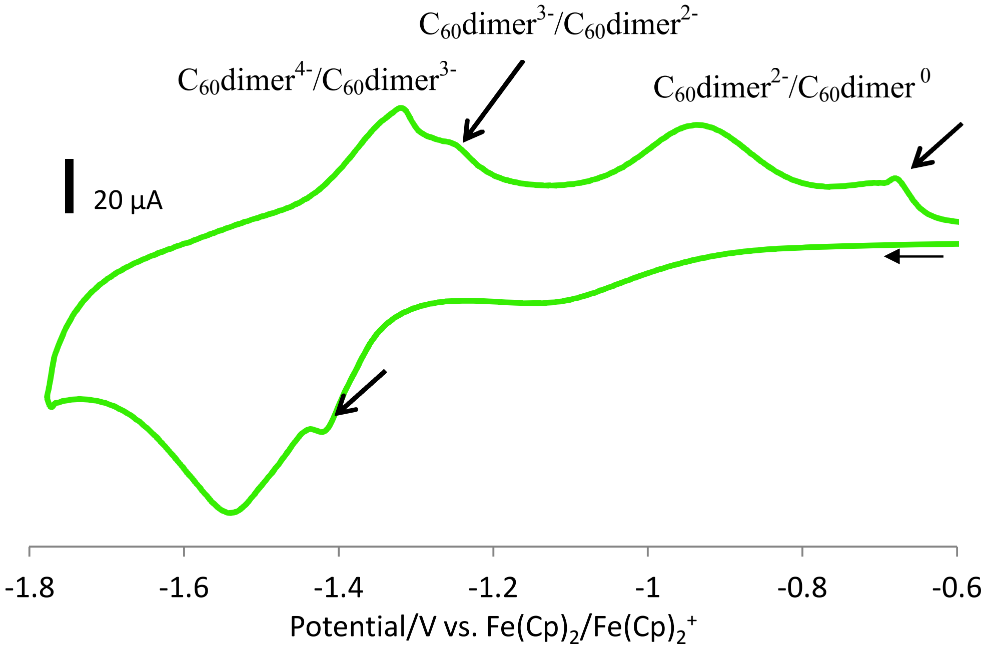

Figure 7. The first CV potential sweep of C_{60}dimer@SWNT in the range of -0.6 V and -1.8 V. Experiments were performed in MeCN containing $[N^nBu_4][BF_4]$ (0.1 M) as the supporting electrolyte at 293 K and at a scan rate of 0.1 Vs^{-1}. There is a shift in the positive direction for C_{60}dimer@SWNT compared to C_{60}dimer/GCE. Reduction processes occur at -1.03 V, -1.43 V, the shoulders appear at -1.25 V and -0.70 V for the oxidations and -1.41 for the reduction (black arrows).

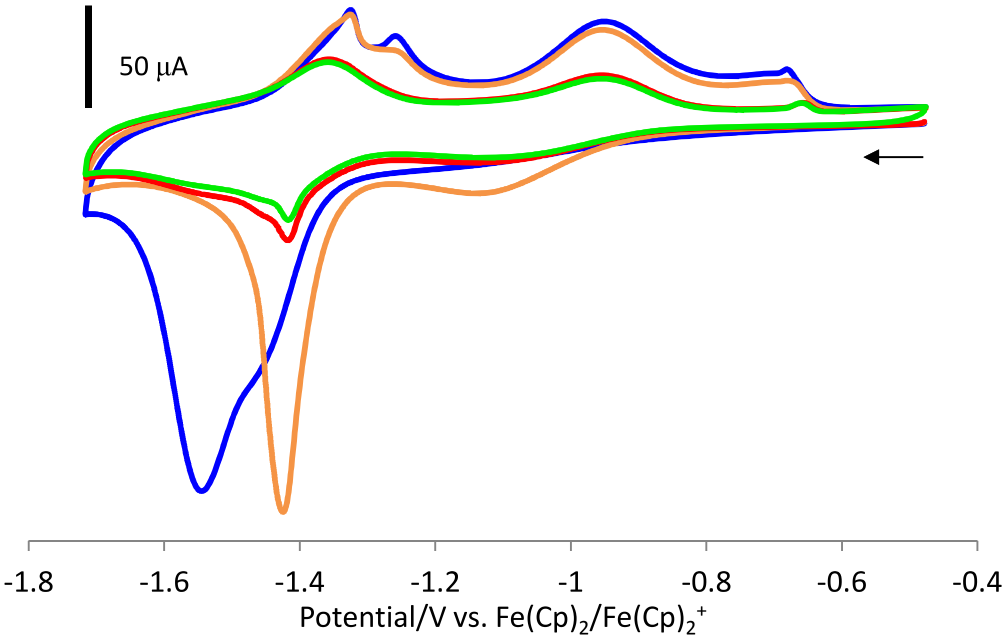

Figure 8. A series of CV of C_{60}dimer@SWNT in the range of -0.5 V and -1.8 V. Experiments were performed in MeCN containing $[N^nBu_4][BF_4]$ (0.1 M) as the supporting electrolyte at 293 K and at a scan rate of 0.1 Vs^{-1}. Arrow indicates direction of potential sweep. The 1st potential sweep is blue and 2nd orange. This was followed by 4 potential sweeps, at varying scan rate. The red plot is of the 7th potential sweep and the green the 8th.

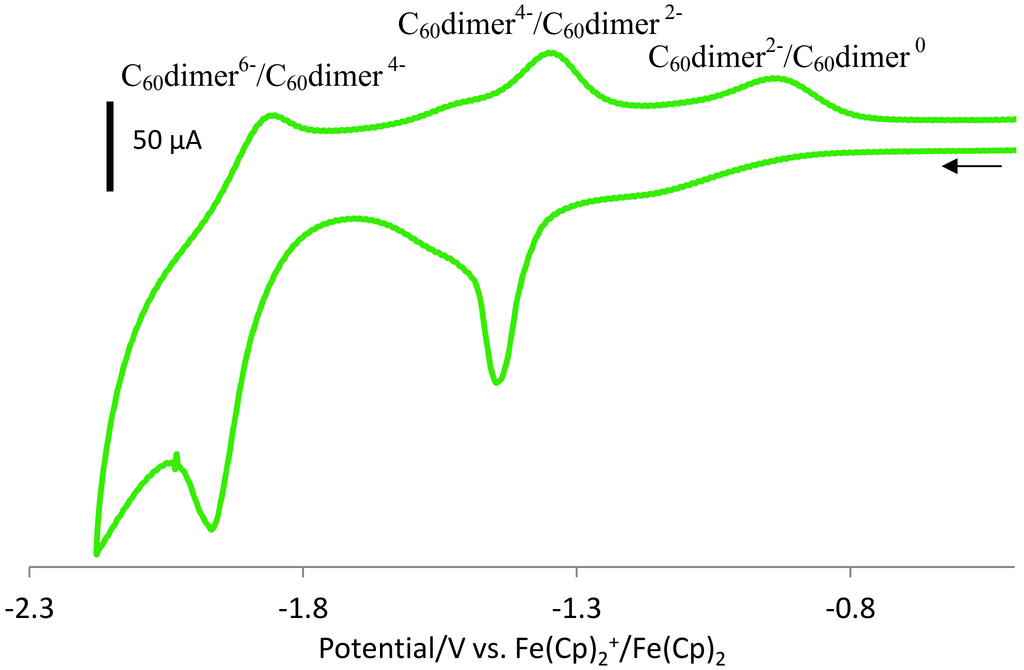

Figure 9. CV of C_{60}dimer@SWNT following a potential sweep between -2.2 V and -0.6 V in the range of -2.2 V and -0.5 V in MeCN containing $[N^nBu_4][BF_4]$ (0.1 M) as the supporting electrolyte at 293 K and at a scan rate of 0.1 Vs^{-1}. Arrow indicates direction of potential sweep. Increased current is observed for the redox processes of C_{60}dimer at -1.40 V and -1.93 V.

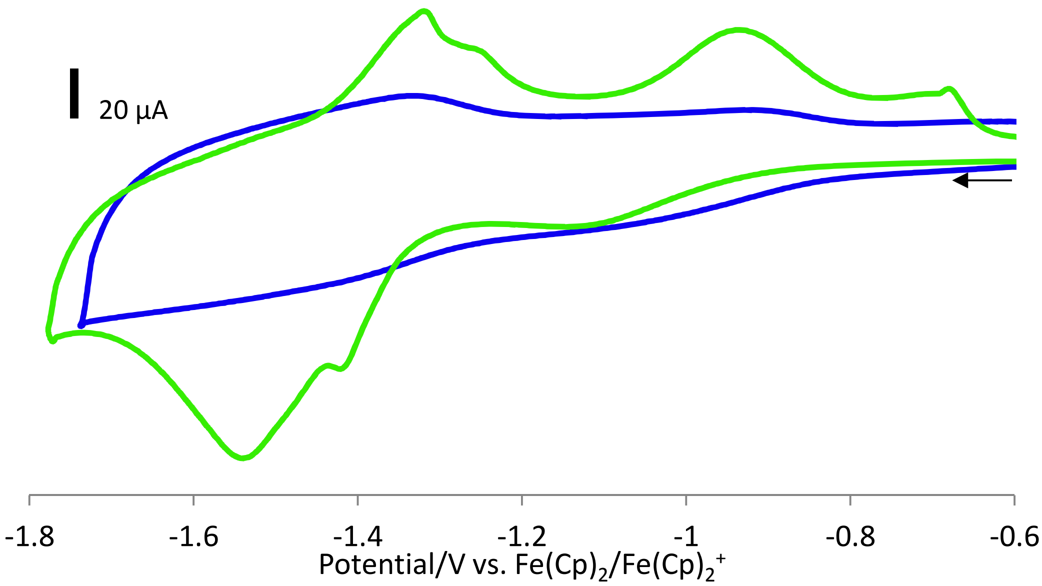

Figure 10. CV of C_{60}dimer@SWNT before (green) and after (blue) in the range of -0.6 V and -1.8 V following a potential sweep to -2.2 V in MeCN containing $[N^nBu_4][BF_4]$ (0.1 M) as the supporting electrolyte at 293 K and at a scan rate of 0.1 Vs^{-1}. Arrow indicates direction of potential sweep. The redox processes after 30 potential sweeps between -1.8 V and -0.6 V) occur at -0.99 V and -1.38 V. See labelled waves in Figure 11 and Figure 7)

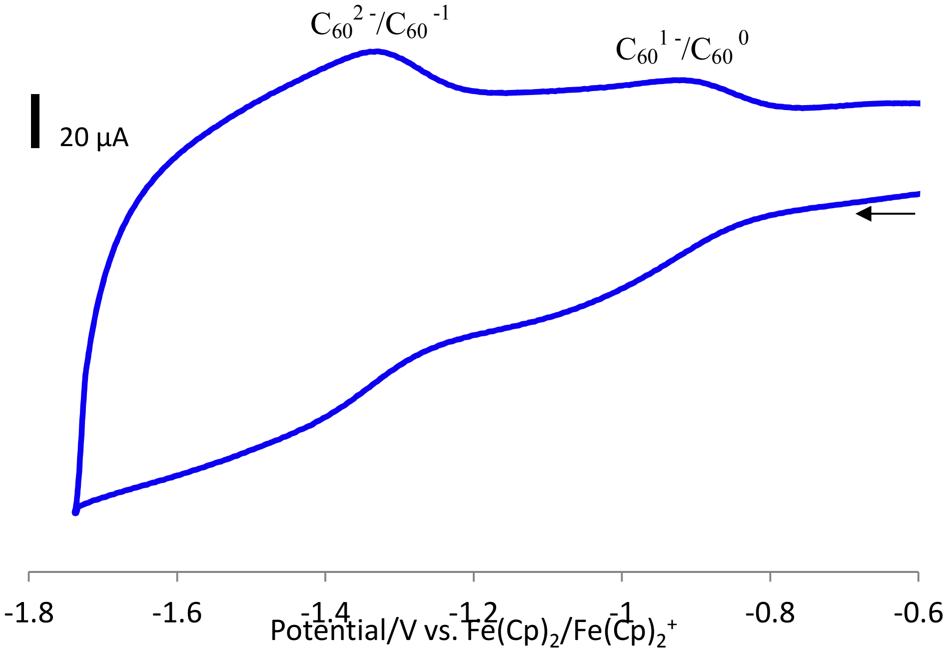

Figure 11. CV of C_{60}dimer@SWNT after ~30 potential sweeps between -1.75 V and -0.6 V and following a potential sweep between -2.2 V and -0.6 V in MeCN containing $[N^nBu_4][BF_4]$ (0.1 M) as the supporting electrolyte at 293 K and at a scan rate of 0.1 Vs^{-1}. The redox processes occur at -0.99 V and -1.38 V.

Redox waves are less prevalent in the CV of guest@SWNT so sometimes it is more appropriate to talk about separate reduction and oxidation processes. The presence of shoulders at -0.70 V, -1.25 V and -1.4 V (Figure 7, black arrows) is attributed to a new phenomenon occurring to the dimer in nanotubes. In solution, the two fullerene cages of C_{60}dimer are insulated by a non-conducting oxalate bridge, so no electrochemical communication takes place between the two C_{60} moieties.[21] In contrast, it is postulated than when the dimer is encapsulated in a SWNT, the nanotube provides a highly conductive bridge between the two tethered C_{60} moieties. As a result, one of the two C_{60} moieties will be reduced first and this reduced C_{60} moiety will interact with the second C_{60} moiety through coupling with the mobile electrons of SWNT so that the electron is effectively delocalised between the fullerene moieties. This makes the reduction potential of the second fullerene moiety more negative, i.e. the addition of a second electron to the molecule is more difficult, as both fullerene cages in the C_{60}dimer are already negatively charged after the first reduction, this differs from the free C_{60}dimer in the solution CV where the charge is localised on the individual C_{60} cages so that they both reduce independently at the same potential (Figure 12). This same effect is not observed for the first reduction of the C_{60}dimer due to the lack of nanotube electronic states of the nanotube at that energy, so there is not a pathway for an electron to be delocalised on the nanotube. In contrast, the second reduction is at a sufficient energy to allow delocalisation in the conduction band of the nanotube.

Encapsulation in SWNT appears to make electrochemical redox processes of the linked fullerene cages non-independent of one another due to their interactions through the nanotube, which is in contrast to the same redox process in solution. To the best of our knowledge this is the first experimental evidence of such an interaction and further work should be performed to confirm this interaction. SWNT-mediated electronic communication may be exploited in charge transfer mediators in solar cells, and it has been proposed to play an important role in quantum information processing schemes in nanotubes.[22, 23]

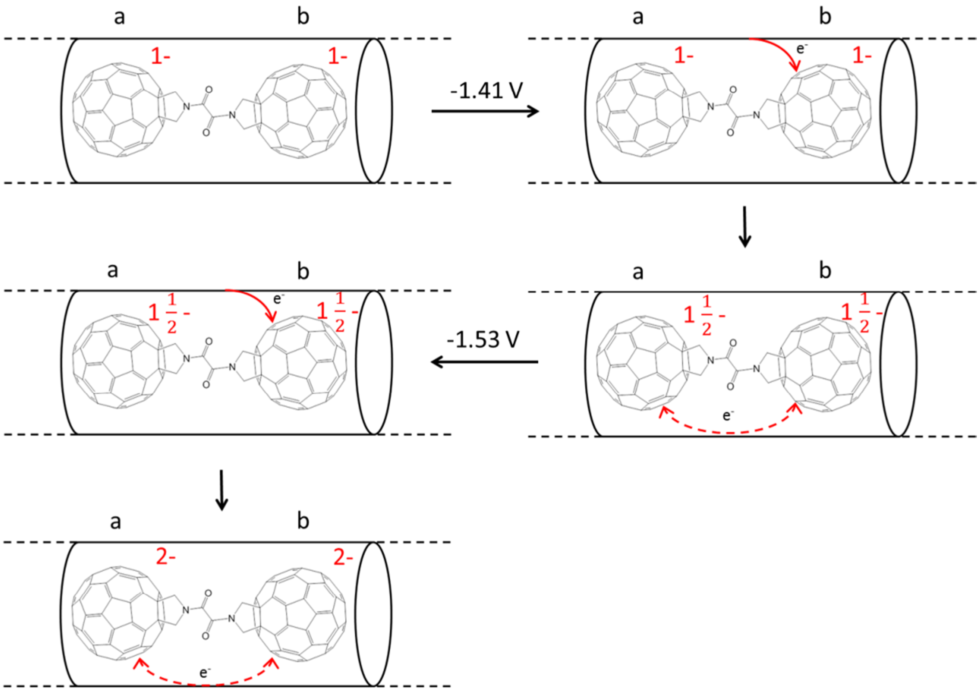

Figure 12. Schematic representation of the second reduction process of C_{60}dimer (each C_{60} moiety is labelled a or b). C_{60} moiety b is reduced (electron transfer marked by solid red arrow) and, unlike in solution, the electron is delocalised over both C_{60} moieties (a and b) through the highly conducting nanotube sidewalls (red dashed arrows). The second reduction is of an already negatively charged species so a more negative potential is required hence the splitting of the reduction wave into two.

Following a potential sweep between -2.2 V and -0.6 V at a scan rate of 0.1 Vs^{-1}, an increased current for redox processes at –1.40 V and -1.93 V were observed (Figure 9) for C_{60}dimer@SWNT compared to the CV of C_{60}dimer in solution. Further potential sweeps between -1.7 V and -0.6 V (~30 sweeps) at a scan rate of 0.1 Vs^{-1} result in the disappearance of the shoulders and high current peaks (Figure 11), and the emergence of the redox processes characteristic of C_{60} (Figure 10).

The disappearance of the C_{60}dimer redox processes after repetitive sweeps of potential between -1.8 V and -0.6 V at a scan rate of 0.1 Vs^{-1} (Figure 8) was attributed to the decomposition of the dimer oxamide linker under the electrochemical conditions.

The reduction of oxamide is known to follow an ECE type mechanism[24, 25] (where a chemical step separates two electrochemical steps[26]). While not observed in the solution electrochemistry of the C_{60}dimer, the C_{60}dimer@SWNT is now constrained next to the nanotube which could result in oxamide linker reduction being forced due to the proximity with the highly negatively charged nanotube and fullerene during the repeated potential sweeps between -2.2 V and -0.5 V. There is also increased strain on the linker due to rotation of the C_{60} moieties in the 3+ state (see section 6.4.3.2 and Figure 19). The two electron reduction of oxamide results in the cleavage of one of the C-N bonds and the loss of ammonia (Figure 13). The same reaction on the C_{60}dimer will result in the cleavage of one of the C-N bonds attached to the fulleropyrrolidine, in the absence of hydrogen, an ethenone type structure is possibly formed. This breaks the bridge between the two fullerene moieties making them act as discrete molecules rather than a dimer (Figure 14), hence, after 30 potential sweeps, the observed redox processes becomes similar to C_{60}@SWNT (Figure 11).

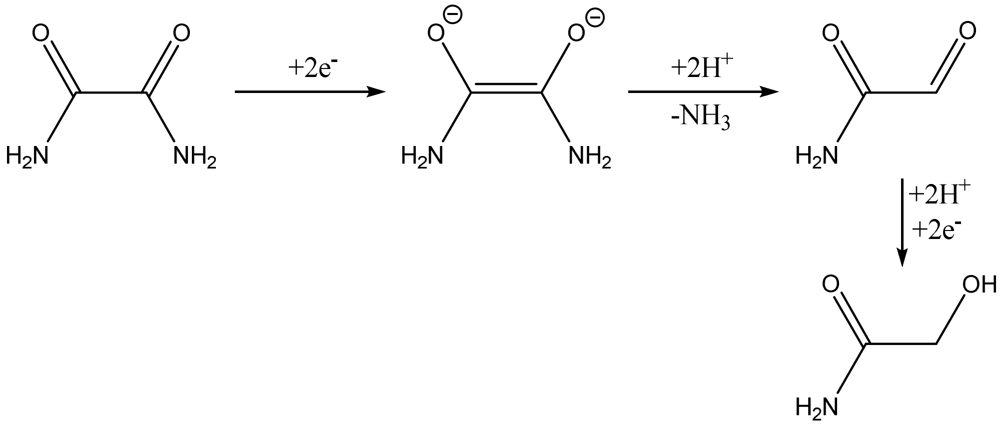

Figure 13. The two electron reduction of oxamide resulting in the loss of ammonia.[24]

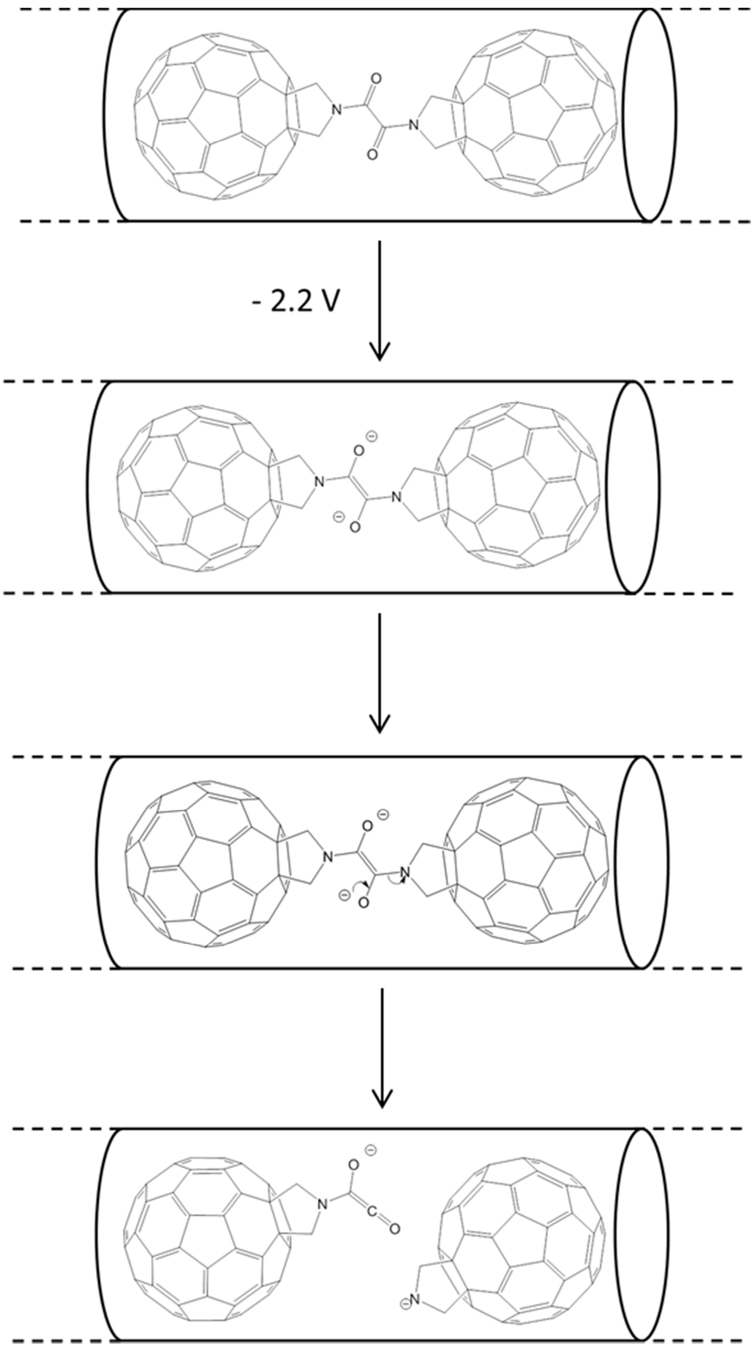

Figure 14. Possible mechanism for the reductive cleavage of the oxamide bridge and subsequent rotation of fulleropyrrolidine at -2.2 V. The two-electron reduction of oxamide results in the cleavage of one of the C-N bonds and the loss of ammonia (Figure 13). The same reaction on the C_{60}dimer will result in the cleavage of one of the C-N bonds attached to the fulleropyrrolidine, in the absence of hydrogen an ethenone type structure is possibly formed as an intermediate, which decomposes further to produce another fulleropyrrolidine.[24, 25]

6.3.3 Electrochemical transformation of fulleropyrrolidino ferrocene ($C_{60}Fe(Cp)_2$)

6.3.3.1 Synthesis of $C_{60}Fe(Cp)_2$

The novel fulleropyrrolidino ferrocene ($C_{60}Fe(Cp)_2$) was synthesised as a model molecule, matching the geometry of the SWNT cavity to probe the effects of electrochemistry in confinement. A Prato reaction was used to functionalise the C_{60} by adapting a similar method from the literature.[27] This was followed by a deprotection of the pyrrolidine nitrogen using trifluoromethane sulfonic acid,[28, 29] then an acylation with ferrocene carboxaldehyde (Figure 15). Silica gel column chromatography was used to purify the compound to yield the functionalised C_{60} ($C_{60}Fe(Cp)_2$) (Figure 15) (13.2 mg, 26 % yield). MALDI-MS shows a peak at 961.5 *m/z* (M^-) and ^1H and ^{13}C NMR confirmed the formation of $C_{60}Fe(Cp)_2$.

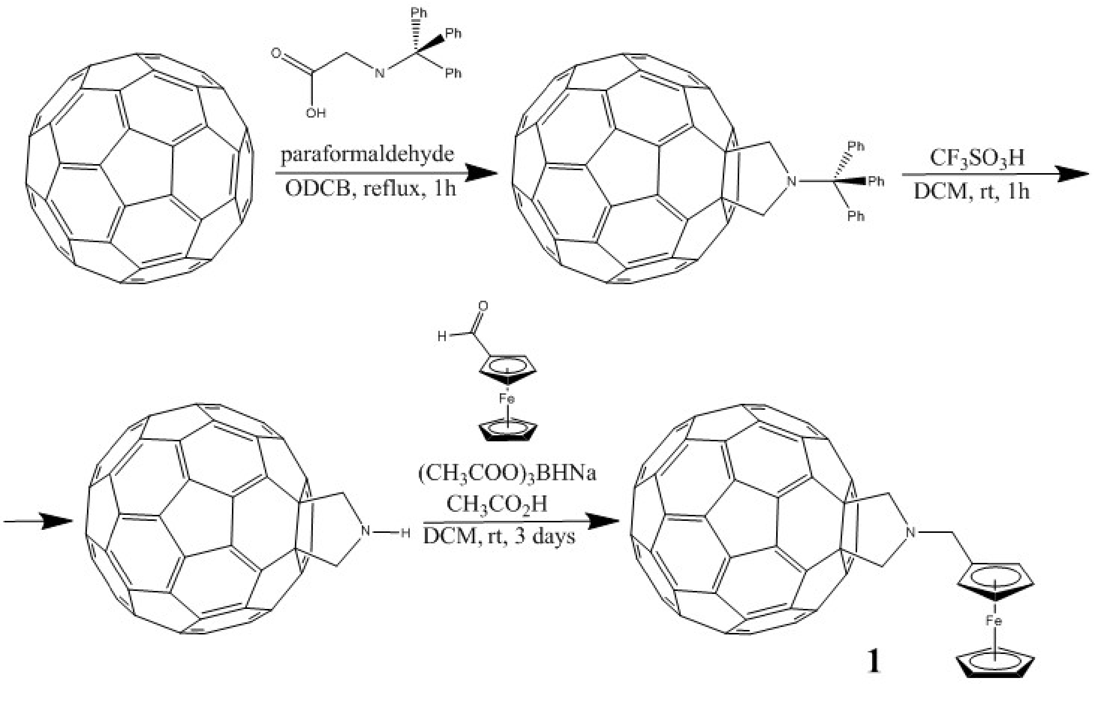

Figure 15. Synthesis of fulleropyrrolidino ferrocene ($C_{60}Fe(Cp)_2$) *via* a Prato reaction.

6.3.3.2 Cyclic voltammetry of $C_{60}Fe(Cp)_2$@SWNT

The CV of $C_{60}Fe(Cp)_2$ (Figure 16) was performed in ortho-dichlorobenzene (oDCB). Three redox processes of C_{60} and a redox process of the ferrocene moiety are observed. The redox processes of the ferrocene and C_{60} moieties in $C_{60}Fe(Cp)_2$ are shifted to 0.05 V (Fe^{III}/Fe^{II}), -1.19 V (C_{60}^{1-}/C_{60}^{0}), -1.57 V (C_{60}^{2-}/C_{60}^{1-}) and -2.10 V (C_{60}^{3-}/C_{60}^{2-}) from 0 V (Fe^{III}/Fe^{II}), -1.00 V (C_{60}^{1-}/C_{60}^{0}), -1.40 V (C_{60}^{2-}/C_{60}^{1-}) and -1.88 V (C_{60}^{3-}/C_{60}^{2-}) observed for unmodified ferrocene and C_{60} recorded in identical conditions. The shift in the potential of the ferrocene redox process and the C_{60} redox processes are +0.05 V, -0.19 V, -0.17 V and -0.22 V respectively and can be explained by an inductive electron withdrawing effect of the C_{60} on the ferrocene moiety through the linker,[30] as well as the linker being long enough to allow the ferrocene to bend around and interact with C_{60} through space.

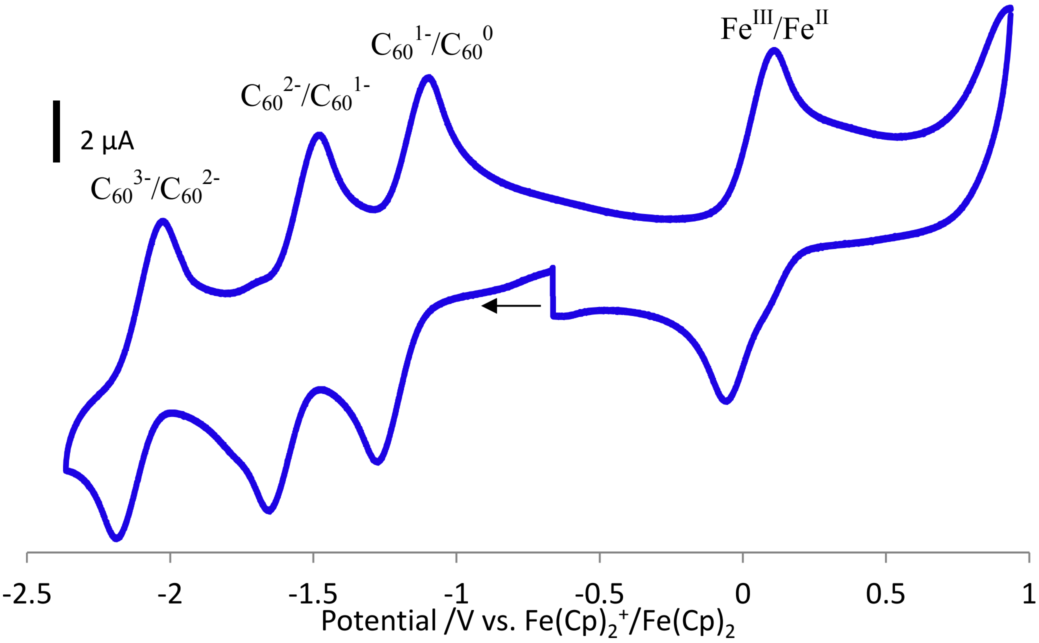

Figure 16. CV of $C_{60}Fe(Cp)_2$/GCE in the range of 1 V and -2.4 V. Experiments were performed in oDCB containing $[N^nBu_4][BF_4]$ (0.4 M) as the supporting electrolyte at 293 K and at a scan rate of 0.1 Vs^{-1}. Arrow indicates direction of potential sweep. Redox processes of $C_{60}Fe(Cp)_2$ at -1.19 V, -1.57 V, -2.10 V and 0.05 V. (vs. $Fe(Cp)_2/Fe(Cp)_2^+$)

$C_{60}Fe(Cp)_2$ was encapsulated in SWNT by a solution filling method in which annealed SWNT were added to a stirred solution of $C_{60}Fe(Cp)_2$ in toluene then sonicated. The suspension was heated (80 °C) for three days then filtered through a PTFE membrane then sonicated and washed with toluene. The presence of $C_{60}Fe(Cp)_2$ in nanotubes was confirmed by HRTEM imaging and EDX spectroscopy (Figure 17 and Figure 18).

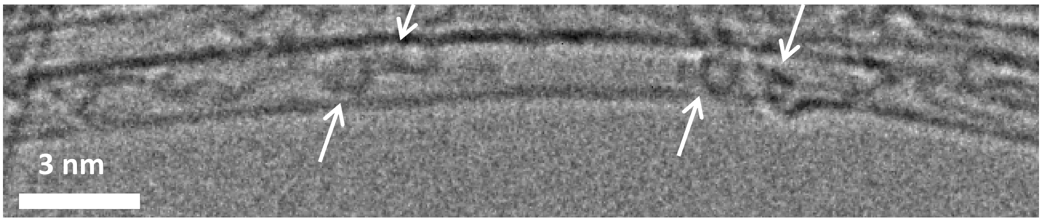

Figure 17. HRTEM micrograph of $C_{60}Fe(Cp)_2$@SWNT showing C_{60} molecules (upward facing arrows) and metal clusters (downward facing arrows).

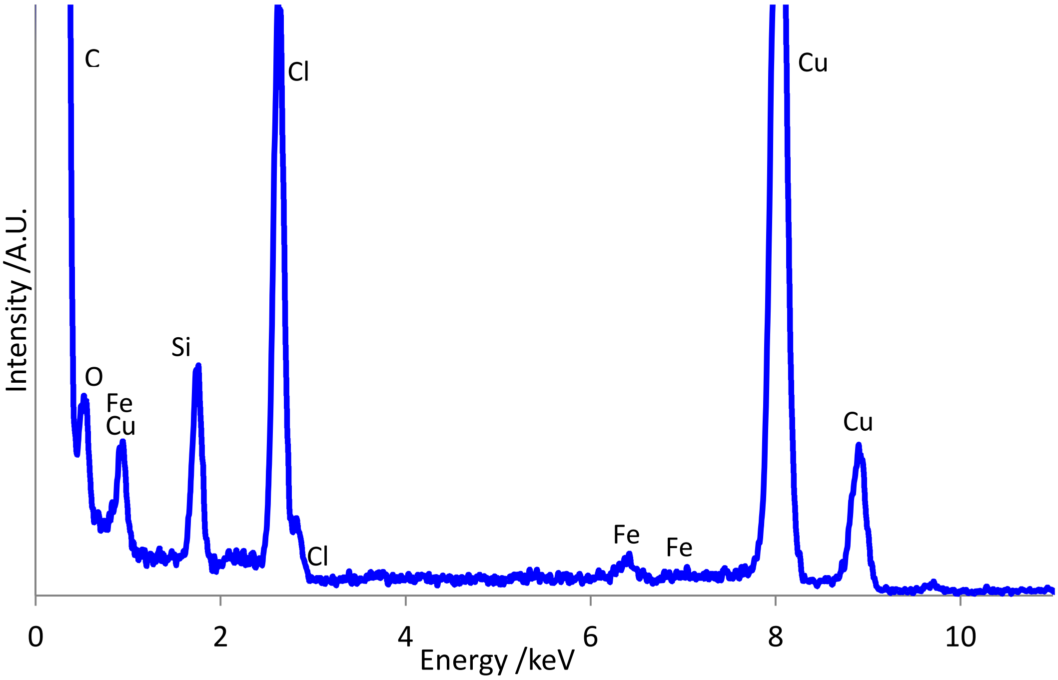

Figure 18. EDX spectrum of $C_{60}Fe(Cp)_2$@SWNT. Iron peaks are observed confirming the presence of $C_{60}Fe(Cp)_2$ inside the nanotube. The Cl peak is likely due to some residual oDCB left in the sample from the synthesis of $C_{60}Fe(Cp)_2$. Copper peaks are due to the sample grid.

The CV of $C_{60}Fe(Cp)_2@SWNT$ shows a weak but clear redox process assigned as the Fe^{III}/Fe^{II} couple and an area of high current at negative potentials which is attributed to the redox processes of the C_{60} moiety with weak peaks which are difficult to distinguish from each other (Figure 19). The Fe^{III}/Fe^{II} redox process in $C_{60}Fe(Cp)_2@SWNT$ shifts by -0.08 V and the oxidation-reduction peak splitting (ΔE_p) has narrowed by 0.05 V compared to the CV of $C_{60}Fe(Cp)_2$ in solution. This signal is unchanged over multiple potential sweeps within the potential window of -2.2 V to 0.3 V. The shift in $E_{1/2}$ of the Fe^{III}/Fe^{II} redox process is of similar magnitude to that of $Fe(Cp)_2@SWNT$ compared to $Fe(Cp)_2$/GCE but in the opposite direction suggesting a charge transfer from the nanotube to $Fe(Cp)_2$, this can be attributed to the HOMO of $Fe(Cp)_2$ being depleted of electrons by the C_{60} moiety which in turn decreases the energy of the $Fe(Cp)_2$ HOMO, allowing electrons to be transferred from the nanotube to $Fe(Cp)_2$ HOMO (see Chapter 3). The narrowed ΔE_p of Fe^{III}/Fe^{II} for $C_{60}Fe(Cp)_2@SWNT$ is explained by the fact that the redox process is no longer diffusion controlled. For species immobilised on an electrode, a zero ΔE_p should be observed as no time is required for diffusion to/from the electrode.[26] However, a small ΔE_p is observed due to an iR (current x resistance) drop from the electrode to the outermost nanotube layers associated with electron tunnelling between nanotubes (see Chapter 2). Positions and orientations of both the ferrocene and C_{60} moieties are constrained by the linker and the nanotube sidewalls. In solution electrochemistry, the redox processes of $C_{60}Fe(Cp)_2$ relies on long range electrostatic forces[31] so the orientation of the molecules is not important. However, when encapsulated in nanotubes and in the absence of solvent molecules,[32] the orientation must be considered. The additional constraints imposed by the linker means that the $Fe(Cp)_2$ moiety is immobilised in the parallel orientation to the SWNT which is not favourable for oxidation and therefore is a preferred orientation of C_{60} within the negatively charged nanotube due to the asymmetric polarisation of electron density through the fullerene orbitals (further detail later in the section).[31] This orientation cannot be achieved while bound to ferrocene, therefore, a weak electrochemical signal is observed due to additional kinetic factors associated with rotation.[33, 34]

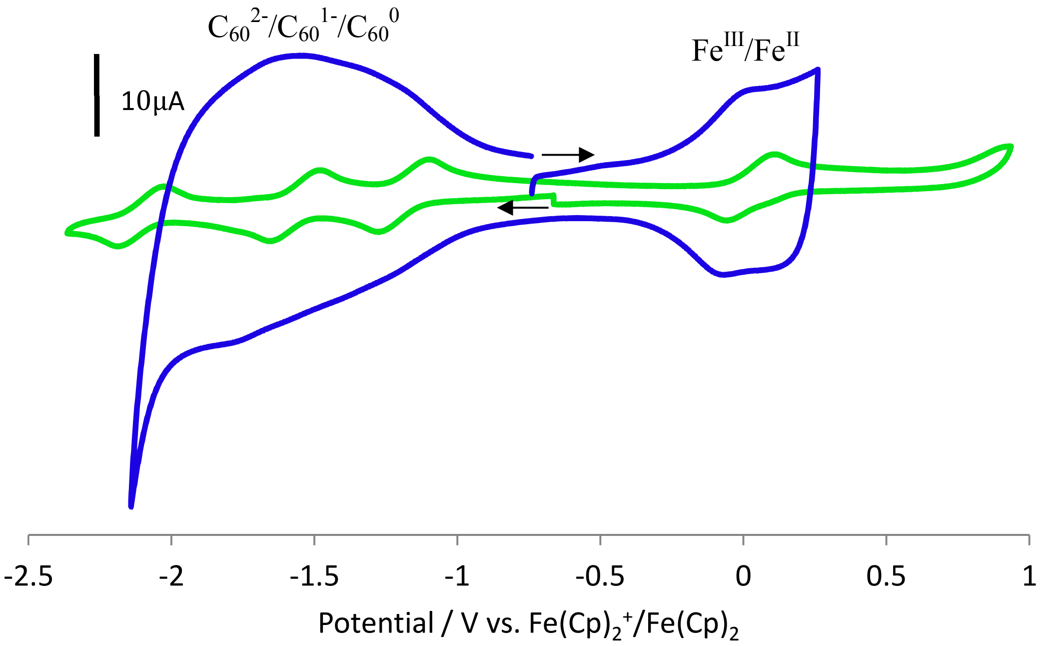

Figure 19. CV of $C_{60}Fe(Cp)_2$@SWNT (blue) in the range of 0.3 V and -2.2 V and $C_{60}Fe(Cp)_2$/GCE (green) in the range of 1 V and -2.4 V. Arrow indicates direction of potential sweep. Experiments were performed in oDCB (green) containing $[N^nBu_4][BF_4]$ (0.4 M) as the supporting electrolyte at 293 K and at a scan rate of 0.1 Vs^{-1}. Redox processes of $C_{60}Fe(Cp)_2$ at -1.19 V, -1.57 V, -2.10 V and 0.05 V. Oxidation process of iron in $C_{60}Fe(Cp)_2$@SWNT at 0.026 V and an area of high current between -2 V and -1 V (vs. $Fe(Cp)_2^+/Fe(Cp)_2$).

Following a potential sweep to -3.3 V at a scan rate of 0.1 Vs^{-1}, a significant negative current is observed between -2.6 V and -3.3 V in the CV of $C_{60}Fe(Cp)_2$@SWNT (Figure 20). A redox process with increased resolution and current is observed in the subsequent CV of $C_{60}Fe(Cp)_2$@SWNT (Figure 21). There is a small shift of -0.07 V for Fe^{III}/Fe^{II} redox process as well as an increased ΔE_p of 0.04 V. It is now possible to assign one negatively shifted redox process at –1.61 V of C_{60} as well as a second redox process with a weak signal at ~ -1.1 V.

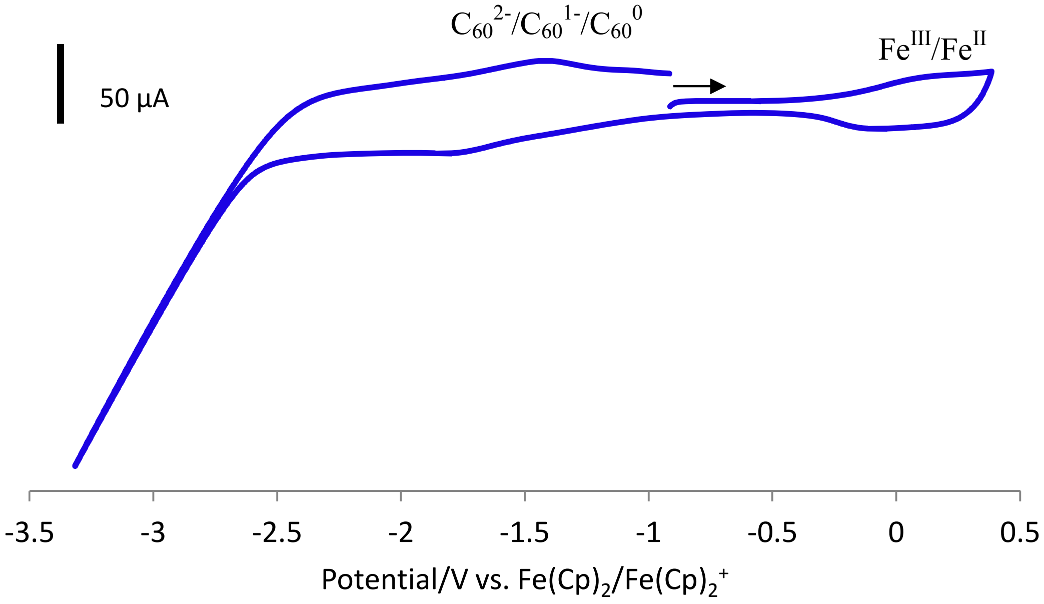

Figure 20. CV of $C_{60}Fe(Cp)_2$@SWNT in MeCN containing $[N^nBu_4][BF_4]$ (0.1 M) as the supporting electrolyte at 293 K and at a scan rate of 0.1 Vs^{-1}. Arrow indicates direction of potential sweep. A high current is observed following a potential sweep to -3.3 V and is consistent with electrochemical cleavage of the linker in the C_{60}dimer.

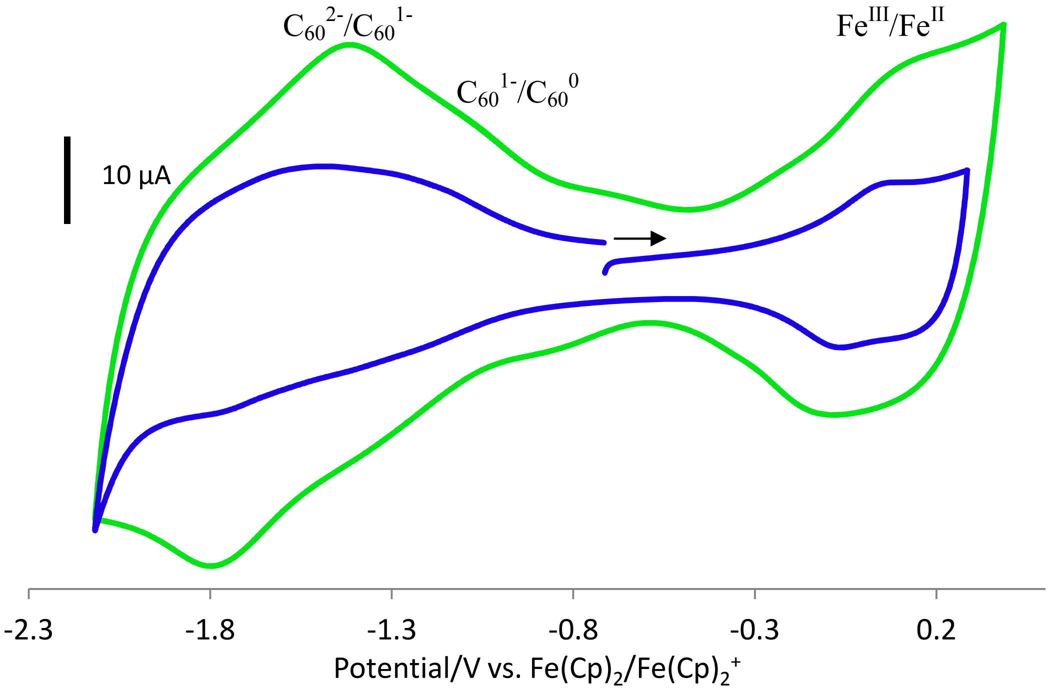

Figure 21. CV of $C_{60}Fe(Cp)_2$@SWNT in the range of -0.3 V and -2.2 V before (blue) and after (green) a potential sweep to -3.3 V. Experiments were performed in oDCB containing $[N^nBu_4][BF_4]$ (0.1 M) as the supporting electrolyte at 293 K and at a scan rate of 0.1 Vs^{-1}. Arrow indicates direction of potential sweep. The redox process of the ferrocene moiety occurs at -0.02 before the potential sweep to -3.3 V and -0.09 V after. The redox process of C_{60} occurs at -1.61 V.

One of the unique properties of C_{60} is that it can accept six electrons with no change to the structure[35] i.e. no change in structure is required upon reduction/oxidation so it is unlikely that a decrease in the amount of imposed constraint would resolve the C_{60} signals further. However, upon reduction of derivatised C_{60} the electron is delocalised and polarised around the C_{60} π system (Figure 22).[36, 37] After the third reduction of fullerene, there are two electrons in the first lowest unoccupied molecular orbital (LUMO) of fullerene and one electron in the LUMO+1. These electrons have a high probability of residing around the “equator” of fullerene due to the distribution of the LUMO orbitals around the two sp^3 carbons of the pyrrolidine group (Figure 18).[31] This band of negative charge around the fullerene moiety may repel the highly negatively charged nanotube, forcing the fullerene moiety to rotate, decreasing the repulsion between the band of negative charge on the fullerene and the highly negatively charged nanotube. This forces the linker with the $Fe(Cp)_2$ moiety into a highly strained position, which might result in the bond between the two moieties breaking (Figure 23).

Both the fulleropyrrolidine and $Fe(Cp)_2$ are now free to rotate and partake in redox processes in optimised configurations with the nanotube sidewalls, thereby increasing the current of the redox process by lowering the kinetic factor of the redox process, which increases the speed of the electron transfer, so that the CV is more defined and appears similar to that of $C_{60}Fe(Cp)_2$/GCE (Figure 24). This is supported by the negative shift in redox process of $Fe(Cp)_2$ compared to before linker decomposition, after which the electron withdrawing C_{60} is lost resulting in increased electron density on the $Fe(Cp)_2$ (see Chapter 3). $Fe(Cp)_2$ can now rotate allowing it to adopt the optimum position for electron transfer. Fullerene can rotate to minimise repulsion in each reduced state, decreasing the kinetic aspect of each reduction. There are possible applications, for this system for controlled release of molecules from SWNT. The C_{60} acts as an anchor for the molecule of interest and the application of potential results in a cleavage from the anchor. Performing this in larger nanotubes would allow for the molecule to diffuse out of the nanotube to the bulk solution on application of negative potentials.

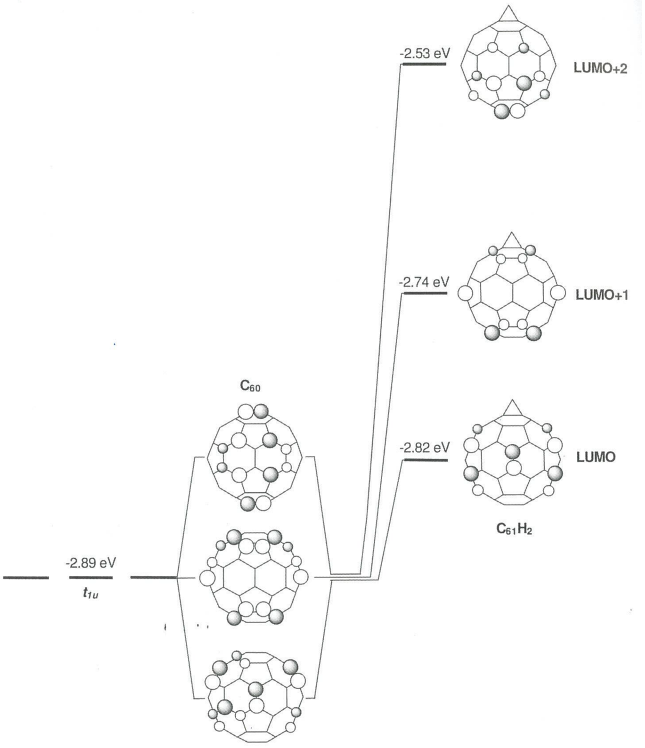

Figure 22. The LUMO of $C_{61}H_2$.[37] It is expected that the LUMO of fulleropyrrollidine are similar to that of $C_{61}H_2$ since both molecules have sp^3 carbon atoms in the carbon cage on a junction between two six membered rings. The third reduction discussed in this section puts two electrons in the LUMO and one electron in LUMO+1 of the functionalise fullerene. The electrons are delocalised and polarised around the π system of the fullerene with the electron having the highest probability of residing on the "equator" of fullerene (horizontally around the centre as shown in the figure) where the propane ring is at the pole (top as shown in the figure).

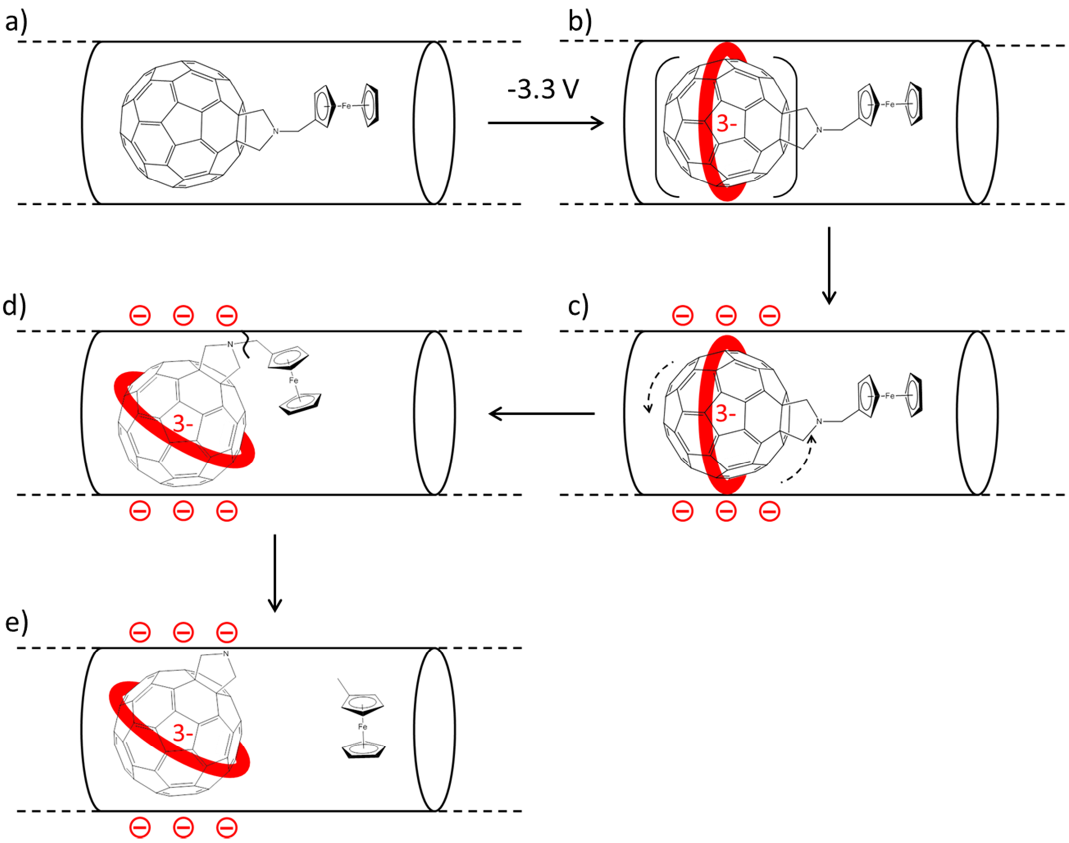

Figure 23. The proposed mechanism of linker cleavage between C_{60} and ferrocene in $C_{60}Fe(Cp)_2$ upon reduction. The highest probability of negative charge distribution is shown as a red band around the "equator" of the C_{60} moiety. After the third reduction of fullerene, there are two electrons in the LUMO of fullerene and one electron in the LUMO+1. These electrons have a high probability of residing around the "equator" of fullerene due to the shape of the LUMO orbitals (Figure 22). This band of negative charge around the fullerene moiety repels the highly negatively charged nanotube c) which forces the fullerene moiety to rotate (dashed black arrows), d). As a result of rotation the linker with the $Fe(Cp)_2$ moiety is forced into a highly strained position, d), leading to rotation and the bond breaking, e). Once the bond is broken both the fulleropyrrolidine and $Fe(Cp)_2$ are free to rotate and partake in redox processes in configurations optimised for electron transfer between the molecules and the nanotube sidewalls.

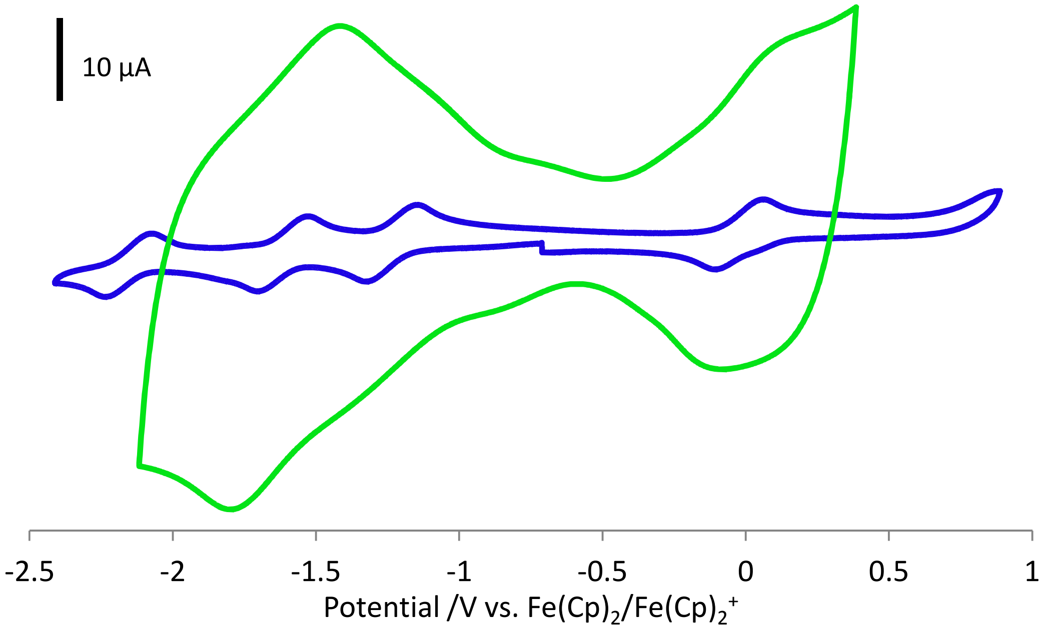

Figure 24. CV of $C_{60}Fe(Cp)_2$ in solution in the range of 1 V to -2.4 V (blue) and $C_{60}Fe(Cp)_2$@SWNT (green) in the range of 0.3 V to -2.2 V after the potential sweep to -3.3 V (green) in oDCB containing $[N^nBu_4][BF_4]$ (0.1 M) as the supporting electrolyte at 293 K and at a scan rate of 0.1 Vs^{-1}. Arrow indicates direction of potential sweep. After the potential sweep to -3.3 V, the redox process of the ferrocene moiety occurs at -0.09 V and the redox processes of C_{60} occurs at -1.61 V with a weak signal at ~1.1 V in $C_{60}Fe(Cp)_2$@SWNT. Redox processes of $C_{60}Fe(Cp)_2$ in solution occur at -1.19 V, -1.57 V, -2.10 V and 0.05 V. See Figure 21 and Figure 16 for labelled waves.

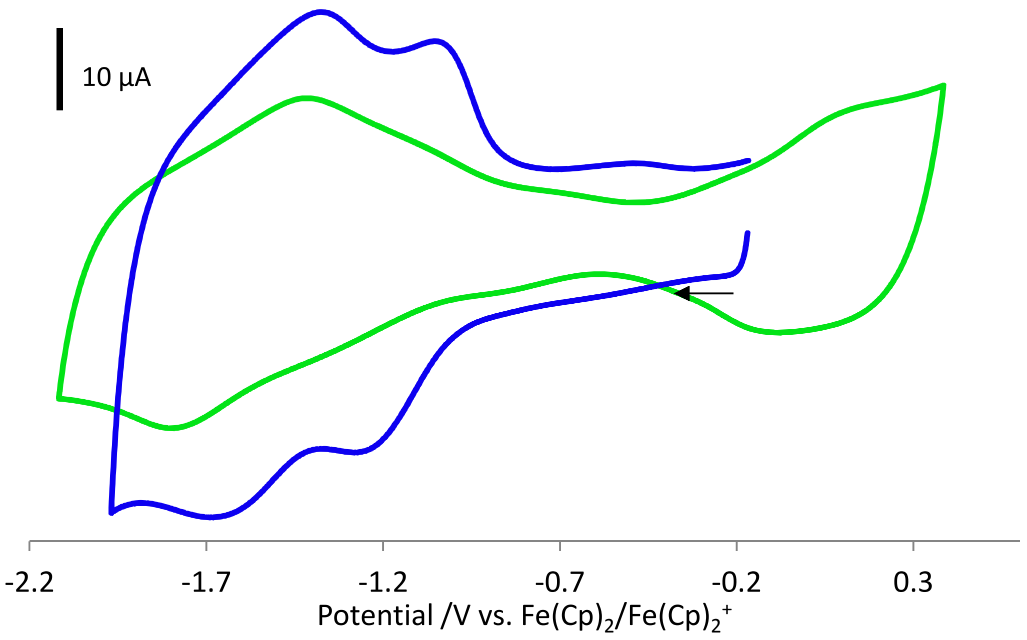

Figure 25. CV of C_{60}@SWNT (blue) in the range of -0.2 V to -2 V and $C_{60}Fe(Cp)_2$@SWNT (green) in the range of 0.3 V to -2.2 V after the potential sweep to -3.3 V (green) in oDCB containing $[N^nBu_4][BF_4]$ (0.1 M) as the supporting electrolyte at 293 K and at a scan rate of 0.1 Vs^{-1}. Arrow indicates direction of potential sweep. The redox process of iron occurs at -0.09 V and the redox process of C_{60} occurs at -1.61 V with a weak signal at ~-1.1 V in $C_{60}Fe(Cp)_2$@SWNT. Reduction processes of C_{60}@SWNT occur at -1.142 V and -1.528 V. See Figure 4 and Figure 21 for labelled waves.

This section demonstrates that electrochemical properties of complexes such as C_{60}dimer and $C_{60}Fe(Cp)_2$ diads are retained inside carbon nanotubes and can be probed by standard CV measurements. However, these experiments also reveal that irreversible chemical transformation can be triggered in SWNT by applying highly negative potentials such as -2.2 V that cleaves the C-N bond in the bridge between C_{60} cages in C_{60}dimer or -3.3 V and causes dissociation of the C-N bond linking the ferrocene group in $C_{60}Fe(Cp)_2$.

6.3.4 Electrochemical conversion of TTF to S-GNR

In the previous section it was demonstrated that the application of electrochemical potential can result in the transformation of guest-molecules in nanotubes, the next step is to investigate the transformation of TTF into S-GNR and to assess whether the use of electrochemical potential can transform the TTF guest-molecules into a new product inaccessible by reactions outside of the SWNT without the application of extreme heat or electron beam irradiation techniques.

6.3.4.1 CV of TTF in solution

TTF is an electron donor which can form a stable charge transfer complex with electron acceptors such as tetracyanoquinodimethane.[38] TTF is known to transfer electrons to SWNT[39, 40] and has two stable oxidation states (Figure 26). In solution, two reversible redox processes of TTF at -0.06 V (TTF^0/TTF^{1+}) and 0.32 V (TTF^{1+}/TTF^{2+}) (Figure 26) and an ECE[26] type reaction initiated at -2.8 V are observed (Figure 27). The two reversible redox processes result in positive charges on two of the sulfur atoms (Figure 26). A potential sweep to -2.8 V results in a reduction process at -2.8 V (TTF^0/TTF^{-1}) and the emergence of the oxidation process X^{1-}/X^0 at -0.6 V of an unknown product (Figure 27, blue wave). A potential sweep to -2.9 V results in a reduction process at -2.8 V (TTF^0/TTF^{-1}) and an increase in the current of the oxidation process X^{1-}/X^0 at -0.6 V (Figure 27, orange wave). A potential sweep to -3.1 V results in the appearance of a shoulder at -3 V on the TTF^0/TTF^{-1} reduction wave and a further increase in the current of the oxidation process X^{1-}/X^0 at -0.6 V (Figure 27, red wave). A potential sweep to -3.4 V results in a large negative current of -6×10^{-4} A corresponding to the TTF^{2-}/TTF^{1-} reduction process and a further oxidation process (Y^{1-}/Y^{0}) is observed at -0.4 V which is attributed to a second unknown product being formed after the second reduction (TTF^{1-}/TTF^{2-}) (Figure 27, green wave). This reaction is attributed to the formation of a radical leading to the synthesis is of dimers, trimers or polymers (Figure 26).

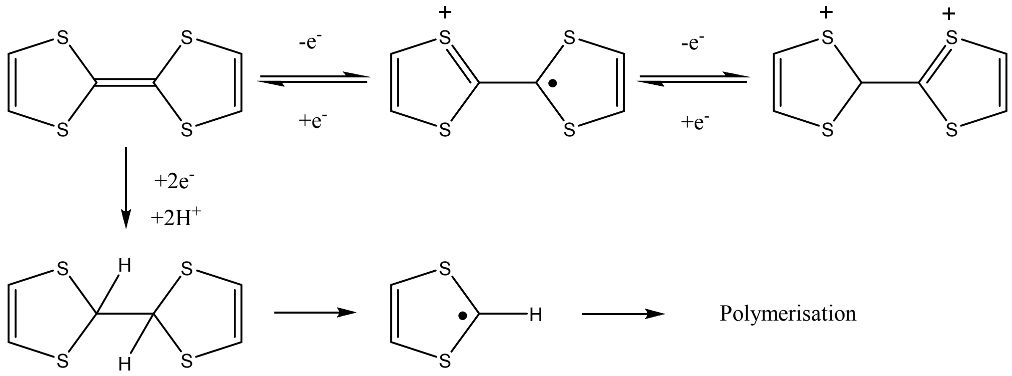

Figure 26. Reversible oxidations of TTF[41] with a possible mechanism for the reduction of TTF initiating the ECE reaction.[42]

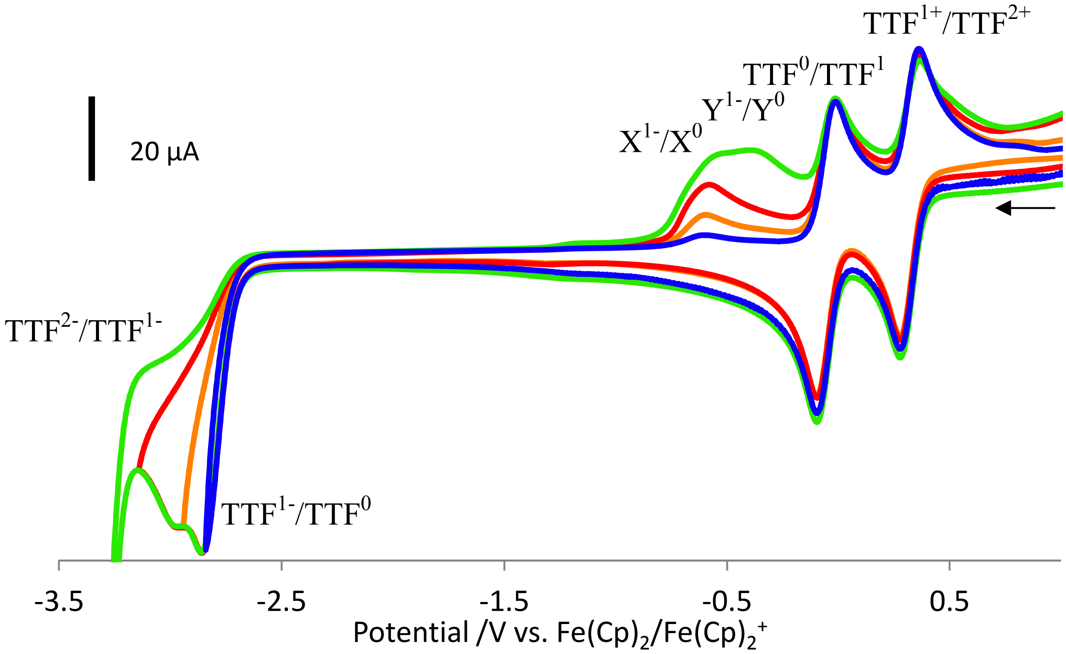

Figure 27. CV of TTF, changing the potential windows in MeCN containing $[N^nBu_4][BF_4]$ (0.1 M) as the supporting electrolyte at 293 K and at a scan rate of 0.1 Vs^{-1}. Arrow indicates direction of potential sweep. Each potential sweep investigates a different switching potential: -2.8 V (blue), -2.9 V (orange), -3.1 V (red) and -3.3 V (green). Two reversible redox processes at -0.06 V and 0.32 V and an ECE type reaction with a reduction process at -2.8 V and an oxidation processes at -0.65 V and 0.45 V, depending on the switching potential, are observed. The oxidation processes are due to unknown products X and Y.

While chemical transformations and CV of reduced forms of TTF have not been reported, observations in sections 6.3.3 and 6.3.2 clearly indicate that guest-molecules in SWNT can undergo transformation under negative potential and the solution CV of TTF show a reduction that produces an unknown product. By analogy, it should be expected that reductions to TTF^{1-} and particularly TTF^{2-} formed at -2.8 V and -3.4 V respectively as part of the ECE reaction in solution would lead to a new product formed from TTF in the nanotube. While the product diffuses away if performed in solution, in the nanotube the products are trapped, can further react and be analysed using different techniques. Furthermore, this product would be templated by the nanotube under electrochemical conditions where the nanotube would act as an electrode and reaction vessel.[39, 40, 43]

6.3.4.2 CV of TTF@SWNT

Using molten phase filling, TTF was encapsulated in SWNT, whereby annealed SWNT were added to stirred liquid TTF under inert conditions and heated at 160 °C for 4 hours.[10] The black powder was washed with THF and the suspension was filtered through a PTFE membrane. The CV of TTF@SWNT showed neither redox process of TTF as observed in solution. Instead, irreversible signals akin to the ECE reaction in solution were observed for TTF@SWNT. A reduction at -1.69 V (TTF^0/TTF^{1-}) and corresponding oxidation of an unknown product at -0.88 V (Z^{1-}/Z^0) were observed (Figure 28). The oxidation and reduction corresponding to the ECE reaction progressively diminish in the subsequent potential sweeps, suggesting that TTF undergoes a transformation to a new chemical structure under reductive electrochemical conditions (Figure 28). Unlike in solution where the diffusion layer is replenished from bulk solution, there is a finite number of TTF reactant available inside the SWNT. As the ECE reaction of TTF to Z proceeds, the concentration of reactants diminish as indicated by the disappearance of the reduction wave (TTF^{1-}/TTF^0) at -1.7 V. Furthermore, a decrease in the current associated with the oxidation process of Z was observed (Figure 28) which is consistent with the consumption of TTF during the ECE reaction and the further reaction of Z, indicating that a new product is formed inside SWNT.

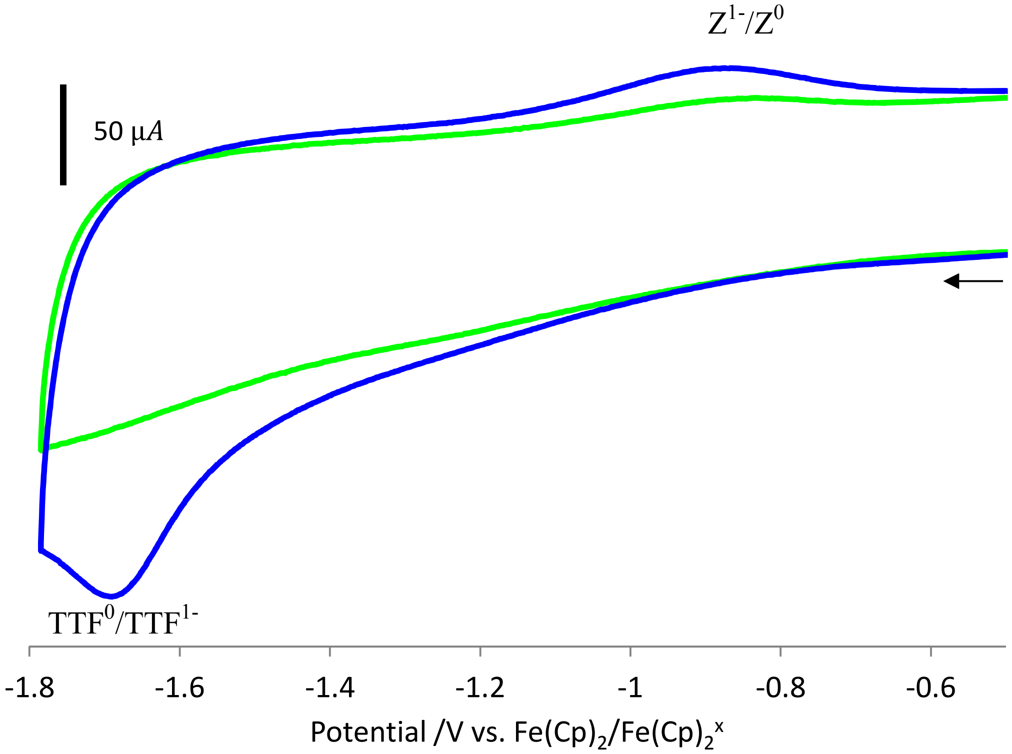

Figure 28. CV of TTF@SWNT in the range of 1.1 V to -1.8 V showing the reduction process of TTF and the oxidation of unknown product Z (blue) followed by the subsequent disappearance of the reduction wave (TTF^{1-}/TTF^0) and oxidation wave (Z^{1-}/Z^0) after three potential sweeps to -1.8 V (green). This is explained by consumption of TTF in an ECE reaction which leads to a product Z^{1-} which oxidises to Z^0 at -0.88 V then subsequently forms a further product. Experiments were performed in MeCN containing $[N^nBu_4][BF_4]$ (0.1 M) as the supporting electrolyte at 293 K and at a scan rate of 0.1 Vs^{-1}.

While the two TTF redox processes (-0.06 V and 0.32 V) are not observed in the CV of TTF@SWNT, there is a small oxidative current between -0.4 V and 0 V, similar to signals due to the DOS in empty carbon nanotubes (see Chapter 2) but this could also originate from a weak signal from TTF^0/TTF^{1+}@SWNT. An irreversible oxidation process develops at 0.4 V (Figure 29, red arrow) while the previous oxidation process diminishes (Figure 29, blue arrow) after four potential sweeps between -1.8 V and 1 V at a scan rate of 0.1 Vs^{-1} (Figure 29). The shift in the potential of the unknown oxidation process (blue to red arrow) is +0.5 V between the first and fourth potential sweep between -0.4 V and 0 V. These weak signals (Figure 29, blue and red waves) are attributed to the addition and removal of electrons from the states of TTF@SWNT and S-GNR@SWNT respectively. The signals observed in Figure 29 are different to those of empty SWNT due to the charge transfer from TTF to SWNT. The oxidation process observed after four potential sweeps between -1.8 V and -0.5 V is characteristic of a non-molecular product inside SWNT. Individual molecules have discrete orbitals at defined energies but a material such as a S-GNR has many overlapping orbitals that form a continuous band and the positive current corresponds so the addition of electrons into a high density of states in the nanotube (see Chapter 3), thus providing further evidence for the formation of S-GNR@SWNT.

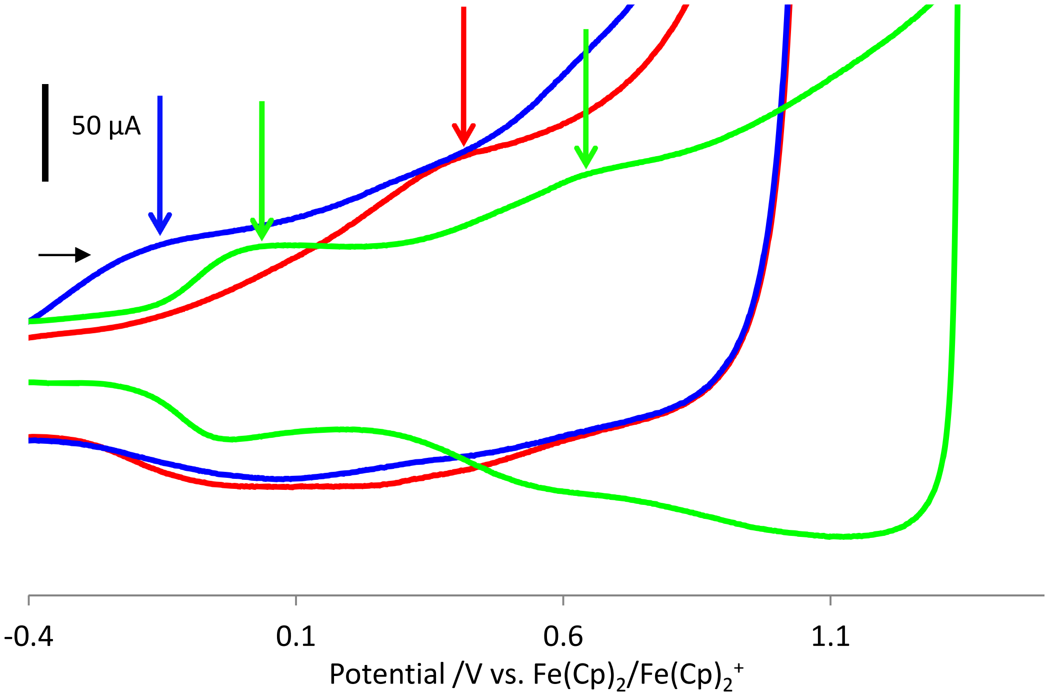

Figure 29. The CV of TTF@SWNT in the range of -0.4 V and 1.4 V (first potential sweep, blue), TTF@SWNT (after the ECE reaction was completed, red) and empty SWNT (green) in MeCN containing $[N^nBu_4][BF_4]$ (0.1 M) as the supporting electrolyte at 293 K and at a scan rate of 0.1 Vs^{-1}. Arrow indicates direction of potential sweep. Redox processes occur at – 0.18 V in the first potential sweep (blue arrow) and 0.4 V in the fourth potential sweep (red arrow). Features of empty SWNT are marked by green arrows.

The reaction, occurring via an ECE mechanism proceeds by reduction of the individual TTF inside the SWNT. Previous work has shown that nanotube encapsulation can have a big influence upon ECE reactions, completely changing the reaction pathway as with $Cp^{Me}Mn(CO)_3$ (Chapter 5).[32] The ECE reaction observed for TTF@SWNT was attributed to the same ECE reaction of TTF in solution. The mechanism proposed for the reduction in solution (Figure 26) involves the formation of radicals. Upon radical formation inside the nanotube, the molecules polymerise and the resultant polymeric species is templated along the nanotube channel forming a high aspect structure i.e. a nanoribbon.[44] Encapsulation in the nanotube facilitates this process by immobilising the reactants in place then templating the reaction.

Thus, CV measurements strongly suggest that the reductions of TTF@SWNT results in the formation of a polymeric product from TTF, which is be similar to S-GNR.

6.3.4.3 HRTEM analysis

HRTEM microscopy was used to image the TTF@SWNT before and after the electrochemical reaction. The formation of S-GNR using the electron beam is well understood,[5, 10] therefore care was taken when imaging the preformed S-GNR. The first image is the most important as it represents the sample at minimal exposure to the electron beam before any electron beam induced transformations can occur. HRTEM imaging of TTF@SWNT before electrochemical treatment clearly shows discrete molecular structures of TTF randomly distributed within the SWNT cavity (Figure 30), which begins to be modified by the electron beam in HRTEM on the time scale of a few seconds. A sulfur peak observed in the EDX spectrum of TTF@SWNT supports the presence of TTF molecules within the nanotubes (Figure 31).

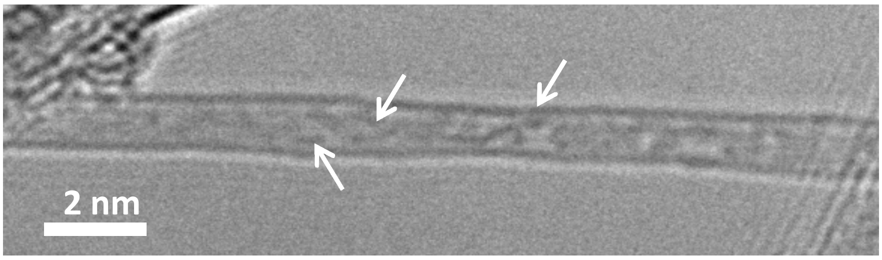

Figure 30. HRTEM image of TTF@SWNT before electrochemical transformation. Most TTF molecules appear as discrete slopes with no continuous structures observed in SWNT.

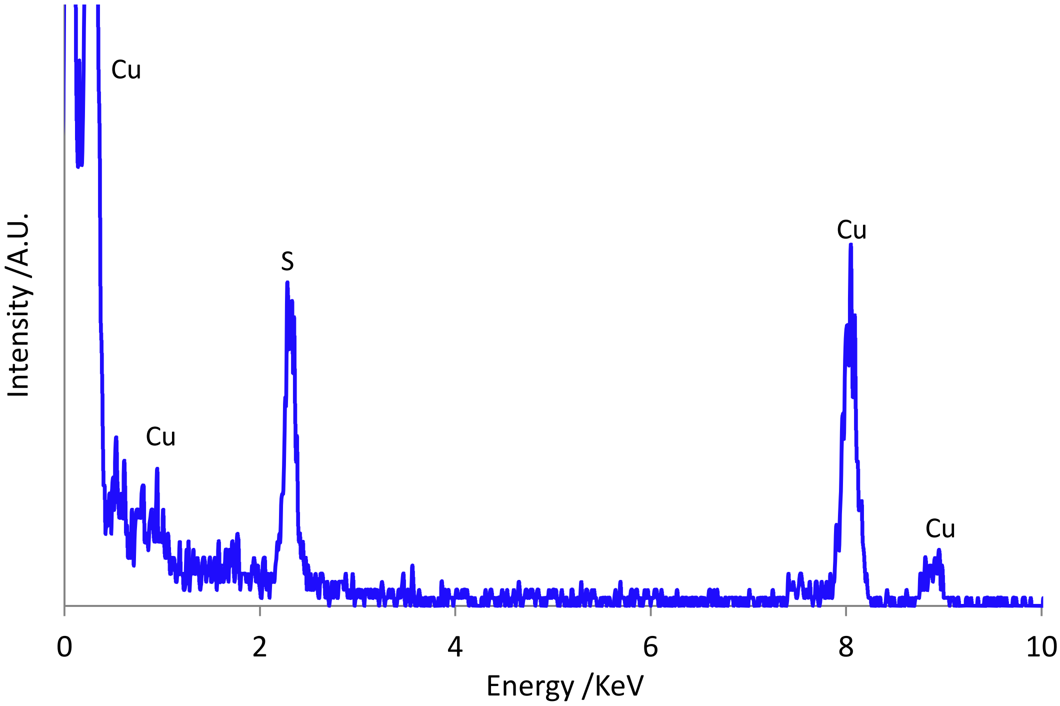

Figure 31. EDX spectrum of TTF@SWNT. There is a sulphur peak supporting the presence of TTF inside the nanotube. Copper is from the sample grid.

After electrochemical transformation, TTF@SWNT exhibits new features in HRTEM images such as a continuous structure and a helical twist that traverses the length of the nanoribbon (Figure 32). These are consistent with S-terminated nanoribbons observed in previous studies.[5, 10]

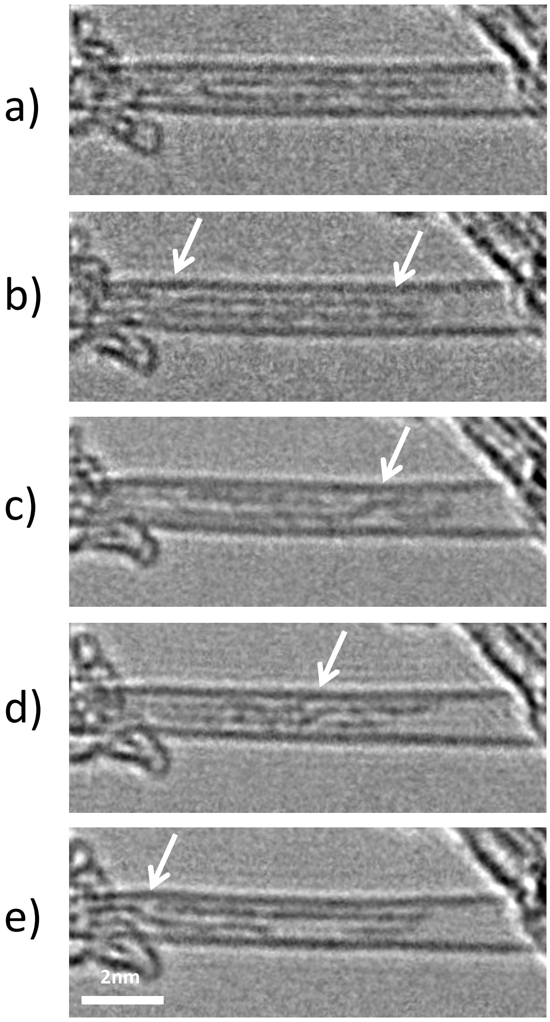

Figure 32. Time series of HRTEM images of TTF@SWNT after electrochemical reaction. The presence of a nanoribbon is confirmed by the helical twist that traverses the length of the nanoribbon. a) S-GNR with a twist near the nanotube bundle, b) another twist starts to develop at the end, (c-e) the twist moves along the nanotube. The first image in the series is the first captured image in this area of the sample which shows continuous S-GNR in contrast to the discrete TTF molecules observed in the original TTF@SWNT sample.

Upon prolonged exposure to the electron beam electrochemically generated S-GNR undergo slow decomposition as demonstrated by a time-series of images (Figure 33). This is attributed to a different atomic structure of nanoribbon formed using electrochemistry as compared to other methods that might not correspond to the most stable form of the nanoribbon. Furthermore, the electron beam provides oxidative conditions because fast electrons knock out valence electrons making it collapse after extensive electron beam damage. This is the opposite of what is observed in the electrochemical transformation, where formally, electrons are added during the reduction (Figure 28).

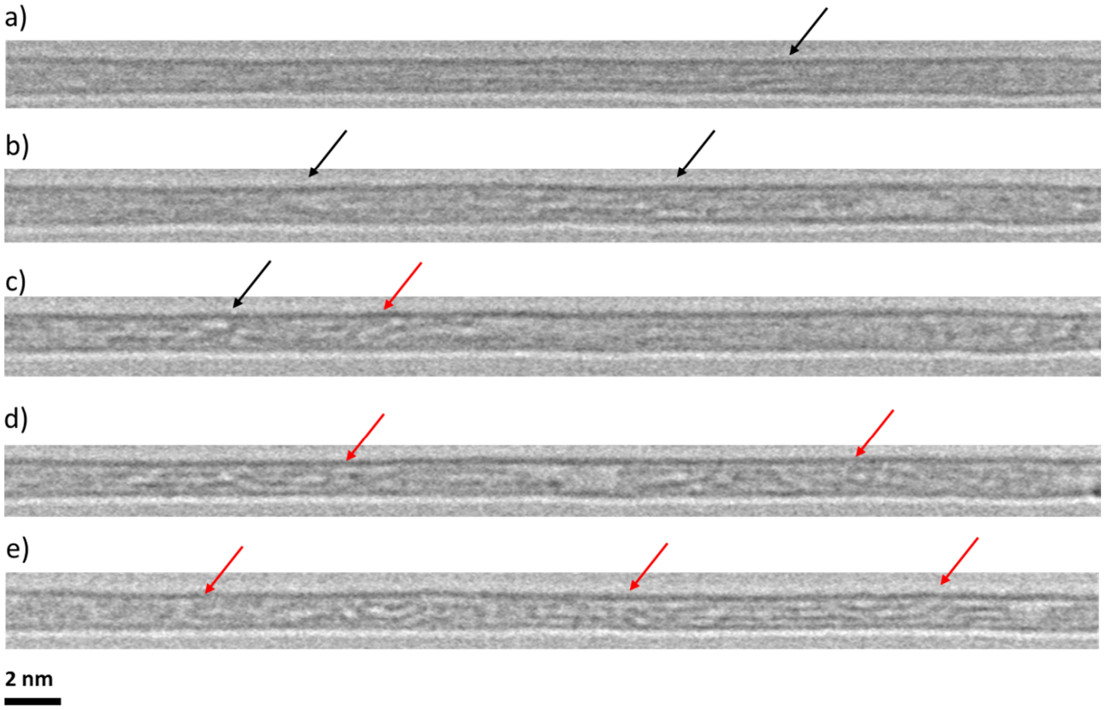

Figure 33. A time series of HRTEM images showing the decomposition of electrochemically generated S-GNR a) as a result of electron beam irradiation decomposing over increasing e-beam exposure (a-e). Black arrows show twists in the nanoribbon and the red arrows show regions of decomposition. The initial image shows a very long S-GNR. Longer than usual S-GNR are observed.

6.4 Conclusions

It was shown that the electrochemical properties of organic molecules can be measured inside SWNT using CV. The nanotube provides both a highly conducting bridge between component parts of guest-molecules and also acts as a nano-test tube to facilitate reactions that would not conventionally occur. The application of potential, most notably negative potential, can result in the transformation of guest-molecules through bond cleavage and rearrangement. In conventional solution electrochemistry the molecules are not constrained next to the electrode or in a sterically confined cavity, so rotations and rearrangements due to reduction or oxidation can occur un-hindered in solution. In contrast, confinement in SWNT entraps the guest-molecules in intimate contact with the highly conductive walls of the nanotube, limiting movement and promoting reactions along the SWNT channel to transform guest-molecules into new polymeric products. Electrochemical generation of new products inside SWNT offers a new platform for scaling-up the fabrication of nano-materials such as S-GNR for electronics or C_{60}dimers and $C_{60}Fe(Cp)_2$ as electron mediators for use in solar cells, controlled release applications and for quantum computing.[22, 23]

6.5 Experimental

Chemicals and solvents were purchased from Sigma Aldrich, Acros and Alfa Aesar and were used without further purification. Carbon nanotubes were purchased from Carbon Solutions (SWNT, Carbon Solutions Inc., USA, lot#: 02-A006, carbonaceous purity: >90%).

6.5.1 Synthesis of $C_{60}Fe(Cp)_2$

6.5.1.1 Synthesis of N-triphenylmethyl [60]fulleropyrrolidine

C_{60} (500 mg, 0.69 mmol), N-trityl glycine (220 mg, 0.69 mmol) and paraformaldehyde (105 mg, 3.478 mmol) were dissolved in anhydrous oDCB (100 mL), degassed with argon for 30 min then refluxed under Ar for 1 h. The reaction mixture was cooled down to room temperature, filtered through a silica gel pad, and the solvent was removed in vacuum. The resultant brown solid was purified by column chromatography (silica gel, CS_2 as eluent). Further purification was carried out by excessive washing of the product with MeOH (40 mL), petroleum ether (40 mL) and diethyl ether (40 mL). It was then dried under vacuum to give N-trityl fulleropyrrolidine as a black powder (275 mg, 39.5 %). ^{1}H NMR (400 MHz, 297 K, $CS_2/CDCl_3$ 7:1 v/v, δ, ppm): 7.85 (s, 6H, Ar C$\underline{H}$), 7.39 (s, 6H, Hz, Ar C$\underline{H}$), 7.23 (t, 3H, J=7.4 Hz, Ar C$\underline{H}$), 4.15 (s, 4H, C$\underline{H_2}$). MALDI-TOF MS (DCTB/MeCN): 1005.2 *m/z* (M$^-$)

6.5.1.2 Synthesis of [60]fulleropyrrolidine

N-trityl fulleropyrrolidine (25 mg, 0.03 mmol) was suspended in dichloromethane (10 mL) and trifluoromethanosulfonic acid (0.1 mL) was added. The mixture was stirred for 1 h at room temperature. The resulting precipitate was centrifuged and washed with portions of diethyl ether (15 mL) several times, then dried under reduced pressure overnight. The product was used in the next step without purification.

6.5.1.3 Synthesis of N- ferrocene carboxaldehyde benzyl [60]fulleropyrrolidine

N-otanoyl [60]fulleropyrrolidine (1.1 mg, 0.0014 mmol) and ferrocene carboxaldehyde (5.2 mg, 0.026 mmol) were mixed in dry dichloromethane (5 mL), then treated with sodium triacetoxyborohydride (96 mg, 0.03 mmol) and glacial acetic acid (2 mg, 0.028 mmol). The mixture was stirred at room temperature under argon (3 days). The solvent was removed under reduced pressure and the product was extracted with chloroform (10 mL). The extract was washed with 1 M $NaHCO_3$ (100 mL) then brine (10 mL) and dried over $MgSO_4$. The solvent was evaporated to give the crude free base as a brown solid. MALDI-MS (DCTB/MeCN): 961.5 *m/z* (M^-) ^{1}H NMR (400 MHz, 297 K, $CS_2/CDCl_3$ 7:1 v/v, δ, ppm): 7.95 (s, 6H, Ar C$\underline{H}$), 7.39 (t, 6H)

6.5.2 Synthesis of C_{60}dimer

Synthesis was performed according to work published by Lebedeva *et al.*[21]

6.5.3 Preparation of SWNT samples

Batches of nanotubes are purchased from Carbon Solutions Inc.. Each new batch is analysed using TEM whereby the diameter of nanotubes is measured over a wide range of tubes and the average diameter (quoted diameter in this thesis) and standard deviation are determined. The method of TEM preparation involves the sonication of a substantial amount of nanotubes which is further diluted meaning the nanotubes that appear in TEM are representative of the whole batch. There is a range of different chiral indices present in the nanotube sample which have been analysed by Pekker *et al.*[45] These are not from the same batch that were used but are from the same company and preparation method. They determine that the ratio of metallic nanotubes to semiconducting nanotubes is 31:69 respectively. Further details of nanotube synthesis and oxidation method are provided in the experimental.

6.5.3.1 Preparation of C_{60}@SWNT

SWNT (25 mg) were annealed (600 ^{o}C, 25 minutes) in air. C_{60} (50 mg, 0.069 mmol) was added to SWNT (10 mg) and sealed in a pyrex ampule under reduced pressure (10^{-6} mbar). The mixture was heated (600 ^{o}C) for three days. The resulting black powder was sonicated in toluene (3 x 20 mL) and filtered through a PTFE membrane.

6.5.3.2 Preparation of $C_{60}Fe(Cp)_2$@SWNT

$C_{60}Fe(Cp)_2$ (3.5 mg, 3.64 x 10^{-3} mmol) was suspended in dry toluene (2 mL) under argon and stirred. SWNT (6 mg) were annealed (600 ^{o}C, 25 minutes) in air. The annealed, SWNT (2 mg) were added to the stirring suspension. The mixture was then heated (80 ^{o}C) for three days. The mixture was filtered through a PTFE membrane. The resulting black powder was sonicated in toluene (3 x 20 mL) and filtered through a PTFE membrane and dried in air.

6.5.3.3 Preparation of TTF@SWNT

Tetrathiafulvalene (20 mg, 0.098 mmol) was melted (160 ^{o}C) and stirred under inert conditions. SWNT (20 mg) were annealed (600 ^{o}C, 25 minutes) in air. The annealed SWNT (10 mg) were added to the stirred tetrathiafulvalene and were heated (160 ^{o}C) for 4 h. The resulting mixture was filtered through a PTFE membrane and washed with THF (3 x 20 mL) and dried in air.

6.5.3.4 Preparation of C_{60}dimer@SWNT

C_{60}dimer (2 mg) was sonicated in toluene (2 mL) then stirred under inert conditions. SWNT (25 mg) were annealed (600 °C, 25 minutes) in air. The annealed SWNT (1.5 mg) were added to the stirred C_{60}dimer and the mixture was heated (80°C, 24 h). The solution was then filtered through a PTFE membrane, washed with toluene (10 mL) and CS_2 (10 mL) then dried in air.

6.5.4 Electrochemistry

Electrochemistry experiments were performed on an Autolab PGSTAT302N potentiostat. Electrodes were purchased from IJCambria and Metrohm. The electrochemistry was performed using a three electrode set up with a Ag/AgCl reference electrode, a platinum counter electrode and a glassy carbon working electrode on which the molecules in nanotubes are deposited. The nanotube sample (0.5 mg) was sonicated (15 mins) in dry DMF (0.5 mL) to form an ink. A portion of the ink (10 μL) was cast onto the GCE and allowed to dry for 1 h. The electrode was then rinsed in dry acetonitrile and allowed to dry in air. All CV experiments start with the application of the starting potential for 5 seconds.

6.5.5 HRTEM

HRTEM analysis was performed on a JEOL JEM-2100F FEG electron microscope with an information limit of 0.12 nm at 100 kV. The imaging conditions were carefully tuned by lowering the accelerating voltage of the microscope to 100 kV and lowering the beam current density to a minimum to avoid electron beam damage to the specimen. Suspensions of guest@nantoube in HPLC grade isopropanol were drop cast onto lacey carbon grids for HRTEM analysis.

6.5.6 EDX

Energy dispersive X-ray spectra were acquired for bundles of SWNT filled with molecules mounted on HRTEM grids using an Oxford Instruments INCA X-ray microanalysis system. The electron beam was condensed onto areas of nanotube bundles suspended over holes of the amorphous carbon film.

6.6 References

1. T. S. Koblenz, J. Wassenaar and J. N. H. Reek, *Chem. Soc. Rev.*, 2008, **37**, 247.
2. D. A. Britz, A. N. Khlobystov, K. Porfyrakis, A. Ardavan and G. A. Briggs, *Chem. Commun.*, 2005, 37.
3. S. A. Miners, G. A. Rance and A. N. Khlobystov, *Chem. Commun.*, 2013, **49**, 5586.
4. X. Pan and X. Bao, *Acc. Chem. Res.*, 2011, **44**, 553.
5. A. Chuvilin, E. Bichoutskaia, M. C. Gimenez-Lopez, T. W. Chamberlain, G. A. Rance, N. Kuganathan, J. Biskupek, U. Kaiser and A. N. Khlobystov, *Nat. Mater.*, 2011, **10**, 687.
6. T. W. Chamberlain, J. Biskupek, S. T. Skowron, P. A. Bayliss, E. Bichoutskaia, U. Kaiser and A. N. Khlobystov, *Small*, 2015, **11**, 510.
7. A. N. Khlobystov, D. A. Britz and G. A. Briggs, *Acc. Chem. Res.*, 2005, **38**, 901.
8. H. Shiozawa, S. R. P. Silva, Z. Liu, K. Suenaga, H. Kataura, C. Kramberger, R. Pfeiffer, H. Kuzmany and T. Pichler, *Phys. Status. Solidi. B*, 2010, **247**, 2730.
9. S. Bandow, M. Takizawa, K. Hirahara, M. Yudasaka and S. Iijima, *Chem. Phys. Lett.*, 2001, **337**, 48.
10. T. W. Chamberlain, J. Biskupek, G. A. Rance, A. Chuvilin, T. J. Alexander, E. Bichoutskaia, U. Kaiser and A. N. Khlobystov, *ACS Nano*, 2012, **6**, 3943.
11. L. Yang, C.-H. Park, Y.-W. Son, M. L. Cohen and S. G. Louie, *Phys. Rev. Lett.*, 2007, **99**, 186801.
12. K. Wakabayashi, *Phys. Rev. B*, 2001, **64**, 125428.
13. D. V. Kosynkin, A. L. Higginbotham, A. Sinitskii, J. R. Lomeda, A. Dimiev, B. K. Price and J. M. Tour, *Nature*, 2009, **458**, 872.

14. S. S. Datta, D. R. Strachan, S. M. Khamis and A. T. C. Johnson, *Nano Lett.*, 2008, **8**, 1912.
15. X. Li, X. Wang, L. Zhang, S. Lee and H. Dai, *Science*, 2008, **319**, 1229.
16. L. Jiao, X. Wang, G. Diankov, H. Wang and H. Dai, *Nat. Nanotechnol.*, 2010, **5**, 321.
17. L. Jiao, L. Zhang, X. Wang, G. Diankov and H. Dai, *Nature*, 2009, **458**, 877.
18. J. Cai, P. Ruffieux, R. Jaafar, M. Bieri, T. Braun, S. Blankenburg, M. Muoth, A. P. Seitsonen, M. Saleh, X. Feng, K. Muellen and R. Fasel, *Nature*, 2010, **466**, 470.
19. B. W. Smith, M. Monthioux and D. E. Luzzi, *Nature*, 1998, **396**, 323.
20. M. A. Lebedeva, T. W. Chamberlain, M. Schröder and A. N. Khlobystov, *Chem. Mater.*, 2014, **26**, 6461.
21. M. A. Lebedeva, T. W. Chamberlain, E. S. Davies, B. E. Thomas, M. Schroder and A. N. Khlobystov, *Beilstein J. Org. Chem.*, 2014, **10**, 332.
22. A. Ardavan, M. Austwick, S. C. Benjamin, G. A. Briggs, T. J. Dennis, A. Ferguson, D. G. Hasko, M. Kanai, A. N. Khlobystov, B. W. Lovett, G. W. Morley, R. A. Oliver, D. G. Pettifor, K. Porfyrakis, J. H. Reina, J. H. Rice, J. D. Smith, R. A. Taylor, D. A. Williams, C. Adelmann, H. Mariette and R. J. Hamers, *Philos. Trans. A Math. Phys. Eng. Sci.*, 2003, **361**, 1473.
23. S. C. Benjamin, A. Ardavan, G. A. D. Briggs, D. A. Britz, D. Gunlycke, J. Jefferson, M. A. G. Jones, D. F. Leigh, B. W. Lovett, A. N. Khlobystov, S. A. Lyon, J. J. L. Morton, K. Porfyrakis, M. R. Sambrook and A. M. Tyryshkin, *J. Phys. Condens. Mat.*, 2006, **18**, S867.
24. P. R. Fielden, S. J. Smith and J. F. Alder, *Analyst*, 1985, **110**, 967.
25. McAllist.Dl, J. P. Pinson and G. Dryhurst, *Anal. Chim. Acta*, 1973, **67**, 415.
26. C. M. A. Brett and A. M. O. Brett, *Electrochemistry principles, Methods and Applications*, Bookcraft (Bath) Ltd., 1993.
27. M. Maggini, G. Scorrano and M. Prato, *J. Am. Chem. Soc.*, 1993, **115**, 9798.
28. M. A. Herranz, B. Illescas, N. Martin, C. P. Luo and D. M. Guldi, *J. Org. Chem.*, 2000, **65**, 5728.
29. M. A. Lebedeva, T. W. Chamberlain, M. Schroder and A. N. Khlobystov, *Tetrahedron*, 2012, **68**, 4976.
30. D. Mancel, M. Jevric, E. S. Davies, M. Schroeder and A. N. Khlobystov, *Dalton Trans.*, 2013, **42**, 5056.
31. A. J. Bard and L. R. Faulkner, *Electrochemical Methods: Fundamentals and Applications*, John Wiley and Sons, Inc., 2001.
32. R. L. McSweeney, T. W. Chamberlain, E. S. Davies and A. N. Khlobystov, *Chem. Commun.*, 2014, **50**, 14338.
33. Y. Iizumi, H. Suzuki, M. Tange and T. Okazaki, *Nanoscale*, 2014, **6**, 13910.
34. X. Liu, H. Kuzmany, P. Ayala, M. Calvaresi, F. Zerbetto and T. Pichler, *Adv. Funct. Mater.*, 2012, **22**, 3202.
35. L. Echegoyen and L. E. Echegoyen, *Acc. Chem. Res.*, 1998, **31**, 593.
36. A. Potocnik, N. Manini, M. Komelj, E. Tosatti and D. Arcon, *Phys. Rev. B*, 2012, **86**, 085109.
37. A. Hirsch and M. Brettreich, in *Fullerenes*, Wiley-VCH Verlag GmbH & Co. KGaA, 2005, pp. 289.
38. H. Alves, A. S. Molinari, H. X. Xie and A. F. Morpurgo, *Nat. Mat.*, 2008, **7**, 574.
39. T. Takenobu, T. Takano, M. Shiraishi, Y. Murakami, M. Ata, H. Kataura, Y. Achiba and Y. Iwasa, *Nat. Mater.*, 2003, **2**, 683.

40. J. Lu, S. Nagase, D. P. Yu, H. Q. Ye, R. S. Han, Z. X. Gao, S. Zhang and L. M. Peng, *Phys. Rev. Lett.*, 2004, **93**, 4.
41. N. M. Brøndsted, L. Christian and B. Jan, *Sulfur Reports*, 2000, **15**, 233.
42. F. D. Saeva, B. P. Morgan, M. W. Fichtner and N. F. Haley, *J. Org. Chem.*, 1984, **49**, 390.
43. A. Coskun, J. M. Spruell, G. Barin, A. C. Fahrenbach, R. S. Forgan, M. T. Colvin, R. Carmieli, D. Benitez, E. Tkatchouk, D. C. Friedman, A. A. Sarjeant, M. R. Wasielewski, W. A. Goddard, III and J. F. Stoddart, *J. Am. Chem. Soc.*, 2011, **133**, 4538.
44. G. Schukat and E. Fanghänel, *Sulfur Reports*, 2003, **24**, 1.
45. A. Pekker and K. Kamaras, *Phys. Rev. B.*, 2011, **84**, 075475.

Concluding remarks

Carbon nanotubes have been attracting increasing interest in the area of nanoreactors and electronics, however, there is a gap in the literature with regard to the electrochemistry of molecules and electrochemical reactions using the internal cavity of carbon nanotubes. Performing electrochemical reactions in solution permits control of only a small amount of molecules within the diffusion layer and is also influenced by the choice of solvent. Reported in this thesis is the dual use of single-walled nanotubes as chemically robust containers for guest-molecules and also nanoscale electrodes. By studying the CV and coulometry of redox active molecules encapsulated inside carbon nanotubes it is possible to control the oxidation state of all molecules within the sample inside carbon nanotubes. This enables control of all redox centres within the sample, providing exciting scope for catalytic applications and also affords an insight into the nature of guest-nanotube interactions. The purpose of this study is to use electrochemistry to delve into the fundamental interactions between carbon nanotubes and guest-molecules, investigate how the nanoscale cavities of carbon nanotubes can affect electrochemical reactions and for the first time follow electrochemical reactions inside SWNT by using CV as a means with which to explore the mechanisms of reactions at the nanoscale.

In order to study the interactions of molecules within the internal cavities of carbon nanotubes, the change in the nanotube electrochemical potential and therefore the injection and removal of electrons was used. Electrochemical potential is the perfect probe due to the high conductivity of nanotubes and also because the electron is responsible for a large proportion of the host-guest interactions. New techniques and concepts are developed in this thesis to adapt existing understanding of both solution and solid-state electrochemistry to the CV and coulometry of molecules in carbon nanotubes including the effect that external solvents and the immobilisation of molecules has on their redox properties.

The encapsulation of metallocenes in carbon nanotubes has attracted increasing interest both experimentally and theoretically but previous methods often used indirect methods for determining the effect carbon nanotube encapsulation has on guest-molecules. Presented in this thesis is the direct measurement of the respective molecular orbital energies of different metallocenes in carbon nanotubes. The increased electron transfer observed for cobaltocene compared to ferrocene is measured and this is related to theoretical studies, considering the energies of the valence and conduction bands of SWNT that are also measured and compared to theory using LSV. It was observed that increasing the number of methyl groups on the cyclopentadienyl ring increased the electron transfer from the guest-metallocene to the nanotube due to the increasing energy of the HOMO with an increasing number of methyl groups allowing access to further electronic states of the SWNT. The internal diameter of the SWNT also changes the magnitude of electron transfer from ferrocene, the narrower the nanotube the more electron transfer observed due to the narrowing of the nanotube bandgap and therefore the increased energy of the nanotube valence band. These results show the interactions of different guest-molecules with nanotubes and also that electrochemistry is the ideal technique for measurements of guests inside nanotubes.

Whilst electron transfer from a guest to the nanotube instils exciting changes of properties in the guest, it also has consequences on the electronic levels of the host-nanotube. Using coulometry, the electronic structure of the nanotubes has been directly gauged, determining whether the change in the occupied electronic states of the nanotube results in an elevation of the Fermi level that is sufficient to change the nanotube from predominately semiconducting to predominantly metallic. Coinciding with other CV results, it was shown that nanotubes containing cobaltocene possess a metallic electronic structure. The band gap of nanotubes containing ferrocene narrows but the host-nanotube remains predominantly semiconducting. Again this change in electronic structure of the nanotube can be related to the energy of the HOMO/SOMO of the guest-molecules. This qualitative method can be developed further to determine the quantitative electron transfer from guest-molecules to the nanotube using the Nernst equation. The coulometry experiment of empty SWNT shows the position of the Fermi level in electrochemical potential of both the metallic and semiconducting nanotubes which is the potential the nanotube exerts on the guest-molecules in the absence of any external applied potential. Applying the Nernst equation, the relationship of the HOMO/SOMO and the Fermi level provides a quantitative electron transfer between carbon nanotubes and guest-molecules.

Not only does confinement in nanotubes influence the electronic factors involved in the host-guest interactions, but also the steric effects because the space around the guest-molecule is severely limited. Results in this thesis show that the extreme spatial confinement by SWNT changes the way the electrochemical ligand exchange in the $Cp^{Me}Mn(CO)_3$ complex proceeds. The nanotube prevents external nucleophiles (e.g. solvents) from entering the nanotube, but also the close proximity of the nanotube sidewalls and tight packing of $Cp^{Me}Mn(CO)_3$ prevents the required ligand elimination. The pathway of this electrochemical reaction is carefully followed using CV and, for the first time, an irreversible oxidation is manipulated by nanotube confinement to become chemically reversible, as shown by the presence of both the oxidation and corresponding reduction when performing the CV of $Cp^{Me}Mn(CO)_3$@SWNT.

This result leads into further manipulation of reactions so that, rather than preventing a reaction, a new product can be formed that is not possible in bulk solution. One of the first examples of SWNT-mediated electronic communication was demonstrated with C_{60}dimer@SWNT which is proposed to play an important role in quantum information processing. Moreover, C_{60}dimers along with other examples such as $C_{60}Fe(Cp)_2$ can then be transformed into different species inside a nanotube using externally applied potential. This only occurs due to the tight constriction of the carbon nanotube around the guest and the way that the molecules interact with the nanotube sidewalls. Another example presented in this thesis is the formation of sulfur terminated graphitised nanoribbon inside nanotubes which is synthesised by applied electrochemical potential for the first time. The use of electrochemistry allows the exploration of the mechanism of S-GNR formation and is also an energy efficient method to make S-GNR compared to the previously reported methods utilising high temperatures or exposure to an electron beam. These results show how SWNT entrap the guest-molecules in intimate contact with the highly conductive walls of the nanotube, limiting their movement and promoting reactions along the SWNT channel to transform guest-molecules into new products, which are otherwise challenging.

In conclusion this study has: (1) developed a method to measure the electronic influence carbon nanotubes have on guest-molecules, (2) determined the effects that guest-molecules have on the electronic properties of the carbon nanotube, including a new method to quantify the electron transfer between guest-molecules and the host-nanotube, (3) developed a method to measure the effect guest-molecule encapsulation has on the electronic properties of a host-SWNT, (4) employed the extreme spatial confinement of the nanotube to change the pathway of an electrochemical reaction occurring in the internal cavity of a SWNT, (5) achieved the SWNT-mediated electronic communication between two C_{60} moieties and (6), exploited the fundamental understanding of the spatial and electronic interactions to direct the pathways of electrochemical reactions inside nanotubes, that wouldn’t occur in bulk solution, and to form polymeric products that are templated by the specific size of the nanotube. Consequently, the work presented in this thesis represents a significant contribution to the field of carbon nanotubes and more specifically the relatively undeveloped field of electrochemistry in nanotube confinement.

Future studies in this area are endless, for instance, using electrochemistry to determine compatibility of hybrid materials for nanoreactors, electronics or other devices that rely upon doping by measuring the electronic influence the guest-molecule has on the host-nanotube and *vice versa*. Furthermore, using the information gained about electronic interactions in combination with the extreme spatial confinement can be exploited to develop the use of organometallic catalysts inside carbon nanomaterials. This can act to change the pathway of the catalysis, immobilise the catalyst and also provide control of an electrocatalytic reaction *via* a change in applied potential. Transformations in nanotubes can be extended towards molecular release by breaking linker bonds to C_{60} anchors and hence releasing a molecule for molecular delivery, for instance, an initiator for a reaction. Other transformations can lead to the energy efficient, large scale preparation of novel products with distinct properties such as nanoribbons. The immediate challenge is to use S-GNR materials as-prepared inside the nanotube for electronic application or to attempt to remove the nanoribbon from the nanotube. These opportunities present an exciting direction for future work and applications for preparative electrocatalysis and the formation of novel materials.